Quantitative Spectroscopy of Galactic BA-type Supergiants

Der Naturwissenschaftlichen Fakultät
der Friedrich-Alexander-Universität Erlangen-Nürnberg
zur
Erlangung des Doktorgrades Dr. rer. nat.

vorgelegt von
Markus Georg Manfred Firnstein

aus Scheßlitz

IV

Zusammenfassung

Massereiche Sterne – Sterne mit mehr als acht Sonnenmassen – sind kurzlebige Objekte, die wegen ihrer hohen Leuchtkräfte das Erscheinungsbild von Sternentstehungsgebieten bestimmen. Über ihre starken Sternwinde und die Supernovaexplosionen am Ende ihres Lebens verteilen sie die in ihrem Inneren erbrüteten Elemente an die umliegende interstellare Materie, und spielen so eine aktive Rolle in der Entwicklung von Galaxien. Überriesen der Spektraltypen B und A (BA-Überriesen) repräsentieren eine späte Entwicklungsphase der massereichen Sterne. Sie zeichnen sich vor allem durch ihre hohe visuelle Helligkeit aus, die sie zu exzellenten Indikatoren für stellare und galaktische Astrophysik macht.

Ziel dieser Arbeit war eine umfassende, homogene Analyse von einer möglichst großen Anzahl von BA-Überriesen in unserer Galaxie, wobei die Atmosphären- und Fundamentalparameter der Sterne sowie die Häufigkeiten der Elemente Helium, Kohlenstoff, Stickstoff, Sauerstoff, Magnesium, Schwefel, Titan und Eisen mit hoher Genauigkeit bestimmt werden. Um das zu erreichen, wurden zunächst hochaufgelöste Echelle-Spektren mit einem hohen Signal-zu-Rausch-Verhältnis und einer umfassenden Wellenlängenabdeckung von ∼3900 bis 9100 Å aufgenommen. Eine ausführliche Datenreduktion war notwendig, um die Rohdaten in wellenlängenkalibrierte, rektifizierte Spektren zu verwandeln, die sich zur Analyse eignen.

Im nächsten Schritt wurde ein großes Gitter von synthetischen Spektren erstellt, das den erwarteten Parameterbereich der Zielsterne abdeckt. Bei den numerischen Berechnungen wurde eine sogenannte non-LTE-Methode angewandt, die dem aktuellen Stand der Forschung entspricht. Um den komplizierten physikalischen Gegebenheiten in den Sternatmosphären von BA-Überriesen gerecht zu werden, müssen Abweichungen von der Standardannahme des lokalen thermischen Gleichgewichts (LTE) – die zu einer deutlichen Vereinfachung der Analyse führt – zugelassen werden, was eine Vielzahl an zuverlässigen atomaren Daten erfordert und die Rechenzeit beträchtlich erhöht. Nur so aber kann die geforderte hohe Genauigkeit gewährleistet werden.

Als nächstes wurde eine Analysestrategie entwickelt, um die wichtigsten atmosphärischen Parameter – Effektivtemperatur, Schwerebeschleunigung an der Oberfläche, Mikroturbulenz und Heliumhäufigkeit – auf eine homogene und effiziente Art und Weise zu bestimmen. Hohe Präzision ist hierbei eine Grundvoraussetzung, um die gewünschte Genauigkeit in der Häufigkeitsbestimmung zu erzielen. Die Resultate konnten genutzt werden, um neue Standards im Bereich der BA-Überriesen zu setzen, wie z. B. eine Neukalibration der Beziehung zwischen Spektralklasse und Effektivtemperatur.

Im Anschluss konnten die Häufigkeiten der Elemente C, N, O, Mg, S, Ti und Fe in den Atmosphären der BA-Überriesen mit einer für eine solch große Anzahl von Objekten bisher unerreichten Genauigkeit aus den jeweiligen Spektrallinien abgeleitet werden. Die Häufigkeiten der leichten Elemente He, C, N und O sind von großem Nutzen, um den

Entwicklungsstand von BA-Überriesen festzustellen. Tatsächlich verbringen massereiche Sterne einen Großteil ihrer Lebenszeit damit, im Kern Wasserstoff zu Helium umzuwandeln, was im sogenannten CNO-Zyklus geschieht. Das führt zu einer Anreicherung von Stickstoff bei gleichzeitiger Abreicherung von Kohlenstoff und, in geringerem Ausmaße, Sauerstoff. Folglich können die Häufigkeitsverhältnisse N/C und N/O verwendet werden, um Spuren dieses Prozesses zu entdecken. Im Rahmen dieser Arbeit konnte zum ersten Mal nachgewiesen werden, dass diese beiden Indikatoren in BA-Überriesen tatsächlich in der engen Beziehung stehen, die von der Sternentwicklungstheorie vorausgesagt wird. Zusätzlich wurde auch die erwartete Korrelation zwischen diesen beiden Indikatoren und der in vorangegangenen Studien zumeist ignorierten Heliumhäufigkeit gefunden.

Verschiedene Mischungsprozesse sind für den Transport von prozessiertem Material vom Sterninneren in die Photosphäre verantwortlich, wobei die Effizienz oft nur unzureichend bekannt ist. Die verschiedenen Entstehungsszenarien für BA-Überriesen unterscheiden sich in der Art der möglichen Mischprozesse. Rein rotationsinduzierte Mischung ist vorausgesagt, falls der Stern sich direkt von der Hauptreihe zum jetzigen Zustand entwickelt hat. Falls jedoch bereits das Rote-Riesen-Stadium durchlaufen wurde, hatte das eine komplette Durchmischung der Hülle aufgrund des tiefen Eindringens der Konvektionszonen zur Folge (sog. „first dredge-up").

Alle Objekte in der Auswahl zeigen klar die Signatur des CNO-Prozesses: Das Massenverhältnis N/C erreicht Werte von 0.63 bis 4.66, im Vergleich zu einem typischen Wert von ungefähr 0.3, der aus Studien der Vorläufersterne auf der Hauptreihe und von der Sonne bekannt ist. Dennoch führt der Vergleich mit gängigen Sternentwicklungsmodellen nicht zu einem eindeutigen Ergebnis: Sowohl eine starke rotationsinduzierte Mischung, möglicherweise verstärkt durch Magnetfelder, als auch ein Szenario mit dredge-up könnte zu solch hohen Werten führen. Einzig die Tatsache, dass sich im Sample keine Sterne ohne Anzeichen des CNO-Prozesses befinden – was erwartet würde von langsamen Rotatoren die keinen dredge-up durchlaufen – deutet darauf hin, dass alle oder zumindest die meisten Sterne das Rote-Riesen-Stadium bereits einmal hinter sich haben.

Ein weiteres Ziel dieser Arbeit war es, Randbedingungen für galaktochemische Entwicklungsmodelle zu liefern. Dazu wurde die Häufigkeitsverteilung in der Galaxie auf Gradienten hin untersucht, und zwar als Funktion des Abstands zum galaktischen Zentrum. Massereiche Sterne wie BA-Überriesen mit ihren kurzen Lebenszeiten eignen sich gut dazu, die gegenwärtigen Elementhäufigkeiten im interstellaren Medium – aus dem sie nach astronomischen Maßstäben erst kürzlich geformt wurden – auszuloten. BA-Überriesen haben dabei den großen Vorteil, dass ihre Entfernungen mittels rein spektroskopischer Methoden abgeschätzt werden können – über die sogenannte flussgewichtete Schwerebeschleunigungs-Leuchtkraft Relation (FGLR). Ursprünglich für extragalaktische Zwecke entwickelt, erlaubte sie es hier, die Position der Sterne im galaktischen Bezugssystem festzustellen.

Die Häufigkeitsgradienten in der Milchstraße in einem Bereich zwischen 6 und 12 kpc Abstand vom galaktischen Zentrum konnten bestimmt werden, und zwar zu -0.041 ± 0.005 dex/kpc für Sauerstoff, -0.034 ± 0.007 dex/kpc für Magnesium, -0.049 ± 0.008 dex/kpc für Schwefel, -0.038 ± 0.012 dex/kpc für Titan und -0.058 ± 0.009 dex/kpc für Eisen. Trotz der eher limitierten räumlichen Ausdehnung des Samples konnten die Gradienten mit geringer Unsicherheit bestimmt werden. Der Vergleich mit im Laufe der letzten Jahre

erschienenen Studien, die auf der Analyse anderer Objekte, wie z. B. H II-Regionen und jungen Hauptreihensternen, beruhen, zeigt gute Übereinstimmung, was die abgeleiteten Gradienten betrifft, aber systematische Unterschiede zwischen den Absolutwerten. Von einer Erweiterung des Samples mit anderen Objekten sollte daher abgesehen werden, um mögliche, aus eben dieser Diskrepanz resultierende, systematische Fehler zu vermeiden.

Ein weiteres, bedeutendes Resultat ist die weitgehende Homogenität des interstellaren Mediums auf kleinen Skalen. Wenn man die Effekte der Gradienten berücksichtigt, findet man nur eine sehr geringe Streuung in den Elementhäufigkeiten vor, was eine gute Durchmischung des interstellaren Materials impliziert. Ein Großteil der in früheren Arbeiten gefundenen Streuung sollte also auf Unsicherheiten in der Häufigkeitsbestimmung zurückzuführen sein.

Die Verhältnisse der Häufigkeitsgradienten untereinander sind vereinbar mit den grundlegenden Zusammenhängen, die aus dem Gebiet der galaktochemischen Entwicklung bekannt sind: Elemente, die auf längeren Zeitskalen produziert werden, zeigen steilere Gradienten. Dies stimmt damit überein, dass der stärkste Gradient für Eisen bestimmt wurde. Aber es zeigt sich auch eine erstaunlich gute Übereinstimmung mit den Voraussagen eines kürzlich erstellten numerischen Entwicklungsmodells: Voraussagen für alle untersuchten Elemente liegen innerhalb der engen Fehlergrenzen.

Zusammenfassend lässt sich sagen, dass durch die homogene Analysemethodik die *relativen* Fehler in der Häufigkeitsbestimmung dramatisch reduziert wurden, was in nahezu allen Anwendungen – egal ob bezogen auf Stern- oder Galaxienentwicklung – in einer verringerten Streuung und einer damit verbundenen erhöhten Aussagekraft deutlich wurde.

VIII

Abstract

Massive stars are short-lived phenomena that dominate the appearance of regions of active star formation. They are important sites of nucleosynthesis and play an active role in the evolution of galaxies by enriching the interstellar medium with nuclearly processed material via supernovae and stellar winds. Supergiants of late B and early A-type (BA-type supergiants) represent an advanced phase of massive star evolution, distinguished by their high visual brightness. As such, they show high potential as versatile indicators for stellar and galactic physics.

The aim of this thesis was to perform a comprehensive and homogeneous study of a large number of BA-type supergiants, in which atmospheric and fundamental stellar parameters, and abundances for light, α-process and iron group elements alike are derived. To this end, high-resolution and high-signal-to-noise spectra with an extensive wavelength coverage from $\sim$3900 to 9100 Å were obtained, using three Echelle spectrographs mounted on telescopes both on the northern and southern hemisphere. Following the observations an extensive data reduction was performed, to transform the raw images into wavelength-calibrated and normalized spectra.

In a next step, an extensive grid of synthetic spectra was constructed, in order to perform quantitative spectroscopy in a consistent, methodical way. For the calculations a state-of-the-art non-LTE analysis technique was adopted, accounting for deviations from the classical assumption of local thermal equilibrium (LTE). The more complicated treatment increases the required computing times, and sophisticated model atoms comprised of accurate atomic data have to be incorporated. Following these preparations, a data analysis strategy was devised to determine the most important atmospheric parameters – effective temperature, surface gravity, microturbulence and surface helium abundance – in an efficient and homogeneous way, which is a crucial prerequisite to reach the principal goals of this study. The results were used to set new standards in the BA-type supergiant regime, e.g., for the relation between spectral type and effective temperature. With precise atmospheric parameters obtained, the surface abundances of the elements C, N, O, Mg, S, Ti, and Fe could be derived from extensive sets of spectral lines with unprecedented accuracy.

Surface abundances of the light elements He, C, N, and O were used to obtain observational constraints on the evolutionary status of BA-type supergiants. Massive stars burn hydrogen to helium via the CNO-bi-cycle in their cores for most of their life. This leads to an enrichment of nitrogen and a depletion of carbon and – to a lesser extent – oxygen. Consequently, the abundance ratios N/C and N/O determined in stellar atmospheres provide valuable insight into the evolutionary status of these stars. The results of the present study show – for the first time – that these two indicators obey a tight relation in Galactic BA-type supergiants, in excellent agreement with the predictions of stellar evolution mod-

els. In addition, the helium abundance – which was mostly ignored in previous studies – was found to be correlated to the other indicators of CNO-mixing, as predicted.

Albeit, the comparison of the results with current models of stellar evolution remained inconclusive. In theory, the formation scenarios for BA-type supergiants differ in the amount of nuclearly processed material found on the surface. However, various mixing processes are responsible for the transport of nuclearly processed material from the core to the surface, and their efficiency is poorly constrained. Purely rotationally-induced mixing is expected, if the stars have evolved directly from the main sequence, while the additional signature of a convective "dredge-up" is predicted, should they have passed through a red supergiant phase during their previous evolution. Clear signatures of CNO-mixing were found in all stars, with the derived nitrogen to carbon mass ratio N/C covering a wide range from 0.63 to 4.66, compared to typical values of ≈ 0.3 found in studies of their progenitors and the Sun. However, both strong rotationally-induced mixing, possibly enhanced by magnetic fields, and a dredge-up scenario can produce these values according to theoretical models. Only the absence of stars in the sample that show no sign of CNO-mixing – which would be expected for slow rotators that experience no dredge-up – favors scenarios involving a dredge-up event for most or even all objects.

Another goal of this thesis was to put constraints on numerical models of Galactochemical evolution by determining the abundance gradients of several elements in the interstellar medium, using BA-type supergiants as tracers. The distances of individual stars were determined based on a purely spectroscopic method, the flux-weighted-gravity-luminosity relationship (FGLR), originally developed for extragalactic applications. Abundances were determined for Galactocentric radii of 6–12 kpc, yielding abundance gradients of -0.041 ± 0.005 dex/kpc for oxygen, -0.034 ± 0.007 dex/kpc for magnesium, -0.049 ± 0.008 dex/kpc for sulfur, -0.038 ± 0.012 dex/kpc for titanium and -0.058 ± 0.009 dex/kpc for iron. Despite the limited spatial extent of the sample, the results establish the existence of rather flat gradients within tight constraints. Comparison to some of the most recent studies using various tracers shows reasonable agreement in the gradients, but systematic differences in absolute abundances. Another important outcome of this thesis is that the interstellar matter is well-mixed and *locally* homogeneous, as low star-to-star scatter is found when accounting for the gradient. This result indicates that the large scatter found in many previous studies is mostly caused by the uncertainties in the abundance determination.

The relative amplitudes of the derived gradients, based mostly on the timescales on which the elements are produced, are consistent with what is expected in the general picture of Galactochemical evolution, i.e., iron abundances most rapidly declining with increasing Galactocentric radius. More specifically, the predictions of a recent model of the chemical evolution of the Milky Way could be successfully verified, as they are within the derived error bounds for all elements under study.

In summary, a significant reduction of systematic scatter in comparison to most previous studies can be noticed in nearly all applications – both in the context of stellar and Galactic evolution. This shows, that the detailed, homogeneous analysis presented in this thesis resulted in a considerable reduction of *relative* uncertainties within the sample. Future expansion of this study to a wider range of objects and distances promises to answer more questions concerning the evolution of massive stars and the Milky Way.

Contents

Contents

1 Introduction

Supergiants of late B and early A-type (BA-type supergiants) are among the *visually* brightest stars, reaching absolute magnitudes of up to $M_V \approx -9.5$. Indeed, some of the most prominent objects in the night sky are part of this study: Deneb (α Cygni) and Rigel (β Orionis, see Fig. 1.1). Consequently, this class of objects shows a high potential to probe stellar and galactic physics over large distances, even beyond the Local Group, using ground-based telescopes of the 8-10 m class.

Tepid supergiants are a rare and short-lived phenomenon, representing an advanced phase of massive star evolution. Hence, they provide an excellent testbed for stellar evolution theory. The most recent generations of evolution models for massive stars account for effects of rotation and mass loss (Heger et al. 2000; Maeder & Meynet 2000; Meynet & Maeder 2003) as well as magnetic fields (Heger et al. 2005; Maeder & Meynet 2005). These models are highly successful in describing many observational aspects of the massive star populations in general. However, many details – in particular related to the subtle processes of mixing of CNO-cycled products in the stars – are subject to intense debate at present, see e.g. Hunter et al. (2009), Maeder et al. (2009) and Przybilla et al. (2010). Here, highly accurate observational data on fundamental stellar parameters and abundances of light element are required to test the models thoroughly. Furthermore, the evolutionary status of BA-type supergiants themselves is still up to discussion: One option is that they have evolved directly from the main sequence to their current state. Alternatively, however, they are passing through so-called blue loops after going through a red supergiant phase. A detailed, quantitative spectroscopic analysis of a sufficient number of stars can shed new light on this controversy.

Understanding the evolution of massive stars is a prerequisite to successfully model the chemical evolution and star-formation history of galaxies. Massive stars enrich the interstellar medium with nuclearly processed material through stellar winds and supernovae events, thus playing a crucial role in the cosmic matter cycle. Furthermore, abundance analyses of massive stars hold the key to understand the chemical evolution of the Galaxy. Luminous BA-type supergiants can be highly useful in mapping elemental abundance patterns throughout the Milky Way. Systematic investigations of these short-lived stars can constrain the present-day abundance gradients in the interstellar matter (ISM) for large parts of the Galactic disk – important observational constraints to Galactochemical evolution models. Previous results are based on the analysis of H II-regions, the typical tracers of the ISM, and young stars. The problems encountered when combining them are illustrated in Fig. 1.2.

The addition of BA-type supergiants into this field could verify, complement and extend studies using other tracers. Accurate and unbiased elemental abundances for a larger sample of objects with well-constrained distances – and sufficient spatial coverage – are

Figure 1.1: The B-type supergiant Rigel is illuminating the Witch Head Nebula (IC 2118), a site associated with current star formation (Kun et al. 2004). Credit: Rogelio Bernal Andreo (DeepSkyColors.com)

required for this. Another great advantage of BA-type supergiants is that they can act as standard candles for distance determinations via a purely spectroscopic method, the flux-weighted gravity-luminosity relationship (FGLR, Kudritzki et al. 2003, 2008). Originally developed for extragalactic applications, it can also be used to determine the distance of individual objects in the Milky Way, thereby simplifying the mapping of the Galactic disk.

The focus of quantitative studies of individual BA-type supergiants lies in extragalactic research at present, however. Objects in many of the star-forming galaxies of the Local Group (e.g., Bresolin et al. 2007; Urbaneja et al. 2008; U et al. 2009) and beyond (e.g., Kaufer et al. 2004; Evans et al. 2007; Kudritzki et al. 2008) have been investigated at high and intermediate spectral resolution, as they became accessible to the new generation of large telescopes and their highly efficient instrumentation.

While the literature on properties of extragalactic objects is rich, few studies have concentrated on Galactic BA-type supergiants in recent years, although these objects provide benchmarks for the spectroscopic methods used in extragalactic applications. Pioneering work was done by Venn (1995a,b), later updated by Venn & Przybilla (2003), who determined atmospheric parameters and chemical abundances for a sample of 22 Galactic
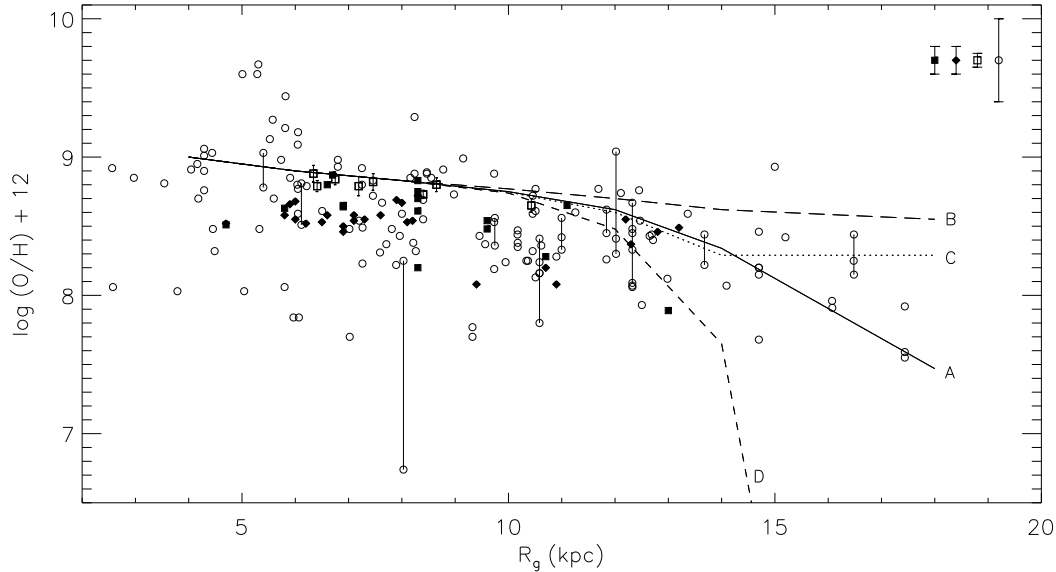
Figure 1.2: Problems encountered in the study of Galactic abundance gradients and their interpretation. Oxygen abundance determinations from H II regions (Esteban et al. 2005: boxes; Rudolph et al. 2006, and references therein: circles) and B-type stars (Gummersbach et al. 1998: filled boxes; Daflon & Cunha 2004: diamonds), representing the current status of the ISM, are frequently compared to Galactochemical evolution models (A-D, see Chiappini et al. 2001 for details), as a function of Galactocentric radius R_g, as shown here. However, a large spread of the observational data and systematic offsets between different data sets are not uncommon. Interconnected symbols represent double observations; typical error bars are shown in the upper right corner.

A-type supergiants, mostly less-luminous ones of luminosity class II and Ib. Verdugo et al. (1999) derived basic stellar parameters for 31 early A-type supergiants, while the compilation of Lyubimkov et al. (2010) provides such data for 8 mostly less-luminous late A-type supergiants. Moreover, atmospheric parameters for a smaller number of late B-type supergiants were provided by McErlean et al. (1999) and Fraser et al. (2010). The most comprehensive study is from Takeda & Takada-Hidai (2000 and references therein) on a representative sample of BA-type supergiants in that it accounts for deviations from the standard assumption of local thermodynamic equilibrium (non-LTE).

As pointed out before, several key issues can be adressed by studies of BA-type supergiants. Their versatility is a strong motivation to perform a comprehensive and homogeneous study, in which atmospheric and fundamental stellar parameters, and abundances for light, α-process and iron group elements alike are derived. To this end, the most comprehensive sample of Galactic BA-type supergiants is constructed, including state-of-the-art observational data based on Echelle spectra. An extended grid of synthetic spectra is constructed, based on a sophisticated non-LTE analysis methodology (Przybilla et al. 2006), which was further refined and automated. All in all, this allows results for a large number of objects with the highest accuracy presently possible to be obtained, both in atmospheric parameters and surface chemical abundances.

The thesis is organized as follows: In Chapter 2 the data reduction methods and the observational database are presented. Chapter 3 gives an introduction into the physical models and numerical techniques behind quantitative spectroscopy, focusing on the method utilized in this study. In Chapter 4, the refined data analysis strategy, a major part of this work, is discussed. Subsequentially, the results of the meticulous determination of the atmospheric parameters, including several checks for consistency, are presented in Chapter 5. In Chapter 6, the derived observational constraints, among them the abundances of the light elements He, C, N, and O – on massive star evolution are discussed and a detailed interpretation in the context of current stellar evolution models is provided. Chapter 7 presents the derived abundance gradients for the elements O, Mg, S, Ti, and Fe, compares them to previous findings and discusses their relevance for current models of Galactochemical evolution. Finally, the outcomes of this thesis are briefly summarized in Chapter 8, and a short outlook into related future work is given.

Some preliminary findings were already published in Firnstein & Przybilla (2006). Results for a subsample of the stars studied in this thesis were presented by Przybilla et al. (2010), successfully show-casing the unprecedented accuracy of this study in the context of evolutionary models. A series of three papers containing the bulk of this thesis is in preparation: Paper I will discuss the derived atmospheric parameters, as presented in Chapter 5, Paper II will concentrate on observational constraints to evolution models for massive stars, as put forward in Chapter 6, and Paper III will focus on the derived abundance gradients in the context of Galactochemical evolution, as discussed in Chapter 7.

2 Observations and Data Reduction

Adequate observational data are needed to achieve high precision in quantitative spectroscopy. High-resolution spectroscopy helps to reduce the influence of instrumental broadening and to avoid excessive line blending, thereby facilitating detailed line-profile fitting. The typical broadening of metal lines – due to macroturbulence and stellar rotation – in spectra of BA-type supergiants is of the same order of magnitude as the broadening by an instrument with a resolution $R \approx 10\,000$. Hence, any significant additional loss of spectral resolution is avoided by choosing observational setups with a minimum resolution $R = 40\,000$. At the same time we demand high signal-to-noise ratios (S/N) in excess of 150 to reduce statistical uncertainties. Additionally, a sufficient wavelength coverage from 3900 to 9000 Å is pivotal for this analysis. It ensures that certain strategic sets of lines both for parameter and abundance analysis are completely available for all stars. As will be seen in the following chapter Echelle-spectrographs are best-suited to fulfill our demands.

2.1 Fundamentals of Echelle-Spectroscopy

Echelle spectrographs combine high resolving power with good wavelength coverage and are therefore extensively used in contemporary astronomy. Some of their properties will be outlined in the following, an extensive discussion can be found, e.g., in Schroeder (2000) or Gray (1997).

The spectral resolution R of a refraction grating is given by

$$R = \lambda/\Delta\lambda_0 = nN, \tag{2.1}$$

where $\Delta\lambda_0$ denotes the smallest distinguishable difference between lines in wavelengths, N the spectral order and n the number of grooves. Hence, an increase in resolution power is possible by either raising the number of grooves, which is costly, or by considering higher orders. The latter method is applied in Echelle-spectrographs. Beside the number of grooves per mm, Echelle-gratings are characterized by their blazing angle δ, i.e., the angle the reflective grooves are tilted relative to the grating normal, as shown in Fig. 2.1.

To understand the general principle behind blazed gratings, first consider an unblazed reflective grating with facet width b and even spacing σ. The normalized intensity I can be written as a product of the grating's interference function IF and the so called blaze function BF:

$$I = \text{IF} \times \text{BF}. \tag{2.2}$$
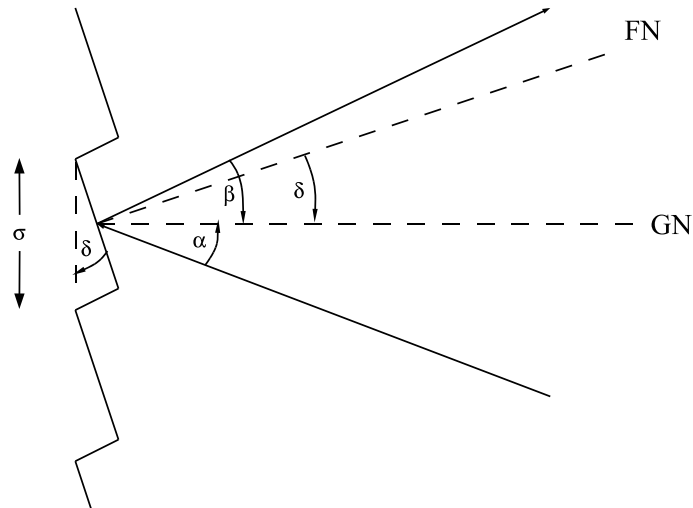
Figure 2.1: As for conventional gratings, diffraction occurs at a regular pattern. In case of Echelle-gratings it takes the form of a stair-like structure. Here α und β denote the angles of incidence and emergence of the light, GN and FN the normals of the grating and the facettes, respectively, while δ is the blazing angle.

The interference function can be derived using geometric optics, and is given as

$$\mathrm{IF} = \left(\frac{\sin n\gamma'}{n \sin \gamma'} \right)^2 , \tag{2.3}$$

where

$$\gamma' = \frac{\pi\sigma}{\lambda} \left(\sin \alpha + \sin \beta \right) . \tag{2.4}$$

The normalized blaze function resembles the diffraction pattern of a single slit:

$$\mathrm{BF} = \left(\frac{\sin \gamma}{\gamma} \right)^2 , \tag{2.5}$$

where

$$\gamma = \frac{\pi b}{\lambda} \left(\sin \alpha + \sin \beta \right) . \tag{2.6}$$

The blaze function can be described as the envelope of the interference pattern in the resulting intensity distribution. It reaches its global maximum where the angle of incidence α equals the angle of emergence β, analogous to ordinary reflection at mirrors. This is also the location of the zeroth order of the interference function, and thus this order gets amplified while other orders lose efficiency.

This picture changes, if we introduce a tilt of the facets, as in the triangular profile of an Echelle grating (see Fig. 2.1). We can modify the blaze function to resemble this by shifting the angles in equation 2.6 by the blaze angle δ ($\alpha \to \alpha - \delta$, $\beta \to \beta - \delta$) and using the
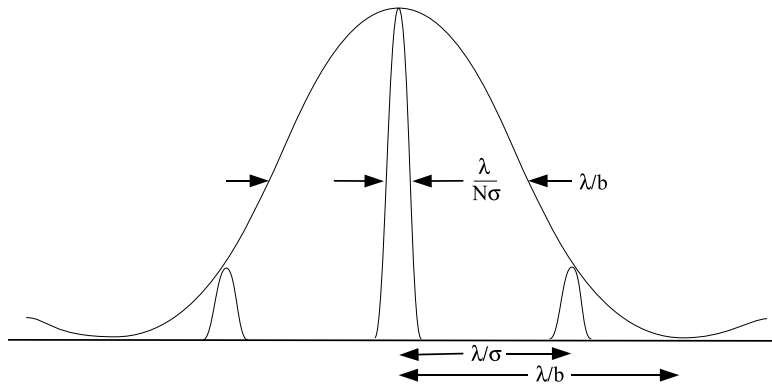
Figure 2.2: Schematic intensity distribution of a blazed grating, where σ is the groove spacing and b the active facet width. The primary quantity determining which spectral order N is amplified the most is the wavelength. Adopted from Gray (1997).

optically active width of a single facet ($b \rightarrow \sigma \cos \delta$). A large δ shifts the maximum of the blaze function and thereby the bulk of the intensity distribution to higher spectral orders ($N \sim 50$ for the instruments used here), while the smaller active width b is widening the profile of the blaze function. The resulting intensity distribution for a single wavelength is sketched in Fig. 2.2. Note that for high blaze angles shadowing effects can decrease the active facet width depending on the angle of incidence, which complicates the problem. Thus, while the principles outlined so far provide good insights, the problem is more complicated in practice.

Due to the nature of the interference pattern, higher spectral orders overlap. A second, perpendicularly mounted dispersive element is required to separate them, the so called cross-disperser. It can be another grating, a prism or a combination of the two, i. e., a grism. The basic layout of an Echelle-spectrograph is depicted in Fig. 2.3.

2.2 Instruments

Data from three high-resolution Echelle-spectrographs were considered for this study. A brief description of the properties of the respective observational data follows:
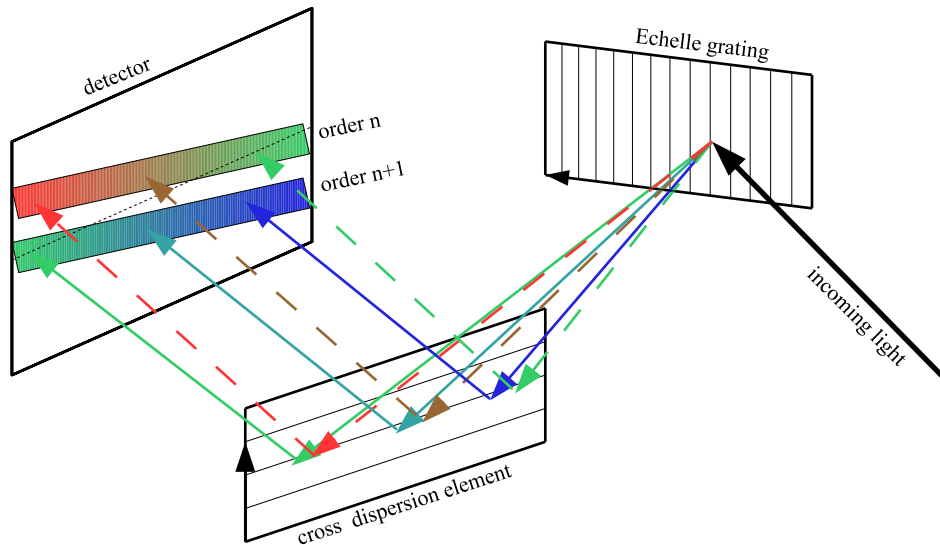
Figure 2.3: Basic layout of an Echelle-spectrograph (courtesy of A. Irrgang).

- **FOCES**

  Most of the spectra were obtained in observing runs with the Fibre Optics Echelle Cassegrain Spectrograph (FOCES, Pfeiffer et al. 1998) on the Calar Alto 2.2 m telescope[1] in 2001 and 2005. They cover a wavelength range from 3860 to 9580 Å at a resolving power $R = \lambda/\Delta\lambda \approx 40\,000$. Only the data for HD 195324 were acquired by K. Fuhrmann with a different setup, trading higher resolution for a lower wavelength coverage. Relatively bright objects were observed in order to reach the desired spectrum quality of more than 150 in S/N ratio.

- **FEROS**

  Additional objects were observed in 2007[2] at the European Southern Observatory in La Silla, using FEROS (Fiber-fed Extended Range Optical Spectrograph, Kaufer et al. 1999) on the 2.2 m telescope. The spectra cover the wavelength range from 3600 to 9200 Å at a resolution of $R = \lambda/\Delta\lambda \approx 48\,000$. The older spectra in common with Przybilla et al. (2006) (see details on the data reduction there) were collected when FEROS was still attached to the 1.52 m telescope also located at La Silla. The wavelength-dependent efficiency of this spectrograph is shown in Fig. 2.4. Both FOCES and FEROS are fiber-fed and bench-mounted to ensure a stable performance independent of factors like temperature or telescope pointing.

- **UVES**

  The UVES Paranal Observatory Project (Bagnulo et al. 2003)[3] provides an atlas of high-resolution spectra of bright stars across the Hertzsprung-Russell Diagram, which also contains high-quality spectra of BA-type supergiants. The UV-visual

---

[1] The Centro Astronómico Hispano Alemán (CAHA) at Calar Alto is jointly operated by the Max-Planck Institut für Astronomie (MPIA) in Heidelberg, Germany, and the Instituto de Astrofísica de Andalucía (CSIC) in Granada, Spain (http://www.caha.es/).

[2] Proposal 079.B-0856(A)

[3] ESO DDT Program ID 266.D-5655
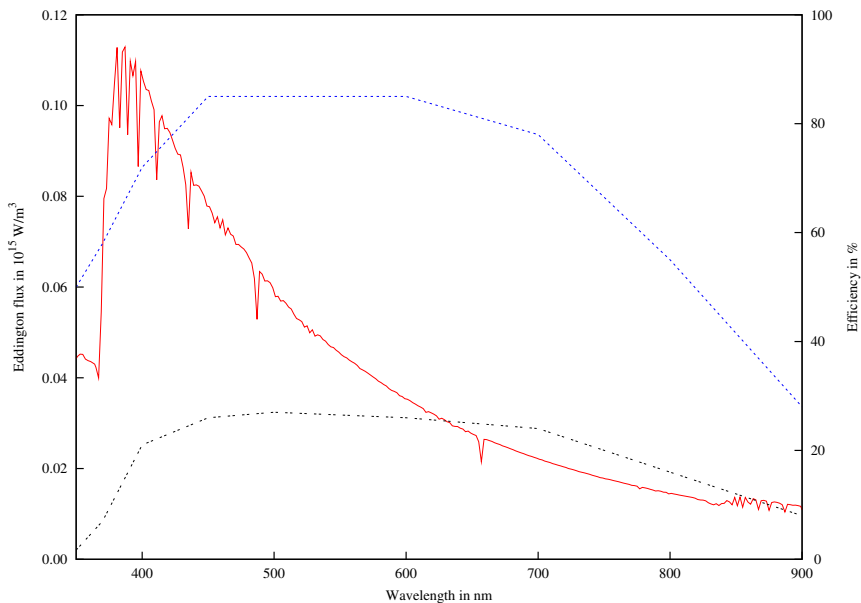
Figure 2.4: The efficiencies of the FEROS spectrograph as a whole (black, double-dashed line) and its CCD alone (dashed, blue line), as given by Kaufer et al. (1999), are compared to the flux distribution of a typical A-type supergiant (ATLAS9-model with $T_{\text{eff}} = 9500\,\text{K}$).

echelle spectrograph (UVES, Dekker et al. 2000) splits the light beam from the telescope in two arms (UV to Blue, and Visual to Red) using a dichroic beam splitter. By combining two spectra from the blue and the red channel each, a wavelength coverage from 3040 to $10\,400\,\text{Å}$ could be obtained, while achieving high resolution ($R = \lambda/\Delta\lambda \approx 80\,000$) and high S/N at the same time. UVES is attached to the Nasmyth focus of unit telescope 2 of the Very Large Telescope (VLT) at Paranal Observatory (diameter: $8.2\,\text{m}$).

2.3 Data Reduction

Extracting the wavelength-calibrated intensity distribution of the starlight from the 2-dimensional raw image (e. g., Fig. 2.5), turns out to be a difficult and even tedious task. Meticulous work during this process is crucial for avoiding systematic errors before the actual analysis even starts. In the following the general reduction procedure for Echelle data will be illustrated using the example of the FOCES observations. It is based upon the Echelle data reduction software presented by Pfeiffer et al. (1998) written in Interactive Data Language (IDL). Special steps for the other datasets will be mentioned at the end of the section.

- **Bias Subtraction:** To convert the number of electrons held by the array of pixels into a 2-dimensional digital image tiny voltages have to be read out, amplified and passed on to an Analog to Digital Converter (ADC), which introduces various sources of noise. However, the electronics of modern cameras add only a small amount of
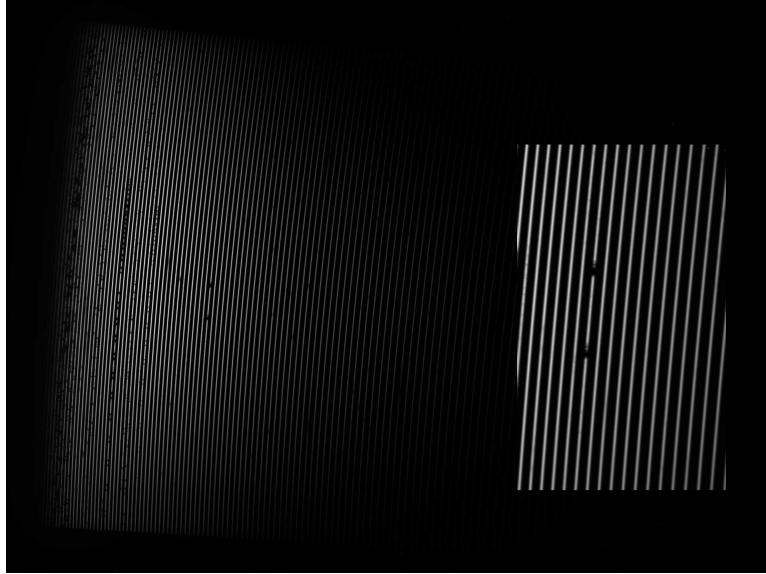
Figure 2.5: Raw image of the spectrum of HD 207673: Individual spectral orders run from top to bottom along the dispersion direction of the Echelle-grating. The perpendicular cross-dispersion separates the orders from each other. The small window on the right shows a magnification of the region around the sodium D doublet.

additional uncorrelated noise as the image is read from the CCD. This – and some deliberately added constant offset to avoid negative intensities – can be determined by taking bias frames, images taken with closed shutter and negligible exposure time. Several such images were averaged and subtracted from the raw data.

- **Removal of Cosmic Ray Hits:** A considerable amount of high-energetic cosmic rays can hit the detector while taking an image, in particular during long exposures. These events cause randomly distributed intensity spikes all across the raw CCD image. Careful application of a median filter can remove a major part of these unwanted signals while conserving spectral information.

- **Flat-fielding:** The shape of the measured intensity distribution differs from the original. Two major effects are responsible: Firstly, the efficiency of the spectrograph is wavelength-dependent. This is caused by all parts of the instrument from the aluminium reflectivity of the telescope mirror to the fibre optical waveguide and dispersive elements all the way up to the efficiency of the CCD itself. Secondly, sensitivity can vary from pixel to pixel. In order to determine these distortions, the exposure of a light source with a continous spectrum is taken, the so-called flat-field (Fig. 2.6). In principle, it is possible to perform the flat-field correction by dividing the raw 2D-image by the flat-field exposure now, but in the case of the FOCES data reduction discussed here the correction is done after a few additional steps.

- **Order Extraction:** Shape and position of the orders are determined by an elaborate algorithm. The flat-field exposures with continous orders are best-suited for this task. The background signal consisting of the dark current and straylight is filtered out by inter-order minimum subtraction from the extracted orders. Subsequently, the
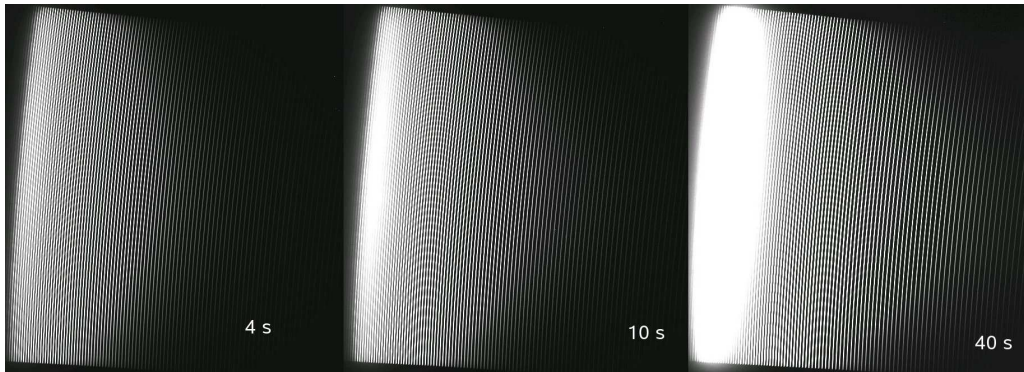
Figure 2.6: Red, green and blue flat-fields: The respective exposure times were optimized for different parts of the spectrum.

Figure 2.7: Excerpt from the emission-line spectrum of the thorium-argon calibration lamp.

resulting intensity distribution is divided by the extracted flat-field orders to correct for the effects mentioned in the previous paragraph.

- **Wavelength Calibration:** In a next step, a relation between the pixel-position within the extracted orders and the wavelength of the detected light is constructed. For this purpose spectra of a thorium-argon lamp were taken (see Fig. 2.7), whose emission lines have well known wavelengths. The dispersion relation can be approximated by a polynomial of low degree after identifying the lines. Manual corrections for lines misidentified by the algorithm increase the quality of the wavelength calibration.

- **Rectification:** In order to compare observation to theory it is helpful to normalize the flux first. This so-called rectification of orders allows the fitting of line-profiles and the determination of equivalent widths without a difficult and elaborate absolute flux calibration. This is done by approximating the shape of the continuum flux without absorption lines and dividing the intensity distribution by the resulting function, i.e., setting the continuum to unity (compare Fig. 2.8). Complications
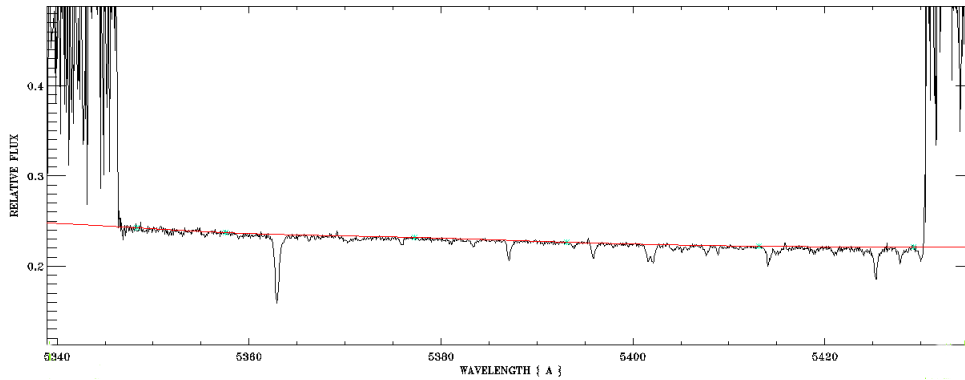
Figure 2.8: In orders containing relatively few absorption lines the shape of the continuum can be easily determined.

arise in regions densely populated by absorption lines or by broad spectral features like the Balmer-lines. In such cases, an interpolation between the continuum approximation of adjacent orders proves to be beneficial. The rectification of FOCES data was especially time-consuming, since every order has to be treated individually before they are merged, which is not the case for our other observational data.

- **Order Merging:** In the last step of the data reduction individual orders are merged into a single normalized spectrum. For this, the useful parts of the overlap between the orders have to be determined to avoid efficiency losses. In general, the merging process is problem-free as long as there is sufficient overlap of good quality. This is the case for the blue parts of the FOCES spectra, while gaps can occur in the red parts.

- **Radial Velocity Correction:** In order to compare the observations with our models the spectra have to be corrected for the Doppler-shift caused by the radial velocity v_{rad} of the stars towards the observer. Therefore a cross correlation of the reduced spectrum with a suitable synthetic spectrum was performed and the observational data were shifted so that the positions of the absorption lines match the laboratory wavelengths of the respective transitions.

- **Data Reduction for other Spectrographs:**

  The work with the FEROS data was greatly facilitated by the automatic reduction pipeline based on the Munich Image Data Analysis System (MIDAS, Grosbøl & Ponz 1990). In addition to spectra of our targets, a template spectrum of the hot subdwarf HD 188112 was obtained and reduced with the pipeline. After dividing this spectrum by a well-fitting theoretical model for this star – made available by Heinz Edelmann – we could successfully filter out undesirable artifacts from the data reduction process. This smoothed the resulting spectra and made it possible to achieve satisfying normalization.

  The published spectra provided by the UVES Paranal Observatory Project[1] were found to be of excellent quality, so that only normalization and radial velocity correction had to be applied.

---

[1]available at http://www.eso.org/sci/observing/tools/uvespop/
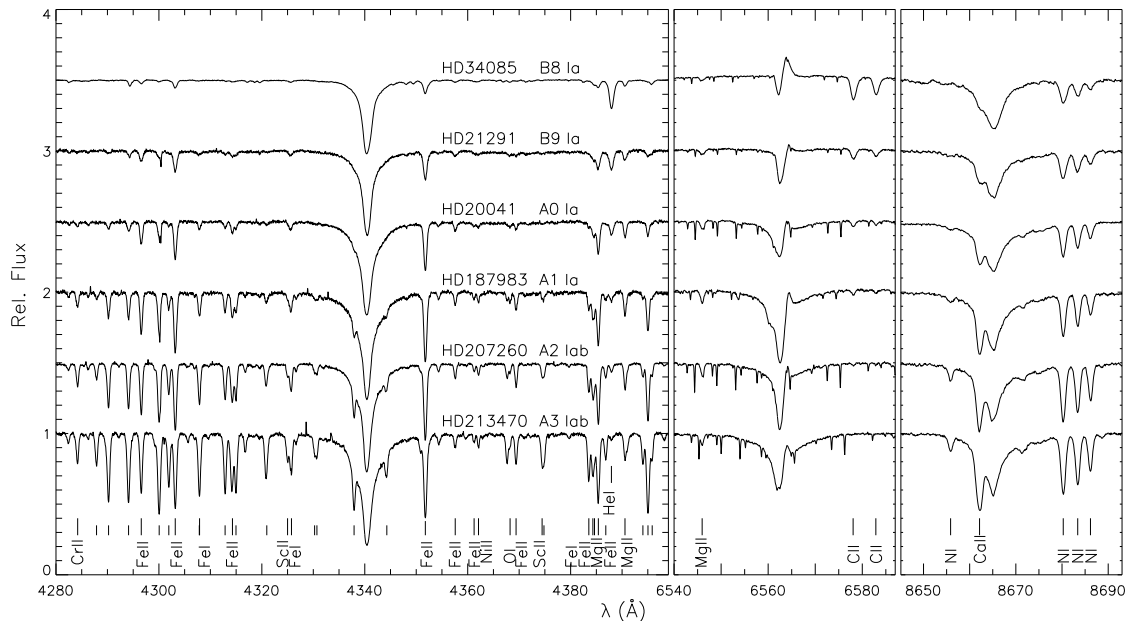
Figure 2.9: Sample spectra of supergiants of luminosity class Ia all across the temperature range covered in this study. Shown are, from left to right, the regions around the strong hydrogen lines H_γ, H_α and H_{13-3}. The major spectral features are identified.

2.4 Target Selection

As we obtained data using spectrographs both on the northern and southern hemisphere, a significant range in Galactic longitude could be encompassed. This allowed us to include stars in various parts of the Galactic neighbourhood. The sample is also intended to cover the examined parameter domain (B8 to A3 in spectral type, Ib to Ia in luminosity class) rather homogeneously, although more luminous objects were preferred in order to extend our study to larger distances. Some sample spectra of objects across the examined temperature range are shown in Fig. 2.9. Stars in both OB associations and the field were considered in order to exclude any selection effects from cluster membership. The desired S/N of 150 limits our target selection to stars brighter than 10 mag in apparent magnitude V for the 2m-class telescopes. The resulting list of programme stars and the properties of our observational data are shown in Table A.3. Note that the objects in common with Przybilla et al. (2006) and Schiller & Przybilla (2008) were reanalyzed in this work for the sake of homogeneity.

Table 2.1: The star sample: id, spectral type, OB association membership[1], apparent magnitude[2], coordinates[3] and observational details[4].

Object	Sp. T[5]	Sp. T[6]	OB Ass.	V (mag)	RA (J2000.0)	Dec (J2000.0)	Date	$T_{\exp}$ (s)	S/N_V
FOCES $R = 40\,000$									
1 HD12301	B8 Ib[7]	B8 Ib	Field	5.589	02 03 00.19	+64 23 24.06	30/09/2001	480	203
2 HD12953	A1 Iae[7]	A1 Iae	PerOB1	5.691	02 08 40.58	+58 25 24.96	26/09/2001	300	230
3 HD13476	A3 Iab	A3 Iab	PerOB1	6.431	02 13 41.61	+58 33 38.11	30/09/2001	900	202
4 HD13744	A0 Iab	A0 Iab	PerOB1	7.592	02 15 58.70	+58 17 37.06	27/09/2005	2700	182
5 HD14433	A1 Ia[7]	A1 Ia	PerOB1	6.401	02 21 55.44	+57 14 34.50	30/09/2001	600	217
6 HD14489	*A2 Ia*[7]	A1 Iab	PerOB1	5.178	02 22 21.43	+55 50 44.35	26/09/2001	360	246
7 HD20041	A0 Ia	A0 Ia	CamOB1	5.795	03 15 47.97	+57 08 26.23	30/09/2001	600	234
8 HD21291	B9 Ia[7]	B9 Ia	CamOB1	4.213	03 29 04.13	+59 56 25.19	26/09/2001	2×240	259
9 HD39970	A0 Ia	A0 Ia	Field	6.018	05 56 56.12	+24 14 58.88	30/09/2001	600	270
10 HD46300	A0 Ib[7]	A0 Ib	MonOB1	4.498	06 32 54.23	+07 19 58.67	29/09/2005	180	206
11 HD186745	B8 Ia	B8 Ia	VulOB1	7.030	19 45 24.35	+23 56 34.38	25/09/2001	900	163
12 HD187983	A1 Ia	A1 Ia	Field	5.590	19 52 01.60	+24 59 31.78	25/09/2001	300	187
13 HD197345	A2 Ia[8]	A2 Ia	CygOB7	1.246	20 41 25.91	+45 16 49.22	21/09/2005	8×20	798
14 HD202850	B9 Iab[7]	B9 Iab	CygOB4	4.233	21 17 24.95	+39 23 40.85	29/09/2001	120	231
15 HD207260	A2 Iab[7]	A2 Iab	CepOB2	4.289	21 45 26.93	+61 07 14.90	26/09/2001	120	370
16 HD207673	A2 Ib[7]	A2 Ib	Field	6.467	21 49 40.09	+41 08 55.64	29/09/2001	720	195
17 HD208501	B8 Ib[7]	B8 Ib	CepOB2	5.796	21 54 53.15	+56 36 40.42	26/09/2001	480	231
18 HD210221	A3 Ib[7]	A3 Ib	Field	6.140	22 07 25.59	+53 18 26.77	26/09/2001	720	271
19 HD212593	*B9 Iab*[7]	B9 Ib	Field	4.569	22 24 30.99	+49 28 35.01	29/09/2001	2×180	403
20 HD213470	*A3 Ia*	A3 Iab	CepOB1	6.650	22 30 18.70	+57 13 31.60	29/09/2001	900	249
21 BD+602582	B8 Iab	B8 Iab	CasOB2	8.694	23 35 30.64	+60 54 46.23	27/09/2001	2400	140
22 HD223960	*A0 Ia*[7]	B9 Ia	CasOB5	6.895	23 53 49.98	+60 51 12.24	25/09/2001	1200	226
FOCES $R = 65\,000$									
23 HD195324	A1 Ib	A1 Ib	Field	5.880	20 29 20.39	+36 27 17.02	07/10/2001	2×1000	618
FEROS $R = 48\,000$									
24 HD34085	B8 Ia[8]	B8 Ia	OriOB1	0.138	05 14 32.27	−08 12 05.91	14/11/1998	20	634
25 HD87737	A0 Ib[8]	A0 Ib	Field	3.486	10 07 19.95	+16 45 45.59	21/01/1999	120	440
26 HD91533	A2 Iab	A2 Iab	CarOB1	6.005	10 32 47.81	−58 40 00.28	23/05/2007	100	229
27 HD111613	*A2 Iabe*	A1 Ia	CenOB1	5.741	12 51 17.98	−60 19 47.24	23/01/1999	600	376
28 HD149076	*B8 Iab*	B9 Ib	AraOB1b	7.373	16 34 38.57	−47 00 15.71	24/05/2007	280	230
29 HD149077	*B9 Ib*	A0 Ib	AraOB1a	7.433	16 34 45.69	−49 23 44.15	24/05/2007	310	261
30 HD165784	*A2/A3 Iab*	A2 Iab	SgrOB1	6.538	18 08 38.59	−21 26 58.42	09/07/2007	140	145
31 HD166167	*B9.5 Ib*	A0 Ib	SgrOB1	8.605	18 10 14.12	−21 19 37.82	09/07/2007	610	117
UVES $R = 80\,000$									
32 HD80057	*A1 Ib*	A1 Iab	VelaOB1[9]	6.044	09 16 04.03	−44 53 55.40	24/02/2003	2×50	293
33 HD102878	A2 Iab	A2 Iab	CruOB1	5.695	11 50 27.28	−62 38 57.77	06/01/2002	54+139	442
34 HD105071	*B8 Ia/Iab*	B8 Iab	Field	6.316	12 05 53.62	−65 32 48.76	26/02/2002	2×74	382
35 HD106068	*B8 Ia/Iab*	B8 Iab	Field	5.920	12 12 21.98	−62 57 02.78	20/07/2001	2×53	415

[1] Blaha & Humphreys (1989); [2] Mermilliod & Mermilliod (1994); [3] adopted from the Simbad database at CDS ; [4] note that the exposure times for UVES objects can vary in different wavelength bands; [5] adopted from the SIMBAD database at CDS, set in italics if revised here; [6] this work; [7] MK standards from Johnson & Morgan (1953); [8] anchor points of the MK system; [9] Reed (2000)

3 Model Atmospheres and Spectrum Synthesis

Nearly all our knowledge about the structure and evolution of stars stems from the interpretation of stellar spectra. It all began, when Fraunhofer invented the spectroscope in 1814, and discovered 574 dark lines appearing in the solar spectrum(Aller 1991). About 50 years later Kirchhoff and Bunsen discovered that each chemical element was associated with a set of spectral lines, and deduced that the dark lines in the solar spectrum were caused by absorption by the elements in the upper layers of the Sun. While this was the beginning of the spectral analysis of stars, it took a long time before quantitative results of stellar spectroscopy could be obtained. Tremendous progress in various scientific fields was necessary, e. g., the work of Schwarzschild (1906, 1914) concerning radiative transfer in stars, steps towards understanding the structure of stellar atmospheres, e. g., by Milne (summarized in his Bakerian lectures 1929), and the advent of quantum mechanics. Unsöld (1928) was the first to derive the composition of the solar atmosphere via quantitative spectroscopy. While the analysis method was still coarse, the conclusion that hydrogen is by far the most prevalent element in the solar atmosphere was an important step for stellar astrophysics and stands to this day. He was also the first to provide a detailed spectral analysis of a star other than the Sun, the B 0 main sequence star τ Scorpii (Unsöld 1942), a progenitor of the stars examined in this thesis.

It was soon realized that the effects of integration along the atmosphere on the spectrum are large, and a detailed understanding of the photospheric structure beyond simple approximations was necessary. Hence the model atmosphere technique was introduced, for which detailed tabulations of the theoretical atmospheric structure are computed, using the basic physics governing the stellar photosphere (e. g., Strömgren 1940). The comparison of the theoretical flux produced by these atmospheres and observations makes it possible to interpret the emergent spectrum quantitatively. With the introduction of computers into stellar astrophysics and the subsequent publication of grids of model atmospheres (Strom & Avrett 1965; Gustafsson et al. 1975, etc.), this method became standard in the quantitative spectroscopy of stars.

The classical one-dimensional, plane-parallel and hydrostatic LTE model atmospheres have reached a high degree of sophistication and today this field is largely dominated by the computer code developed by Kurucz (1970). Although these classical atmospheres can actually model the continuum shapes and line spectra of many stars across the HR diagram, deviations are found, in particular for hot stars, where the simplifying assumptions break down. Modern stellar atmosphere theory therefore concentrates on constructing more realistic models.

Auer & Mihalas (1969) made an important step by substituting the restrictive LTE assumption with the rate equations of statistical equilibrium (non-LTE), a method that had immediate success in the modelling of O-type stars. Since that, the construction of non-LTE models was continuously refined. An overview of more recent developments in this field is given by Hubeny (2003).

Another major step forward was the calculation of 3D-atmospheres including convection for the Sun by Asplund et al. (2000), that reproduce the solar line-shifts and line-profiles without the need of parameters like macro- or microturbulence (while so far assuming LTE in most respects).

The most sophisticated approach in the regime of BA-type supergiants is the development of spherical symmetric non-LTE models, that account for radiatively driven winds based in the photosphere by relaxing the hydrostatic assumption, introducing hydrodynamic equations instead. A successful example for these so-called *unified models* is the code FASTWIND (Santolaya-Rey et al. 1997; Puls et al. 2005).

Despite technological advancements, however, computing power is still a bottleneck of calculating stellar atmospheres. In order to treat some aspects of the modelling more realistically, other parts of the problem have to be simplified to reach convergence on reasonable timescales. Therefore classical models are still used in the hybrid non-LTE approach, i. e., non-LTE line formation computations on prescribed LTE model atmospheres, that was adapted for this study. This method has been shown to be the state-of-the-art for the quantitative spectroscopy of BA-type supergiants by Przybilla et al. (2006). It allows for utilizing highly sophisticated and well-tested model atoms via a non-LTE treatment and the computation of extensive model grids in a manageable amount of time compared to a full non-LTE approach.

This chapter gives an overview of the physics and computational techniques behind the model atmosphere codes, orienting on textbook knowledge given by Mihalas (1978) and, for later developments, Hubeny (1997). Finally the validity of the method for the purposes of this study is discussed.

3.1 Basic Assumptions

Classical atmospheres make a number of far-reaching assumptions and simplifications, the validity of which will be discussed later on.

- **Homogeneity:** The matter is homogeneously mixed and no chemical gradients exist.

- **Stationarity:** The star's atmosphere is in a steady state, i. e., there are no explicitly time-dependent variables ($\partial/\partial t = 0$).

- **Plane-parallel Geometry:** An important simplification stems from the assumption that the spatial extension of the atmosphere is negligible compared to the star's radius ($\eta = \Delta R/R \ll 1$). This allows to treat the atmosphere as a set of homogeneous parallel layers through which energy is transported. Thus the only coordinate needed to describe the atmosphere is the height z. Additionally it is assumed that
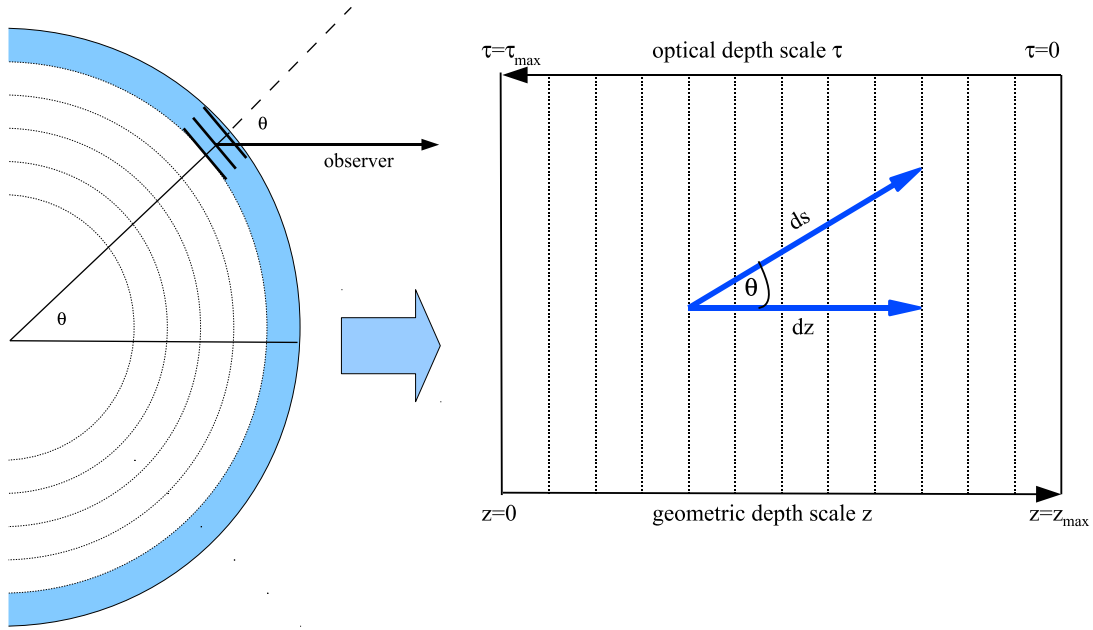
Figure 3.1: The plane-parallel approximation of the stellar atmosphere compared to the more realistic spherical symmetry. The dotted lines represent isotherms/isosteres.

the total mass of the star is located below the atmosphere, which means that the gravitational acceleration is constant throughout the atmosphere and equals the surface gravity

$$g = \frac{GM}{R^2}, \tag{3.1}$$

where M and R are the mass and radius of the star, respectively, and G denotes the gravitational constant.

- **Radiative Equilibrium:** Nuclear energy is released in the star's interior but not in the atmosphere, thus the energy flux is conserved throughout our model:

$$F = \int_0^\infty F_\nu \mathrm{d}\nu \equiv \sigma T_{\mathrm{eff}}^4 = \mathrm{const.}, \tag{3.2}$$

where σ is the Stefan-Boltzmann constant and T_{eff} the effective temperature (compare Fig. 3.2).

- **Hydrostatic Equilibrium:** The atmosphere's weight is supported by the total pressure P in the following way:

$$\mathrm{d}P/\mathrm{d}z = -\rho(g - g_{\mathrm{rad}}). \tag{3.3}$$

Here ρ denotes the mass density and g_{rad} the radiative acceleration.

- **Charge Conservation:** The stellar plasma is not charged. The number of free electrons equals the combined charge of all ions:

$$\sum_i n_i Z_i - n_e = 0. \tag{3.4}$$

The resulting 1D-problem can be translated into a numerical model, in which the atmosphere consists of a finite set of homogeneous layers on a discrete depth (z) grid. Each layer is then characterized by distinct values of mass density ρ, pressure P, temperature T and electron density n_e. These quantities are connected by the equation of state of the stellar material. Generally the *ideal gas law*

$$P = \frac{\rho k T}{\mu_{\text{mol}} m_{\text{H}}}, \tag{3.5}$$

holds in stellar photospheres, where m_{H} denotes the mass of the hydrogen atom and k is the Boltzmann constant. The so-called mean molecular weight μ_{mol} is the mean weight of all particles – including electrons – in units of m_{H}. This quantity is reflecting the fact that the total pressure is a sum over all partial pressures. Two major parameters of model atmospheres have already been introduced: The surface gravity g, mainly governing the pressure stratification, and the effective temperature T_{eff}, characterizing the radiation field. These are stellar parameters that are to be determined in a quantitative spectroscopic analysis. The third important parameter is the metallicity of the star, or more exactly the chemical composition of the photosphere.

3.2 Thermodynamic State

Thermodynamic equilibrium (TE) allows a single temperature T and a particle number density N to be attributed to an entire system. As it is known from statistical physics, the population densities of excited states and the degree of ionization can be specified uniquely if these two macroscopic parameters are known. Two of the hallmarks of thermodynamic equilibrium, however, are isotropy – properties are the same in all directions – and homogeneity – properties are the same in all places. Given that stars emit radiation and that the effects of gravity and spherical symmetry must result in pressure and temperature gradients, the assumption of TE is clearly not valid for stars. A very successful idea in stellar atmosphere theory is that TE could hold at least locally, an assumption known as *local thermodynamic equilibrium* (LTE). It can be closely tied to the principle of *detailed balance* – the statement that, at thermodynamic equilibrium, each individual reaction occurs at the same rate as its reverse reaction, as implied by microscopic reversibility.

Under the premise of LTE, the massive particles are assumed to be in a state that can be characterized by two parameters: the local temperature T and the local electron density n_e. As a consequence the state of the plasma can be described by the following equations:

- **The Maxwell-Boltzmann Distribution:**

$$f(\vec{v}_{\text{th}})\mathrm{d}v_x\mathrm{d}v_y\mathrm{d}v_z = \left(\frac{m}{2\pi k T}\right)^{\frac{3}{2}} e^{-\frac{m}{2kT}(v_x^2+v_y^2+v_z^2)}\mathrm{d}v_x\mathrm{d}v_y\mathrm{d}v_z \tag{3.6}$$
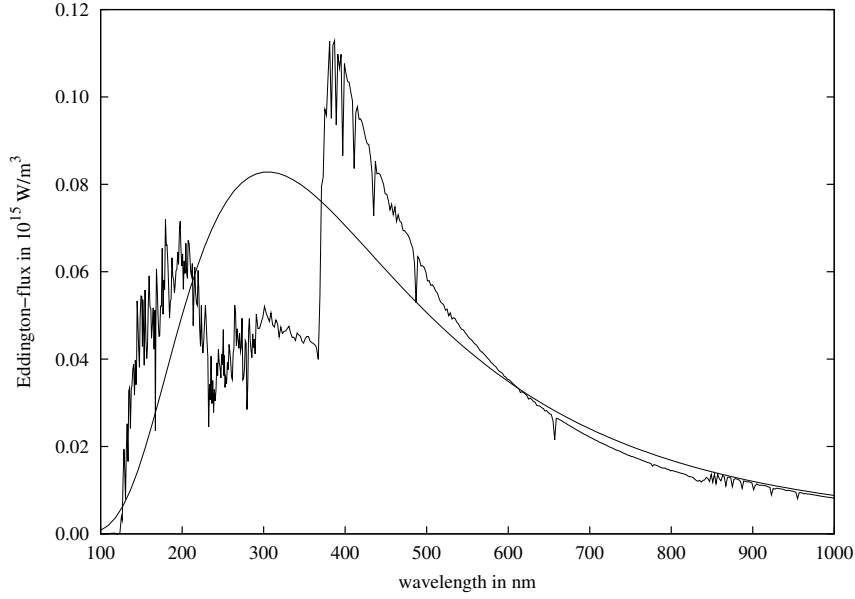
Figure 3.2: Theoretical spectral energy distribution of a supergiant with $T_{\mathrm{eff}} = 9\,500\,\mathrm{K}$ and $\log g = 1.7$ compared to black-body radiation of the same temperature characterizing thermal equilibrium. Note that, by definition of the effective temperature, the area under both curves must be equal.

This formula describes the thermal velocity distribution as a function of particle mass m and temperature T.

- **The Boltzmann Formula:**

$$(n_j/n_i) = (g_j/g_i)e^{\frac{-(E_j - E_i)}{kT}} \tag{3.7}$$

The number density of atoms in different energy states (population number n_i) is specified as a function of T, where g_i is the statistical weight and E_i is the excitation energy.

- **The Saha Equation:**

$$\frac{N_I}{N_{I+1}} = \frac{n_{\mathrm{e}}}{2}\left(\frac{h^2}{2\pi m k}\right)^{\frac{3}{2}}\frac{U_I}{U_{I+1}}T^{-\frac{3}{2}}e^{\frac{\chi_I}{kT}}, \tag{3.8}$$

where χ_I denotes the ionization potential of the Ion I and h the Planck constant. In analogy to the Boltzmann-equation the distribution of atoms over ionization stages is specified, where $U = \sum_{i=1}^{i_{\max}} g_i \exp(-E_i/kT)$ describes the partition function. Note that, beside the temperature T, the electron density n_{e} is governing the ionization of the plasma.

It is important to note that LTE applies only to particles with mass. It is not necessary that the radiation field has a Planckian character or that the photons are in thermodynamic equilibrium with the particles of the gas in order for LTE to be established.

Any state departing from LTE is denoted as non-LTE. Whether or not the assumption of LTE holds, depends on whether the particles obey the aforementioned distributions at least locally. An important parameter hereby is the mean-free-path. Particles that are confined to a small part of the atmosphere will adhere to the local distributions after a sufficient number of interactions with the surrounding particles, in other words they are thermalized. This is the case for particles with short distances between interactions, i.e. a short mean free path. Generally, the photon mean free path in stellar atmospheres is larger than that of massive particles, hence they tend to couple distant layers of the atmosphere by transporting non-local information. Collisions between massive particles, on the other hand, tend to retain LTE. The electrons are the most important particles for this effect, because they suffer many more collisions per unit time than the ions. When the electron density is sufficiently high, radiative processes may be neglected relative to collisional processes and thus thermodynamic equilibrium is established. Quantitative criteria for the validity of LTE are discussed, for e.g., by Griem (2005). As a guideline, a combination of high temperature and low density demands a non-LTE approach.

In non-LTE the more restrictive assumption of detailed balance, in which every process must be matched by its inverse, is substituted by the assumption of statistical equilibrium, which is just a consequence of stationarity, i.e. the level populations are constant in time. Hence the flow into any energy level must be balanced by the flow out of that level:

$$n_i \sum_{i \neq j} (R_{ij} + C_{ij}) = \sum_{i \neq j} n_j (R_{ji} + C_{ji}). \tag{3.9}$$

For this equation all processes are considered that govern the population flow between the energy levels i and j. Hereby R_{ij} are the absorption rates and R_{ji} the rates of (spontaneous and stimulated) emission of photons, while C_{ij} and C_{ji} denote the collisional rates..

To understand the difference between the assumption of statistical equilibrium and detailed balance, consider the following simple example: a time-independent equilibrium could also be established by a cyclical flow of electrons from levels $1 \rightarrow 3 \rightarrow 2 \rightarrow 1$. Yet, this obviously wouldn't be possible if the principle of detailed balance holds true, balancing each flux with its inverse. Keeping in mind that model atoms are generally much more complex than this simple example, one can see that solving the non-LTE problem is much more expensive in terms of computing time than the far more restricted LTE-problem.

3.3 Radiative Transfer

Radiative transfer is the dominant energy transport mechanism in the outer parts of hot stars. The details of the propagation of radiation in stellar atmospheres are decisive for the calculation of the emergent spectrum. But if one considers the interaction of stellar matter and radiation, it becomes clear that radiative transfer also plays an important role for the structure of stellar atmospheres and the state of the plasma, thereby complicating the problem at hand.

The fundamental quantity which characterizes the field of radiation is the *specific intensity* I_ν, which is defined as the amount of radiative energy dE_ν flowing across a surface element of area dA in time dt into the solid angle $d\Omega$ within the frequency interval ν to $\nu + d\nu$:

$$dE_\nu = I_\nu \cos\theta \, d\nu \, dA \, d\Omega \, dt, \tag{3.10}$$

where θ is the angle between the direction of propagation and the surface normal (Mihalas 1978).

It is useful to extract the first few moments of the intensity with respect to $\mu \equiv \cos\theta$ for a better description of the radiation field. The zero-order moment is the mean intensity

$$J_\nu = \frac{1}{2} \int_{-1}^{1} I_\nu d\mu, \tag{3.11}$$

which is related to the energy density of the radiation field $u_\nu = 4\pi/c J_\nu$. The first-order moment is known as the Eddington flux

$$H_\nu = \frac{1}{2} \int_{-1}^{1} I_\nu \mu d\mu, \tag{3.12}$$

which corresponds to the monochromatic radiative flux used earlier, as $F_\nu = 4\pi H_\nu$.

The second-order moment

$$K_\nu = \frac{1}{2} \int_{-1}^{1} I_\nu \mu^2 d\mu \tag{3.13}$$

is related to the radiation pressure via $p_\nu = 4\pi/c K_\nu$, where c denotes the speed of light.

The interactions between radiation and matter can be grouped into true absorption, emission and scattering. True absorption and emission processes exchange energy between the radiation field and the stellar material by destroying and creating photons. Absorption processes include photoionizations (bound-free transitions) and excitations (bound-bound transitions), while true emission constitutes of the inverse processes. The respective coefficients for absorption and emission κ_ν and η_ν can be derived microscopically according to

$$\kappa_\nu = \text{number of absorbers} \times \text{atomic cross-section}(\nu) \tag{3.14}$$

$$\eta_\nu \propto \text{number of emitters} \times \text{transition probability}(\nu) \tag{3.15}$$

whereby the latter values are determined via atomic physics. In the case of scattering, no photons are created or destroyed, but the absorbed photon is immediately re-emitted in a different direction at a Doppler-shifted frequency. For simplification, the coefficients of true absorption (κ_ν) and scattering (σ_ν) are often combined into a single absorption coefficient: $\chi_\nu = \kappa_\nu + \sigma_\nu$. In realistic stellar atmosphere models the quantities χ_ν and η_ν are functions of the variables defining the state of the matter, for instance density ρ, temperature T or composition $\{X_Z\}$ (X_Z denoting the fraction by weight of the element with atomic number Z). Macroscopically, the change in intensity along the path $ds = dz\mu^{-1}$ can be described as $dI_\nu = -\chi_\nu I_\nu ds$ for absorption and $dI_\nu = \eta_\nu ds$ for emission. With these definitions,

the radiative transfer equation can be derived, simply stating that as a beam of radiation travels, it loses energy to absorption and gains energy by emission:

$$\mu \frac{\mathrm{d}I_\nu}{\mathrm{d}z} = \eta_\nu - I_\nu \chi_\nu. \tag{3.16}$$

Interpreting χ_ν^{-1} as the characteristic distance a photon can travel before being absorbed, we introduce the *optical depth* $\mathrm{d}\tau_\nu = -\chi_\nu \mathrm{d}z$ as a substitute for the geometric depth, with $\tau_\nu = 1$ defining the mean free path of the photons. After defining the *source function* by $S_\nu \equiv \eta_\nu / \chi_\nu$, we can rewrite equation 3.16 as:

$$\mu \frac{\mathrm{d}I_\nu}{\mathrm{d}\tau} = I_\nu - S_\nu \tag{3.17}$$

Note that in thermodynamic equilibrium, according to the principle of detailed balance, $I_\nu \chi_\nu = \eta_\nu$, and therefore $I_\nu = S_\nu = B_\nu$, where B_ν is the Planck function for the continuous spectrum of a blackbody

$$B_\nu = \frac{2h\nu^3}{c^2} \frac{1}{e^{\frac{h\nu}{kT}} - 1}. \tag{3.18}$$

The source function approaches the Planck function deep in the atmosphere, where virtually no photons escape.

If the source function is known, the formal solution of radiative transfer gives the emergent intensity I_ν for a semi-infinite atmosphere by integration over all depths:

$$I_\nu(\mu) = \int_0^\infty S_\nu(t) \exp(-t/\mu) \mathrm{d}(t/\mu). \tag{3.19}$$

The specific form of S_ν, however, is by no means trivial and a function of many parameters, including the specific intensity, so that the formal solution is not easily applicable. The angle-averaged mean intensity can be obtained by integrating Eq. 3.19 over μ, yielding

$$J_\nu(\tau_\nu) = \int_0^\infty S_\nu(t) E_1(|t - \tau_\nu|) \mathrm{d}t, \tag{3.20}$$

where E_1 is the first exponential integral (see Abramowitz et al. 1988). To solve the problem of radiative transfer, the mean intensity is reformulated as an operator acting on the source function, the so-called Λ-operator (e. g., Hubeny 2003):

$$J_\nu(\tau_\nu) = \Lambda_{\tau_\nu}[S(t)]. \tag{3.21}$$

In practice, Eq. 3.21 is discretized and replaced by a quadrature sum. The Λ-operator is then realized in the form of a matrix, which describes how the contributions of the source function from all depth points are coupled.

3.4 Line Blanketing

A vast number of different lines from various elements influence the atmospheric structure and the emergent spectrum. Essentially, there is a redistribution of the photon flux by these lines (line-blocking). This does change the shape of the emergent spectrum and leads to the effects of backwarming and surface cooling, as it shifts the flux to longer wavelength by virtue of flux conservation (Eq. 3.2). The UV region of BA-type supergiants is densely packed with numerous absorption features. Especially the enormous complexity of the iron-peak elements (hundreds of energy levels as well as ten thousands of transitions have to be considered for every ion) makes it difficult to account for the effects of this so called line-blanketing. Two statistical methods were devised to solve this problem:

- **Opacity Sampling:**

  In the OS approach (Peytremann 1974), the line opacity is sampled Monte-Carlo-like on a fine grid of wavelength points using line profiles for each individual spectral line. Tables of sampling opacities are constructed for given wavelengths grids and for different elements, offering many advantages in the treatment of line blends.

- **Opacity Distribution Function:**

  This approach was first introduced by Strom (1966). ODFs are tabulated opacities, e. g., as a function of temperature and pressure. They are calculated once for a certain chemical composition and a fine frequency grid. From this detailed computation, a monotonic function of frequency is formed and listed. ODFs have the advantage of providing quick access to the source function as one only has to interpolate pre-tabulated values. On the other hand they have the drawback that they are not suited to handle stars with non-standard chemical composition.

The tabulations for ODFs and OS are typically constructed under the assumption of LTE, the more complex non-LTE case requires that energetically close levels are grouped into so called 'superlevels', for which the statistical equilibrium has to be solved.

3.5 Computational Methods

If one combines the equations governing the atmospheric structure, the thermodynamic state and the radiative transfer, a system of integro-differential equations is formed. Using the radiative transfer equation 3.17 one can rewrite the condition for radiative flux conservation 3.2 as

$$\int_0^\infty \kappa_\nu \left(J_\nu - S_\nu \right) \mathrm{d}\nu = 0. \tag{3.22}$$
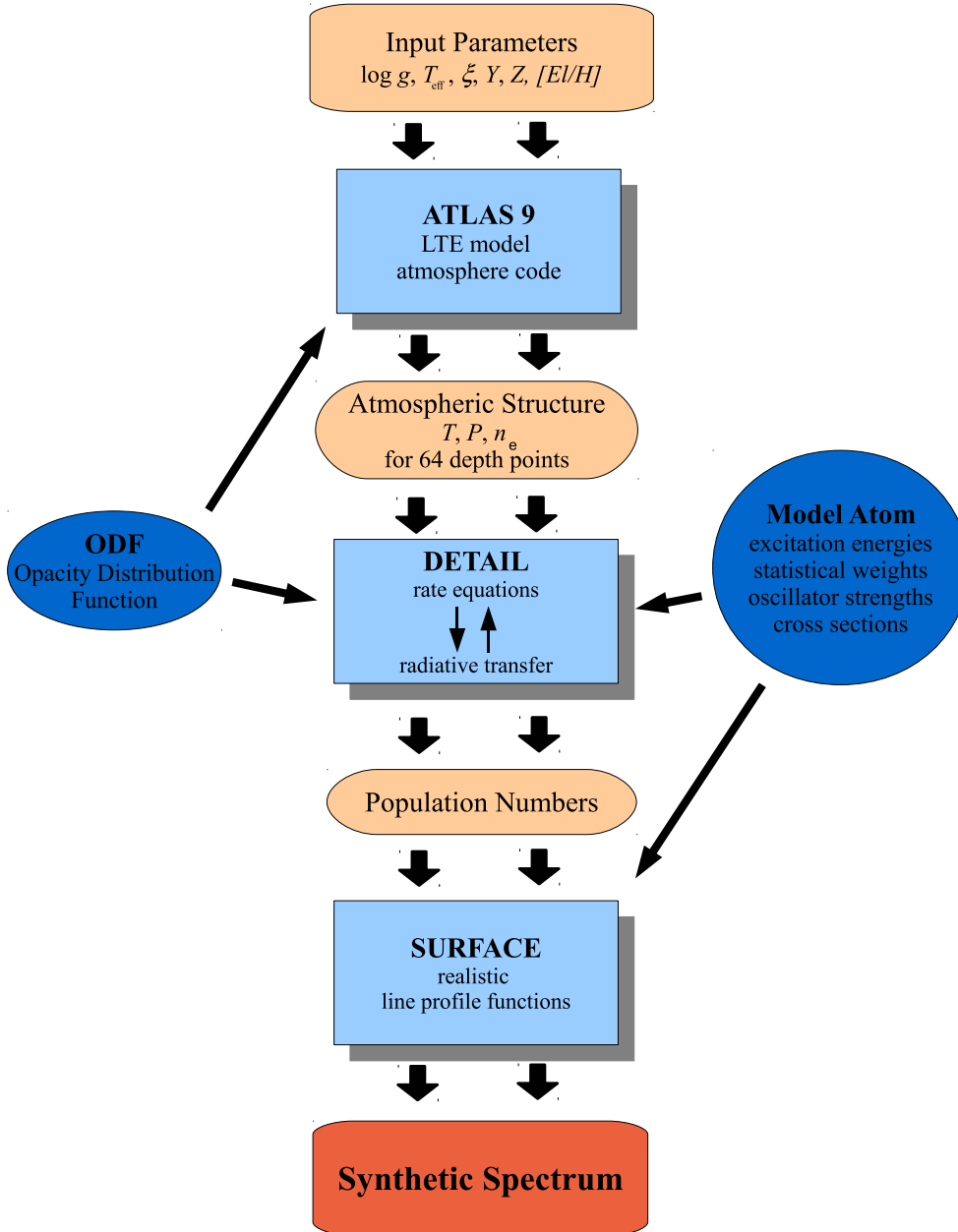
Figure 3.3: Overview of the spectrum synthesis procedure.

Additionally, the radiative acceleration g_{rad} can be expressed as an integral over the absorption-weighted Eddington flux and integrated into the condition of hydrostatic equilibrium (Eq. 3.3):

$$\frac{\mathrm{d}P}{\mathrm{d}z} = -\rho \left(g - \frac{4\pi}{c} \int_0^\infty \chi_\nu H_\nu \mathrm{d}\nu \right) \tag{3.23}$$

We now have a complex set of coupled equations to be solved numerically. The principle idea behind the hybrid LTE/NLTE approach is to split up the problem in three parts (see Fig. 3.3. The individual computational steps during the calculation of extensive models grids for this thesis are listed in the following:

- **Atmospheric Structure in LTE:**

  In this step the classical LTE model atmosphere code ATLAS9 (Kurucz 1993a) was used to determine the atmospheric structure. For this, a temperature-correction scheme is used to solve the problem numerically. Basically the temperature structure is modified, so that the model atmosphere has the desired properties. Temperature corrections are evaluated using different procedures:

  The first procedure is the flux-correction (Avrett & Krook 1963), which uses the relative flux error $\Delta H = 4\pi \int_0^\infty H_\nu \mathrm{d}\nu - \sigma T_{\mathrm{eff}}^4$ and is performed in the deep layers. This method fails in the upper layers, where the flux-correction for the temperature gets very small. For this reason a second procedure is needed, the Λ-correction. In this method the temperature correction for a particular depth is derived from the error in radiative balance, which works well for small optical depth but fails in deeper layers of the atmosphere. A combination of both temperature-correction schemes yields good convergence over the entire model atmosphere. See Kurucz (1970) for a more detailed description.

  In practice, the iteration procedure is repeated until the relative flux error and the relative flux derivative error are smaller than 1%. Some additional modifications are necessary to allow model convergence close to the Eddington limit (Przybilla et al. 2001b). Line blanketing is accounted for via Opacity Distribution Functions from Kurucz (1993b).

- **Radiative Transfer in non-LTE:**

  The resulting ATLAS9 atmosphere is the starting point of non-LTE computations with DETAIL (Giddings 1981; Butler & Giddings 1985, the DETAIL/SURFACE package is updated by K. Butler). While the temperature and density structure of the atmosphere remains fixed, the coupled rate and radiative transfer equations are solved. The collisional rates C_{ij} in the rate equations 3.9 are functions of the velocity distribution of massive particles, but the radiative rates R_{ij} are directly coupled to the problem of radiative transfer.

  In order to solve the radiative transfer problem for the more complex non-LTE case in a reasonable amount of time, ingenious computation methods had to be devised. Judging from Eq. 3.21, there seems to be an obvious solution: The lambda iteration method. A first estimate of the source function (e. g., derived from population numbers in LTE) allows to calculate J_ν at different depth points, from which in turn new population numbers can be computed via the rate equations. This iteration scheme converges only very slowly in optical thick cases, however: one iteration is analogous to photons travelling their mean-free-path once, which can be very short, especially in line cores. Therefore, more efficient alternatives had to be found.

An improvement of the lambda iteration came from a method commonly known as *operator splitting.* The idea consists of writing

$$\Lambda = \Lambda^* + (\Lambda - \Lambda^*), \tag{3.24}$$

where Λ^* is the *approximate lambda operator.* Then the i-th iteration step can be written as

$$J^i = \Lambda^* S^i + (\Lambda - \Lambda^*) S^{i-1} = \Lambda^* S^i + \Delta J^i, \tag{3.25}$$

where Λ^* acts on the current, yet to be determined source function S^i, while the correction term ΔJ^i contains only quantities known from the previous iteration. Λ^* can be chosen completely arbitrarily, because in case of convergence ($S^i = S^{i-1}$) Eq. 3.25 gives the exact solution. An overview of this so-called *accelerated lambda iteration*(ALI) and the construction of efficient approximate lambda operators is given by Hubeny (2003). Werner & Husfeld (1985) were among the first to apply this technique to model atmosphere calculations. A very successful recipe for the realization of the ALI scheme for radiative transfer was presented by Rybicki & Hummer (1991), and it is this formulation that is implemented in the DETAIL code.

- **Line Formation and Profiles:**

  While most of the overall problem is solved by this point, the DETAIL flux is still a crude approximation of the actual absorption line spectrum. Therefore the population numbers computed by DETAIL are used to create a model spectrum with realistic line-profile functions using the SURFACE code. The details of line formation will be discussed in the next two sections.

3.6 Line Formation

Most of the information we can learn about the physical state of stellar atmospheres is encoded in the absorption features of the spectrum. The spectral lines superimposed upon the continuum of the star are caused by bound-bound atomic transitions occurring in the atoms comprising the stellar matter. These transitions are accompanied by the creation or destruction of photons. To get an overview of the physical processes behind spectral lines, let us consider two atomic levels i and j of respective energies E_i and E_j and populations n_i and n_j, so that the energy of photons emitted or absorbed during transitions between these levels is $h\nu_{ij} = E_j - E_i$. It is instructive to write down the radiative transfer equation for the case that *only* bound-bound transitions between these levels are taken into account (Mihalas 1978):

$$\mu \frac{\mathrm{d}I_\nu}{\mathrm{d}z} = [n_j A_{ji} \psi_\nu - (n_i B_{ij} \phi_\nu - n_j B_{ji} \psi_\nu) I_\nu] (h\nu_{ij}/4\pi). \tag{3.26}$$

The three parts of the sum represent the contributions of different processes connecting the two energy levels to the changes in specific intensity I_ν: *Spontaneous emission* with transition probability A_{ji}, *absorption* proportional to B_{ij} and *stimulated emission* described by B_{ji}. ϕ_ν and ψ_ν are normalized profiles for absorption and emission, respectively. For

the case of complete redistribution they are identical. A_{ji}, B_{ij} and B_{ji} are called *Einstein coefficients* and connected via the *Einstein relations*

$$A_{ji} = \left(2h\nu^3/c^2\right) B_{ji} \tag{3.27}$$

and

$$g_i B_{ij} = g_j B_{ji}. \tag{3.28}$$

As we are particularly interested in absorption lines, we can now define a line absorption cross-section (unaccounted for stimulated emission)

$$\alpha_{ij} = B_{ij} \frac{h\nu_{ij}}{4\pi} \phi_\nu = \frac{\pi e^2}{mc} f_{ij} \phi_\nu, \tag{3.29}$$

where m is the electron mass, e the electron charge and f_{ij} the *oscillator strength*. The latter can be obtained from a quantum mechanical treatment of electric dipole transitions between the electron shells of atoms (Hilborn 1982):

$$f_{ij} = \frac{8\pi^2 m\nu_{ij}}{he^2 g_i} |\langle j|\mathbf{D}_L|i\rangle|^2, \tag{3.30}$$

where the dipole length operator $\mathbf{D}_L = e \sum_k \mathbf{r}_k$ is applied.[1]

3.7 Line Profiles

The line opacity increases from near-continuum values in the line wings to reach a maximum in the line core. Consequently, spectral lines provide a sampling over a wide range of atmospheric depths (the higher, and therefore cooler layers are seen in the core). The line profiles are shaped by various line-broadening mechanisms, as discussed by the textbooks of Griem (1974) or Collins (1989), of which the most important will be outlined in the following.

- **Natural Line Width:**

  Excited atomic states have a finite characteristic lifetime Δt that is typically of the order 10^{-8} s. Consequently Heisenberg's uncertainty principle $\Delta E \Delta t \geq h$ dictates that the energy difference $E_j - E_i$ between excited and de-excited level has an intrinsic spread. This effect is known as *radiative dampening*. The corresponding normalized distribution ϕ_ν of photon energies can be derived from a classical damped oscillator or from quantum mechanical considerations to give a Lorentz profile:

$$\phi_\nu^{\text{natural}} = \frac{\gamma_{\text{rad}}/4\pi^2}{(\nu - \nu_{ij})^2 + (\gamma_{\text{rad}}/4\pi)^2}. \tag{3.31}$$

---

[1] The sum is taken over all atomic electrons.

Table 3.1: The perturbing forces responsible for pressure broadening.

Type of Perturber	First Order Effect	Second Order Effect
Ion or Electron	Linear Stark Effect ($\propto r^{-2}$)	Quadratic Stark Effect ($\propto r^{-4}$)
Neutral Atom	Resonance Broadening($\propto r^{-3}$)	Van der Waals broadening ($\propto r^{-6}$)

The damping constant γ_{rad} can be measured experimentally or obtained from transition probabilities via

$$\gamma_{\mathrm{rad}} = \sum_{n<i} A_{in} + \sum_{m<j} A_{jm}, \qquad (3.32)$$

where the sum accounts for all possible decays of the upper and the lower states.

- **Pressure Broadening:**

  The collisional interactions between the atoms absorbing and emitting the light and the other particles of the surrounding plasma lead to additional broadening. This effect can be classified by the nature of the perturbing force as shown in Table 3.1.

  Resonance broadening and van der Waals broadening, both connected to the dipole moment of neutral atoms, can be neglected in the atmospheres of BA-type supergiants, since the most abundant element, hydrogen, is mostly ionized. That leaves linear and quadratic Stark broadening, that result from the interaction of the emitter with the electric field of a perturber, as the most important effects. The quadratic Stark effect (the shift in the energy of effected states is quadratic in electric field strength) has to be taken into account for the lines of all non-hydrogenic atoms, while the lines of hydrogen and singly-ionized helium are particularly subject to the linear Stark effect.

  Most of the pressure broadening, except for the linear Stark effect at high densities, can be accounted for via the impact phase-shift theory, where it is assumed that the collision is of a very short duration compared to the span of time during which the atom is actually radiating (or absorbing) the photon. This approach yields once again a Lorentz profile, with the parameter γ_{col} being proportional to the number of collisions per unit time. Utilizing the properties of convolutions between Lorentz dispersion profiles, one can see that the combined line profile of collisional and radiative damping is a Lorentzian with a total width of $\gamma = \gamma_{\mathrm{rad}} + \gamma_{\mathrm{col}}$, assuming both broadening processes to be uncorrelated.

  For the complex Stark broadening of hydrogen lines, tables from Stehlé & Hutcheon (1999) are used. They are based on the Model Microfield Method for both the electronic and ionic broadenings and give an accurate description of the line profile from the center to the wings. Other references for collisional broadening data can be found in the Appendix.

- **Thermal Doppler broadening:**

  This type of broadening stems from the velocity of the atoms along our line of sight due to their thermal motion. If we once again make the reasonable assumption, that

the atoms of the stellar plasma obey the Maxwell-Boltzmann distribution, then the profile resulting from *Doppler broadening* is a Gaussian of the form

$$\phi_\nu^{\text{Doppler}} = \frac{1}{\sqrt{\pi}\Delta\nu_{\text{D}}} \exp\left(-\frac{\Delta\nu}{\Delta\nu_{\text{D}}}\right)^2, \tag{3.33}$$

where $\Delta\nu = \nu - \nu_{ij}$ and $\Delta\nu_{\text{D}}$ is the Doppler width of the line,

$$\Delta\nu_{\text{D}} = \frac{\nu_{ij}}{c} v_0, \tag{3.34}$$

with $v_0 = \sqrt{2kT/m_A}$, where m_A is the atomic mass of an element under consideration.

- **Microturbulence:**

  Another non-thermal small-scale broadening agent is required to explain the properties of the spectra of hot massive stars. This so-called microturbulence is routinely used to derive consistent surface abundances for one element from different lines. It has only recently been suggested by Cantiello et al. (2009) to be linked to the presence of sub-surface convection fields driven by the opacity of iron group elements. For the sake of simplicity, and in the absence of a better description, this additional velocity field is assumed to have a Gaussian distribution. This allows a convolution of this distribution with the existing thermal Doppler profile, yielding once again a Gaussian. So to account for microturbulence, Equation 3.33 just needs to be modified by setting

  $$v_0 = \sqrt{\frac{2kT}{m_A} + \xi^2}, \tag{3.35}$$

  with ξ being the microturbulent velocity.

Assuming the above listed processes to be uncorrelated, they can be combined via multiple convolutions of the individual line profiles to give the total profile:

$$\phi_\nu^{\text{total}} = \phi_\nu^{\text{natural}} * \phi_\nu^{\text{pressure}} * \phi_\nu^{\text{thermal}} * \phi_\nu^{\text{microturb.}} = \phi_\nu^{\text{Lorentz}} * \phi_\nu^{\text{Gauss}} \equiv \phi_\nu^{\text{Voigt}}. \tag{3.36}$$

This convolution between Gaussian and Lorentzian distribution yields a so-called *Voigt profile*, which can be expressed using the definitions introduced earlier as

$$\phi_\nu^{\text{Voigt}} = \frac{\gamma/4\pi^2}{\sqrt{\pi}\Delta\nu_D} \int_{-\infty}^{\infty} \frac{\exp[-(\Delta\nu/\Delta\nu_D)^2]}{(\Delta\nu - \Delta\nu_D)^2 + (\gamma/4\pi)^2} \, d\Delta\nu. \tag{3.37}$$

As a rule, the line wings are dominated by the Lorentz profile while the line core is approximately Gaussian.

The shifting of the absorption and emission frequencies caused by the broadening agents presented so far may expose each single atom to a somewhat different radiation field. This allows the line to act on a broader range of frequencies, and thus to avoid saturation, strengthening the line. Hence we can expect changes in the equivalent width as well as in the profiles.
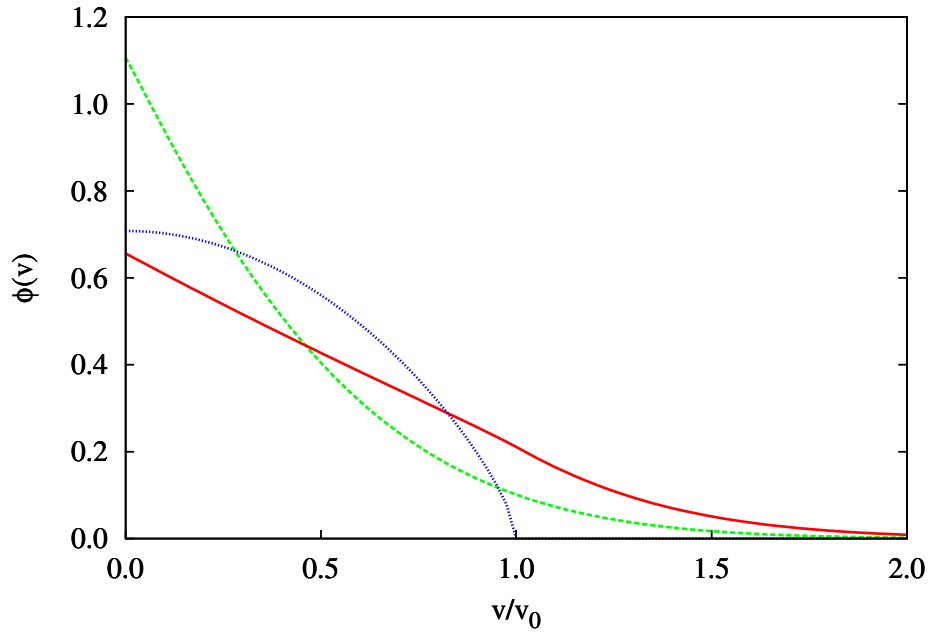
Figure 3.4: Macrobroadening functions calculated for different combinations of macroturbulence ζ and projected rotational velocity $v \sin i$. The dotted line represents a pure rotational profile $(v \sin i = v_0, \zeta = 0)$, the dashed line a pure macroturbulence profile $(v \sin i = 0, \zeta = v_0)$ and the continuous line a mixed profile $(v \sin i = \zeta = v_0)$. In all cases $\epsilon = 0.5$ is adopted.

For large-scale motions, however, entire collections of particles will have their rest wavelengths shifted by the same amount with respect to the observer. If these ensembles of atoms move collectively on scales that exceed the mean-free path for the photons in the atmosphere, the equivalent widths will not be affected but the profiles may change considerably. These effects, which work on a macroscopic level, will be listed in the following.

- **Rotational Broadening:**

  The rotation of a star leads to a characteristic Doppler-shift distribution over the stellar disk. Integration over the disk gives the line-profile function of rotation. Its width is a function of the projected equatorial velocity $v_{\mathrm{rot}} \sin i$, where i is the inclination angle between the rotational axis and the line-of-sight. When evaluating the contributions from different parts of the stellar disk, the decrease in intensity towards the limb has to be taken into account, the so-called *limb darkening*. It is commonly approximated by a linear relation,

  $$I(\mu)/I(1) = 1 - \epsilon(1 - \mu). \tag{3.38}$$

  The limb-darkening coefficient ϵ can be derived by fitting the theoretical limb-darkening from model atmosphere calculations, extensive tabulations are given by Wade & Rucinski (1985) as a function of T_{eff}, $\log g$ and λ. In practice, the theoretical line-profile is convolved with a broadening function of rotation. This is possible under the assumption that the line-profile derived earlier from microscopic considerations (Eq. 3.37) is independent of disk position. An analytical formula for the appropriate broadening function is given by Gray (2005, pp. 458–467) as

  $$G(\lambda, \Delta\lambda) = \frac{2(1-\epsilon)\sqrt{1 - \left(\frac{\Delta\lambda}{\Delta\lambda_{\mathrm{max}}}\right)^2} + \frac{1}{2}\pi\epsilon\left(1 - \left(\frac{\Delta\lambda}{\Delta\lambda_{\mathrm{max}}}\right)^2\right)}{c\pi\Delta\lambda_{\mathrm{max}}\left(1 - \frac{\epsilon}{3}\right)}\lambda \quad, \; |\Delta\lambda| \leq |\Delta\lambda_{\mathrm{max}}|. \tag{3.39}$$

- **Macroturbulence:**

  The line shapes of many stars are not explicable by rotation as the sole macrobroadening agent. Therefore macroturbulence was introduced to represent large-scale turbulent motions in the stellar atmosphere. A physical explanation of the macroturbulent velocity parameter was only recently found for hot stars, as being the collective effect of pulsations (Aerts et al. 2009). The most commonly used model is the radial-tangential (R–T) macroturbulence, as described by Gray (2005, pp. 433–437). The Doppler-shift distribution corresponding to this process can be expressed as

  $$\Theta(\Delta\lambda) = \frac{A_{\mathrm{R}}}{\sqrt{\pi}\zeta_{\mathrm{R}}\cos\theta}\mathrm{e}^{-(\Delta\lambda/\zeta_{\mathrm{R}}\cos\theta)^2} + \frac{A_{\mathrm{T}}}{\sqrt{\pi}\zeta_{\mathrm{T}}\sin\theta}\mathrm{e}^{-(\Delta\lambda/\zeta_{\mathrm{T}}\sin\theta)^2}, \tag{3.40}$$

  where A_R and A_T are the surface areas and ζ_R, ζ_T the macroturbulent velocities of radial and tangential motion, respectively. For the computations in this study, symmetry between the radial and tangential velocity profiles is assumed ($A_R = A_T$ and $\zeta_{\mathrm{R}} = \zeta_{\mathrm{T}} = \zeta$). As macroturbulence, just like the velocity distribution of rotation over the disk, is not isotropic, sequential convolution of the line-profile with separate distribution functions is bound to introduce errors and numerical integration over the stellar disk, including rotation, macroturbulence and limb-darkening has to be preferred:

  $$M(\Delta\lambda) = \oint I_0(1 - \epsilon + \epsilon\mu)\Theta(\Delta\lambda - \Delta\lambda_R)\mu\mathrm{d}\omega, \tag{3.41}$$

  where $\Delta\lambda_R$ denotes the projected rotational Doppler shift, that is constant along lines parallel to the rotation axis. To evaluate this integral, the apparent disk of the
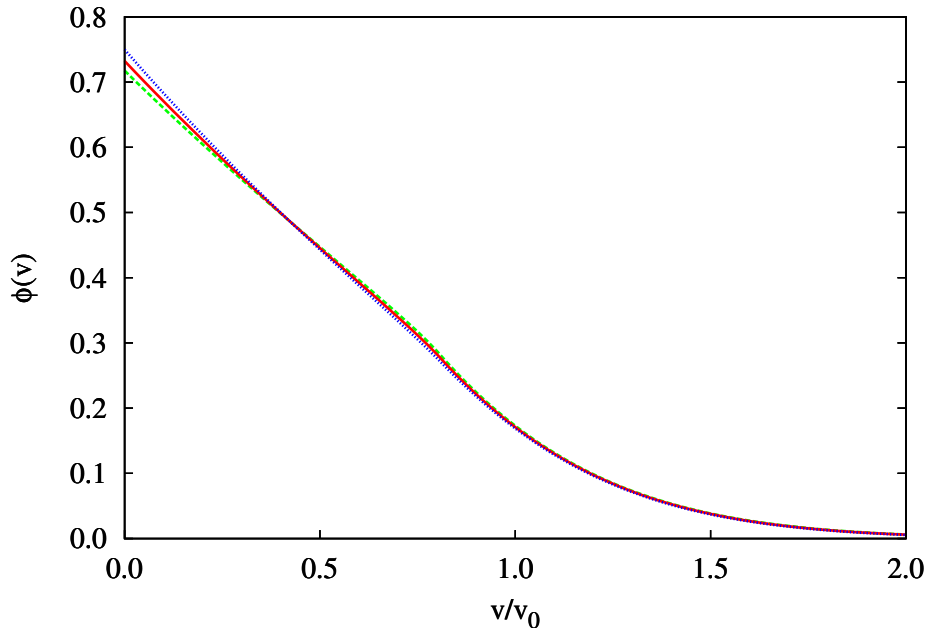
Figure 3.5: Sensitivity of the combined macrobroadening profile ($v \sin i = \zeta = v_0$) to changes in the linear limb-darkening coefficient. The continuous line represents the profile for $\epsilon = 0.5$, the dashed and dotted lines for changes in ϵ by ± 0.2. This covers the variations found over the parameter space examined in this study (as given by Wade & Rucinski 1985).

star was divided into 16 million parts of equal size. The resulting profile $M(\Delta\lambda)$ is characterized by three parameters: the projected rotational velocity $v \sin i$, the macroturbulent velocity ζ, and the limb-darkening coefficient ϵ. Examples from the grid calculated for this study are depicted in Fig. 3.4. The addition of macroturbulence decreases the sensitivity of the dispersion profile for changes in limb darkening, so that a constant coefficient $\epsilon = 0.5$ could be assumed for all lines and stars included in this study (see Fig. 3.5 for a comparison).

- **Instrumental profile:**

  The finite resolution of the spectrograph introduces an additional broadening of spectral lines. This broadening is assumed to have a Gaussian form with a standard deviation of $\sigma(\lambda) = R\lambda(2\sqrt{\ln(2)})^{-1}$, where R is the resolving power of the spectrograph defined in Chapter 2.

3.8 Model Atoms

A large amount of atomic data are needed to solve the rate equations and to compute accurate synthetic spectra, including excitation energies, oscillator strengths, ionization energies and cross-sections for collisional (de-)excitation and photoionization. Collections of such data prepared for use in model atmosphere and line formation computations are called *model atoms*. An illustration of the complexity of a model atom is given in Fig. 3.6.

Table 3.2: Non-LTE model atoms used in DETAIL/SURFACE calculations.

Ion	Source	Ion	Source
H	Przybilla & Butler (2004)	O I/II	Przybilla et al. (2000)
He I	Przybilla (2005)	Mg I/II	Przybilla et al. (2001a)
C I/II	Przybilla et al. (2001b)	S II/III	Vrancken et al. (1996)
	Nieva & Przybilla (2006, 2008)	Ti II	Becker (1998)
N I/II	Przybilla & Butler (2001)	Fe II	Becker (1998)

Realistic model atoms play a crucial role for modern quantitative spectroscopy, since the predictive power of non-LTE computations can only be as good as the models atoms used. While some of the necessary data can be determined under laboratory conditions, most of the atomic data are inferred from qunatum mechanical ab-initio calculations. Important collections of data were provided by the Opacity Project (Seaton et al. 1994) and the Iron Project (Hummer et al. 1993), and vast amounts of data are contained within the line lists of Kurucz (1992) and the National Institute of Standards and Technology (NIST, Reader et al. 2002). The collection of improved atomic data remains an active field of research in atomic physics, and new developments are continuously published.

The use of data from different sources may lead to noticeable differences in the model predictions. A comparison with observed spectral lines of stars can provide the means to choose the best model atom realization for a particular parameter regime. Sources for the model atoms used here are listed in Table 3.2, all tested for use with BA-type supergiants.

3.9 Validity of the Method

During the construction of the model atmospheres several assumptions were made, whose applicability to analyses of BA-type supergiants is not obvious.

A first example for this is the *stationarity*. It is well known that BA-type supergiants show photometric as well as spectral variability, and stars of this type are called α Cygni variables. Low-degree nonradial pulsation modes are proposed to explain this behavior (see, e. g., Gautschy 2009). Long-time monitoring of H_α in the spectrum of, e. g., Deneb shows ample variations (Morrison et al. 2005). Kaufer et al. (1996, 1997) conducted the most comprehensive study to date to assess the spectral variability of this type of stars. They find line-profile variations, but no significant line-strength variations within their accuracy of 5%, and provide an upper limit of 1% for the amplitude of line-strength variations coupled to line-profile variations.

To prevent possible inconsistencies in the analysis, the usage of spectral data from different epochs was avoided. The observations were performed on a timescale of days, for which stationarity can be considered a very reasonable assumption. In a way, the derived atmospheric parameters therefore describe a snapshot of the stellar atmospheric conditions and the abundance determination should be unaffected by variability.
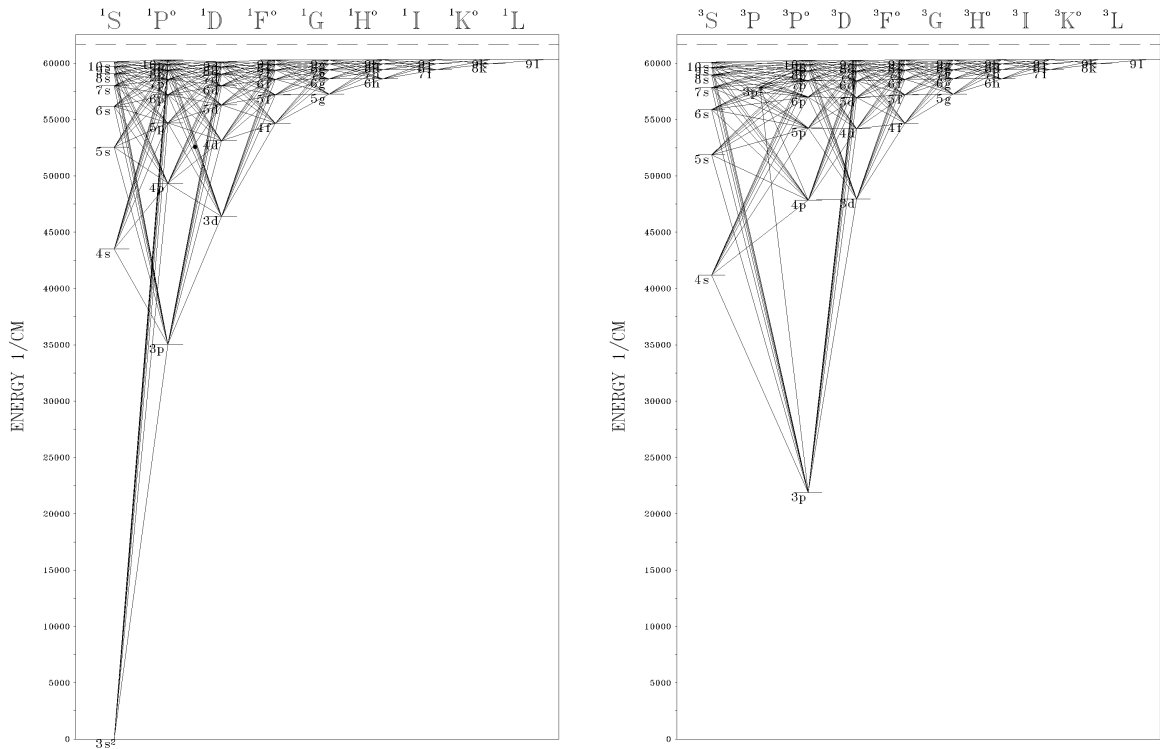
Figure 3.6: Grotrian-diagrams for the neutral magnesium atom (Przybilla et al. 2001a). Depicted in the left panel is the singlet-, in the right panel the triplet-spin system. All transitions shown are treated explicitly in non-LTE. Not shown here, but included in the computations, are additional transitions between the two spin systems and towards the ionized stage of magnesium.

The atmospheric structure is computed postulating *local thermodynamic equilibrium.* To test this assumption, the results were compared to the atmospheric structures of non-LTE models (TLUSTY, Hubeny & Lanz 1995) by Przybilla et al. (2006). They found reasonable agreement. An increase of discrepancies due to non-LTE effects is expected for higher temperatures and luminosities, so that the usage of line-blanketed non-LTE atmospheres should prove necessary starting at early B- and highly luminous mid-B-supergiants. This limits the applicability of the hybrid non-LTE technique towards higher temperatures. Another problem, not related to the assumption of LTE, is the development of pressure inversion in atmospheres cooler than about 8200 K. This phenomenon is badly understood, see Przybilla et al. (2006) for a discussion. Consequently stars below this limit were excluded from our study.

As *plane-parallel, hydrostatic* model atmospheres are used, some geometrical effects are neglected. The extent of the model atmospheres can reach up to several percent of the derived stellar radii, so that the neglect of sphericity could cause problems. Note however, that the line formation region of weak lines occupies only a fraction of that space. Another uncertainty can be introduced by macroscopic velocity fields, i.e., a stellar wind. This be-
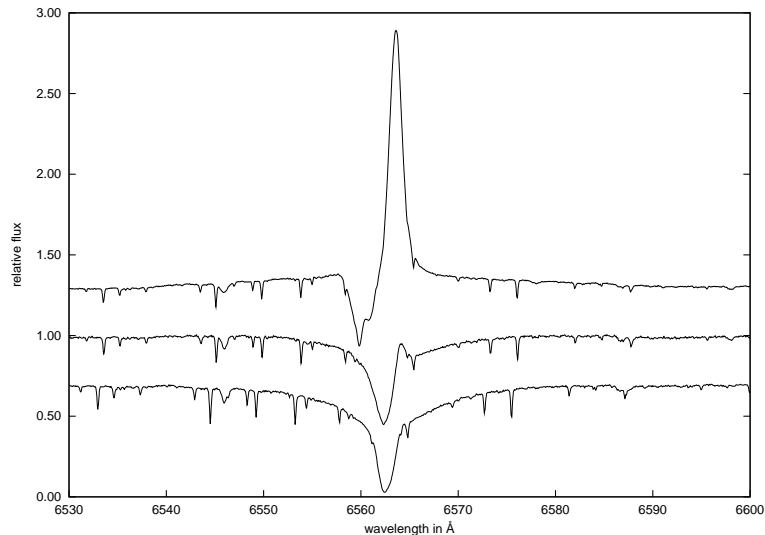
Figure 3.7: H_α is very sensitive to the effects of stellar wind, which are roughly proportional to luminosity. Shown are the line-profiles for three supergiants of spectral type A3. From top to bottom: HD 223385, an extreme object of luminosity class Iae showing strong emission, HD 13476 (LC Iab) with signs of a P-Cygni profile, HD 210221 (luminosity class Ib) with small line asymmetries. Objects as affected by stellar wind as HD 223385 were excluded from the study.

comes evident in the sample spectra, the effects ranging from typical P Cygni profiles to small line asymmetries (see Fig. 3.7). One can test the validity of the assumptions by comparing the model predictions to spherical and hydrodynamic (unified; wind + photosphere) non-LTE codes like, e. g., FASTWIND (Puls et al. 2005). Such a comparison was done by Dufton et al. (2005) for early B-supergiants, which ascertained good agreement with hydrostatic plane-parallel model atmospheres. Schiller & Przybilla (2008) find that, while improved matches between theory and observation are achieved for the hydrogen lines, the resulting parameters of both methods are practically identical and that some discrepancies between theory and observation remain even in the unified approach.

At present, however, FASTWIND does not consider line formation for metal ions relevant for the spectral analysis of BA-type supergiants. Line-blanketed LTE model atmospheres plus non-LTE line formation remain the best option, as long as their limitations are considered. Problems may arise for very luminous supergiants and in the analysis of strong and wind-affected lines. This study is therefore mostly based on the evaluation of weak metal lines (equivalent width $\lesssim 300$ mÅ), which are formed deep in the atmosphere and are least affected by sphericity and the stellar wind. The consistency of the results shown in later chapters indicates the validity of the approach.

4 Data Analysis Strategy

Very detailed quantitative studies of BA-type supergiants using the hybrid non-LTE technique described earlier were so far only done for a handful of stars (Przybilla et al. 2006; Schiller & Przybilla 2008) and were based on a time-consuming manual construction of micro-grids and visual inspection to bring theory and observations to match. A prime objective of this thesis was the streamlining and partial automization of this process in order to increase the sample size and to reduce the time required for future analyses. To this end, an extensive grid of synthetic spectra was computed with the programs described in the previous chapter. A simple iteration scheme was devised to determine the basic stellar atmospheres via line-profile fitting. The individual steps of this procedure are discussed in the following sections, an overview gives Fig. 4.1.

4.1 Comparing Models and Observation

The automatized procedure was improved in several steps. Early results for a sub-sample of 10 stars are described in Firnstein & Przybilla (2006), using a smaller, less flexible model grid and a modified version of the fitting routine FITPROF (Napiwotzki 1999).

For a second, more refined spectroscopic analysis around 25 000 model spectra per element were combined into 5-dimensional grids. The parameter space covered effective temperatures T_{eff} from 8300 K to 15 500 K in steps of 250-500 K, logarithmic surface gravities $\log g$ (cgs units) from 2.50 to the convergence limit at 0.95 (at the lower T_{eff}-limit) or 1.90 (at the upper T_{eff}-limit) in steps of 0.1 dex, microturbulences ξ from $3\,\text{km}\,\text{s}^{-1}$ to $8\,\text{km}\,\text{s}^{-1}$ in $1\,\text{km}\,\text{s}^{-1}$ steps and in helium abundances y from 0.09 to 0.15 (by number, steps of 0.015). Finally, elemental abundances were varied over one decade in steps of 0.25 dex. Overall, this amounts to several years of computing time when using a single present-day processor. Hence the computations were spread over the local computer cluster to speed up completion.

Theoretical and observed line profiles are compared via the software package SPAS (Spectral Plotting and Analysis Suite, Hirsch 2009), replacing the less flexible FITPROF in the new analysis. The program provides the means to interpolate between model grid points for up to three parameters simultaneously. It also allows to apply instrumental and rotational broadening to the resulting theoretical profiles. This part of the program was modified to include the macrobroadening functions computed for this study, which consider both macroturbulence and projected rotational velocity. Furthermore, the program uses the downhill simplex algorithm (Nelder & Mead 1965) to minimize χ^2 in order to find the best match to the observed spectrum. It allows to fit a set of lines in two modes: simultaneously and individually. The first mode is helpful to derive parameters from a
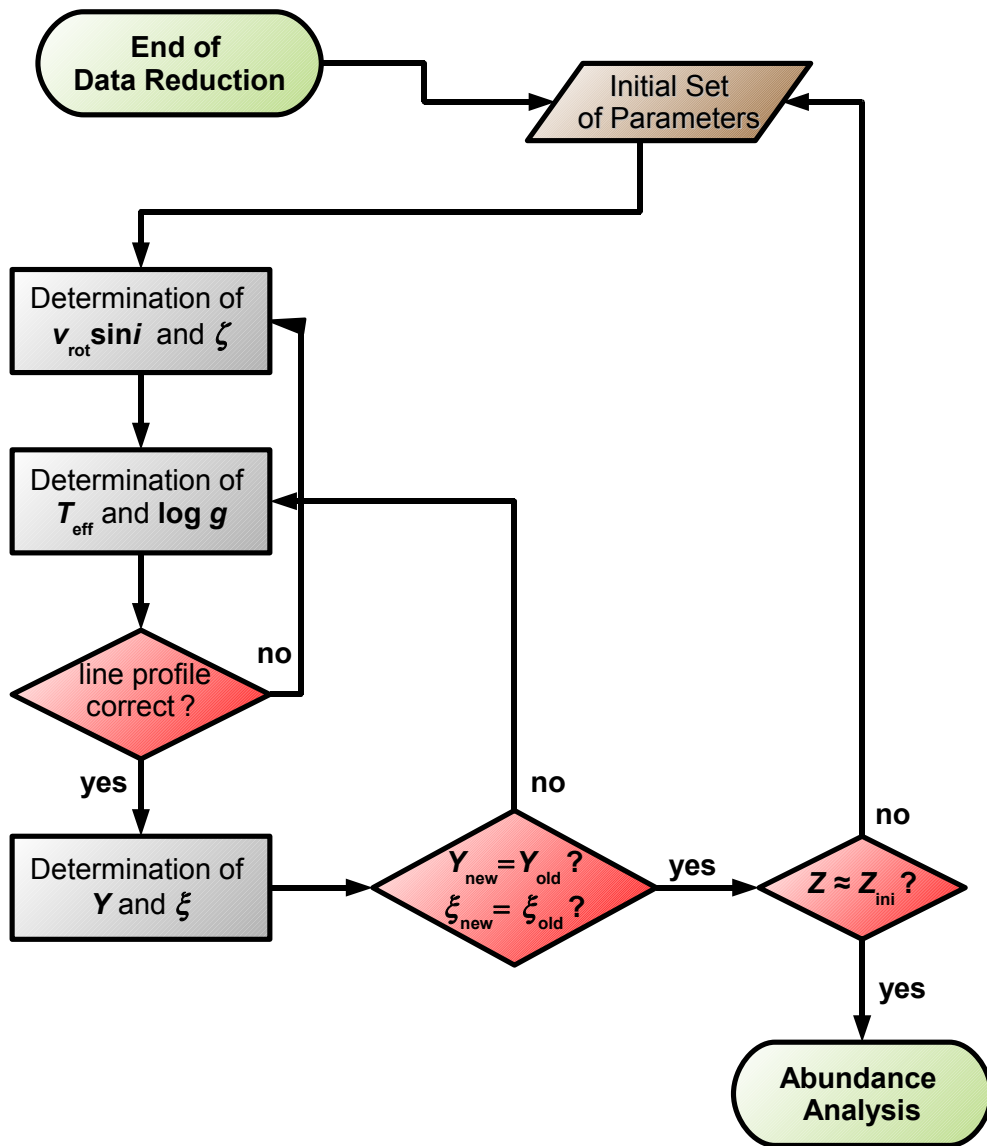
Figure 4.1: Simplified flowchart of the parameter determination process.

whole set of lines, utilizing information contained in all of them. The second mode allows to compute the line-to-line scatter, which can be used, for example, to derive the micro-turbulence, and to identify individual outliers, which helps to find errors in the continuum normalization or possible line-blends that distort the results.
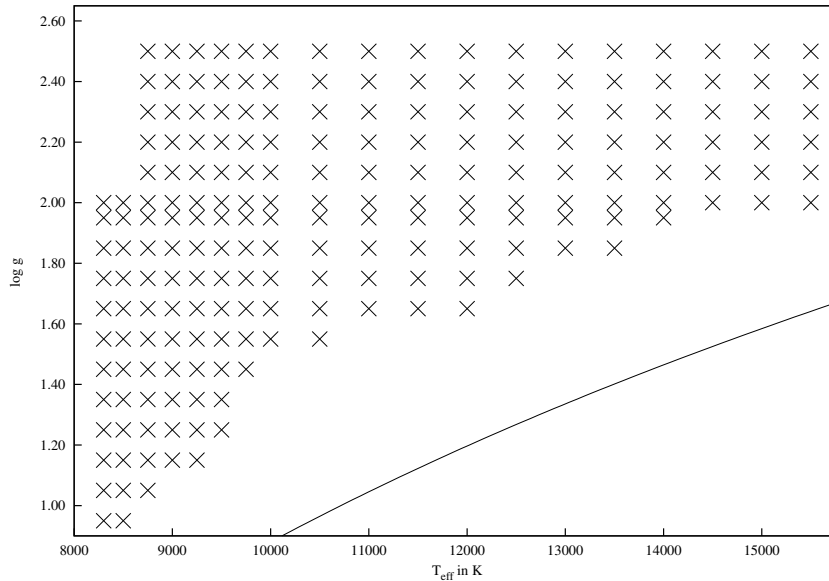
Figure 4.2: The model grid at $y = 0.12$ and $\xi = 8\,\mathrm{km\,s^{-1}}$. At every point models for five different abundances of all elements included in the analysis were computed. Similar grids in the T_{eff}-$\log g$-plane exist for other helium abundances and microturbulences. The continuous line indicates the Eddington-limit (where the gravitational force inwards equals the radiation force outwards), taking only Thomson-scattering into account.

4.2 The Iterative Process

As we have seen in the previous chapter, the main parameters describing the properties of the stellar atmosphere are effective temperature T_{eff} and logarithmic surface gravity $\log g$ and metallicity Z. Nonetheless, secondary parameters like microturbulence ξ and surface helium abundance y have significant effects on the majority of spectral lines (see Fig. 4.8). These additional parameters also influence the atmospheric structure: For example, a change in helium abundance mainly modifies the electron density, while an increase in microturbulence affects the temperature structure by strengthening the line blanketing effect (see Fig. 4.7). In order to find a globally satisfying solution, it is helpful to derive the basic atmospheric parameters T_{eff}, $\log g$, ξ and y in individual steps, utilizing different spectral indicators on the way.

4.2.1 Effective Temperature and Surface Gravity

The strength of hydrogen lines peaks in A-type stars, and lines of the Balmer-series dominate the blue part of the sample spectra. The amount of broadening by the linear Stark effect seen in these lines is traditionally used as a sensitive surface gravity indicator. The temperature sensitivity of their line-profiles is non-negligible, however, as shown in Fig. 4.4. To constrain both temperature and surface gravity at once, at least one additional indicator is required. So-called ionization equilibria are a good choice for this role: If lines
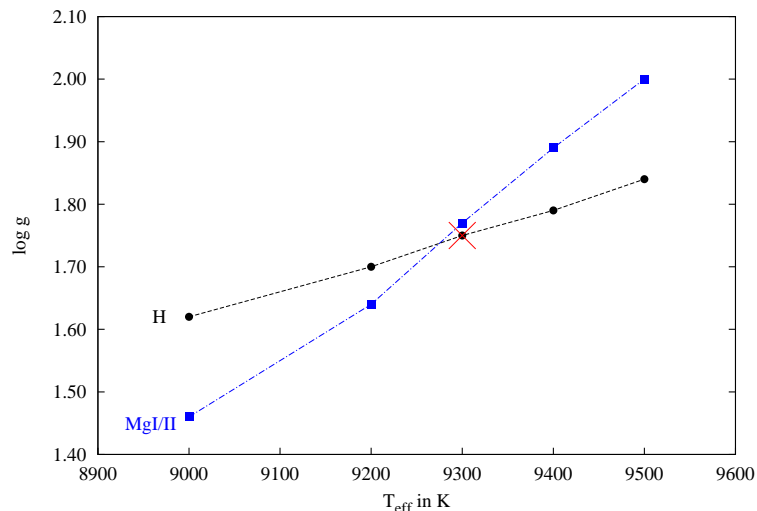
Figure 4.3: $\log g$ und T_{eff} can be constrained using the sensitivity of ionization equilibria and hydrogen lines, as shown here at the example of HD 165784. The cross marks the parameters adopted for the abundance analysis. Note that the adopted values for microturbulence and helium abundance affect the result.
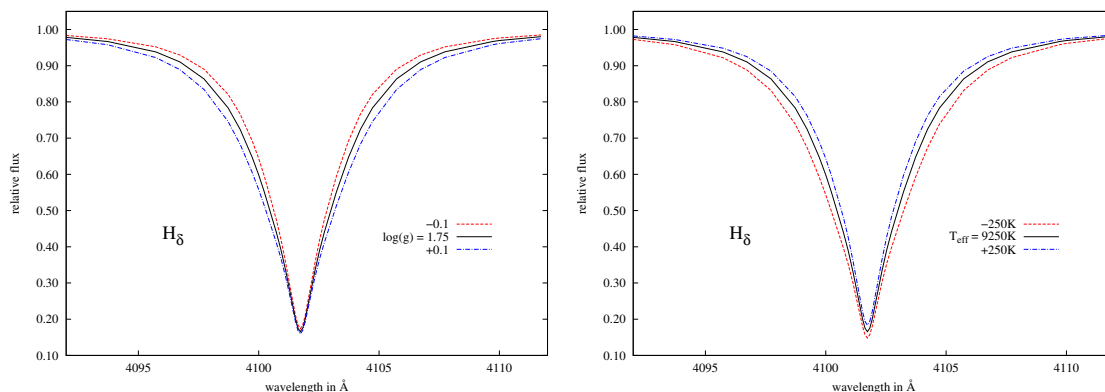
Figure 4.4: Sensitivity of the Balmer lines to variations in T_{eff} and $\log g$ using the example of H_δ in a parameter range typical for supergiants of early A-type.

of several ionization stages of a single element are present in the stellar spectrum, the abundance analysis of all stages must give the same result for the total abundance of the element. Utilizing this condition, a relation between T_{eff} and $\log g$ can be constructed. The information provided by several indicators allows to resolve the ambiguity in the parameter determination (Fig. 4.3 provides an example).

The ionization equilibria of several elements are evaluated for the parameter determination, most importantly Mg I/II-lines for the low-temperature regime and the N I/II-lines in the high-temperature regime of our sample. Additionally, the C I/II ionization equilibrium
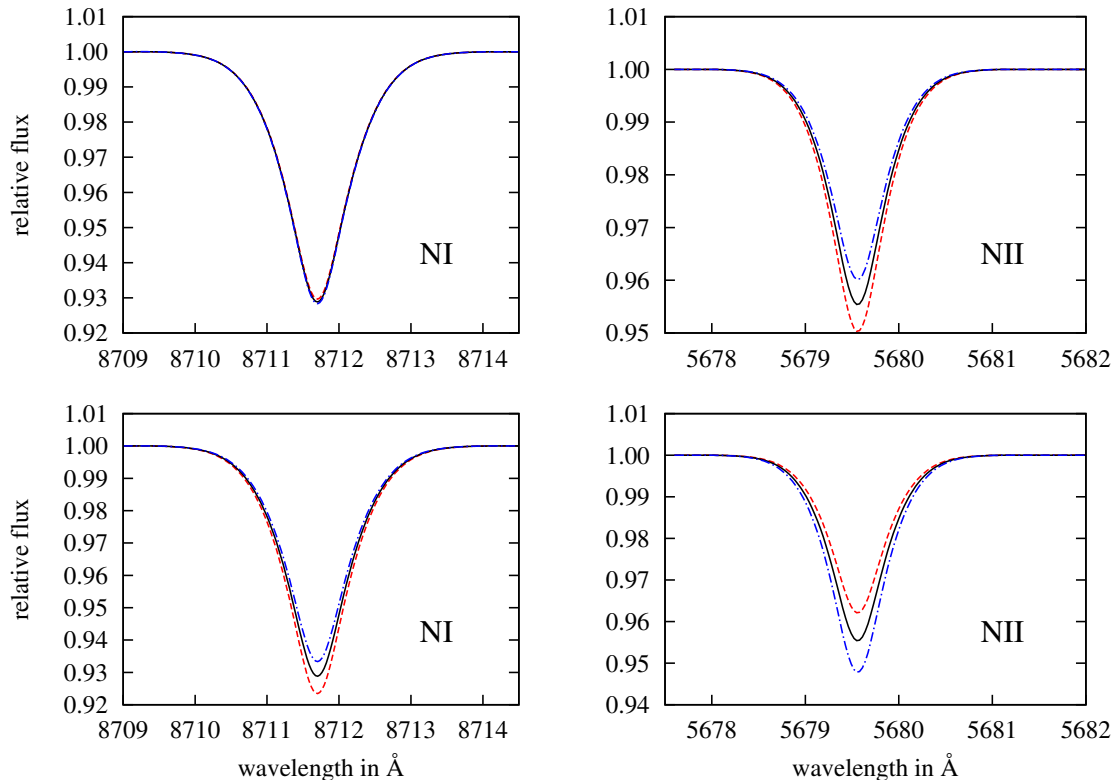
Figure 4.5: Sensitivity of N I/II-lines to variations in $\log g$ (upper panels) and T_{eff} (lower panels) in a parameter range typical for supergiants of late B-type ($T_{\text{eff}} = 12\,500\,\text{K}$, $\log g = 2.1$). The same variations and according designations as in Fig. 4.4 are used.

is available to confirm the results for the coolest stars, while the O I/II-lines are useful for hotter objects. For the majority of the stars two or in some cases even three metal ionization equilibria can thus be utilized. An example for the reactions of typical diagnostic lines to changes in T_{eff} and $\log g$ is given in Fig. 4.5. In general, lower temperatures and higher surface gravities shift the balance towards lower ionization stages.

Hα (see Fig. 3.7) and, in the most luminous objects, even Hβ and Hγ can be affected by the presence of a significant stellar wind and have to be omitted from the analysis in these cases. However, agreement between theory and observations is restored for the higher Balmer lines, which are formed deeper in the atmosphere.

In practice, first estimates for ξ and y are used to determine initial values for T_{eff} and $\log g$ in a first iteration step (using elemental abundances as third fit parameter), which are in turn adopted to derive ξ and y in a next step. Convergence is quickly achieved using our comprehensive model grids and Spas.
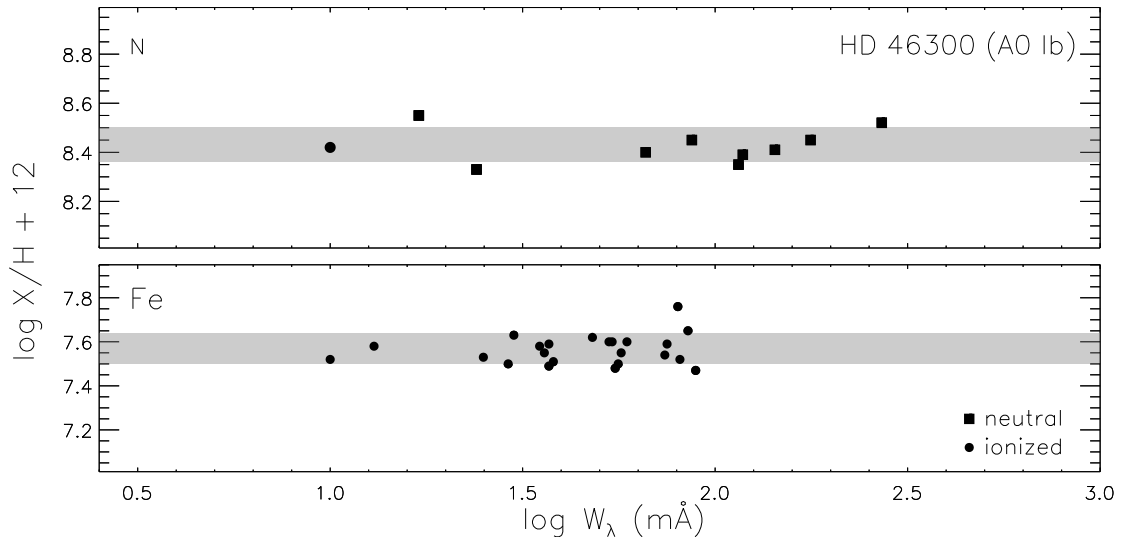
Figure 4.6: Abundance values derived from single lines are presented versus respective equivalent widths for a selection of nitrogen and iron lines in the spectrum of HD 46300 (A0 Ib). The 1σ-scatter around the mean value is indicated by the gray bands. Results from linear regression are consistent with a slope of zero in both cases.

4.2.2 Microturbulence

The strengthening effect of microturbulence on absorption lines in stellar spectra is dependent on the equivalent width. Weak lines are virtually unaffected apart from profile changes. The microturbulent velocity ξ is therefore usually determined by demanding that the abundances indicated by the lines of a particular ion are independent of equivalent width. In practice, this can be achieved by finding the microturbulence value that minimizes the line-to-line scatter in derived abundances. The extensive Fe II line spectrum proved to be most useful for this task. An example is shown in Fig. 4.6, using the traditional form of illustration. Typically, the spectra of all elements analysed in individual stars are consistent with the values derived from iron lines. A good knowledge of the microturbulent velocity is crucial to determine the atmospheric parameters due to its influence on the ionization equilibria, while the Balmer-lines are virtually insensitive to variations of this parameter.

4.2.3 Helium Abundance

A change in the atmospheric helium abundance gives rise to a modified mean molecular weight of the atmospheric plasma, which has similar effects on model predictions than a variation of $\log g$ (Kudritzki 1973; Przybilla et al. 2006). Virtually all diagnostic lines in the stellar spectrum are affected (compare Fig. 4.8). Therefore, the helium abundance y has to be constrained simultaneously with the other atmospheric parameters. This is done via line-profile fitting of helium lines. Results for individual fits to the He I-lines of the sample stars can be found in the appendix.
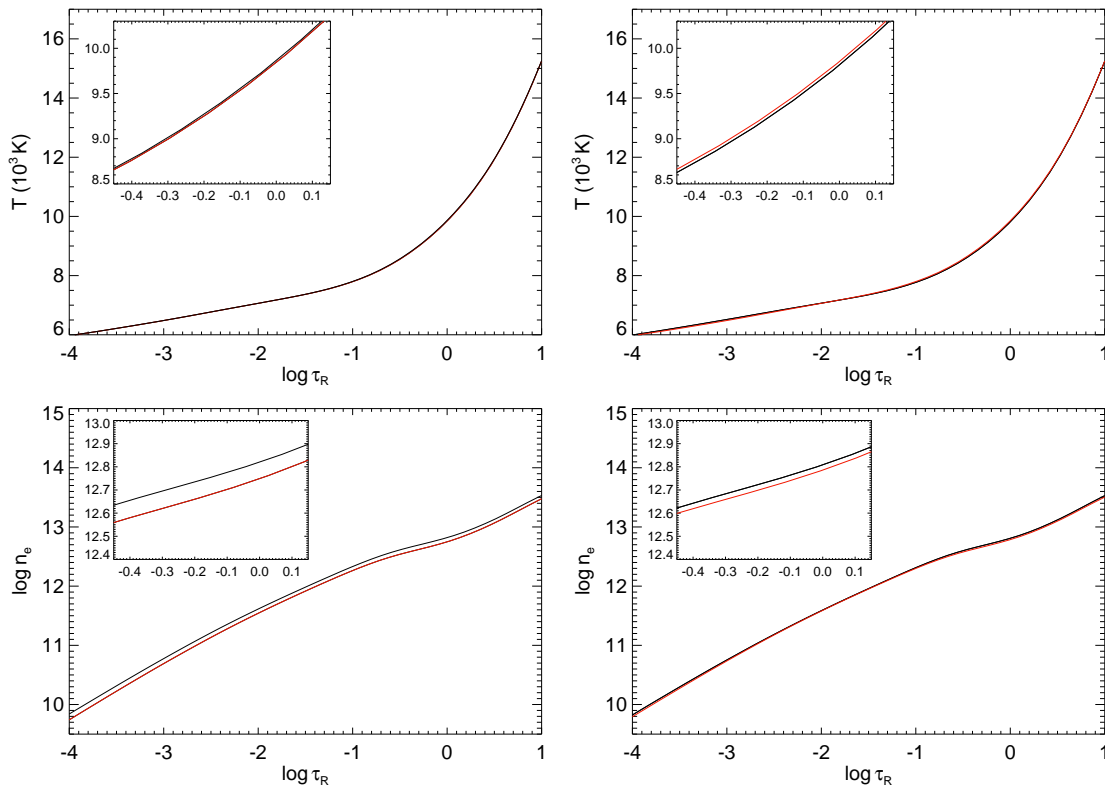
Figure 4.7: Influence of the helium abundance and microturbulence on the atmospheric structure for ATLAS models with $T_{\text{eff}} = 9\,000\,\text{K}$, $\log g = 1.5$. Shown are temperature structure (upper panels) and electron density (lower panels). In the inset, the formation region of weak lines is magnified. On the left models for atmospheric helium abundances of $y = 0.09$ (red line) and $y = 0.15$ (black line) and on the right models using ODFs with $\xi = 4$ (black line) and $\xi = 8$ (red line) are presented.

4.2.4 Metallicity

Low star-to-star scatter in metallicity was found in recent analyses of early B-type dwarfs – the progenitors of BA-type supergiants on the main sequence – in the solar neighbourhood (Przybilla et al. 2008), using similar analysis techniques. Given the low sensitivity of our analysis to small changes in metallicity (Przybilla et al. 2006), this parameter was held fixed throughout our model grid. The metallicity to slightly subsolar values (with respect to the solar standard of Grevesse & Sauval 1998) in accordance with the B-dwarf results (the cosmic abundance standard). This approximation was proved correct *a-posteriori* by our abundance analysis for most of the sample stars. The fact that there are only small variations from the norm, which will be discussed later on, also justifies the ODF-approach to line blanketing. If significant discrepancies were found, as was the case for the most metal-rich stars of our sample objects were reanalyzed by means of fine-tuned micro-grids, adopting a higher value for the metallicity in order to rule out any possible bias.
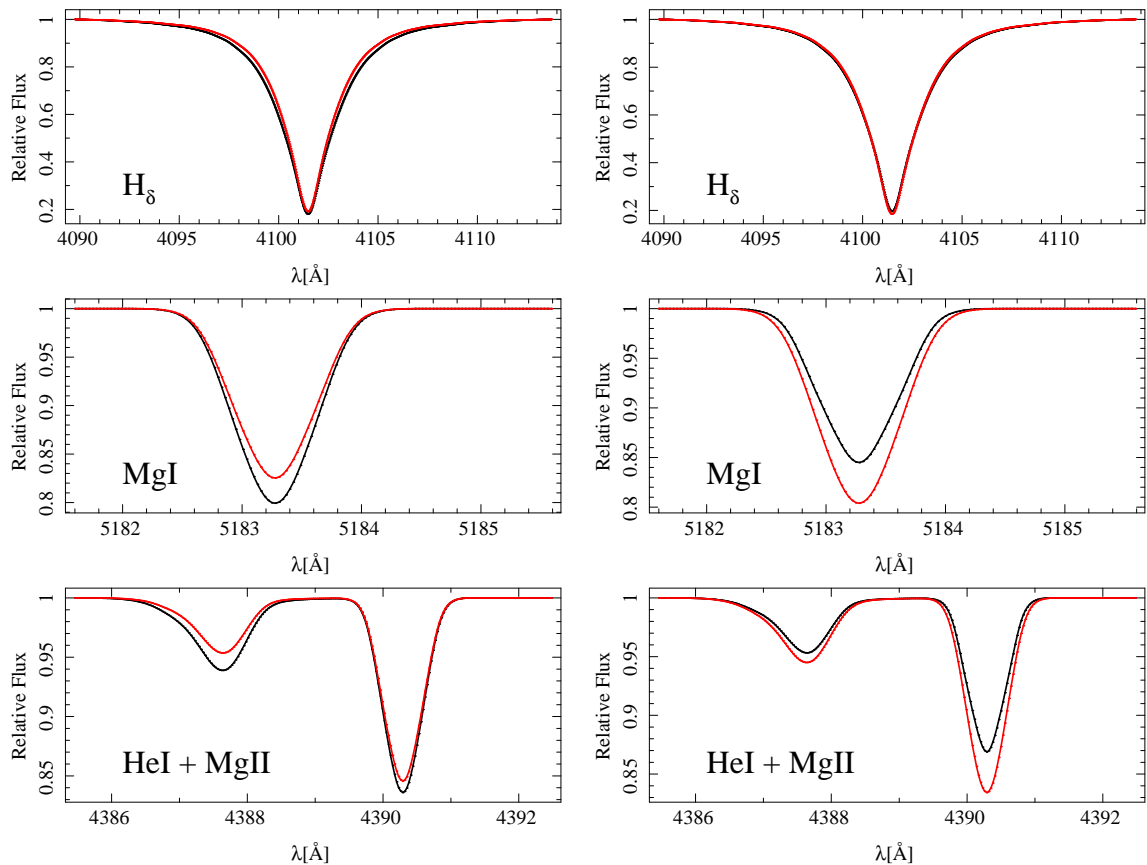
Figure 4.8: Influence of the helium abundance (on the left) and microturbulence (on the right) on a set of diagnostic lines. The same model atmospheres and designations as in Fig. 4.7 are used. DETAIL and SURFACE calculations were performed on top of the LTE model atmospheres. To obtain realistic line profiles, line broadening typical for our object spectra was applied, including the effects of macroturbulence, rotation and the spectral resolution.

4.2.5 Projected Rotational Velocity and Macroturbulence

In order to perform line-profile-fitting it is necessary that the models are able to reproduce the line-shapes accurately. To achieve this, the synthetic spectra are convolved with the functions for rotational and macroturbulent broadening discussed in the previous chapter. The same set of metal lines was chosen to derive $v \sin i$ and ζ in most of our targets, including the Mg II line at 4390 Å, the Mg I line at 5183 Å, the Fe II pair around 6148 Å, and the O I triplet around 6157 Å. However, for the two hottest objects in our sample only the S II line at 5354 Å was used. Just as other recent studies of rotational broadening in BA-type supergiants (Verdugo et al. 1999; Ryans et al. 2002), we found disentanglement of the effects of projected rotational velocity and macroturbulence to be difficult. Values of $v \sin i$ and ζ representing the best fits show a large scatter from line to line. The reason for this is a certain degree of degeneracy in the solutions, which is shown for two exemplary cases in Fig. 4.9. Fits without macroturbulence contribution agree very well
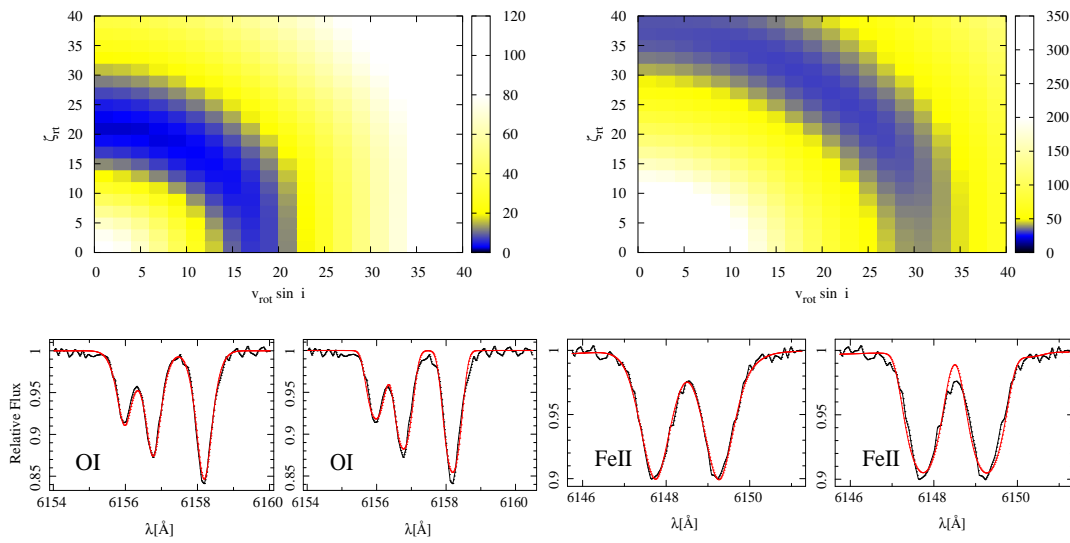
Figure 4.9: Derivation of $v \sin i$ and ζ from the O I triplet around $6157\,\text{Å}$ (left) in HD 207673 and the Fe II pair around $6148\,\text{Å}$ (right) in HD 14433. The upper panels show contour plots of a goodness-of-fit parameter in $(v \sin i, \zeta)$ space, lower values representing a better fit. The lower panels display the best line-profile-fits with and without macroturbulence (left and right, respectively).

in the resulting $v \sin i$ for different absorption features. However, they can not reproduce observations in such a satisfactory way as fits that consider both effects.

5 The Atmospheric Parameters

The focus of this study is on the determination of surface abundances and distances for a sample of Galactic BA-type supergiants from spectroscopy. An important prerequisite for this kind of analysis is the derivation of accurate and precise atmospheric parameters. Special emphasis is put on identifying and eliminating sources of systematic error, which allows us to constrain all relevant parameters with unprecedented accuracy. A good way to test the quality of the results is to check the final solution for consistency across elements and ionization stages. Additionally, the spectral energy distribution (SED) of the models is compared to spectrophotometric measurements.

This study presents the most comprehensive collection of atmospheric parameters from a homogeneous non-LTE analysis of Galactic BA-type supergiants to date. As expected, a continuous distribution over the temperature range from 8400 to 12 700 K is obtained, displaying no signs of systematic shifts or gaps stemming from the use of different temperature indicators. The resulting atmospheric parameters for the sample of 35 stars are presented in Table 5.1. Moreover, abundances for all ionization stages involved in the atmospheric parameter determination are listed there.

Over the course of this chapter, the results are compared to previous studies of BA-type supergiants and to empirical spectral-type–T_{eff} relations, as they are found in the literature. The applicability of the reddening-free Q-index to derive effective temperatures of the sample stars from photometry is discussed at the end of the chapter.

5.1 Spectral Energy Distribution

As a verification of the spectroscopic analysis the ATLAS9 fluxes computed for the final parameters are compared to photometric data in the optical and near-IR, and UV spectrophotometry. Thus, it was investigated whether the models reproduce the SEDs of the stars, and as a consequence also their global energy output.

Table 5.1: Stellar parameters of the programme stars.

#	Object	$T_{\rm eff}$ K	$\log g$ cgs	ξ km s^{-1}	$v\sin i$ km s^{-1}	ζ km s^{-1}	$\log X/{\rm H}+12$								
							He I	C I	C II	N I	N II	O I	O II	Mg I	Mg II
1	HD 12301	12600±200	2.15±0.10	7±1	10±10	20±10	11.06±0.06			8.16±0.05	8.12±0.04	8.72±0.06	8.65±0.03		
2	HD 12953	9200±200	1.15±0.10	8±1	22±7	32±11	11.12±0.03			8.40±0.03	8.49				
3	HD 13476	8500±150	1.40±0.10	6±1	12±2	24±2	11.16±0.08	8.18±0.12	8.20±0.13					7.44±0.03	7.46±0.04
4	HD 13744	9500±250	1.55±0.15	6±1	12±10	29±9	11.16±0.05							7.49±0.04	7.39±0.07
5	HD 14433	9150±150	1.40±0.10	7±1	17±3	29±5	11.10±0.08	8.25	8.23±0.05					7.49±0.06	7.40±0.04
6	HD 14489	9350±250	1.45±0.15	7±1	13±2	35±2	11.15±0.04			8.51±0.05	8.54±0.08				
7	HD 20041	10000±200	1.65±0.10	7±1	14±2	37±3	11.08±0.04			8.25±0.04	8.35±0.04				
8	HD 21291	10800±200	1.65±0.10	7±1	32±4	33±9	11.11±0.04			8.44±0.04	8.48±0.03				
9	HD 39970	10300±200	1.70±0.10	7±1	2±3	45±2	11.08±0.05			8.13±0.05	8.22±0.14				
10	HD 46300	10000±200	2.15±0.10	3±1	0±2	14±2	11.11±0.06			8.43±0.07	8.42				
11	HD 186745	12500±200	1.80±0.10	8±2	22±10	40±14	11.06±0.05			8.37±0.05	8.33±0.03	8.77±0.01	8.77		
12	HD 187983	9300±250	1.60±0.15	7±1	15±6	29±8	11.08±0.07	8.25	8.31±0.12					7.58±0.04	7.50±0.03
13	HD 197345	8700±150	1.20±0.10	8±1	10±9	29±7	11.19±0.06	8.12±0.06	8.07±0.09					7.5±0.05	7.47±0.05
14	HD 202850	10800±200	1.85±0.10	6±1	14±5	35±5	11.20±0.07			8.68±0.04	8.74±0.07				
15	HD 207260	8800±150	1.35±0.10	7±1	15±3	25±3	11.17±0.04	8.26±0.07	8.17±0.09					7.51±0.05	7.48±0.02
16	HD 207673	9250±100	1.80±0.10	5±1	1±2	23±2	11.11±0.10	8.18	8.16±0.11	8.48±0.03	8.45			7.51±0.07	7.44±0.04
17	HD 208501	12700±200	1.85±0.10	8±2	16±10	56±14	11.07±0.06			8.25±0.08	8.22±0.07	8.74	8.77±0.01		
18	HD 210221	8400±150	1.40±0.10	6±1	0±2	27±2	11.13±0.04	8.24±0.07	8.17±0.01					7.51±0.06	7.48±0.03
19	HD 212593	11200±200	2.10±0.10	5±1	6±2	24±2	11.15±0.06			8.45±0.02	8.43±0.09				
20	HD 213470	8400±150	1.30±0.10	7±1	13±2	27±2	11.08±0.09							7.46±0.03	7.50±0.06
21	BD+602582	11900±200	1.85±0.10	7±2	35±7	14±8	11.14±0.07			8.51±0.04	8.56±0.07				
22	HD 223960	10700±200	1.60±0.10	8±1	25±6	37±6	11.12±0.08			8.57±0.07	8.52				
23	HD 195324	9200±150	1.85±0.10	4±1	3±3	20±3	11.19±0.06	8.11±0.14	8.08±0.06					7.59±0.03	7.54±0.03
24	HD 34085	12100±150	1.75±0.10	8±1	25±3	31±7	11.08±0.05			8.50±0.04	8.42±0.05	8.73±0.04	8.76±0.06		
25	HD 87737	9600±200	2.05±0.10	4±1	2±2	17±2	11.17±0.05	8.23±0.10	8.26±0.04	8.54±0.07	8.49±0.06			7.54±0.05	7.52±0.04
26	HD 91533	9100±150	1.50±0.10	6±1	20±2	29±2	11.15±0.04	8.24	8.15±0.03					7.49±0.12	7.46±0.08
27	HD 111613	9150±150	1.45±0.10	6±1	17±2	27±2	11.13±0.06	8.21	8.33±0.11	8.46±0.04	8.43			7.54±0.03	7.46±0.04
28	HD 149076	11100±200	2.05±0.10	5±1	7±6	37±2	11.14±0.05			8.43±0.09	8.44±0.10	8.78±0.04	8.83		
29	HD 149077	9900±150	2.20±0.10	3±1	1±2	13±2	11.14±0.06			8.48±0.05	8.41			7.58±0.04	7.51±0.04
30	HD 165784	9000±200	1.50±0.10	7±1	18±2	35±4	11.13±0.03	8.41	8.37±0.05					7.58±0.08	7.54±0.08
31	HD 166167	9600±150	2.00±0.10	4±1	9±6	20±7	11.09±0.06							7.66±0.07	7.70±0.04
32	HD 80057	9300±150	1.75±0.10	5±1	13±3	27±2	11.16±0.04	8.22±0.08	8.28±0.13	8.34±0.04	8.29			7.42±0.06	7.40±0.06
33	HD 102878	8900±150	1.50±0.10	6±1	0±2	35±3	11.15±0.05	8.26±0.12	8.27±0.13					7.50±0.06	7.45±0.06
34	HD 105071	12000±150	1.85±0.10	7±1	23±7	39±8	11.13±0.06			8.55±0.06	8.54±0.07	8.78±0.04	8.73±0.09		
35	HD 106068	11600±200	1.90±0.10	6±1	20±8	45±14	11.13±0.01			8.60±0.04	8.60±0.04	8.75±0.04	8.82±0.04		
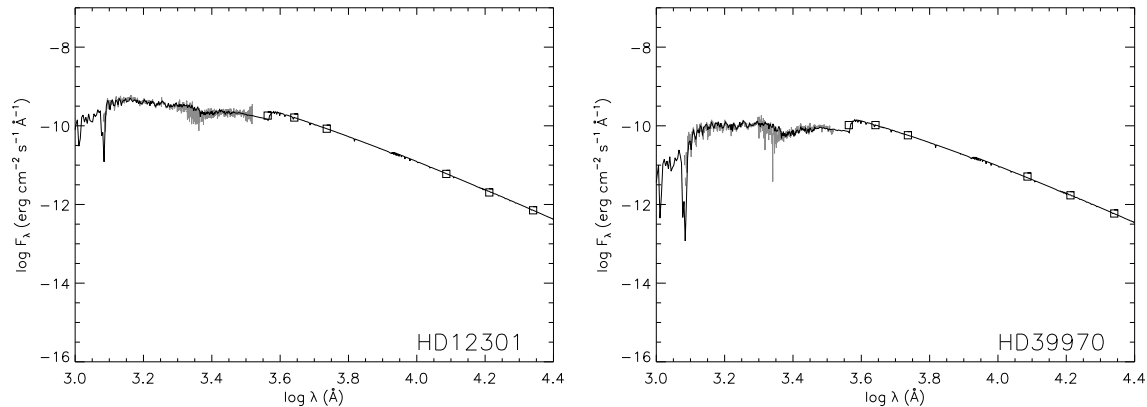
Figure 5.1: Examples for a comparison of the Atlas9 model fluxes (black lines) with UV spectrophotometry from the IUE satellite (gray lines) and with photometric measurements – UBV from Mermilliod & Mermilliod (1994), JHK from 2MASS – for two of the sample stars. The SEDs shown are dereddened according to the values of $E(B-V)$ and R_V in Table 5.1, and normalized in V-band flux.

Various (spectro-)photometric data were adopted from the literature for constructing SEDs. Johnson UBV-magnitudes were taken from Mermilliod & Mermilliod (1994), which are means of previously published photoelectric data, and JHK-magnitudes from the Two Micron All Sky Survey (Cutri et al. 2003; Skrutskie et al. 2006,2MASS). Additionally, flux-calibrated, low-dispersion spectra observed with the International Ultraviolet Explorer (IUE) were extracted from the MAST archive[1], where available (i.e., for 15 objects). These data cover the range from 1150 to 1980 Å for the short (SW) and from 1850 to 3290 Å for the long wavelength (LW) range camera. Typically, both wavelength ranges were observed the same day. A summary of all spectrophotometric data used in this study is given in the appendix.

The UBV and JHK magnitudes were transformed into absolute fluxes using zeropoints from Bessell et al. (1998) for Johnson photometry and from Cohen et al. (2003) for the 2MASS photometric system. Note that the U photometric zero point was lowered by 3%, as suggested by the results of Bohlin & Gilliland (2004) for the photometric standard star Vega.

The observed fluxes were subsequently dereddened according to a reddening law described by Cardelli et al. (1989), based on the colour excess $E(B-V)$ between theoretical (Atlas9) and observed colours. An additional free parameter introduced hereby is the ratio of total-to-selective extinction $R_V = A_V/E(B-V)$, which could also be determined by fitting the overall run of the theoretical to the observed SED. The sensitivity of the SED to this parameter means that a meaningful verification of the atmospheric parameters was only possible in cases where both UV and near-IR data were available, i.e., for 14 targets. For other objects, it could only be tested if the derived values for R_V match reasonable expectations. The results will be discussed in Chapter 7.

---

[1]`http://archive.stsci.edu/`

Two examples of the typical good agreement between theoretical and observed SEDs are shown in Fig. 5.1. Notable deviations from the final model fluxes were only found in three cases:

1. An IR colour excess is found for HD 21291, whereas the UV-flux is in excellent agreement. This can be attributed to HD 21291 being part of a close visual binary separated only by 2.39″ (Prieur et al. 2008), which could not be resolved by 2MASS photometry.

2. An UV colour excess in HD 187983 can be resolved by adding flux from a main sequence companion of early B-type, which is consistent with a radial velocity variation found by Hendry (1981).

3. There are also some problems to reproduce the SED of HD 12953, the most luminous object in the sample, similar to those found for HD 92207 (A0 Iae) by Przybilla et al. (2006). This could indicate that there is a limit to the validity of the approach, which is based on hydrostatic LTE model atmospheres to determine atmospheric structure, for very high absolute magnitudes. Further investigations are required to address the issue, but these are beyond the scope of the present work. The SEDs of slightly less luminous BA-type supergiants like Deneb and Rigel are well matched.

The comparison of theoretical and observed SEDs provided an independent test for the validity of the atmospheric parameters derived by spectroscopy. Principle limitations of this method to determine stellar parameters stem not only from the relatively low sensitivity compared to the spectroscopic method, but also from the fact that BA-type supergiants exhibit photometric variability of typically small amount on short (days) to long timescales (years), see, e. g., Sterken (1977), Maeder (1980) or Bresolin et al. (2004). The magnitudes/colours adopted from databases are therefore likely *not* representative for the physical state of the supergiants' atmospheres at the time when the optical and UV-spectra were taken. However, the collection of UBV-magnitudes by Mermilliod & Mermilliod (1994) shows mostly only moderate scatter around the mean values and this includes systematic effects from merging different data sets. The scatter is particularly low for supergiants of luminosity class Ib. Hipparcos photometry for 12 of the sample stars also indicates moderate variability by $0\overset{m}{.}02$–$0\overset{m}{.}07$ (Adelman & Albayrak 1997).

5.2 Error Estimates

Although the computation of the synthetic spectra is based on well-known principles of physics, the various necessary simplifications in the models and the uncertainties in input data like, e. g., oscillator strengths, photoionization and collisional cross-sections introduce a variety of sources for systematic errors. Additional uncertainties are due to unaccounted line-blends and errors in continuum determination. The uncertainties on the observational side are small in comparison due to the high spectral resolution and S/N-ratio.

To estimate the total error budget, it is useful to check the results for consistency, preferably by comparing a variety of indicators. Uncertainty estimates for several parameters are discussed in the following.

Table 5.2: Bootstrapping uncertainty for selected fits on individual $T_{\text{eff}}(\text{K})/\log g$-indicators.

	BD+602582	HD 12301	HD 166167	HD 20041	HD 13476	HD 165784
$T_{\text{eff}}(\text{N\,I/II})$	11933	12550		9992		
error	$\pm$ 52	$\pm$19		$\pm$12		
$\log g(\text{N\,I/II})$	1.832	2.181		1.620		
error	$\pm$ 0.020	$\pm$ 0.013		$\pm$0.060		
$T_{\text{eff}}(\text{Mg\,I/II})$			9600		8506	8947
error			$\pm$ 29		$\pm$6	$\pm$17
$\log g(\text{Mg\,I/II})$			1.974		$\pm$1.393	$\pm$1.549
error			$\pm$0.032		$\pm$0.009	$\pm$0.016
$T_{\text{eff}}(\text{H})$	11901	12680	9509	10008	8531	9045
error	$\pm$25	$\pm$29	$\pm$10	$\pm$18	$\pm$ 7	$\pm$13
$\log g(\text{H})$	1.849	2.200	2.035	1.669	1.373	1.489
error	$\pm$0.008	$\pm$0.003	$\pm$0.005	$\pm$0.005	$\pm$0.003	$\pm$0.005

- **T_{eff} and $\log g$**

  Formal uncertainties in the atmospheric parameter determination can be determined during the fitting process. A bootstrapping method implemented in Spas indicates uncertainties of (in most cases considerably) less than 0.05 dex in $\log g$ and 1% in T_{eff}. When all other parameters are held constant at the values of the final solution, fits with only one free parameter give very low errors even while only using individual indicators, as is shown in Table 5.2 for the Balmer lines and the prime ionization equilibria, respectively. Note that the examples presented include the lowest-quality spectra of the sample (with S/N-ratios down to 120) and are distributed across the parameter range of the targets. It is also reassuring that fits to individual Balmer lines – the main indicators for $\log g$ throughout the sample – show a scatter of less than 0.05 dex around the mean value of this parameter in individual stars. This excludes major systematic effects from order merging and normalization in the hydrogen lines. Overall, the uncertainties arising from the observational data prove to be small. An example for the quality of the line fits and the agreement between different ionization stages of magnesium is shown in Fig. 5.2.

  To probe the parameter determination for systematic effects, results from the evaluation of different ionization equilibria were compared. This was possible only when line sets of sufficient quality for two or more elements are available, an overview gives Fig. 5.3. Moreover, abundances for all ionization stages involved in the atmospheric parameter determination were derived, as summarized in Table 5.1. Overall, good to excellent agreement between different ionization stages of the elements was found, indicating a proper derivation of the atmospheric parameters. As expected, however, the results imply higher total uncertainties than derived during the fitting process, since they include systematic effects.

  Discrepancies were found in cases where magnesium is almost completely ionized. As shown in Fig. 5.3, deviations from the Mg I/II-equilibrium were allowed for some objects. In some cases the last residual Mg I lines of the set were even excluded from the abundance analysis. Note that the Mg II-lines in these objects show no noticeable
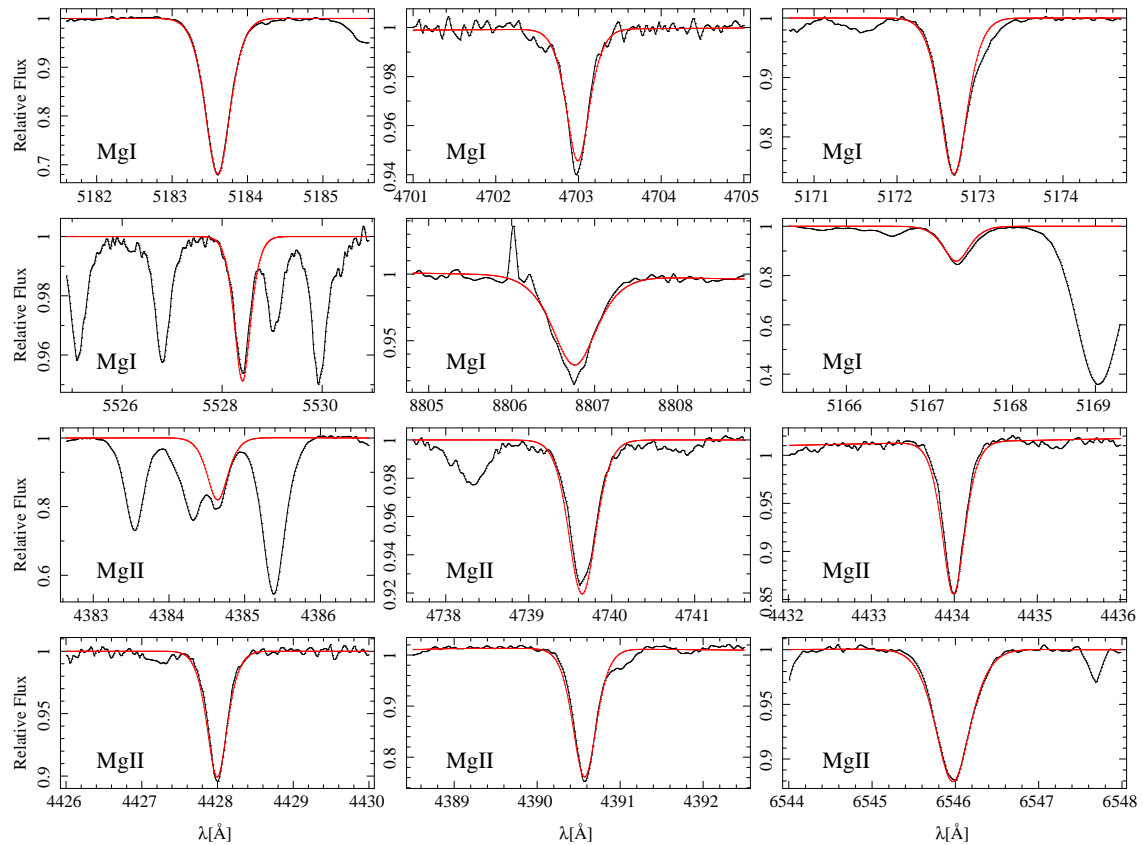
Figure 5.2: Example for fits to the Mg I/II-lines used in the determination of the atmospheric parameters T_{eff} and $\log g$ in the supergiant HD 195324 (A1 Ib). The models calculated for the final parameters (red lines) are compared to observation (black lines). The same Mg-abundance is adopted for all lines, regardless of ionization stage.

problems like trends with effective temperatures, so that the derived Mg-abundances should be reliable. This is not surprising considering the low Mg I population makes the Mg I-lines highly sensitive to even small model weaknesses.

Nevertheless, the temperature scale constructed with the help of ionization equilibria seems robust, as the N I/II ionization equilibrium is in good agreement with the Mg I/II-equilibrium at low temperatures and the O I/II-equilibrium at high temperatures. It is therefore available to bridge the gap, in which the Mg I/II-equilibrium seems to give unreliable results. This is also confirmed by the spectral energy distributions and *a-posteriori* by the consistency of the abundance analysis. The results from the evaluation of the Mg I/II-equilibrium itself at low temperatures are confirmed by the C I/II- and N I/II-equilibria and SEDs. Considering all this, the uncertainty estimates were chosen carefully across the parameter space, remaining conservative in the values given in Table 5.1. The highest uncertainties are assumed for objects that show deviations from the Mg I/II-equilibrium. An example for the excellent agreement of most final solutions with observations is shown in Fig. 5.4.
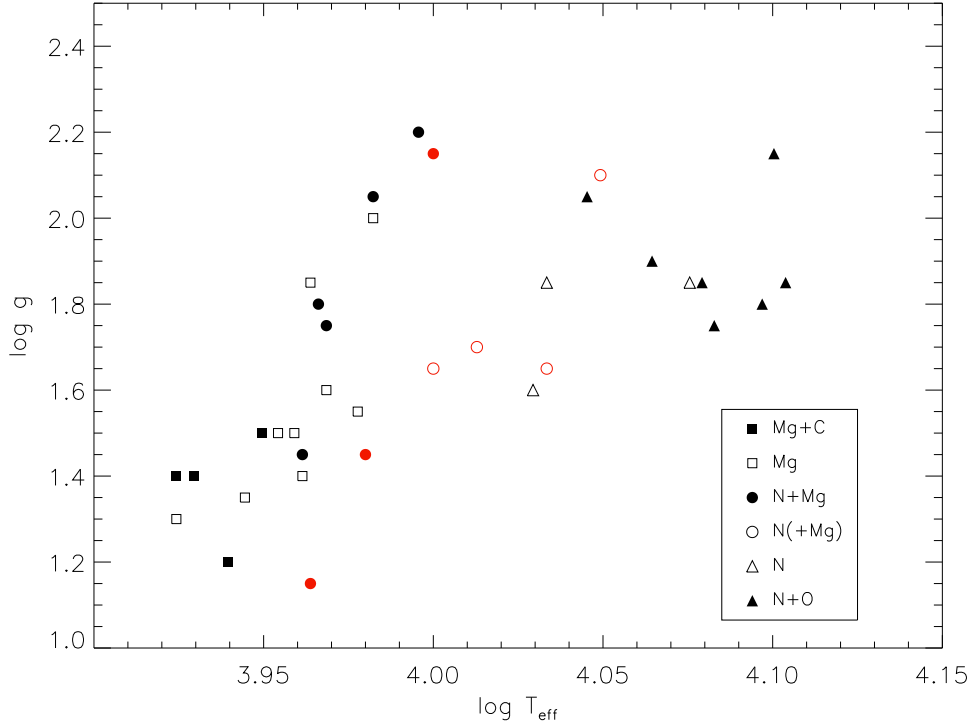
Figure 5.3: The ionization equilibria used for atmospheric parameter determination across the parameter range. Significant deviations ($\gtrsim 0.1$ dex) from the Mg I/II-equilibrium are marked red. N(+Mg) designates objects were at least one strategic Mg I-line (usually the line at 5183 Å) is present but excluded from the abundance analysis.

- **Microturbulence**

  As the fitting routine Spas is laid out to interpolate only for up to three parameters simultaneously, interpolation between grid parts with different microturbulences was avoided. As the stepsize of 1 km/s is close to the precision that can be achieved, this means no significant loss of accuracy for the abundance analysis. The diagnostic sets of Ti II- and Fe II-lines provide tight constraints in the low-to-mid-temperature regime of the sample, since they contain a sufficient number of lines over a wide range of equivalent widths. The lines of other species considered in the abundance analysis are usually consistent with the derived values within the adopted error of 1 km/s, although deviations can occur if the number of lines is low. The ξ-determination is less sensitive in the high-temperature regime, where the Fe II-lines are much weaker. In this case the results from the evaluation of line sets of several elements are averaged and the uncertainties increase to about 2 km/s.

- **Abundances**

  The elemental abundances were derived by fitting the individual lines of a species – regardless of ionization stage – and taking the mean of the resulting values. The line-to-line scatter in abundances derived from this – which is present even after accounting for microturbulence – indicates low-level systematic uncertainties from within the model atoms and errors in the normalization of weak lines. Therefore the
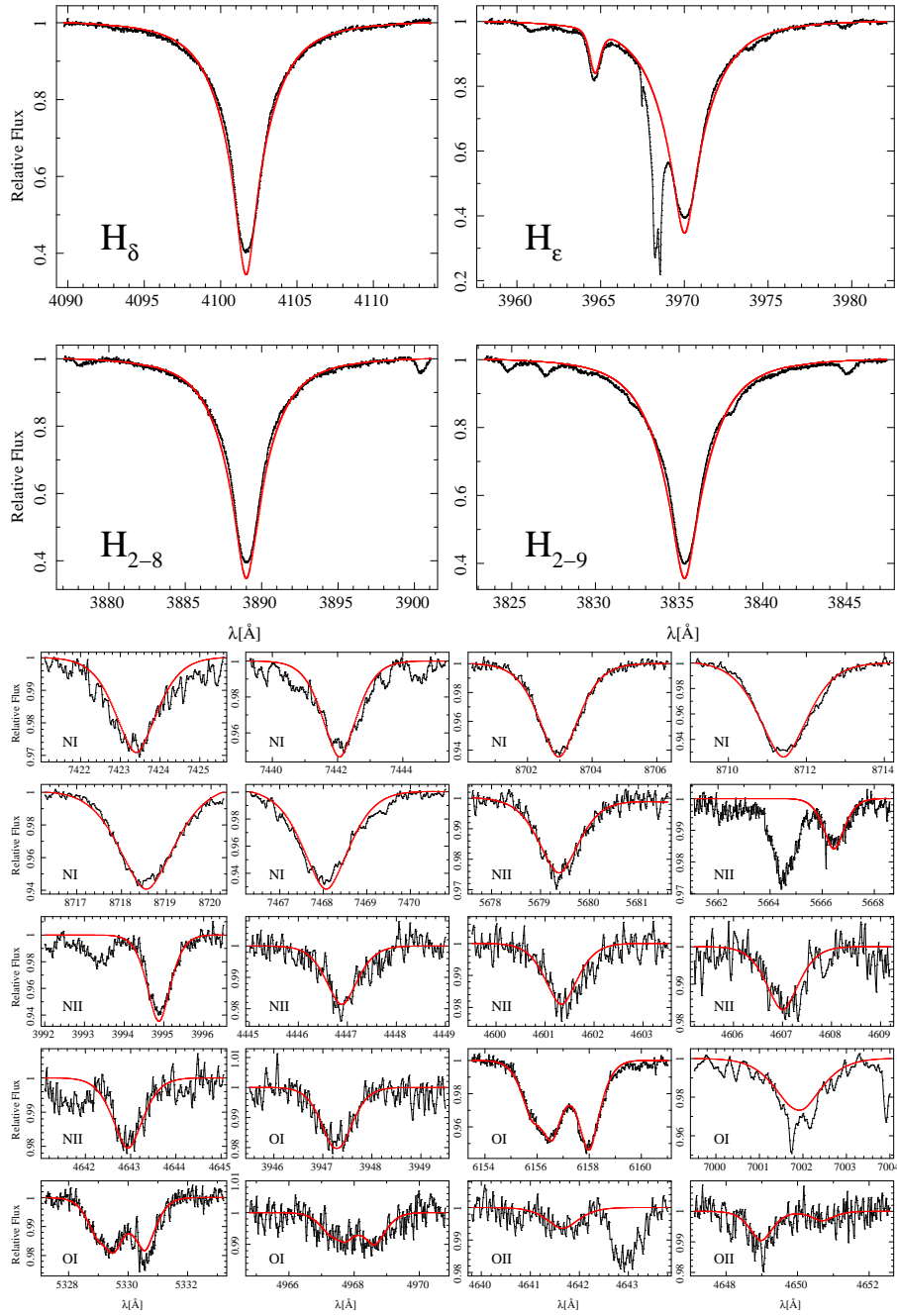
Figure 5.4: Example for a set of diagnostic lines used in the determination of the atmospheric parameters T_{eff} and $\log g$ in the supergiant HD 106068 (B8 Iab), consisting of hydrogen, nitrogen and oxygen lines. The models calculated for the final parameters (red lines) are compared to observation (black lines). The same values of oxygen and nitrogen abundance are adopted for all lines, regardless of ionization stage. The ionization equilibria and the Balmer lines unaffected by the stellar wind are reproduced simultaneously. Note that various line blends of stellar, interstellar and terrestrial nature seen in the plots are exempted from the fitting process.

Table 5.3: Systematic uncertainties in the abundance determination for selected stars (in dex).

HD 91533 ($T_{\mathrm{eff}} = 9100\,\mathrm{K}$, $\log g = 1.50$)

	He	C	N	O	Mg	S	Ti	Fe
$T_{\mathrm{eff}} + 150\,\mathrm{K}$ $\log g + 0.1\,\mathrm{dex}$	0.06	−0.01	−0.04	−0.01	−0.01	0.03	−0.11	−0.05
$T_{\mathrm{eff}} - 150\,\mathrm{K}$ $\log g - 0.1\,\mathrm{dex}$	−0.08	0.02	0.05	0.01	0.04	−0.04	0.12	0.05
$\xi + 1\,\mathrm{km/s}$	0.02	0.02	0.03	0.01	0.01	0.00	0.04	0.03
$y + 0.03$	. . .	0.02	0.01	0.03	0.02	0.01	0.04	0.01
σ_{sys}	0.07	0.03	0.06	0.03	0.04	0.04	0.13	0.06

HD 34085 ($T_{\mathrm{eff}} = 12\,100\,\mathrm{K}$, $\log g = 1.75$)

	He	C	N	O	Mg	S	Ti	Fe
$T_{\mathrm{eff}} + 150\,\mathrm{K}$ $\log g + 0.1\,\mathrm{dex}$	0.05	0.00	0.00	0.01	0.03	0.00	. . .	−0.01
$T_{\mathrm{eff}} - 150\,\mathrm{K}$ $\log g - 0.1\,\mathrm{dex}$	−0.04	−0.01	0.00	−0.01	−0.03	0.01	. . .	0.01
$\xi + 1\,\mathrm{km/s}$	0.03	0.02	0.01	0.01	0.00	0.03	. . .	0.01
$y + 0.03$	. . .	0.00	0.01	0.02	0.04	0.01	. . .	0.03
σ_{sys}	0.05	0.02	0.01	0.02	0.05	0.03	. . .	0.03

1-σ standard deviation based on the individual line abundances is chosen as an error estimate.

The sensitivity of the determined abundances to changes in the derived atmospheric parameters is summarized in Table 5.3 for one object in the low- and high-temperature regime of our sample. Listed there are the results from fits to the line sets of the examined elements using the final atmospheric parameters while varying one parameter at a time according to the respective error margins. This allows to estimate the total error budget σ_{sys} propagated from uncertainties in the atmospheric parameter determination. T_{eff} and $\log g$ were varied simultaneously, as their uncertainties are highly correlated. In most cases, the estimates are comparable to the line-to-line scatter or lower. However, the He I- and Ti II-line sets are particularly sensitive.

Individual lines that are close to the detection limit and bear significant statistical uncertainties, were therefore excluded from the analysis. In addition they would be more affected by systematic errors stemming from undetected line blends or erroneous continuum normalization. Only for the weakest lines used in the analysis the uncertainties induced by noise are comparable to the line-to-line scatter.

Note that the persistent line-to-line scatter leads to the emergence of selection effects in the atmospheric parameter determination, in particular in cases where only a few lines in one of the two ionization stages used for establishing ionization balance are available. This explains some of the discrepancies found between atmospheric parameters derived using different ionization equilibria.

Table 5.4: Comparison of the atmospheric parameters (T_{eff} [K], $\log g$) with previous studies.

#	Object	Takeda[1]	Venn[2]	McErlean[3]	this work
1	HD 12301	12500, 2.30	...	14000, 2.15	12600, 2.15
3	HD 13476	9000, 1.50	8400, 1.20	...	8500, 1.40
6	HD 14489	...	9000, 1.40	...	9350, 1.45
8	HD 21291	12000, 1.80	...	11500, 1.60	10800, 1.65
9	HD 39970	10500, 1.70	...	...	10300, 1.70
10	HD 46300	10000, 2.00	9700, 2.10	...	10000, 2.15
13	HD 197345	9500, 1.50	...	...	8700, 1.20
14	HD 202850	11500, 1.80	...	...	10800, 1.85
15	HD 207260	9500, 1.50	...	...	8800, 1.35
16	HD 207673	...	9300, 1.75	...	9250, 1.80
17	HD 208501	12500, 2.30	...	13000, 1.80	12700, 1.85
18	HD 210221	...	8200, 1.30	...	8400, 1.40
19	HD 212593	...	...	...	11200, 2.10
23	HD 195324	...	9300, 1.90	...	9200, 1.85
24	HD 34085	13000, 2.00	...	13000, 1.75	12100, 1.75
25	HD 87737	10200, 1.90	9700, 2.00	...	9600, 2.05

[1] Takeda & Takada-Hidai (2000)

[2] Venn (1995a)

[3] McErlean et al. (1999)

5.3 Comparison with Previous Analyses

Samples of supergiants in the BA-star regime were subject to non-LTE analyses in three previous studies (Venn 1995a; McErlean et al. 1999; Takeda & Takada-Hidai 2000). Effective temperatures and surface gravities from these sources for stars in common are compared with results of the present study in Table 5.4. Typical uncertainties $\Delta T_{\text{eff}}/\Delta \log g$ of these studies are 200 K/0.2 dex, 500–1000 K/0.5 dex and 1000 K/0.2 dex, respectively.

Venn (1995a) used a method comparable to ours for the stellar parameter determination in A-type supergiants, i. e., utilizing the Balmer- and Mg I/II-lines, however without a simultaneous derivation of the helium abundance. While there are some differences, good overall agreement is found in T_{eff} and $\log g$ within the errors. Her values for microturbulence can also lie within the uncertainty ranges for the stars in common.

Takeda & Takada-Hidai (2000) tried to construct a $T_{\text{eff}}/\log g$ vs. spectral type relation, utilizing published data. They emphasized, however, that this approach is subject to considerable uncertainties. Indeed, notable deviations between the values for both T_{eff} and $\log g$ derived in this work and their data are found, though agreement is still found when considering their large uncertainties.

Finally, there is some overlap with the B-type supergiants studied by McErlean et al. (1999). Their estimates for $\log g$, inferred from the Balmer lines, are in excellent agreement with our values. Yet, a systematic shift in T_{eff} towards higher values compared to results
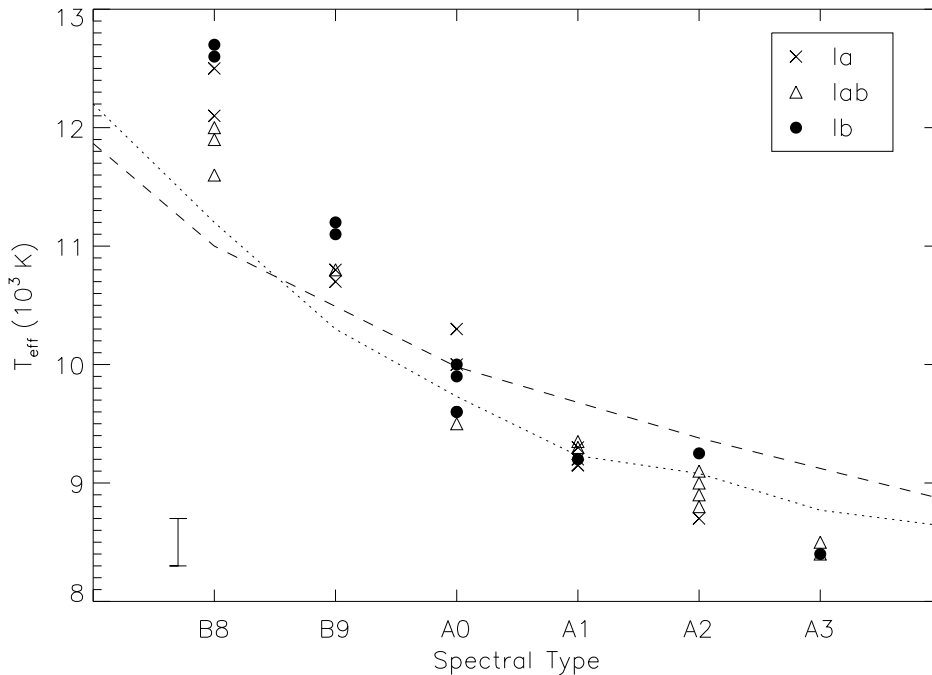
Figure 5.5: Comparison of the results for the individual sample stars with reference spectral type–T_{eff} scales of Schmidt-Kaler (1982, dotted line) and Cox (2000, dashed line). Luminosity classes are encoded according to the legend. A typical error bar is indicated to the lower left.

obtained in this work is found. Their temperatures are based on the non-LTE Si II/III ionization balance for the stars in common (except for HD 21291, where photometry was used as substitute). However, the non-LTE model atmospheres used for their analysis did not consider the effects of metal line-blanketing, which can be identified as the likely cause of the T_{eff} differences. Moreover, they could not derive reliable microturbulences for late B-type supergiants due to the insufficient quality of their spectra, which could affect temperatures derived by ionization equilibria.

5.4 Spectral Type–T_{eff} Relation

Empirical spectral-type–T_{eff} relations provide important starting points for all kinds of stellar studies and for quantitative spectroscopy in particular, and they are therefore an essential part of the *reference literature* on stellar properties. The high-precision/high-accuracy dataset facilitates to reassess the existing knowledge in the BA-type supergiant regime in view of improved models and analysis techniques.

The high-quality spectra allow a much closer look to be taken on trends in spectral line strengths and line ratios than possible with traditional classification spectra at much lower resolution. Therefore the spectral classification of the sample stars was reassessed. Starting point of the approach were the anchor points of the MK system (as identified in Table A.3), supplemented by MK primary standards as given by Johnson & Morgan (1953), see also

Table 5.5: Spectral type–T_{eff} scale for BA-type supergiants.

	reference values		this work
Sp. T.	T_{eff} (K)[1]	T_{eff} (K)[2]	T_{eff} (K)
B6	13000	...	...
B7	12200	...	...
B8	11200	11100	12200±410
B9	10300	...	10920±220
A0	9730	9980	9840±290
A1	9230	...	9240± 80
A2	9080	9380	8960±200
A3	8770	...	8430± 60
A5	8510	8610	...

[1] Schmidt-Kaler (1982)

[2] Cox (2000)

Table A.3. These cover about half of the sample stars. Spectral types for the remaining stars were assessed on basis of the helium and metal lines, luminosity classes by the width of the Balmer lines. In general, good agreement with the classification as obtained from SIMBAD was found. Maximum changes indicated by the inspection, for about half of the non-MK stars, amount to one spectral subtype or to one subtype (higher or lower) within the supergiant luminosity class. The reclassification is indicated in Table A.3. It has to be noted that two of the primary MK standards (HD 14489 and HD 223960) were found to differ significantly in spectral morphology from the stars of similar original spectral type. Also the luminosity appears overestimated for HD 212593, which shows a nearly symmetric Hα absorption profile. A (slight) reclassification for these stars is therefore proposed, based on the *available high-resolution spectra*.

Effective temperatures of the sample stars (see Table 5.1) as a function of their spectral type (according to the refined classification presented in Table A.3) are displayed in Fig. 5.5. In comparison with established reference work (Schmidt-Kaler 1982; Cox 2000) a significantly steeper spectral-type–T_{eff} relation is found, i. e., higher T_{eff} at spectral types B8 and B9, and lower T_{eff} at A2 and A3. As no apparent correlation of T_{eff} with luminosity subtype is indicated in Fig. 5.5, average T_{eff}-values from all stars of a spectral subtype were computed to provide refined reference values which are presented in Table 5.5.

Obviously, this work has to be extended in the future to provide a unified picture from the present work and recent developments concerning hot (e. g., Repolust et al. 2004; Markova & Puls 2008) and cool Galactic supergiants (e. g., Levesque et al. 2005). Also more objects of luminosity class Ib would be desirable within the spectral range covered here, to round out the work.
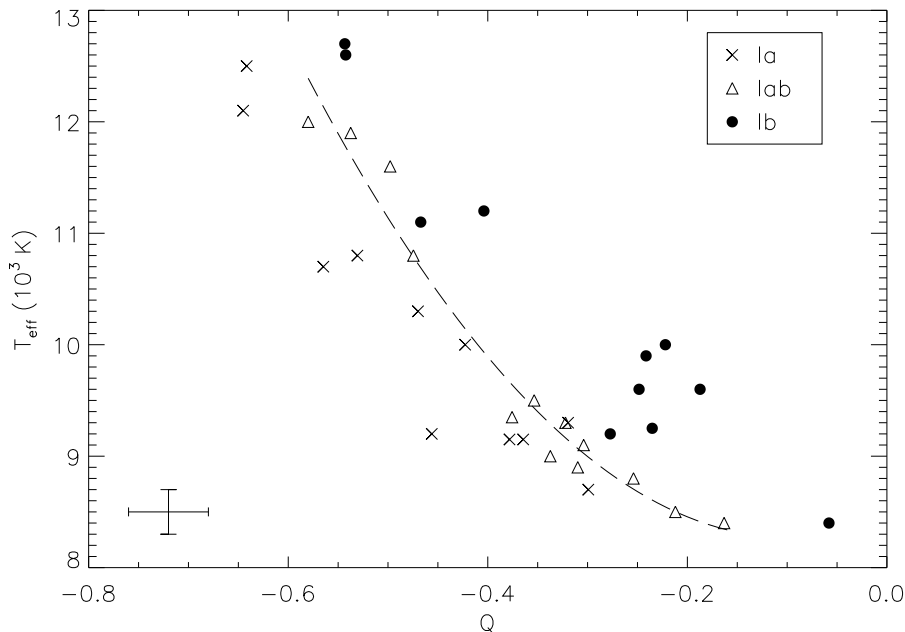
Figure 5.6: Relation between the reddening-free Q-index, $Q = (U - B) - 0.72(B - V)$, and the spectroscopic T_{eff}-values of the sample stars. A typical error bar is indicated. The dashed line represents the regression line of the Q-based T_{eff}-calibration for Iab supergiants.

5.5 The Reddening-free Q-Index as T_{eff}-Indicator

As one often wishes to analyze larger samples of stars, easy-to-apply and fast stellar parameter indicators are in high demand. Photometric T_{eff}-indicators are among the preferred ones, because of the easy accessibility of photometric data. In particular T_{eff}-calibrations based on the reddening-free Q-index (Johnson 1958), $Q = (U - B) - X(B - V)$ with $X = E(U - B)/E(B - V)$, have come into wide use recently, as Johnson photometry is available for most stars. Examples in this context encompass studies of the evolutionary progenitors of BA-type supergiants, OB-type stars on the main sequence (e. g., Daflon et al. 1999; Lyubimkov et al. 2002), and their cooler siblings, late-A to G-type supergiants (Lyubimkov et al. 2010). Usually, a standard value of 0.72 is adopted for X, but see (Johnson 1958) for a discussion of this.

The applicability of the Q-index as possible T_{eff}-indicator for BA-type supergiants is tested in Fig. 5.6. The spectroscopically derived T_{eff}-values are displayed as a function of Q. A trend with luminosity subclass becomes apparent, the more luminous Ia objects being coolest and the Ib objects being hottest at a given Q. The loci of the three luminosity subclasses in the diagram may be approximated by a quadratic fit function, yielding the following relations
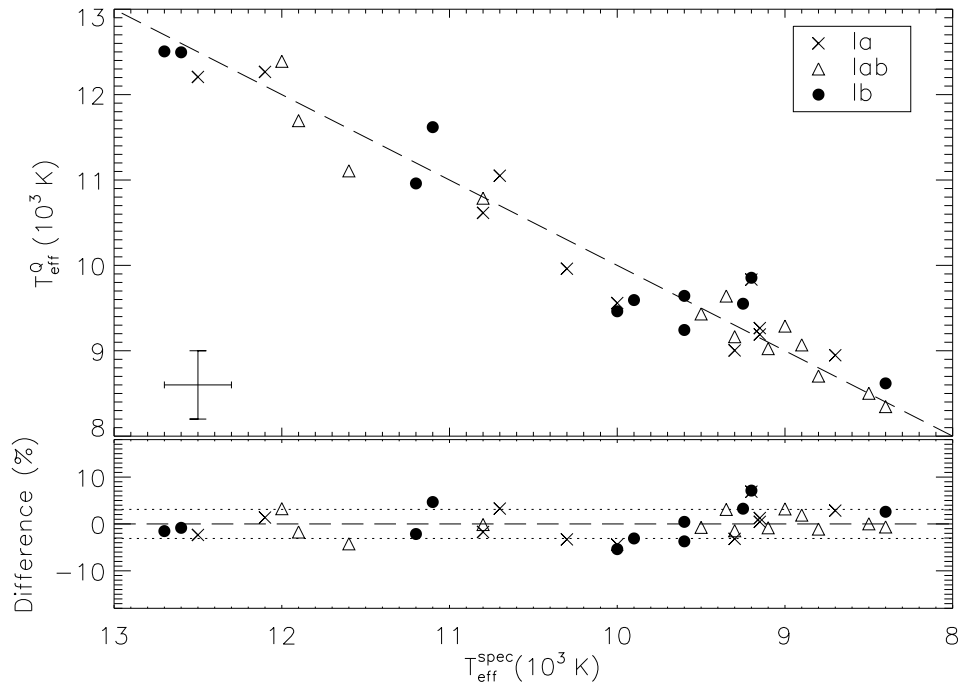
Figure 5.7: Upper panel: comparison of the spectroscopically derived $T_{\mathrm{eff}}^{\mathrm{spec}}$ with the Q-based T_{eff}^{Q} computed with Eqns. 5.1–5.3. The dashed line indicates the 1:1 relation. The error bar shows a typical conservative uncertainty from the spectroscopic determination, and the uncertainty in T_{eff}^{Q}, accounting for *typical uncertainties in the colours only*. Lower panel: percent difference of the two T_{eff} values for the individual objects. These quantify the *systematic differences* from application of the Q–T_{eff} calibrations. The dotted lines indicate the 1σ-scatter range.

$$T_{\mathrm{eff}}^{Q}\,(10^3\,\mathrm{K}) =$$

$$\text{Ia}: \quad 10.104 + 10.107\,Q + 20.861\,Q^2\,, \quad -0.30 \gtrsim Q \gtrsim -0.65 \qquad (5.1)$$

$$\text{Iab}: \quad 8.435 + 3.430\,Q + 17.672\,Q^2\,, \quad -0.15 \gtrsim Q \gtrsim -0.60 \qquad (5.2)$$

$$\text{Ib}: \quad 8.725 - 0.026\,Q + 12.631\,Q^2\,, \quad -0.05 \gtrsim Q \gtrsim -0.55 \qquad (5.3)$$

with their respective area of validity. For clarity, only the fit function for Iab supergiants is visualized in Fig. 5.6.

The differences between the spectroscopically derived effective temperatures $T_{\mathrm{eff}}^{\mathrm{spec}}$ and the Q-based T_{eff}^{Q} computed with Eqns. 5.1–5.3 are quantified in Fig. 5.7. The sample stars follow the 1:1 relation rather tightly, with the 1σ-scatter of the computed T_{eff}^{Q} around the spectroscopic reference values amounting to less than 4%. This is the *systematic uncertainty* adherent to an application of the method. In addition, *random errors* because of the uncertainties in the colours also have to be considered, typically amounting to twice the statistical uncertainty of the spectroscopically derived values (see the error bar in the upper panel of Fig. 5.7 and note the different scale projection of the axes). In consequence, the resulting error margins render this simple approach to Q-based effective

temperatures not competitive with spectroscopic determinations for BA-type supergiants. Moreover, starting points for the iterative refinement of the stellar parameters are more easily obtained from the spectral type–T_{eff} relation established in Sect. 5.4. Note also that the same limitations due to photometric variability as for the SED-method apply.

6 Observational Constraints on Massive Star Evolution

Studies of stellar structure and evolution are the basis for our understanding not only of stellar populations, but also the synthesis of elements and the cosmic matter cycle. Viable stellar models for main-sequence stars incorporating radiative energy transport were constructed quite early in the 20th century. Most of the early developments are summarized in the groundbreaking textbook "The Internal Constitution of the Stars" (Eddington 1926). In there, even the energy yield of hydrogen burning was calculated – without knowing how the energy was released – making hydrogen the prime suspect for fuelling the Sun's energy output. The occurrence of this process in stars could only be understood after Gamow (1928) showed that quantum mechanical tunneling allowed fusion to occur at temperatures far lower than previously seemed plausible. A detailed understanding of the nuclear processes occurring in stars, as later provided, e. g., by Bethe (1939) and von Weizsäcker (1938) for the case of hydrogen burning, made detailed computations of stellar structure and evolution possible.

Various sets of stellar evolution models were developed over time, changing in the detailed treatment of stellar physics, such as, e. g., the parametrization of convection and mass-loss, the cross-sections of the nuclear reaction network and initial element ratios. Classical models predict the time-evolution of stars based on only two fundamental parameters, the initial mass and metallicity (one of the most successful model grids was published by Schaller et al. 1992). They can successfully reproduce the color-magnitude-diagrams of star clusters and galaxies via population synthesis, accounting for the initial mass function and the star formation history (see the review by Gallart et al. 2005). Recent developments in the field focus on the importance of additional parameters for stellar evolution, like for example binarity, rotation and magnetic fields, in order to explain deviations from that picture as indicated by observations.

In this chapter the basic principles of stellar evolution models are sketched as they are outlined, e. g., in the textbooks of Kippenhahn & Weigert (1990) and Clayton (1983). Additionally, effects incorporated in the most recent models – rotation and mass-loss (Heger et al. 2000; Maeder & Meynet 2000; Meynet & Maeder 2003) as well as magnetic fields (Heger et al. 2005; Maeder & Meynet 2005) – are discussed. These latest models make predictions for surface abundances – in particular for elements involved in the CNO-bi-cycle – and rotation rates of massive stars on their way from the main sequence to the red supergiant phase, which can be verified using the results of quantitative spectroscopic analyses. The details of these predictions depend critically on the efficiency of chemical mixing and angular momentum transfer, as well as mass-loss rates – parameters that can only be constrained by observation. Yet, the second part of the chapter aims not only

to compare theory and observation, but also to determine the still uncertain evolutionary status of BA-type supergiants, in order to understand the evolution of massive stars.

6.1 Stellar Evolution Models

6.1.1 Stellar Structure

To understand the results of stellar evolution codes, it is instructive to discuss the principle laws governing the structure of stars. For this aim, it is helpful to simplify the picture and to construct the model of a spherical symmetric ball of gas, thereby neglecting second-order perturbations like rotation, magnetic fields or binarity. The first task is to choose a suitable coordinate for the description, and it will turn out to be useful to take the mass m contained in a concentric sphere of radius r, starting at $m = 0$ in the center, while the total mass $m = M$ is reached at the surface, where $r = R$. It is connected to the radius r via the density $\rho(m)$:

$$\frac{\mathrm{d}r}{\mathrm{d}m} = \frac{1}{4\pi r^2(m)\rho(m)}. \tag{6.1}$$

The advantage of this choice is that the independent variable always extends over the same interval, whereas R can vary strongly. The other independent variable is of course the time t, as – unlike for the case of stellar atmospheres discussed earlier – the focus is on the time-evolution of the star. The second defining equation for the problem is a variant of the hydrostatic equation 3.3 encountered earlier:

$$\frac{\mathrm{d}P(m)}{\mathrm{d}m} = -\frac{Gm}{4\pi r^4(m)}. \tag{6.2}$$

This equation follows from the application of Newton's second law, where the explicitly time-dependent terms of the equation of motion for the spherical symmetrical case are neglected. It is safe to do so in most cases, as the hydrostatic timescale, on which the star reacts to perturbations of hydrostatic equilibrium, is very short compared to typical evolutionary timescales. The next important equation expresses the conservation of energy inside a star:

$$\frac{\mathrm{d}l(m)}{\mathrm{d}m} = \epsilon - T(m)\frac{\mathrm{d}S}{\mathrm{d}t}, \tag{6.3}$$

where $S = S(\rho(m), T(m), \{X_Z\})$ is the entropy per unit mass of stellar matter, $l(m)$ the energy flux emerging from the sphere of radius $r(m)$ and $\epsilon = \epsilon(\rho(m), T(m), \{X_Z\})$ the power liberated per unit mass of stellar matter by nuclear reactions. The second term on the right expresses the fact that energy can be absorbed or released in form of heat $\mathrm{d}Q = T\mathrm{d}S$. ϵ can also be negative, if the major reactions are endothermic. In addition, energy can be lost to the star via neutrinos, which can often reach the surface without further interaction. The temperature stratification can be governed by different equations:

$$\frac{\mathrm{d}T(m)}{\mathrm{d}m} = -\frac{3}{64ac}\frac{\kappa}{T^3}\frac{l(m)}{\pi^2 r^4} \qquad \text{or} \qquad \frac{\mathrm{d}T(m)}{\mathrm{d}m} = \frac{\Gamma_2 - 1}{\Gamma_2}\frac{T(m)}{P(m)}\frac{\mathrm{d}P(m)}{\mathrm{d}m}, \tag{6.4}$$

where $\Gamma_2\left(\rho(r), T(r), \{X_Z\}\right)$ is the second adiabatic exponent. The left hand equation is valid if radiation dominates the energy transport, whereas the right hand side is an approximation applied if the energy is carried by convection. The chemical composition of a star is subject to change via the nuclear reactions occurring in the stellar interior. The time-evolution of the mass fractions of nuclei is governed by a set of equations, one for each species i under consideration:

$$\dot{X}_i = \frac{m_i}{\rho}\left(\sum_j r_{ji} - \sum_k r_{ik}\right) \qquad , \qquad \sum_i X_i = 1, \tag{6.5}$$

where m_i is the mass of the nuclei, r_{ji} are the rates of reactions that synthesize the species per unit volume and r_{ik} the rates at which they are consumed by nuclear reactions. If no mixing occurs, Eq. 6.5 will give the total rate of composition change.

It is often assumed that convection occurs if the radiative temperature gradient ∇_{rad} exceeds the adiabatic temperature gradient ∇_{ad}:

$$\nabla_{\mathrm{rad}} > \nabla_{\mathrm{ad}}, \tag{6.6}$$

which means that energy transport by radiation is not effective enough to ensure dynamical stability. This is the famous *Schwarzschild criterion*, using the following definitions:

$$\nabla_{\mathrm{ad}} := \left(\frac{\partial \ln T}{\partial \ln P}\right)_s, \nabla_{\mathrm{rad}} := \left(\frac{\mathrm{d}\ln T}{\mathrm{d}\ln P}\right)_{\mathrm{rad}} = \frac{3}{16\pi acG}\frac{\kappa l P}{m T^4}, \tag{6.7}$$

where the subscript s denotes constant entropy. Other criteria are used in stellar evolution models, such as, e. g., the *Ledoux criterion*, which includes the effects of a gradient in mean molecular weight. These simple recipes can only approximately describe the complex properties of convection, however (see Maeder 2009 for a discussion).

The inclusion of rotation into the models leads necessarily to deviations from spherical symmetry due to the effects of centrifugal forces. Current models account for rotation by implementing shellular rotation, i.e., they use mass shells that correspond to isobars instead of spherical shells (Heger et al. 2000; Maeder & Meynet 2000). Constant angular velocity Ω is assumed for each shell, which is often represented by an approximate radial law of the form $\Omega = \Omega(r)$ (Zahn 1992). This approach allows to retain a one-dimensional approximation. The specific angular momentum of a mass shell is treated as a local variable. This introduces the problem of the transport of angular momentum across mass shells, which is either treated essentially as a diffusion process (Heger et al. 2000), or more rigorously by taking advection into account (Maeder & Meynet 2000; Meynet & Maeder 2003). The inclusion of rotation, as it is implemented in most evolutionary models, also modifies the mass-loss rates according to the relation

$$\dot{M}(v) = \dot{M}(v = 0)\left(\frac{1}{1 - v/v_{\mathrm{crit}}}\right)^\xi, \tag{6.8}$$

where v_{crit} is the equatorial break-up velocity and $\xi \simeq 0.5$. This means the model mass-loss rates increase with rotation.

Figure 6.1: Reactions in the CNO-bi-cycle of hydrogen burning: The incoming protons are marked blue, while the reaction product helium is marked red. The carbon, nitrogen and oxygen atoms act as catalysts. Typical lifetimes of the precursor nuclei – in the core of a $15\,M_\odot$-star during the main sequence phase – are indicated, based on the tabulations of Caughlan & Fowler (1962).

Rotating models for massive stars indicate that they use the nuclear fuel more sparingly in the beginning, which means that they have lower luminosities on the main sequence. This – and the additional fuel mixed into the core – leads to longer lifetimes. Yet, the models possess higher luminosities during the supergiant phase due the development of larger cores (Heger & Langer 2000, also compare Fig. 6.11).

6.1.2 The CNO-Bi-Cycle

Stars spend most of their lifetimes on the main sequence, where the conversion of hydrogen to helium in the core provides stability. The merging of four protons into one helium nucleus does not occur in a single reaction but in reaction networks. The most important are the so-called proton-proton (PP) chain and the CNO-bi-cycle. Their efficiency is sensitive to temperature, density and hydrogen abundance in the stellar interior. While the PP-chain plays the primary role in stars like the Sun, the hydrogen burning in massive stars is dominated by the CNO-bi-cycle due to their higher core temperatures. The latter is also the case in progenitors of BA-type supergiants, main-sequence stars of type O and B.

The CNO-bi-cycle consists of two subcycles, as collisions between ^{15}N and protons not always produce ^{12}C and an α-particle, but also result in ^{16}O for about 4 times in 10^4. The primary cycle is also called CN-cycle. The resulting reaction network is shown in Fig. 6.1, along with the typical lifetimes of the involved nuclei in the core of a 15 $M_\odot$-star during core hydrogen burning (temperature and density taken from a stellar evolution model by Meynet & Maeder (2003)). While the elements carbon, nitrogen and oxygen only function as catalysts, meaning that no net production or loss occurs during a cycle, their relative numbers change over the period of hydrogen burning, due to the different lifetimes. The β-unstable isotopes like ^{13}N and ^{15}O have half lives of several minutes, while collisional processes may occur only once in many years. The reaction ^{14}N$(p,\gamma)^{15}$O is the bottleneck of the CN-cycle, as it is the slowest by far. The abundance of this stable nitrogen isotope increases while the abundances of the stable carbon and oxygen isotopes decrease, with the most abundant oxygen isotope ^{16}O being transformed more slowly in the minor ON-branch of the cycle. Of course, for each completed cycle helium is produced from 4 protons. The outcome of stellar evolution computations depend on the cross sections of the nuclear reactions involved, especially those of the slowest reactions, as they have a major influence on the resulting chemical composition and the total energy output. The exact rates are still subject to change, as newer measurements of the ^{14}N$(p,\gamma)^{15}$O cross section (Lemut et al. 2006) on energy scales relevant for the stellar interior show, that reduce previous estimates significantly.

6.1.3 Chemical Mixing

Stellar spectra trace abundances only of the photospheric layers, whereas the energy production and the bulk of the nuclear reactions occur in the core. In order for nuclearly processed matter to be recognizable, it has to travel a long way from the center of the star to the outer layers. A number of mixing mechanisms can be involved in this process, the most prominent of them will be discussed in the following.

Compositional mixing of the stellar interior is generally treated as a diffusive process as defined by the diffusion equation

$$\left(\frac{\partial X_i}{\partial t}\right)_m = \left(\frac{\partial}{\partial m}\right)_t \left[\left(4\pi r^2 \rho\right)^2 D \left(\frac{\partial X_i}{\partial m}\right)_t\right] + \left(\frac{\partial X_i}{\partial t}\right)_{\text{nuc}}, \tag{6.9}$$

where D denotes a general diffusion coefficient constructed from the sum of individual mixing processes (Heger et al. 2000). The efficiency of mixing processes can be characterized by the mixing time τ_{mix}, after which an initially inhomogeneous region of the star reaches homogeneity (provided no new inhomogeneities are created). This can be roughly estimated by

$$\tau_{\text{mix}} \approx \frac{R^2}{D}, \tag{6.10}$$

where R is the extension of the region. Diffusion processes can have many causes, some of which are discussed by Kippenhahn & Weigert (1990). The simplest case is the *concentration diffusion* that tends to smooth out inhomogeneities. Another effect is the *temperature diffusion*, where heavier atoms can migrate towards regions of higher temperature. The mixing times of these processes are however so vast that they are irrelevant in most cases.
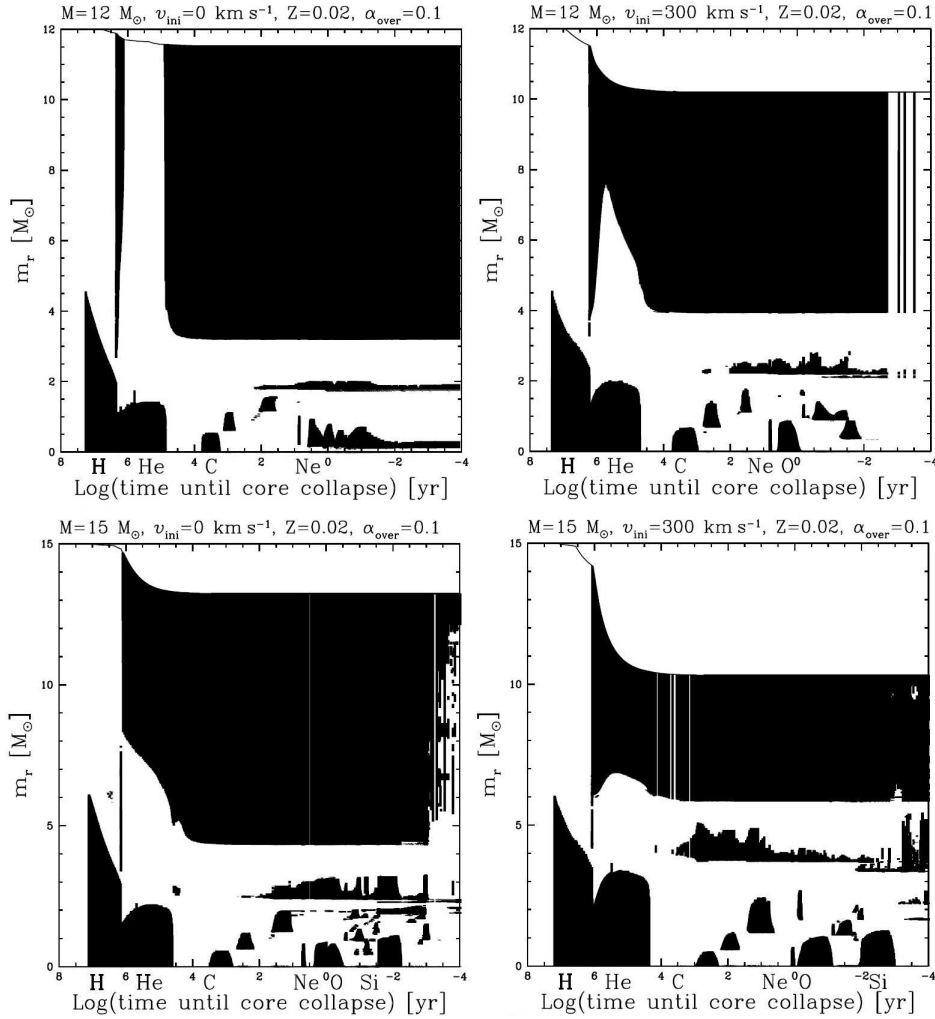
Figure 6.2: Kippenhahn-diagrams created using the stellar evolution models of Meynet & Maeder (2003), from Hirschi et al. (2004). The stages of nuclear burning are indicated along the logarithmic time axis. Displayed is the extension of the convection zones (black areas) for various input parameters. During the evolution of the $12\,M_\odot$-model without rotation the blue-loop-phase is clearly discernible, since the stellar envelope is partly non-convective during helium burning (upper left panel). Here the convection zone deeply penetrates the star during the RSG-phase ("first dredge up"), only to recede completely during the blue loop. The rotating model as well as the models with higher masses avoid the blue-loop-phase. Comparing the different panels, it is evident that the mass-loss increases with rotation rate and stellar mass.

Pressure diffusion, manifesting itself in many stars in the form of gravitational settling, also exists. This type of mixing is, however, also negligible for the stars examined in this study. Other mixing processes have to be found.

The most obvious choice would be convection, which is not only important as an efficient energy transport mechanism, but is also the most effective means for chemical mixing in stellar interiors. The timescale of chemical mixing in convection zones is indeed so small compared to evolutionary timescales, that convection zones are assumed to be chemically
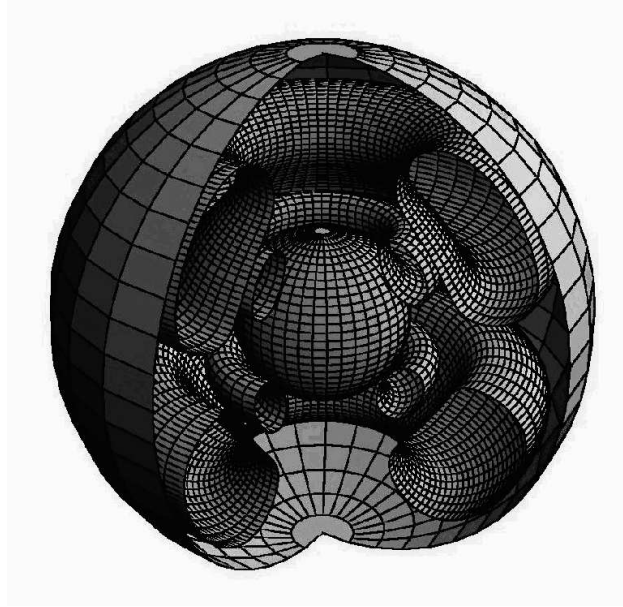
Figure 6.3: This 3D-contour-plot by G. Meynet illustrates the meridional circulation inside a rotating massive star. The material flows along the torus-like planes indicated.

homogeneous in most stellar evolution computations – implying instantaneous mixing. This approximation only breaks down during the last rapid burning stages of the stellar life (e. g., Hirschi et al. 2004). The distribution of convection zones in massive stars is different from that in solar-like stars, however. They have convective cores on the main sequence – as the high energy output of the core needs to be transported – but mostly radiative envelopes for most of their lifetimes (Fig. 6.2), which rules out convection as a transport mechanism to the surface.

Indeed, non-rotating models of massive stars show no signs of nuclearly processed material on the stellar surface during the entire main sequence phase (Maeder & Meynet 2000; Heger & Langer 2000). The inclusion of rotation into evolutionary models, however, allowed for other mixing mechanisms to be explored, as it introduces several instabilities that can lead to chemical mixing between different shells. Shear turbulence that is induced by differential rotation is most likely among the most efficient of the rotationally induced mixing processes. Various estimates for the associated diffusion coefficient D_{shear} were derived in the literature (for a discussion see Maeder & Meynet 2000). Another important mixing mechanism considered in contemporary models is the meridional circulation, as illustrated in Fig. 6.3. The equipotentials at the poles of a rotating star are much closer than at the equator, which is why the poles are hotter than the equator. This drives a circulation that rises at the poles and descends at the equator. Maeder & Zahn (1998) proposed an improved formalism to account for these currents in evolutionary models.

There are several other rotationally induced mechanisms that can lead to chemical mixing (see, e. g., Heger et al. 2000, for a discussion), and their efficiencies are up to discussion. The sum of their contributions is combined into the diffusion coefficient D. Counteracting

the rotationally induced mixing are gradients ∇_μ in the mean molecular weight. The fusion products are heavier on average than the overlying unprocessed material, mixing processes between different depths are therefore inhibited. Heger & Langer (2000) compare the surface abundances of computations for different degrees of mixing inhibition by μ-gradients.

While the details of the implementation vary, the models of Heger et al. (2000) and Maeder & Meynet (2000) agree that rotationally induced chemical mixing brings a significant amount of nuclearly processed matter to the surface of the star during the course of the main sequence phase.

Another active topic of research are effects of magnetic fields on chemical mixing. Spruit (2002) proposed a dynamo mechanism for differentially rotating stars, which was adopted for calculations of evolutionary models by Heger et al. (2005) and – slightly modified – by Maeder & Meynet (2005). The results of both studies are somewhat contradictory, however. While Heger et al. (2005) find the chemical mixing slightly suppressed compared to purely rotational models, Maeder & Meynet (2005) report a significant enhancement. The latter stress that, while the interaction with the magnetic field suppresses differential rotation and therefore mixing by shear turbulence, the meridional circulation is enhanced, which more than compensates for the former effect in terms of chemical transport.

Note that compositional mixing is not only important for the transport of processed material to the surface, but can also change the general outcome of stellar evolution computations significantly. The size of the well-mixed convective core of massive stars is decisive for the amount of nuclear fuel available during the core burning of later evolutionary stages (Kippenhahn & Weigert 1990). Also convective *overshooting* – which expresses the fact that chemical mixing through convection does not just stop at the borders, but penetrates adjacent layers – is poorly constrained and varying amounts of overshooting are found in evolutionary models (as discussed by Gallart et al. 2005). For example, Heger et al. (2000) neglect overshooting due to the fact that rotationally induced mixing has effects similar to moderate overshooting, but Meynet & Maeder (2003) retain moderate overshooting when introducing rotation.

6.1.4 BA-type Supergiants in the Context of Massive Star Evolution

The evolution of massive stars ($M \gtrsim 8\,M_\odot$) proceeds on short timescales compared to other stars. Their lifetimes range from some 10^6 to several 10^7 years (for comparison, the Sun has a lifetime of 10^{10} years). However, the details of this short-lived evolution, in particular the later stages, are still subject to considerable discussions.

The latest generation of stellar evolution models including mass-loss and rotation has brought considerable advancements towards understanding the evolution of massive stars. For example, the new models have been used to explain the behavior of blue to red supergiant ratios (Maeder & Meynet 2001; Eggenberger et al. 2002) and Wolf-Rayet populations (Meynet & Maeder 2005) as a function of metallicity.

The most recent grid of that kind for massive stars at solar metallicity (Meynet & Maeder 2003) suggests that BA-type supergiants represent a transition phase between main-sequence
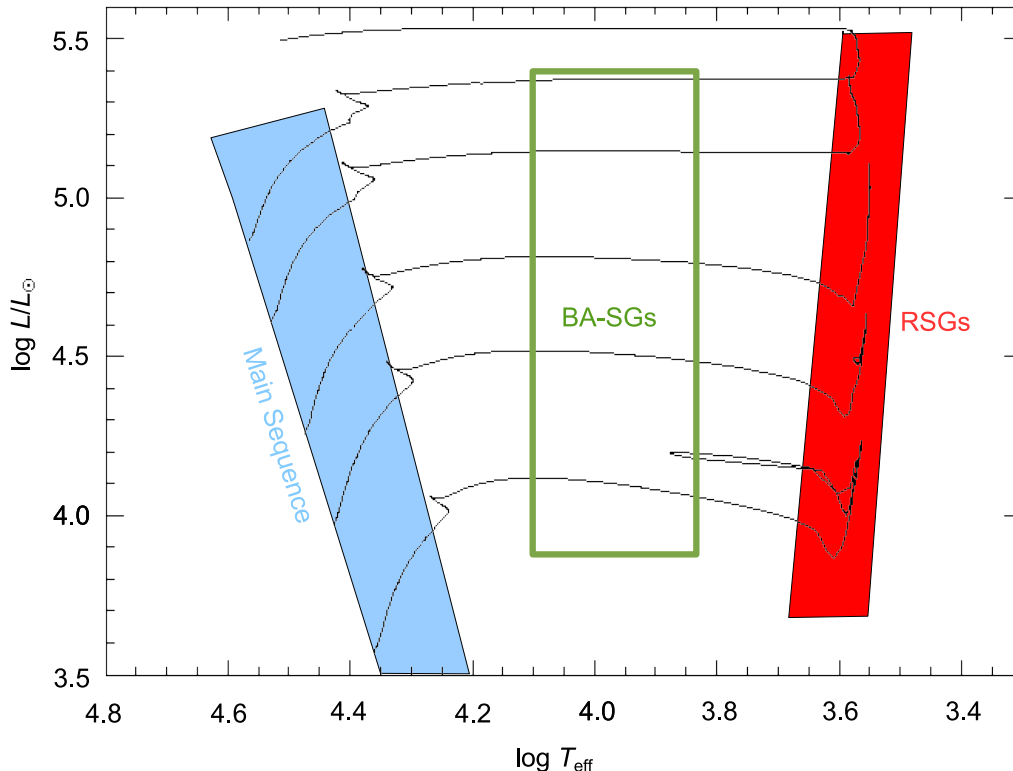
Figure 6.4: The position of the sample stars in the HRD. The examined BA-type supergiants are located along theoretical evolution tracks of stars with initial masses of $9\,M_\odot$, $12\,M_\odot$, $15\,M_\odot$, $20\,M_\odot$ and $25\,M_\odot$ (from bottom to top) including mass-loss and rotation (Meynet & Maeder 2003). They represent an advanced stage of stellar evolution, their progenitors being massive OB-stars on the main sequence. After core hydrogen exhaustion the stars cross the HRD to become red supergiants (RSGs), passing through the region of BA-SGs along the way.

stars and red supergiants (see Fig. 6.4). In this picture, the progenitors of our sample stars are OB-stars on the main sequence with initial masses between $9\,M_\odot$ and $25\,M_\odot$. After the core runs out of fuel hydrogen shell burning sets in, the track moves redwards in the HRD and the star expands. It passes the regime of BA-type supergiants on its way to the red supergiant (RSG) phase. The core continues to contract until central helium burning ignites, followed by subsequent stages of C-, Ne-, O- and Si-burning. After the core runs out of nuclear fuel for energy conversion, the star ends in a core-collapse supernova, leaving behind a neutron star or – for initial masses of more than $20\,M_\odot$ – possibly collapses quietly into a black hole(Fryer 1999). Indeed, the minimum initial mass that can produce supernovae has converged to $8 \pm 1\,M_\odot$ (Smartt 2009). BA-type supergiants could even be direct progenitors to supernovae: the progenitor of the best-studied supernova 1987A in the Large Magellanic Cloud was classified as spectral type B3 (Walborn et al. 1989).

Often another formation channel for BA-type supergiants is discussed, especially for the lower mass segment ($M^{\mathrm{ZAMS}} \lesssim 15\,M_\odot$) of our sample: the so-called *blue loop*. In this scenario, the objects evolve back into core helium burning blue supergiants after passing through the RSG-stage. Blue loops were first predicted for stars of intermediate mass by

Hayashi et al. (1962). Nearly all current evolutionary models predict blue loops, but the extent and the upper mass limit varies. Several investigations into the trigger mechanism of blue loops were conveyed (e. g. Renzini et al. 1992; Maeder & Meynet 2001; Xu & Li 2004a,b), looking into the effects of metallicity, overshooting, mass-loss rates, nuclear reaction rates and other model parameters. Kippenhahn & Weigert (1990) calls this phase "a sort of magnifying glass, revealing relentlessly the faults of calculations of earlier phases". The most comprehensive approach to the problem was presented by Maeder & Meynet (2001), who find that the blue-red motions in the HR diagram mainly hinge on the relation between the core potential Φ_c, being a function of the He-core mass, and some critical limit Φ_{crit}, dependent on the stellar mass. The star moves blueward if

$$\Phi_c < \Phi_{crit} \tag{6.11}$$

is fulfilled. This means that, e. g., large overshooting suppresses the blue loop due to the increased core potential. The effect of rotation on blue loops is very complex. It is noteworthy that the rotating models of Maeder & Meynet (2000) show equally or even more extended blue loops than their non-rotating counterparts, whereas blue loops are greatly suppressed in the more recent rotating models of Meynet & Maeder (2003). Both model sets were computed for solar metallicity using mostly the same physical ingredients – the largest difference are the improved mass-loss rates by Vink et al. (2001).

A long known problem in the modelling of massive star evolution is the so-called *Blue Hertzsprung Gap* (BHG, e. g., Chiosi et al. 1992; Vanbeveren et al. 1998), i.e., evolutionary models cross the HRD on Kelvin-Helmholtz timescales[1] after leaving the main sequence. Most models of Heger et al. (2000) and Meynet & Maeder (2003) with solar metallicity pass through the temperature range examined in this study within a few thousand years, which is a much too small fraction of the total lifetime to reproduce the observed numbers of supergiants. Notable exceptions are the non-rotating models of Meynet & Maeder (2003) for more than $15\,M_\odot$, where He-core burning is ignited during the crossing, which in turn is greatly prolonged. Hirschi et al. (2004) show, however, that adding even small amount of rotation ($v_{rot}^{ini} = 100\,\text{km/s}$) delays the He-ignition until the RSG-stage, thereby reintroducing the problem.

Blue loops provide a possible solution to this problem, but in most evolutionary models they only occur for initial masses up to $15\,M_\odot$ and are not extended enough. In a parameter study, Salasnich et al. (1999) found that models stripped of most of their hydrogen envelopes by high mass loss rates during the RSG-phase can experience very extended blue loops, thereby reducing the unwanted gap in the HRD (see Fig. 6.5). This can lead to a loss of more than 50% of the initial mass, however. Similarly, Hirschi et al. (2004) report that models with high initial rotation rates – which have higher luminosities and therefore higher mass-loss-rates during the RSG-phase – evolve back towards the blue part of the HRD, where homogeneous helium stars are found, before they end in a supernova explosion – a final, not necessarily complete, crossing of the HRD.. In conclusion, various scenarios leading up to blue supergiants seem possible given the significant uncertainties in the pulsational-driven mass loss rates of RSGs (see van Loon 2010 for a review).

---

[1]timescale of gravitational contraction
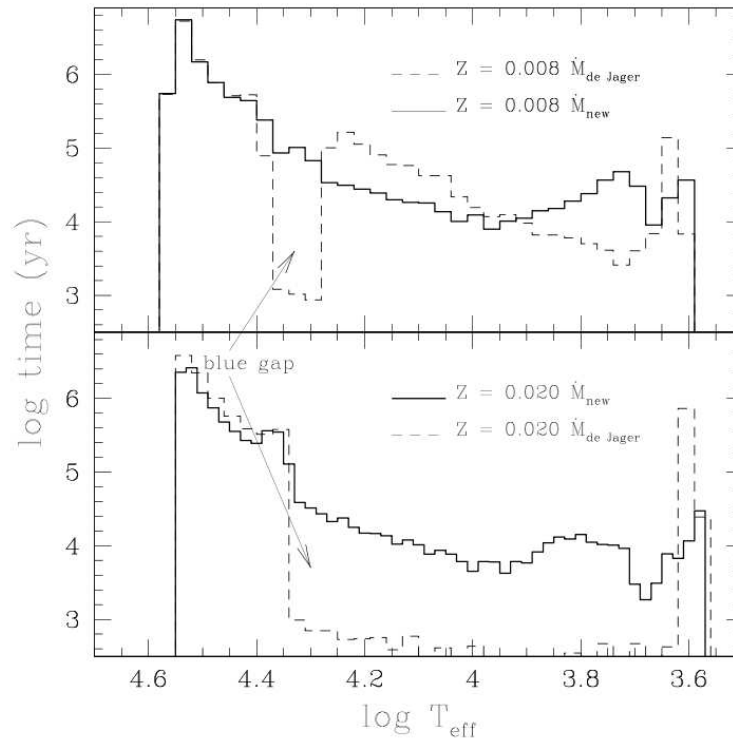
Figure 6.5: From Salasnich et al. (1999): Histogram of the elapsed time as a function of the effective temperature for their 20 $M_\odot$ models (Z=0.008, Y=0.250: upper panel; Z=0.020, Y=0.280: bottom panel). The solid lines incorporate their new mass-loss prescription, the dotted lines the rates published by de Jager et al. (1988).

6.2 Observational Constraints

Many results from the detailed spectroscopic analysis can be directly compared to the predictions of numerical stellar evolution models, such as surface abundance ratios or projected rotational velocities. The reliability of the most important indicators for the evolutionary status of the sample stars is discussed in the following. In addition, the fundamental stellar parameters luminosity, mass and radius are derived from atmospheric parameters, in order to search for the correlations predicted by evolutionary models.

6.2.1 Indicators for the Evolutionary Status

Abundance Ratios: The N I/II- and O I/II-line sets are of excellent quality throughout the examined parameter space, show very low line-to-line scatter and the abundance determination is very robust against atmospheric parameter variations. Consequently, the derived abundances – as well as the N/O-mass-ratio as an indicator for the evolutionary status – are amongst the most reliable results of this study.
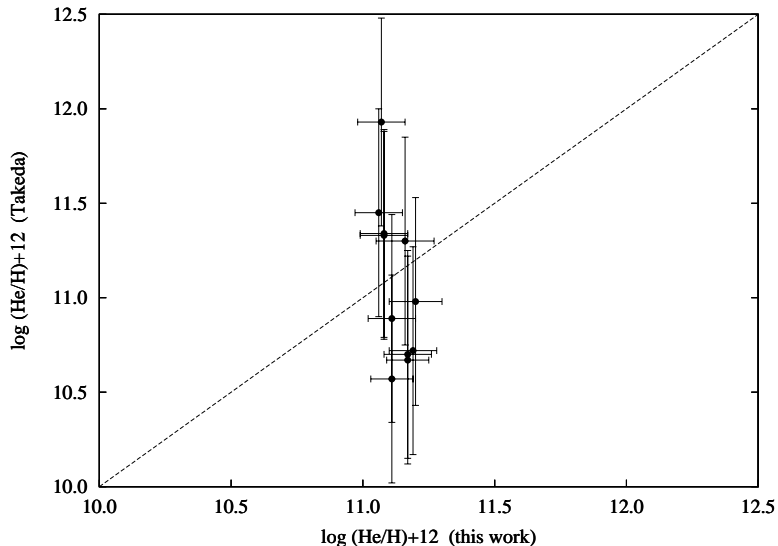
Figure 6.6: Helium abundances derived in this study compared to the results of Takeda & Takada-Hidai (2000). The scatter is dramatically reduced, as can be expected given the lower uncertainties.

Only at the fringes of the examined parameter range satisfying numbers of C$\,$I and C$\,$II-lines are available for abundance analysis. For the bulk of the stars the C-abundance relies on the evaluation of the C$\,$II-doublet at 4267$\,$Å and the C$\,$II-doublet at 6578 and 6582$\,$Å, both of which pose a challenge to non-LTE line formation (see Nieva & Przybilla 2008 for an extensive discussion). The latter can additionally be affected by telluric line absorption (H$_2$O). The differences between the abundances indicated by these two features can amount to up to 0.2$\,$dex. However, no significant trends with T_{eff} or $\log g$ are visible, which gives reason to believe that the gap between the more reliable results for the hottest and the coolest stars of the sample could be successfully bridged. Yet the derived indicator N/C is of somewhat lesser quality than N/O, resulting in larger error bars.

The derived helium abundances vary between 10 and 14% in number fraction, with uncertainties of around 20% in these values. Note, however, that the high sensitivity of the helium lines to T_{eff} variations makes the values prone to substantial systematic effects even from small errors in the parameter determination. This is the first time that consistent helium abundances were derived for a large set of Galactic B- or A-type-supergiants (cooler supergiants show no helium lines at all). The only other available data were obtained by Takeda & Takada-Hidai (2000) and were subject to uncertainties of more than 0.5$\,$dex due to their rather large errors in the atmospheric parameter determination. A comparison for stars in common is provided in Fig. 6.6. Given our lower uncertainties, a meaningful comparison of the observed surface mass fraction Y_{S} of BA-type supergiants to theory seems for the first time realistic.

Rotational Velocities: Recently Aerts et al. (2009) have provided a physical explanation for macroturbulence in the spectra of hot stars. They attribute the broadening excess to the accumulated effect of a large number of non-radial gravity-mode stellar oscillations present in the stellar photosphere. They modelled the effect on the profile of a Si$\,$III line at 4552$\,$Å for a supergiant of spectral type B2$\,$Ia. The resulting synthetic line profiles
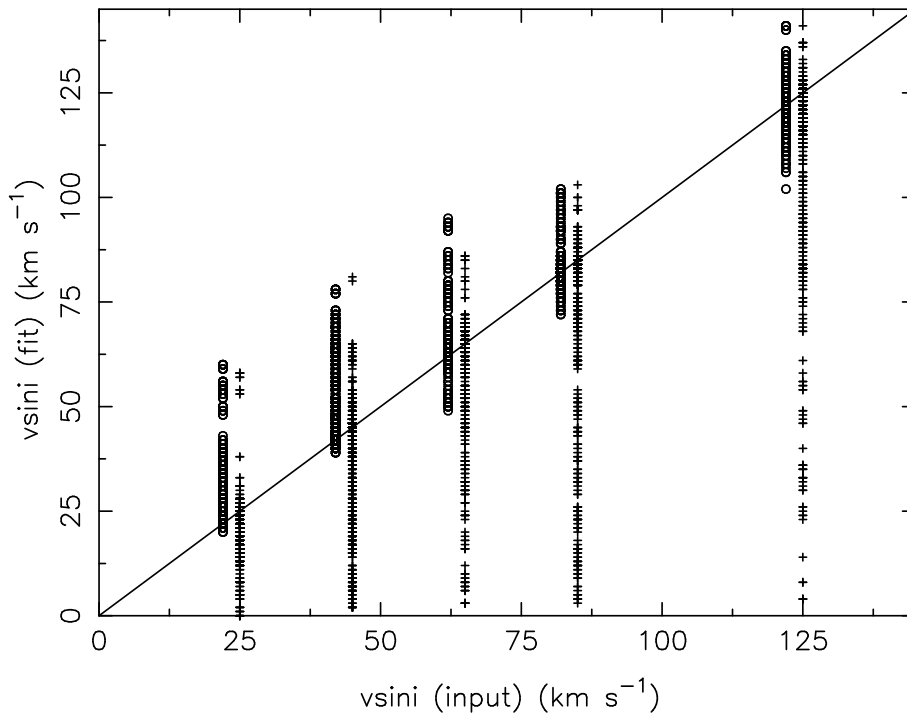
Figure 6.7: Results for $v \sin i$ from fits to synthetic line-profiles without macroturbulence (circles) and with macroturbulence (crosses) as a function of the input $v \sin i$. The circles are slightly shifted for the sake of clarity. From Aerts et al. (2009).

were fitted either with pure rotational models or models incorporating radial-tangential macroturbulence. They conclude that, while fits incorporating macroturbulence produce a better match for the observations, they tend to underestimate the true projected rotational velocity. Consequently, they recommend fits without macroturbulence to estimate the projected rotational velocity. Looking at their results (see Fig. 6.7), it was decided to use the $v_{\mathrm{l}} \sin i$ values from fits including macroturbulence as a lower limit for the true projected rotational velocity, and $v_{\mathrm{u}} \sin i$ from fits with pure rotational profiles as upper limits. Given that typical projected rotational velocities of BA-type supergiants are below $50\,\mathrm{km/s}$, this should provide quite accurate constraints.

An ubiquitous problem in astronomy is that in general not the rotational velocity at the equator, but its projection on the line-of-sight can be measured – $v \sin i$. Therefore, the mean over all angles, assuming a random distribution, $\langle \sin i \rangle = pi/4$ is used to compare theory and observation. The probability of very large deviations from the average seems manageable – only $\approx 1/7$ of the targets are expected to have $\sin i < 0.5$.[1]

---

[1] $\int_0^{\arcsin 0.5} \sin x \mathrm{d}x \approx 0.133975$

Table 6.1: CNO-abundances and other indicators of stellar evolution.

#	Object	log X/H+12				$v_{\mathrm{l}} \sin i$	ζ	$v_{\mathrm{u}} \sin i$	Y_{S}	N/C	N/O	M^{ZAMS}	M^{evol}	$\log L$	R	M^{spec}
		C	N	O	ΣCNO	km s^{-1}	km s^{-1}	km s^{-1}	by mass fraction			$M_\odot$	$M_\odot$	$L_\odot$	$R_\odot$	$M_\odot$
1	HD12301	8.41±0.08	8.14±0.05	8.69±0.06	8.95±0.04	0±10	36±15	30±6	0.31±0.05	0.63±0.13	0.25±0.04	14.5	13.5	4.77±0.14	51±9	13.3
2	HD12953	8.13±0.09	8.42±0.04	8.60±0.05	8.90±0.03	22±7	32±11	33±6	0.34±0.03	2.25±0.51	0.57±0.08	26.0	22.0	5.38±0.15	194±34	19.5
3	HD13476	8.18±0.11	8.58±0.04	8.63±0.06	8.98±0.04	12±2	24±2	23±2	0.36±0.08	2.91±0.81	0.78±0.14	16.0	15.0	4.86±0.14	124±21	14.1
4	HD13744	8.19±0.03	8.29±0.04	8.61±0.05	8.88±0.03	12±10	29±9	27±1	0.36±0.05	1.47±0.16	0.42±0.06	17.0	16.0	4.91±0.21	106±27	14.6
5	HD14433	8.24±0.04	8.24±0.03	8.67±0.05	8.91±0.03	17±3	29±5	29±2	0.33±0.07	1.16±0.14	0.32±0.04	19.0	17.5	5.03±0.14	131±22	15.7
6	HD14489	8.16±0.08	8.51±0.05	8.68±0.03	8.98±0.03	13±2	35±2	31±1	0.35±0.04	2.65±0.56	0.60±0.08	19.0	17.5	5.01±0.15	123±21	15.5
7	HD20041	8.21±0.09	8.27±0.06	8.65±0.04	8.90±0.03	14±2	37±3	31±4	0.32±0.03	1.35±0.34	0.36±0.06	16.5	15.5	4.90±0.15	94±16	14.5
8	HD21291	8.21±0.11	8.45±0.04	8.66±0.04	8.96±0.03	32±4	33±9	40±1	0.33±0.03	2.04±0.53	0.55±0.08	19.5	17.5	5.08±0.14	100±17	16.2
9	HD39970	8.23±0.08	8.15±0.08	8.64±0.05	8.87±0.04	2±3	45±2	35±3	0.32±0.04	0.97±0.25	0.29±0.06	16.0	15.0	4.90±0.15	89±15	14.5
10	HD46300	8.10±0.07	8.43±0.07	8.71±0.05	8.96±0.04	0±2	14±2	12±1	0.33±0.06	2.48±0.56	0.45±0.09	9.5	9.5	4.22±0.15	43±8	9.5
11	HD186745	8.28±0.09	8.35±0.05	8.77±0.01	9.00±0.02	22±10	40±15	38±6	0.31±0.04	1.36±0.32	0.33±0.04	23.0	20.0	5.22±0.14	88±15	17.7
12	HD187983	8.29±0.09	8.19±0.04	8.78±0.02	8.98±0.02	15±6	29±8	28±3	0.32±0.06	0.92±0.21	0.23±0.02	15.0	14.0	4.80±0.22	97±25	13.6
13	HD197345	8.09±0.07	8.56±0.07	8.69±0.04	8.99±0.03	10±9	29±7	27±2	0.37±0.07	3.43±0.78	0.65±0.12	22.0	19.5	5.18±0.14	172±29	17.2
14	HD202850	8.15±0.04	8.70±0.06	8.75±0.05	9.08±0.03	14±5	35±5	31±3	0.38±0.07	4.12±0.66	0.78±0.13	15.0	14.0	4.81±0.14	73±12	13.7
15	HD207260	8.22±0.08	8.53±0.06	8.71±0.02	9.01±0.03	15±3	25±3	26±2	0.36±0.04	2.42±0.58	0.59±0.09	18.5	17.0	5.01±0.14	137±23	15.4
16	HD207673	8.16±0.09	8.47±0.03	8.72±0.04	8.98±0.03	1±2	23±2	19±1	0.33±0.09	2.40±0.52	0.50±0.06	12.0	11.5	4.51±0.14	70±12	11.4
17	HD208501	8.25±0.14	8.23±0.08	8.76±0.02	8.97±0.03	16±10	56±15	42±6	0.31±0.05	1.11±0.41	0.26±0.05	22.0	19.5	5.19±0.14	82±14	17.3
18	HD210221	8.22±0.06	8.52±0.06	8.70±0.05	9.00±0.03	0±2	27±2	21±1	0.34±0.04	2.34±0.48	0.58±0.10	15.5	14.5	4.83±0.14	123±21	13.8
19	HD212593	8.30±0.08	8.44±0.06	8.74±0.04	9.01±0.03	6±2	24±2	19±1	0.36±0.06	1.60±0.36	0.44±0.07	12.5	12.0	4.55±0.15	50±9	11.7
20	HD213470	8.16±0.08	8.53±0.04	8.64±0.03	8.97±0.02	13±2	27±2	25±2	0.32±0.08	2.73±0.56	0.68±0.08	18.0	16.5	4.96±0.14	144±24	15.1
21	BD+602582	8.17±0.13	8.54±0.06	8.57±0.07	8.94±0.04	35±7	14±8	37±4	0.35±0.07	2.70±0.87	0.81±0.17	18.5	17.0	5.04±0.14	78±13	15.8
22	HD223960	8.12±0.15	8.56±0.07	8.62±0.05	8.96±0.04	25±6	37±6	37±1	0.34±0.08	3.24±1.25	0.76±0.15	20.5	18.5	5.13±0.14	107±18	16.7
23	HD195324	8.10±0.11	8.70±0.08	8.74±0.04	9.07±0.04	3±3	20±3	16±1	0.37±0.06	4.66±1.46	0.81±0.17	11.0	10.5	4.43±0.15	65±11	10.8
24	HD34085	8.23±0.09	8.46±0.06	8.74±0.05	9.00±0.04	25±3	31±7	35±3	0.32±0.04	2.00±0.51	0.46±0.08	23.0	20.0	5.21±0.14	92±15	17.6
25	HD87737	8.25±0.06	8.53±0.07	8.73±0.06	9.02±0.04	2±2	17±2	14±1	0.36±0.05	2.24±0.47	0.55±0.11	10.0	9.5	4.26±0.15	49±9	9.8
26	HD91533	8.18±0.06	8.51±0.08	8.71±0.04	8.99±0.03	20±2	29±2	31±3	0.35±0.04	2.49±0.55	0.55±0.11	16.0	15.0	4.88±0.14	111±19	14.3
27	HD111613	8.29±0.10	8.45±0.04	8.72±0.04	9.00±0.03	17±2	27±2	27±1	0.34±0.06	1.71±0.44	0.47±0.06	17.0	16.0	4.96±0.14	121±20	15.0
28	HD149076	8.51±0.08	8.43±0.09	8.78±0.04	9.08±0.04	7±6	37±2	29±3	0.34±0.04	0.99±0.27	0.39±0.09	13.0	12.5	4.60±0.15	54±9	12.0
29	HD149077	8.16±0.05	8.47±0.05	8.74±0.04	8.99±0.03	1±2	13±2	10±1	0.35±0.06	2.39±0.40	0.47±0.07	9.0	9.0	4.13±0.15	39±7	9.0
30	HD165784	8.38±0.04	8.62±0.05	8.80±0.04	9.11±0.03	18±2	35±4	33±3	0.34±0.03	2.02±0.29	0.58±0.08	18.0	16.5	4.85±0.15	110±19	14.1
31	HD166167	8.51±0.06	8.49±0.08	8.86±0.04	9.14±0.03	9±6	20±7	19±2	0.32±0.06	1.12±0.26	0.37±0.08	10.5	10.0	4.33±0.15	53±9	10.2
32	HD80057	8.25±0.1	8.33±0.04	8.71±0.05	8.96±0.04	13±3	27±2	25±1	0.36±0.04	1.41±0.35	0.37±0.06	13.0	12.5	4.59±0.14	76±13	12.0
33	HD102878	8.26±0.11	8.52±0.05	8.71±0.03	9.01±0.03	0±3	35±3	27±3	0.35±0.05	2.13±0.59	0.57±0.08	15.5	14.5	4.83±0.14	109±18	13.8
34	HD105071	8.25±0.13	8.55±0.06	8.75±0.07	9.04±0.04	23±7	39±8	39±1	0.35±0.06	2.32±0.75	0.54±0.11	19.0	17.5	5.06±0.14	79±13	16.0
35	HD106068	8.35±0.13	8.60±0.04	8.77±0.06	9.08±0.04	20±8	45±14	41±3	0.34±0.01	2.09±0.67	0.60±0.09	16.5	15.5	4.91±0.14	71±12	14.6
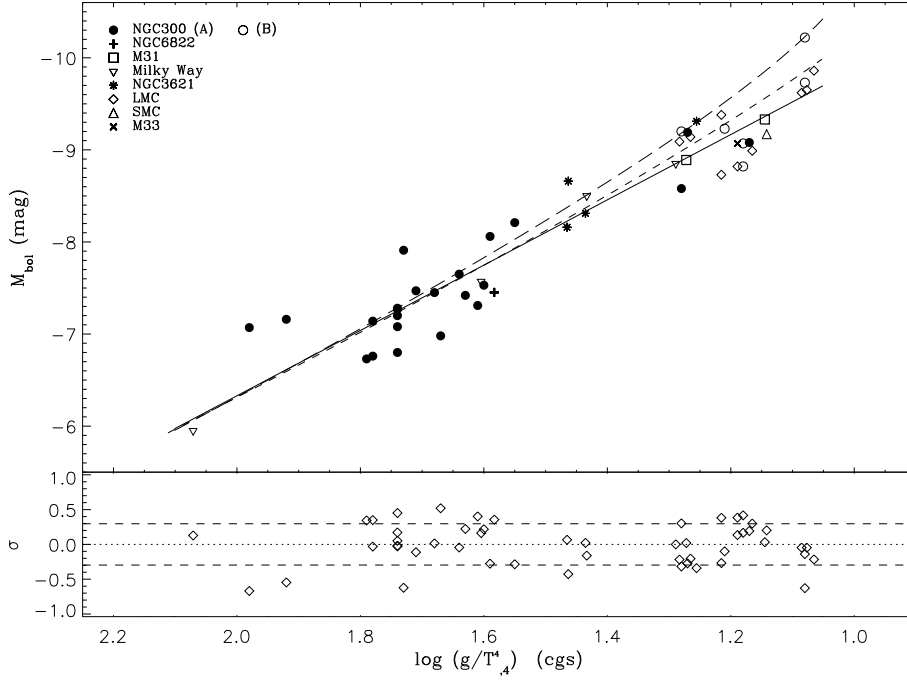
Figure 6.8: The FGLR of BA-type supergiants in 8 galaxies and the linear regression (solid). The stellar evolution FGLRs for models by Maeder & Meynet (2005) are also overplotted (dashed: Milky Way metallicity, long-dashed: SMC metallicity). From Kudritzki et al. (2008).

6.2.2 Derivation of Fundamental Stellar Parameters

While knowing the Eddington flux H_ν and the apparent magnitude m_V is sufficient to derive the angular diameter of an object (undisturbed by the atmosphere), additional information is needed to derive the luminosity L, like for example a distance estimate. Therefore the flux-weighted gravity-luminosity relationship (FGLR, Kudritzki et al. 2003, 2008), which is normally used to derive distances of other galaxies by purely spectroscopic means, was adopted for the distance and luminosity determination of individual stars in the Galaxy.

The FGLR is based on the assumption, that massive stars evolve through the B and A supergiant stage at roughly constant luminosity. This is supported by stellar evolution models (compare Fig. 6.4). Since the evolutionary timescale of the crossing of the HRD is rather short, the amount of mass-loss during this transition is small. This means that the evolution proceeds at roughly constant mass and luminosity.

Starting from

$$L \propto R^2 T_{\mathrm{eff}}^4 = \mathrm{const.}; M = \mathrm{const.} \tag{6.12}$$

it is apparent that

$$M \propto gR^2 \propto L(g/T_{\mathrm{eff}}^4) \equiv Lg_{\mathrm{F}} = \mathrm{const.} \tag{6.13}$$

Thus, along the evolution through the B and A supergiant regime the *flux-weighted gravity* $g_{\mathrm{F}} = g/T_{\mathrm{eff}}^4$ should remain constant. Hence it is possible to characterize each evolutionary track of a distinct luminosity in the examined domain by a specific value of g_{F}.
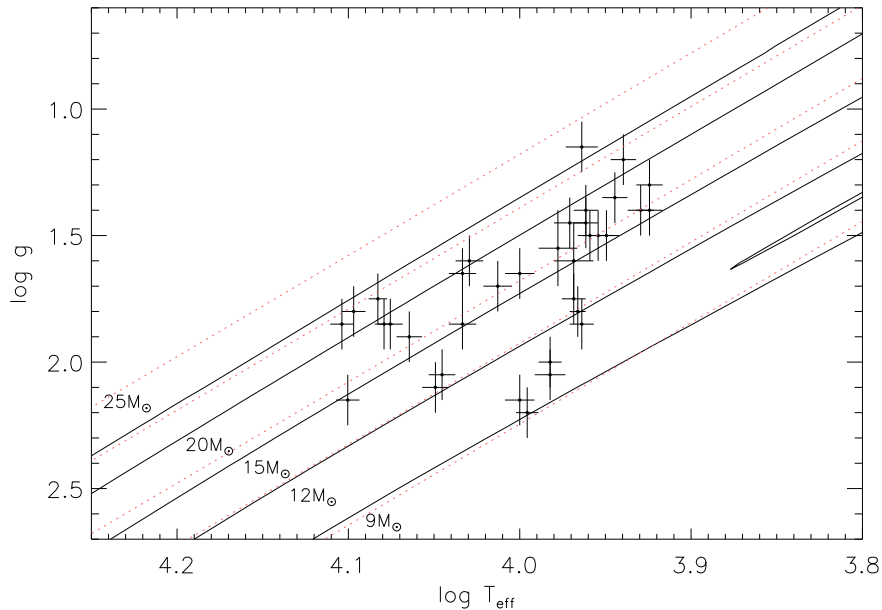
Figure 6.9: The positions of the sample stars in the $\log T_{\mathrm{eff}}$-$\log g$-diagram are used to determine M^{evol} and M^{ZAMS} by comparison to evolutionary tracks of Meynet & Maeder (2003) with an initial rotational velocity of $300\,\mathrm{km/s}$. The values for the respective starting masses are denoted in the diagram. The dashed, red lines indicate the locations of FGLR-solutions computed for the evolutionary masses indicated by the tracks, the discrepancies increase for higher masses. The error bars indicate the uncertainties of the atmospheric parameter determination.

Based on the aforementioned considerations, an empirical relationship between g_{F} and the absolute bolometric magnitude M_{bol} of BA-type supergiants could be constructed:

$$-M_{\mathrm{bol}} = a\left(\log\left(\frac{g}{(T_{\mathrm{eff}}/10000\,\mathrm{K})^4}\right) - 1.5\right) + b \qquad (6.14)$$

The latest calibration based on the evaluation of targets in 8 different galaxies yielded $a = 3.41 \pm 0.16$ and $b = 8.02 \pm 0.04$ (Kudritzki et al. 2008). There it was concluded that the simple linear regression fit is the best way to describe the empirical FGLR at this point ($\sigma = 0.32\,\mathrm{mag}$), even compared to more sophisticated models based on stellar evolution theory (see Fig. 6.8). The accuracy for extragalactic distance measurements based on ensembles of supergiants is estimated to $\lesssim 0.1\,\mathrm{mag}$. The uncertainty estimates for single stars from error propagation based on the uncertainties of the atmospheric parameters as well as of the fit parameters a and b leads to $\Delta M_{\mathrm{bol}} \approx 0.35\,\mathrm{mag}$, which is surprisingly larger than the standard deviation found by Kudritzki et al. (2008) based on medium-quality spectra. Note, however, that the uncertainties derived by error propagation are likely overestimated, since – as Kudritzki et al. (2008) point out – the Balmer-lines are even more sensitive to $\log g_{\mathrm{F}}$ than they are to $\log g$.

M_{bol} is related to the stellar luminosity L as follows:

$$M_{\mathrm{bol}} = -2.5 \log L/L\odot + M_{\mathrm{bol},\odot}, \qquad (6.15)$$
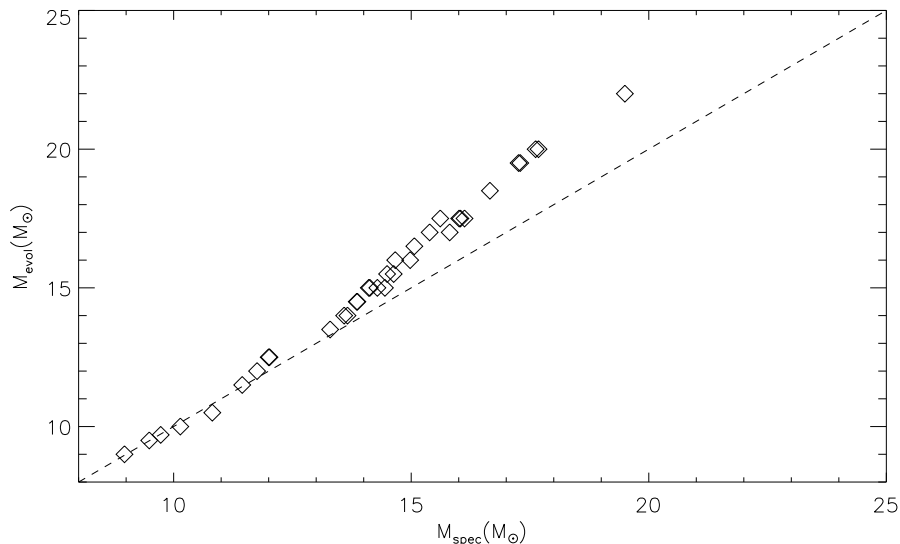
Figure 6.10: Comparison of evolutionary and spectroscopic masses. The evolutionary masses derived from the rotating evolution models of Meynet & Maeder (2003) are considerably higher in the high-mass-regime of the sample than the estimates based on the FGLR.

where $M_{\text{bol},\odot} = 4.74$ is the absolute bolometric magnitude of the Sun. Now the stellar radius R can be derived:

$$L = 4\pi R^2 \sigma T_{\text{eff}}^4. \tag{6.16}$$

The so-called spectroscopical mass M^{spec} can then be computed from

$$M^{\text{spec}}/M_\odot = g/g_\odot (R/R_\odot)^2. \tag{6.17}$$

The uncertainties amount to $\approx 30\,\%$, however, mainly due to the uncertainty in the calibration of a.

Another method to derive stellar masses is by comparison of the positions in the $\log T_{\text{eff}}$-$\log g$-diagram to evolutionary tracks (see Fig. 6.9), which leads to so-called evolutionary masses M^{evol} and theoretical starting masses M^{ZAMS} on the zero-age-main-sequence (ZAMS). The rotating evolution models of Meynet & Maeder (2003) were used for the mass estimation, under the assumption the objects evolved directly from the main sequence. Error propagation yields uncertainties of only $\approx 15\,\%$ in the so derived values – much smaller than the $30\,\%$ for M^{spec} – but this excludes significant uncertainties from the evolutionary models, such as, e.g., mass-loss rates and formation channel. If some targets stars are actually on a blue loop, this method would overestimate their masses, considering the location of the different tracks and the mass-loss during the RSG-phase. The distinct mass estimates for the sample are compared in Fig. 6.10. Note that the different methods to determine the current stellar mass are *not* based on independent measurements, but are both relying on the $T_{\text{eff}}/\log g$ values, only that one calibration is empirical (FGLR), the other theoretical (evolution tracks). The differences could indicate that the mass-loss of stars with more than $\approx 15\,M_\odot$ is higher than predicted by the evolutionary models. This would favor a post RSG-scenario for these stars, as recent developments in the study
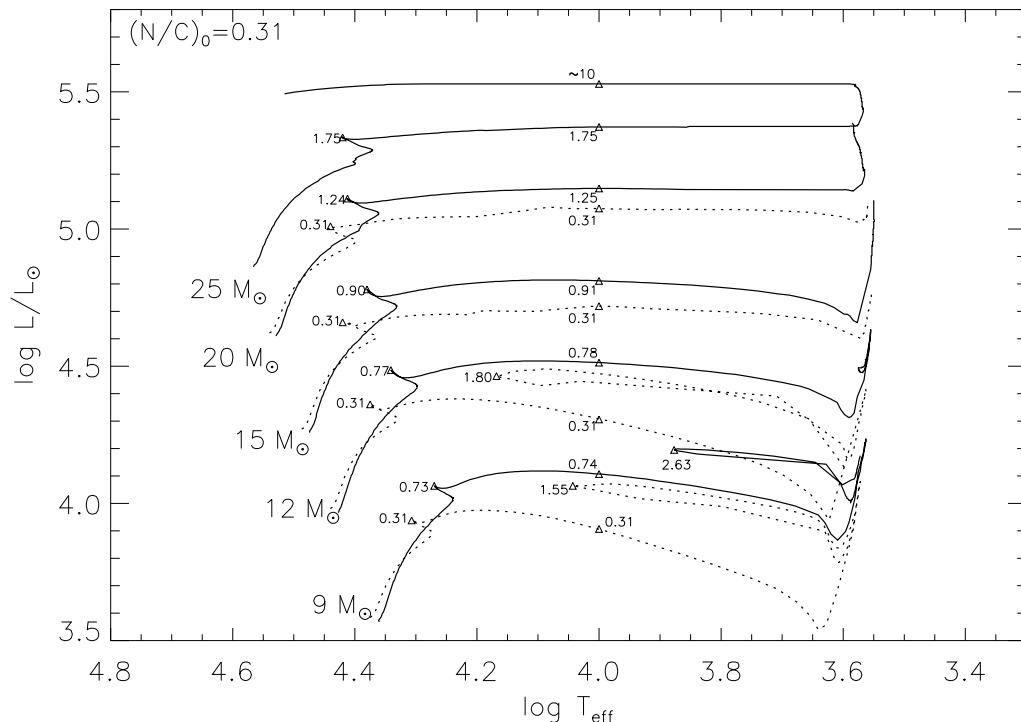
Figure 6.11: Evolutionary tracks from Meynet & Maeder (2003) for rotating ($v_{\rm rot}^{\rm ini} = 300\,{\rm km/s}$, continuous lines) and non-rotating (dashed lines) models. The models start with a N/C ratio of 0.31 on the main sequence and predict ratios of 0.7 to 1.7 for rotating BA-type supergiants in the mass range of 9 to 25 $M_\odot$ evolving redwards and 1.6 to 2.6 for stars of 9 to 12 $M_\odot$ on a blue loop. In the non-rotating case no surface enrichment is predicted before the first dredge-up during the RSG-phase.

of mass-loss rates (see Puls et al. 2008, for a review) indicate even lower mass-loss rates for OB-stars on the main sequence than previously assumed. Nonetheless, the low sensitivity of the FGLR-calibration for stellar mass (Kudritzki et al. 2008) precludes any firm conclusions,

6.2.3 Comparison of Theory and Observation

Many details of massive star evolution – in particular related to the signatures of CNO-cycled products in the stars and rotationally induced mixing – are subject to intense debate at present, see e. g., Hunter et al. (2009), Maeder et al. (2009) and Przybilla et al. (2010). BA-type supergiants represent an advanced phase in the evolution of massive stars, hence providing an excellent testbed for stellar evolution theory, which is compared to observations in the following.
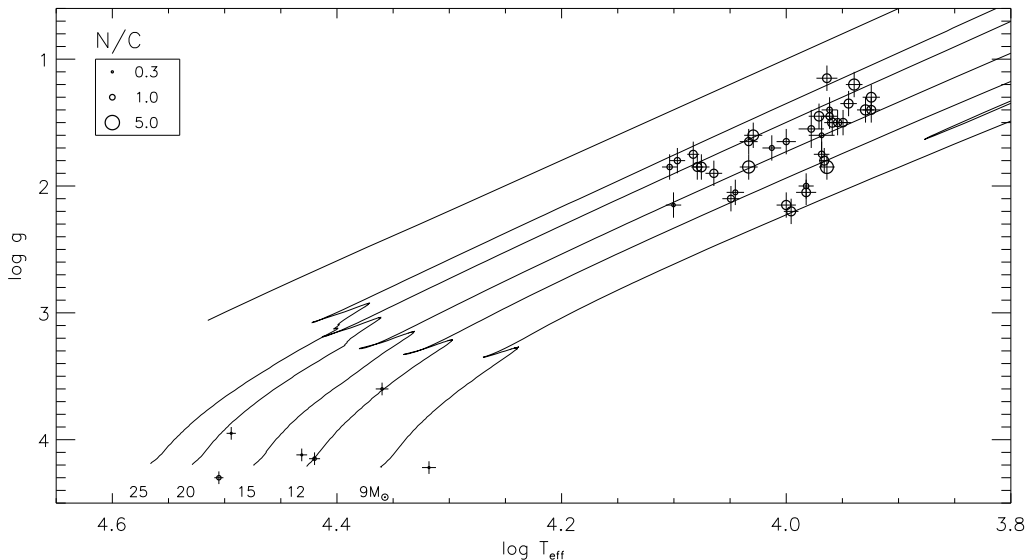
Figure 6.12: The $\log T_{\mathrm{eff}}$-$\log g$-diagram of the sample stars combined with a sample of six of their progenitors – main sequence B-stars as tabulated by Przybilla et al. (2010), located at the bottom left. They are connected by the evolutionary tracks of Meynet & Maeder (2003) for rotating stars ($v_{\mathrm{rot}}^{\mathrm{ini}} = 300\,\mathrm{km/s}$), initial masses as indicated. The symbol size encodes N/C (by mass fraction) .

Surface Abundances

The current models of massive star evolution including rotation, as discussed in the previous sections, make similar predictions for the surface abundances of CNO-processed material in BA-type supergiants. Should they have evolved directly from the main sequence, no major changes in the abundance patterns are expected during the short post-MS phase, as their envelope is still in radiative equilibrium, and the timescale τ_{mix} of rotationally induced mixing is large compared to the post-MS evolution. The abundances correspond to those at the end of the main sequence phase. According to the models, the amount of mixing would be strongly correlated with the initial rotation rate.

If the star is on a blue loop, its envelope has been fully convective and intense mixing has taken place during the red supergiant phase (the so-called *first dredge-up*). This strengthens the signature of CNO-processed material in the photosphere considerably. This effect is considerably stronger than pure rotationally-induced mixing in the rotating $9\,M_{\odot}(v_{\mathrm{rot}}^{\mathrm{ini}} = 300\,\mathrm{km/s})$ of Meynet & Maeder (2003), but virtually not discernible from pure rotation in the $12\,M_{\odot}$ of Heger & Langer (2000) at their highest $v_{\mathrm{ini}} = 450\,\mathrm{km/s}$. An overview of the predicted N/C-values in the models of Meynet & Maeder (2003) across the HRD gives Fig. 6.11. Given the sharp drop of rotational velocities during the post-MS evolution and the uncertainties in the rotational velocities stemming from macroturbulence, a reconstruction of that trend seems difficult. Fraser et al. (2010) tried that for their somewhat faster rotating B-supergiants, and found a slight correlation between nitrogen abundance and initial rotational velocities in their data. Their somewhat crude
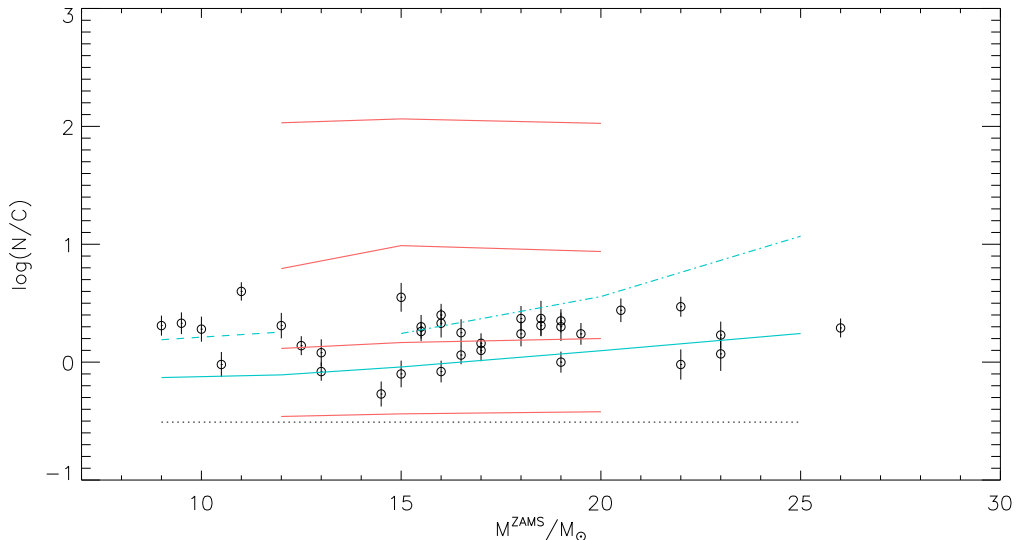
Figure 6.13: The logarithm of N/C-ratios against M^{ZAMS}: the circles show the position of the sample stars, the errors in mass were omitted for the sake of clarity, but amount to about 15%. The black dotted line marks the initial ratio $(N/C)_0$. Red lines represent results from Heger & Langer (2000), $v_{\mathrm{rot}}^{\mathrm{ini}}$ from top to bottom: $450\,\mathrm{km/s}$, $300\,\mathrm{km/s}$, $200\,\mathrm{km/s}$ and $100\,\mathrm{km/s}$, abundances after core hydrogen exhaustion. Blue lines represent models from Meynet & Maeder (2003); continuous: $v_{\mathrm{rot}}^{\mathrm{ini}} = 300\,\mathrm{km/s}$, abundances after core hydrogen exhaustion; dashed: non-rotating with blue loop, abundances after first dredge-up; dashed-dotted: non-rotating without blue loop, abundances after core helium exhaustion.

reconstruction of the initial velocities via the present-day radii is only poorly supported by the evolutionary models, however.

A prediction by both models, although to somewhat different extent, is that the characteristic mixing timescales decrease faster with increasing mass than the lifetimes of the stars, which means that more massive stars should show an enhanced mixing signature. In spite of this, no significant correlation of the indicators for CNO-processed material (Y_{S}, N/C, N/O) with either luminosity or mass could be found.[1] This result is somewhat mitigated by the large expected scatter induced by the distribution of initial velocities. Indeed, the effect of mass is almost negligible compared to the effect of rotation in the models of Heger et al. (2000), although that is less pronounced for the models of Meynet & Maeder (2003).

Figure 6.13 shows that rotationally induced mixing can account for the observed amount of mixing – the models of Heger & Langer (2000) might even show too efficient mixing, while the mixing in the models of Meynet & Maeder (2003) would probably need enhancement by magnetic fields – without the need for a first dredge-up. Given a possible $v_{\mathrm{rot}}^{\mathrm{ini}}$-distribution (compare Fig. 6.14), one may wonder why no supergiants without very weak mixing signatures are found – as one would expect for slow rotators given the low mixing efficiency of the $100\,\mathrm{km/s}$-model of Heger et al. (2000).

A first dredge-up scenario could well account for the high observed N/C-values at $M^{\mathrm{ZAMS}} \approx 10\,M_\odot$ (dashed line in Fig. 6.13). However, a dichotomy in surface abundance ratios, as one

---

[1]correlation coefficients, as defined in the Appendix: $\mathrm{corr}(L, Y_{\mathrm{S}}) = -0.19$; $\mathrm{corr}(L, (N/O)) = 0.09$;
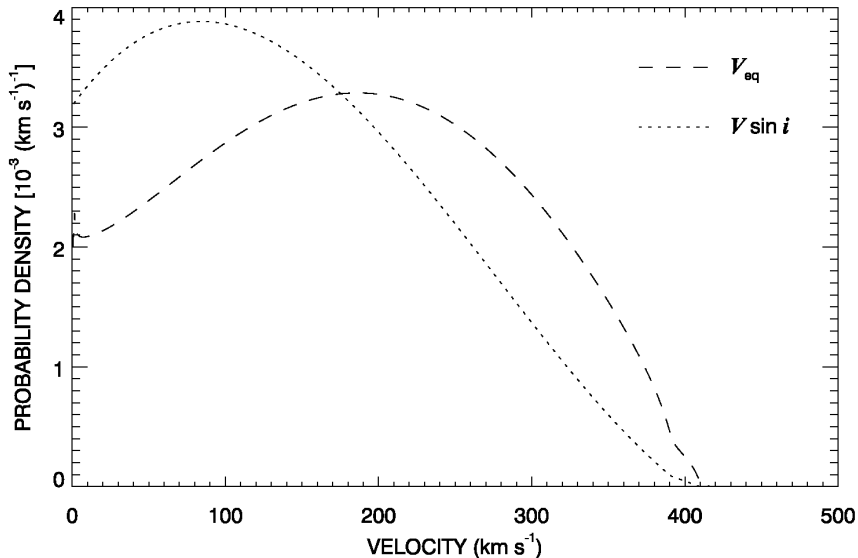
Figure 6.14: A polynomial fit of the $v \sin i$-distribution (dotted line) and the corresponding distribution of equatorial velocity v_{eq} (dashed line) for 497 B-stars in Galactic clusters. From Huang & Gies (2006b). Note that many of these stars have already slowed down considerably during their life on the main sequence.

would expect in a composite population of blue-loop objects and objects directly evolved from the main sequence, is not seen. Such a scenario is still possible, if the rotationally induced mixing in the high-mass regime of the sample has a similar efficiency as the convective dredge-up in the low-mass regime, which also would provide an explanation as to why indicators for CNO-mixing like N/O are not increasing with luminosity over the whole sample.

The possible signatures of a final crossing-scenario for stars of more than $15 M_\odot$ are indicated in Fig 6.13 by the abundance ratios found in the non-rotating models of Meynet & Maeder (2003) after core helium exhaustion (dashed-dotted line). At least the high values for $25 M_\odot$-stars, most likely to perform such a crossing in the models due to the large mass loss during the RSG-phase, are not seen in the sample.

It is somewhat disappointing, that no firm conclusions about the evolutionary status of BA-type supergiants can be drawn, even though the accuracy in abundance determination is unprecedented for such a large sample of these stars. The high accuracy can be confirmed, however, in selected comparisons with evolutionary models and previously published data. One can take advantage of the fact that the predicted trends of N/C with N/O are similar for the entire mass range under investigation, and only the extent of the abundance changes is increasing with mass. The trends are also mostly insensitive to the mixing mechanism (convective dredge-up vs. rotationally induced mixing), but controlled by initial CNO-abundances and nuclear reaction rates (Przybilla et al. 2010). A comparison of this *common* trend with observations of the whole sample is therefore justified. The large scatter found in previously published data – which is expected considering the uncertainties – is displayed in Fig. 6.15a. Note that the scatter persists even for objects in common with
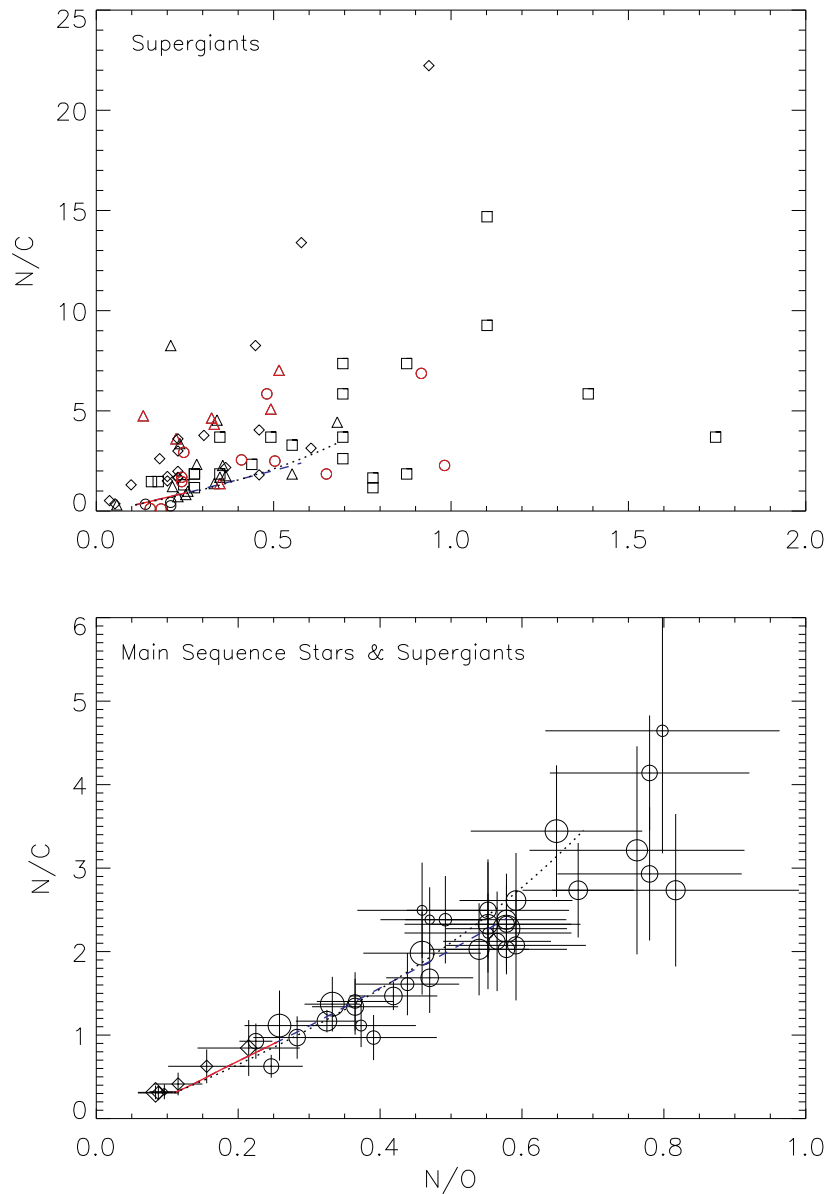
Figure 6.15: **Upper Panel:** Previous status of observational constraints on the mixing of CNO-burning products in massive stars from non-LTE analyses of BA-type supergiants. Mass ratios N/C versus N/O are displayed. Triangles: Venn (1995b); Venn & Przybilla (2003); circles: Takeda & Takada-Hidai (2000); squares: Crowther et al. (2006); diamonds: Searle et al. (2008); objects in common with this study are marked red. Error bars are omitted for clarity: uncertainties in the abundances of the individual elements are typically about a factor 2, such that the error bars can be larger than the plotting range. **Lower Panel:** N/C vs. N/O for the sample stars plus a small number of main sequence B-stars as tabulated by Przybilla et al. (2010). The symbol size encodes the stellar mass. **Both panels:** Lines represent predictions from evolution calculations, for a rotating $15 M_\odot$ star ($v_{\rm rot}^{\rm ini} = 300\,{\rm km/s}$, Meynet & Maeder (2003); until the end of the MS: solid red line, until the end of He burning: dashed blue line) and for a star of the same mass and $v_{\rm rot}^{\rm ini} = 300\,{\rm km/s}$ that in addition takes the interaction of rotation and a magnetic dynamo into account (Maeder & Meynet (2005); until the end of the MS: dotted line), respectively.
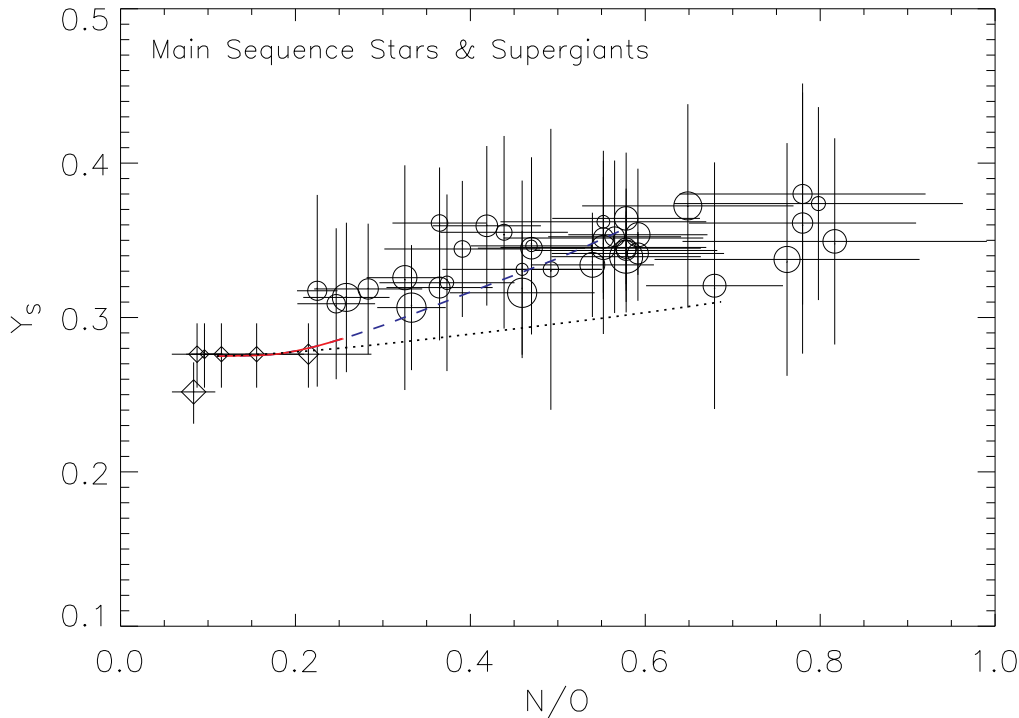
Figure 6.16: Surface helium abundance Y_S as a function of N/O ratio (both by mass) for the sample stars plus a small number of main sequence B-stars as tabulated by Przybilla et al. (2010). Symbol and line encoding as in Fig. 6.15a.

this study. In contrast, the results of our study follow the predicted trend tightly within the small uncertainties, as can be seen in Fig. 6.15b.

Also displayed in the same plot are carefully analyzed data on six slowly rotating early B-type stars on the main sequence (Nieva & Przybilla 2006, 2008; Przybilla et al. 2008, 2010), that are located in the solar neighborhood. These data are interesting for a comparison both because these stars represent progenitors of BA-type supergiants and because they were analyzed in a similar fashion, thereby providing a reference point for evolutionary considerations. In consequence, Fig. 6.15b and Fig. 6.12 show that our analysis method gives consistent CNO-abundances for different stages of massive star evolution.

Another predicted correlation between indicators for mixing with nuclearly processed material, Y_S and N/O, is inspected in Fig. 6.16. More helium than expected is found in the supergiants compared to the models. In addition a slight jump in helium abundance between the main-sequence stars and the supergiants is found. This could possibly be attributed to systematic errors, as a downward shift by a mere 10–15% is needed to bring the observations and the magnetic model in Fig. 6.16 into agreement. The trend of 0.81 ± 0.22[1] in Y_S per 1.0 change in N/O found in our data is located somewhere between the predictions of the magnetic and the purely rotational model. The predicted trend is clearly not independent from the mixing mechanisms, and Y_S and N/O also react quite differently to changes in the effectiveness of the μ-barrier (Heger & Langer 2000), so that the uncertain-

---

[1] 90% confidence interval or $\Delta\chi^2 = 2.7$; correlation coefficient corr(Y_S, (N/O)) = 0.65

ties in the predictions are larger. On the observational side, the recent study of Huang & Gies (2006b) found helium enrichment trends of $23\% \pm 3\%$ between ZAMS and TAMS in the high mass range $(8.5\,M_\odot < M < 16\,M_\odot)$ of their of OB-main-sequence star sample, which would be consistent with the helium abundances of supergiants obtained here, even without additional mixing during the post-MS-evolution.

Velocity Fields

The velocity fields that shape the stellar spectra can contain important information about the physical status of the star. The relevance of the derived velocities is discussed in the following.

Microturbulence: The microturbulences derived in this study – originally seen only as a by-product of the parameter and abundance determination – show some interesting properties. Przybilla et al. (2006) already suspected a correlation of microturbulence and luminosity class in BA-type supergiants. The results of this study confirm this suspicion. Indeed a tight relation between microturbulence and luminosity is found, as can be seen in Fig. 6.18. On the other hand only a very weak correlation with effective temperature is found.[1] Reassuringly, the derived values agree within the errors with the results of Landstreet et al. (2009) and Venn (1995a) for objects in common. Also the absolute values (the maximum of ξ is $8\,\text{km/s}$) stay well below the speed of sound in the line formation region as computed from model atmospheres, even for the coolest objects in the sample. This is an important test for the consistency of the physics behind the concept.

Recently, Cantiello et al. (2009) provided a physical explanation for microturbulence in hot stars. They investigated the properties of sub-surface convection zones in evolutionary models of massive stars, in particular the average convective velocity $\langle v_c \rangle$ in the iron convection zone (FeCZ), as defined by

$$\langle v_c \rangle := \frac{1}{\alpha H_P} \int_{R_c - \alpha H_P}^{R_c} v_c(r)\mathrm{d}r, \tag{6.18}$$

where H_P is the pressure scale height, R_c the upper boundary of the convective zone and $\alpha = 1.5$. The authors found a correlation with the distribution of microturbulences in the HRD, as they were derived by Trundle et al. (2007) and Hunter et al. (2008) for B-type stars in the Galaxy and the Magellanic Clouds. Unfortunately their method to derive microturbulences might be incompatible with the values found in this study, as the comparison with Fraser et al. (2010) for the one object in common shows a striking discrepancy.

The FeCZ in BA-type supergiants is located deeper in the atmosphere than the line formation region. The proposed mechanism to generate the effect of microturbulence on the lines is the excitation of acoustic and gravity waves in the upper part of a convection zone

---

[1] correlation coefficients: $\text{corr}(L, \xi) = 0.92$; $\text{corr}(T_\text{eff}, \xi) = 0.25$
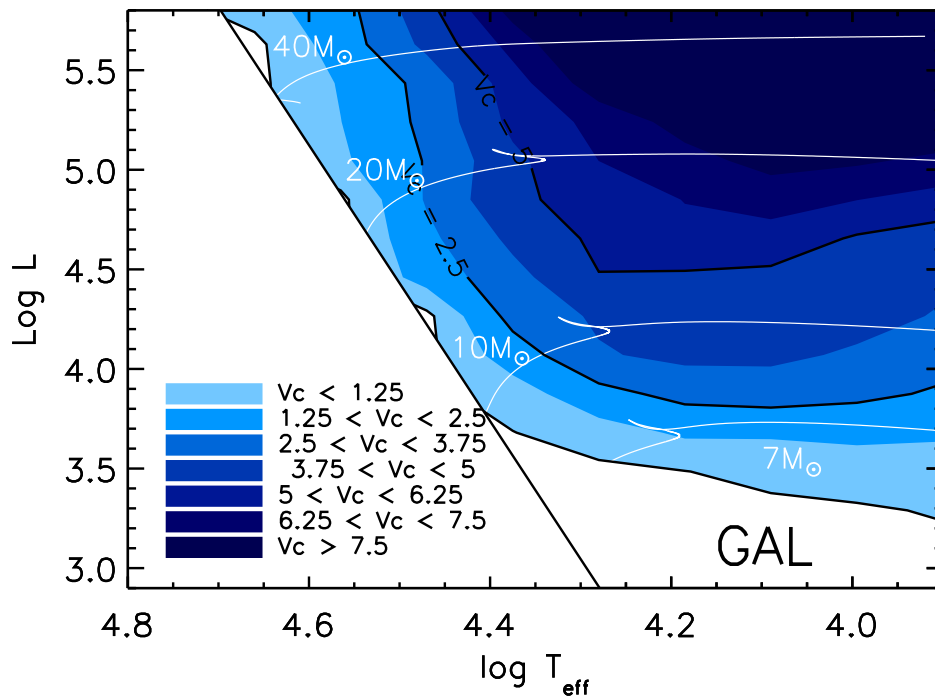
Figure 6.17: The average convective velocity within 1.5 pressure scale heights of the upper border of the iron convection zone is displayed as a function of T_{eff} and $\log L$, based on evolutionary models (white lines) between $5\,M_\odot$ and $100\,M_\odot$ (provided by M. Cantiello, see Cantiello et al. 2009).

that propagate towards the surface. An estimate for the maximum velocity field amplitude at the surface v_{s} is provided by

$$v_{\text{s}} \leq \langle v_{\text{c}} \rangle \sqrt{M_{\text{c}} \frac{\rho_{\text{c}}}{\rho_{\text{s}}}}, \tag{6.19}$$

where M_{c} is the mass fraction of the convection zone and ρ_{s} and ρ_{c} are the densities at the surface and the top of the convection zone, respectively. The authors find that $\sqrt{M_{\text{c}} \frac{\rho_{\text{c}}}{\rho_{\text{s}}}}$ is of order 1 in their models. The distribution of $\langle v_{\text{c}} \rangle$ across the HRD including the BA-type supergiant regime is illustrated in Fig. 6.17. It is striking that the iso-contour lines in this region approximately follow lines of constant luminosity. To test the agreement between this theory and observations, a local linear trend was constructed from the model of Fig. 6.17, including all points between 3.5 and 5.8 in $\log L/L_\odot$ and between 3.77 and 4.23 in $\log T_{\text{eff}}$. Note that $\langle v_{\text{c}} \rangle$ drops to zero in the models below the lower limit of $\log L/L_\odot$. The comparison with the derived microturbulences is found in Fig. 6.18. The model trend matches the observations surprisingly well, even in terms of absolute values. Interestingly, $\langle v_{\text{c}} \rangle$ vanishes at $\log L/L_\odot = 3.34$ according to the trend derived from the models, which is close to the zero-point 3.47 ± 0.08 extrapolated from the linear trend fitted to the data.[1]

---

[1] 90% confidence-interval or $\Delta \chi^2 = 2.7$
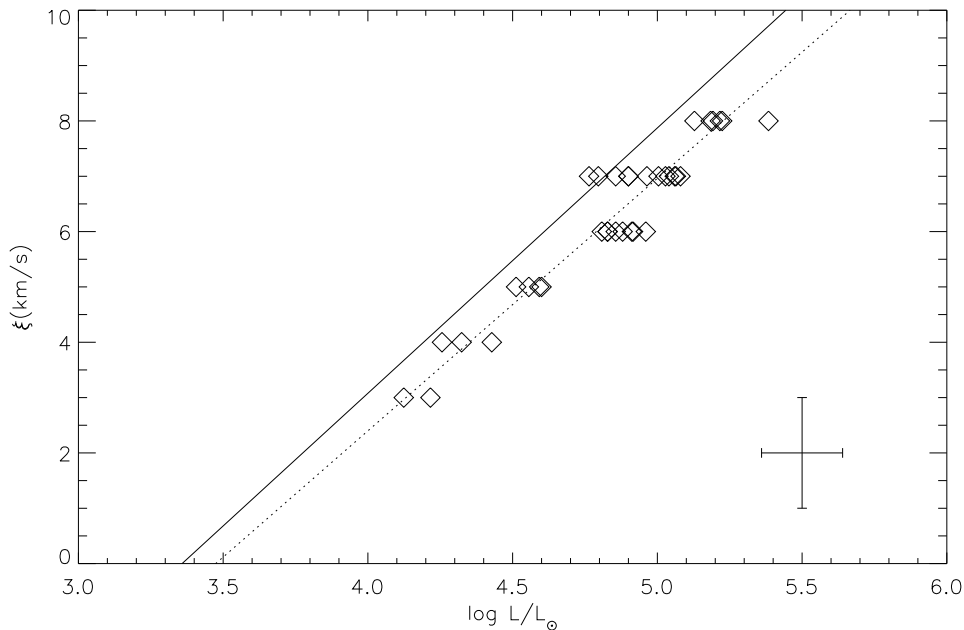
Figure 6.18: Comparison of the trend (dashed line) in the derived microturbulence values (diamonds) for our sample is compared to the trend (continuous line) in the data of Cantiello et al. (2009, compare Fig. 6.17) for the temperature range between $\log T_{\mathrm{eff}} = 3.77$ and 4.23. The cross in the bottom right corner illustrates typical errors in the parameter determination.

From a first glance also the lower luminosity objects analyzed by Landstreet et al. (2009) and the lower metallicity sample of supergiants in the Small Magellanic Cloud studied by Schiller (2010) match the predicted trends with luminosity and metallicity, continuing the astounding success of this theoretical approach for spectral types A and B.

Note, however, that there are some caveats:

- The accordance between the absolute values of ξ and $\langle v_{\mathrm{c}} \rangle$ is most likely a coincidence, as would be suggested by Eq. 6.19.

- The helium convection zone is neglected in the theoretical approach due to, among other things, the low convective velocities in it (for a discussion of this see Cantiello et al. 2009)

- The FeCZ is located deeper in BA-type supergiants than in the hotter objects originally examined, the effects of this are not quite clear yet.

Macroturbulence: The other velocity field introduced in the analysis, the macroturbulence, also shows some trends across the parameter range. The distribution of the derived values in the HRD is illustrated in Fig. 6.19. Slight trends towards higher values with increasing effective temperature and luminosity are visible.

The physical mechanism behind this parameter was recently investigated by Aerts et al. (2009). While non-radial oscillations were proposed as to explain macroturbulence before (Lucy 1976), this is the first quantitative study of this effect, albeit only for one line
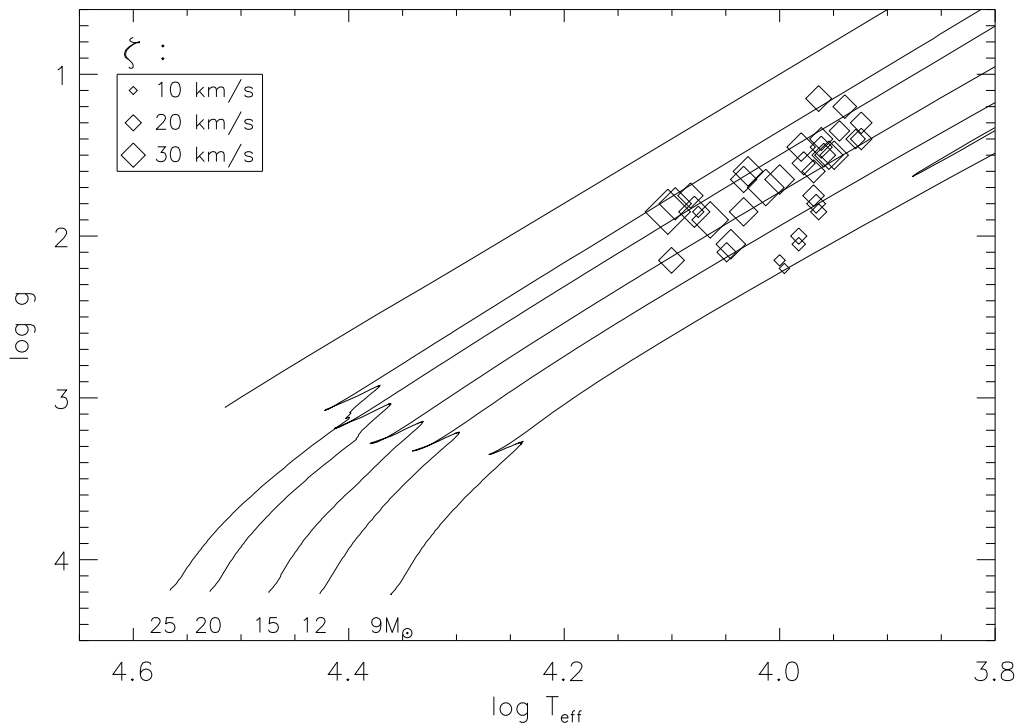
Figure 6.19: The distribution of the radial-tangential macroturbulence ζ over the $\log T_{\text{eff}}$-$\log g$-diagram, encoded by the symbol size. The values tend to increase toward higher masses and temperatures.

in one stellar object. Their conclusions are rather bleak: the derived macroturbulences are heavily entangled with the projected rotational velocity, and the actual value is time-dependent due to the nature of the oscillations and therefore rather arbitrary. If this theoretical framework proves to be successful, the macroturbulence should be viewed as a parameter introduced to reproduce the lineshapes, but not as a very significant indicator for stellar physics. Nonetheless, a comparison of the derived values with the largest such study of hotter B-type supergiants (Fraser et al. 2010) shows a continuation of their observed trend with effective temperature into the A-type regime (compare Fig. 6.20). Note that discrepancies between the two studies are expected, as they use a simple Gaussian to approximate the line profile of macroturbulence, while a radial-tangential profile was used here. Finding trends with temperature and luminosity, one could hope that the macroturbulence could still serve as a tracer for the strength of pulsations across the HRD, but Fig. 6.7 indicates that these trends rather stem from a correlation with $v \sin i$.

Projected Rotational Velocity: As the most recent stellar evolution models include the effects of rotation, they naturally also predict the evolution of the equatorial rotational velocity on the surface of massive stars. Indeed, the models of Meynet & Maeder (2003) were already successful in reproducing the drop in rotational velocities due to the bi-stability-braking at 22 000 K (Vink et al. 2010) and the subsequent evolution of rotational velocities in B-type supergiants (Fraser et al. 2010).
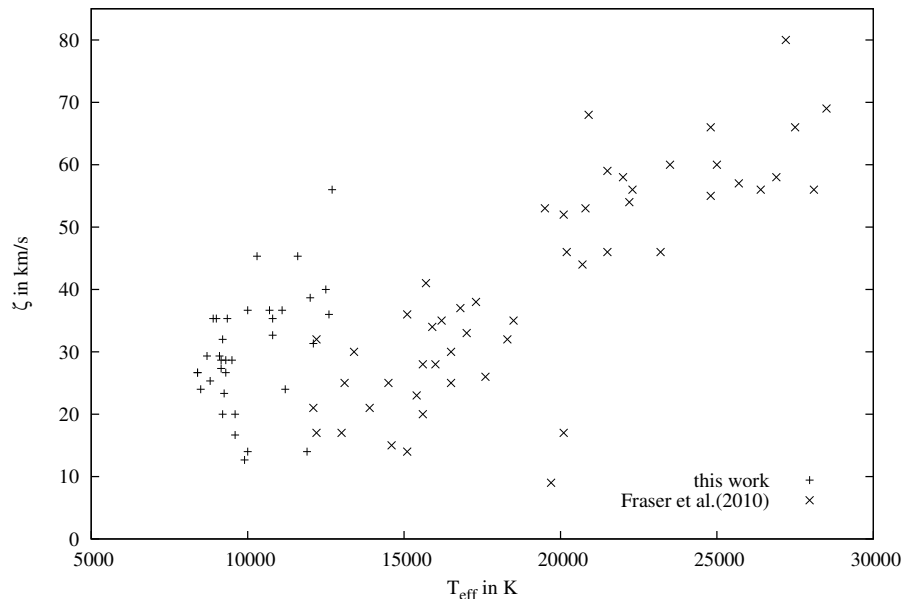
Figure 6.20: The macroturbulences derived in this study (marked +) compared to the values derived by Fraser et al. (2010) using a sample of 57 Galactic B-type supergiants (marked x), presented as a function of T_{eff}. The trend with temperature found in their study appears to continue in our data.

The models of Meynet & Maeder (2003) for an initial rotational velocity of 300 km/s are well suited for comparison with observations, as this value – considering that a significant slowdown is expected during the main sequence phase – is compatible with the average rotational velocity of 200 km/s derived by Huang & Gies (2006a) for 497 main sequence B-stars in Galactic clusters (see Fig. 6.14). Indeed, Dufton et al. (2006) find a peak at 250 km/s with a FWHM of 180 km/s for objects in two supposedly unevolved clusters. It is therefore reassuring, that the distribution of the projected rotational velocities, or more correctly the upper and lower limits derived in this study – scaled by $4/\pi$ to account for the average inclination angle – are matched reasonably well by the models (Fig. 6.21). In particular the predicted trend with decreasing T_{eff} appears to agree with observations. If one breaks the distribution down into different mass ranges, however, the predicted trend seems to be inverse to what is found in observations. Stars with higher M^{ZAMS} seem to rotate faster than their counterparts with lower M^{ZAMS}, contrary to model predictions. This trend is found in both the upper and the lower limits (see Fig. 6.22). Even if one mistrusts the macroturbulence formalism and the derived lower limits for the projected rotational velocity, the derived upper limits are hardly disputable, as any additional rotational broadening could not be hidden. Indeed, Fraser et al. (2010) also find surprisingly low projected rotational velocities for stars with $M^{\text{ZAMS}} < 15 M_{\odot}$ among their B-type-supergiants sample. The models of Heger & Langer (2000) seem to describe the data even less, as they predict higher rotational velocities overall.

At first glance, the distribution in Fig. 6.22 looks like one of the dichotomies in the parameters one expects to find in a composite population. In this case, the blue-loop-formation
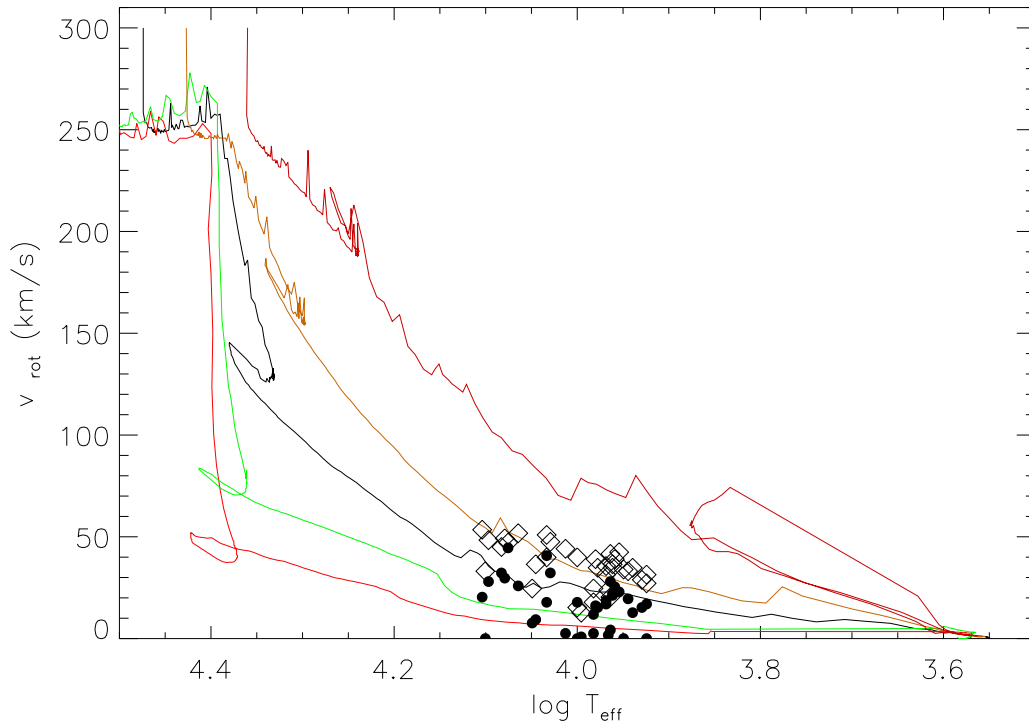
Figure 6.21: Evolution of the rotational velocity in the models of Meynet & Maeder (2003). From top to bottom: Models with initial masses of $9\,M_\odot$, $12\,M_\odot$, $15\,M_\odot$, $20\,M_\odot$ and $25\,M_\odot$. All models start with an initial velocity of $300\,\mathrm{km/s}$, and the velocity decreases as the star expands during the crossing of the HRD. Models with higher starting masses end up with lower rotational velocities. The $9\,M_\odot$-models experiences a spin-up during the blue-loop-phase. Also indicated are the upper limits v_u (open diamonds) and lower limits v_l (filled circles) of the projected rotational velocities of the sample stars, multiplied by $4/\pi$ to account for the average inclination angle.

should be responsible for the lower rotational velocities of the less massive stars. However, this is contrary to what is expected: the stars should experience a spin-up during the blueward motion in the HRD, that possible even increases the rotational velocity close to the break-up point (Heger & Langer 1998). The data of Heger & Langer (2000) suggest rotational velocities in excess of $100\,\mathrm{km/s}$ during the blue loop, and the $9\,M_\odot$-model by Meynet & Maeder (2003) in Fig. 6.21 also shows a spin-up in this phase.

Taking the timescales of the evolutionary scenarios into account, one can find a possible solution to the problem, which is in agreement with the models of Meynet & Maeder (2003). Looking at the post-MS evolution of the rotating and non-rotating models including blue loops (see Fig. 6.23), it seems reasonable to assume that the extent and duration of the loop decreases with $v_\mathrm{rot}^\mathrm{ini}$ (compare Eq. 6.11). The time spent on a loop is longer by orders of magnitude than the timescale of crossing the HRD. Thus it seems possible that the part of the HRD that contains the $9M_\odot$ and $12M_\odot$ tracks is mostly populated by stars with low $v_\mathrm{rot}^\mathrm{ini}$ that experience a blue loop – even if those objects only represent a small fraction of the $v_\mathrm{rot}^\mathrm{ini}$-distribution. This could explain the low average projected rotational velocity in this regime.
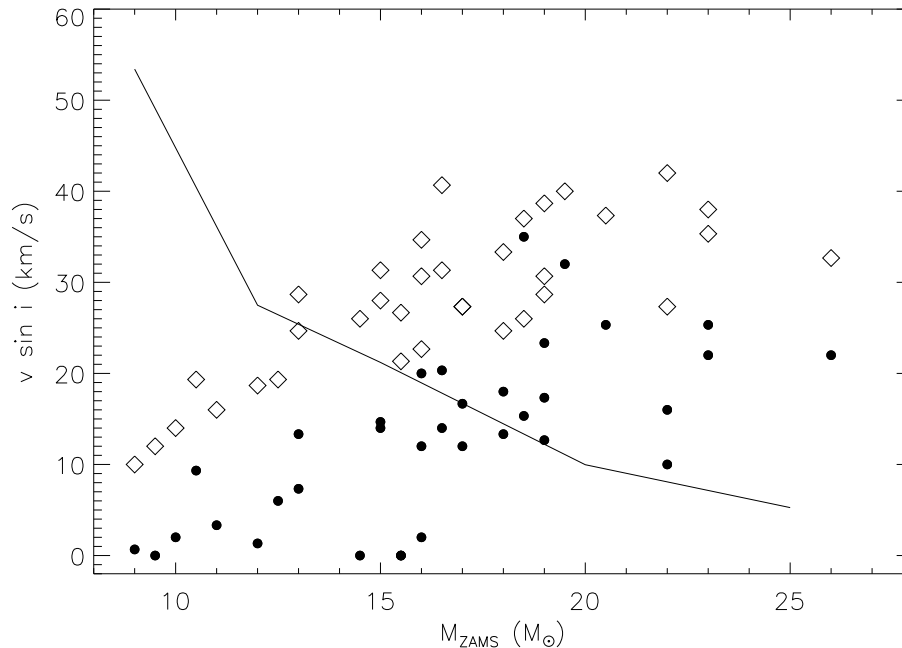
Figure 6.22: Comparison of rotational velocities of models starting with $v_{\rm rot}^{\rm ini} = 300\,{\rm km/s}$ (Meynet & Maeder 2003) at $\log T_{\rm eff} = 4.0$ (continuous line) with upper limits $v_{\rm u} \sin i$ (open diamonds) and lower limits $v_{\rm l} \sin i$ (filled circles) for the projected rotational velocities of the sample stars as a function of the zero-age-main-sequence mass $M^{\rm ZAMS}$, as derived from the position in the $\log T_{\rm eff}$-$\log g$-diagram (uncertainty $\approx 15\%$). The model predictions are scaled by $\pi/4$ to describe the average over all inclination angles.

Another possibility is a more efficient angular momentum loss of lower-mass progenitor stars on the main sequence. Indeed, Huang & Gies (2006a) find a steeper drop of rotational velocities from ZAMS to TAMS (terminal-age main sequence) in their intermediate-mass sample ($4\,M_\odot < M < 8.5\,M_\odot$) than in their high-mass sample ($8.5\,M_\odot < M < 16\,M_\odot$). This and the results of the present study could indicate that there is a change in the qualitative behavior of the angular momentum loss below a certain temperature, similar to what is proposed for B-type supergiants (e.g., bi-stability-braking is supposed to set in at $22\,000\,{\rm K}$ Vink et al. 2010), which is not incorporated in the models.

Conclusions for the Evolutionary Status

The indicators for the evolutionary status of the sample stars are multivariate functions, depending not only on age and mass, but also on the initial rotation rate, multiplicity and the previous history of the star. Despite the high accuracy in the abundance analysis, it appears to be difficult to disentangle the various effects. In particular, rotationally induced mixing, the efficiency of which is subject to considerable uncertainties, introduces a scatter into the predictions that makes it difficult to discern the possible signature of the first dredge-up. Nevertheless, the pros and cons of three formation scenarios for the observed BA-type supergiant population are summarized in the following:
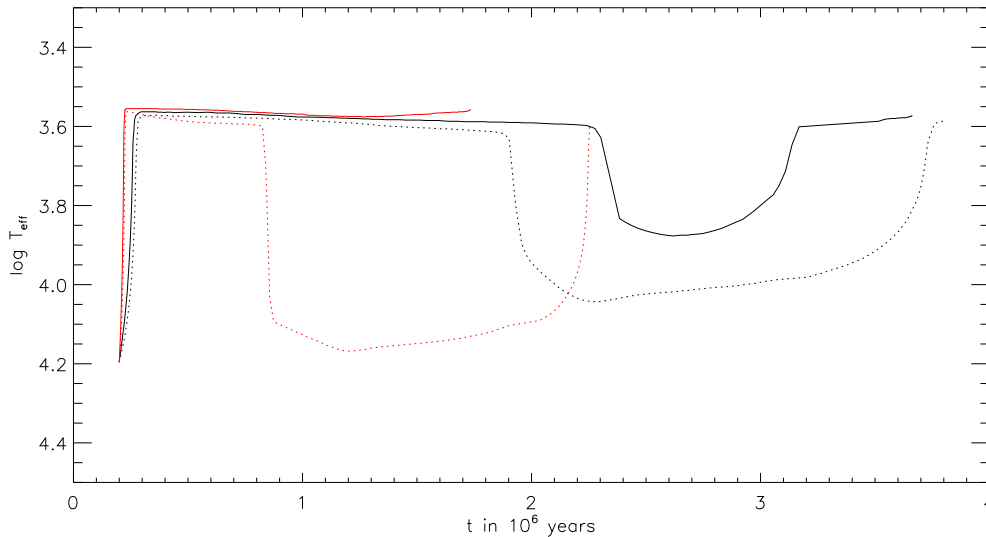
Figure 6.23: The time-evolution of the effective temperature after the star leaves the main sequence (models from Meynet & Maeder 2003). Shown are models with initial masses of $9M_\odot$ (black lines) and $12M_\odot$ (red lines); rotating models ($v_{\mathrm{rot}}^{\mathrm{ini}} = 300\,\mathrm{km/s}$) are represented by continuous lines, non-rotating models by dashed lines.

1. **Direct Evolution from the Main Sequence:**

   In this case, purely rotational-induced chemical mixing accounts for the signatures of the CNO-process found in the sample, as is suggested by the high mixing efficiencies of the models of Heger et al. (2000) or the models incorporating magnetic fields of Maeder & Meynet (2005). Nevertheless, this scenario seems to be precluded by the short timescales, on which current models that include rotation cross the HRD at solar metallicity. In addition, all sample stars show enhanced CNO-mixing compared to the reference B-star sample, which is not expected for slow rotators, of which some should exist. A more exotic variation of this scenario is the extension of the main sequence towards very low temperatures, which would mean that BA-type supergiants are still core hydrogen burning. This is predicted by models with a large overshoot-parameter (as discussed by Vink et al. 2010), and could naturally explain the abundance of hot B-type supergiants.

2. **Post-RSG Evolution:**

   Here, every star has experienced a convective mixing in the envelope during the RSG-phase, as suggested by Salasnich et al. (1999), which would account for the helium and nitrogen enrichment observed in all sample stars. The large star-to-star scatter found in N/C and N/O is naturally explained by the distribution of initial rotation rates. Contrary to observations, however, a more pronounced signature of the CNO-process is expected in the most luminous objects. The predicted masses would be lowered due to the considerable mass-loss during the RSG-phase.

3. **Composite Formation of the Population:**

   This scenario is suggested by many evolutionary models, such as, e. g., the non-rotating models of Meynet & Maeder (2003). Two components are distinguished: on one hand stars with initial masses below a limit of $\approx 14\,M_{\odot}$, that evolve on extended blue loops, on the other hand stars above that limit, which have ignited core helium burning during the first crossing of the HRD, thereby prolonging the transition from blue to red. The first component provides the high amount of mixing observed in the less massive stars of the sample and maybe even explains their surprisingly low rotational velocities – as it is predicted that only stars with low initial rotational velocities pass through extended blue loops. The purely rotational-induced mixing of the second component yields more moderate mixing than a dredge-up scenario, which explains why no trend of increasing CNO-mixing with luminosity is found. Despite this, there remain some inconsistencies in this scenario. For example, the rotation rates required for sufficient mixing in the more luminous stars delay the ignition of helium core burning in current models until the RSG-phase.

However, none of the presented scenarios appears to provide a fully consistent picture of the population of Galactic BA-type supergiants within the framework of the current evolutionary models. Moreover, the comparison of theory and observations is complicated by the influence of the initial rotation rate not only on surface abundances but also on the predicted stellar evolution tracks. Population synthesis computations based on evolutionary models including mass-loss and rotation, that incorporate observed $v_{\mathrm{rot}}^{\mathrm{ini}}$-distributions, could be helpful to shed more light on this topic, but are not available at this time. Despite the ambiguity in the conclusions, it is clear that the current understanding of massive star evolution is insufficient to reproduce the properties of Galactic BA-type supergiants in detail, for example the distribution of rotation rates. Consequentially, there is hope that the results of this study help to calibrate future evolutionary models.

7 Observational Constraints on Galactochemical Evolution

The study of Galactochemical evolution (GCE) connects the nucleosynthesis of elements occurring in stars with the evolution of the chemical composition of a galaxy by investigating the transformation of gas into stars and vice versa. The results improve our understanding of the formation and evolution of the MilkyWay – and thereby spiral galaxies in general. They also allow conclusions about stellar nucleosynthesis, which is constrained in a statistical way.

The quantitative spectroscopy of Galactic BA-type supergiants can help with this endeavor by deriving the abundance gradients of several elements in the Milky Way. Indeed, all massive stars can act as tracers for the current interstellar medium (ISM) due to their short life-times and the proximity to regions of active star formation, thereby putting constraints on Galactochemical calculations. At the same time they play an active role in the Galactochemical evolution by enriching the interstellar medium with nuclearly processed material through stellar winds and supernovae events. Studying massive stars can therefore constrain both the input and the output of Galactochemical calculations.

In this chapter a short overview of the basic equations and ingredients of GCE is given, as they are described, e.g., by Matteucci (2004) or Pagel (1997), before discussing some of the more recent developments and possible observational constraints. Then the abundance gradients derived from the study of BA-type supergiants are presented and compared to results of studies using other tracers and to GCE-model predictions.

7.1 Models of Galactochemical Evolution

Early models of chemical evolution in the solar neighborhood considered a closed uniform system without inflows or outflows and a primordial composition of the initial gas and instantaneous recycling of the enriched matter produced in stars. This so-called *simple model* still allows insights into the field. Modern GCE-models usually describe the Galactic disk as divided into a number of annuli, and their various levels of sophistication can include interaction with the intergalactic medium (IGM) and the Galactic halo, radial mixing of stars and gas, changing stellar yields and lifetimes with metallicity or the inclusion of results from Cold Dark Matter models. Most details are beyond the scope of this introduction, and the next few sections concentrate on the basic principles that all models have in common and some of the major differences. The number of models discussed will be limited to some of the more recent ones that make relevant predictions.

7.1.1 Equations of the Matter Cycle

The matter flows in galaxies can be sketched with a few integro-differential equations that describe a single cell of a GCE-model. First of all the total mass consists of matter in the form of stars M_s and gas M_g:

$$M_\mathrm{tot} = M_\mathrm{s} + M_\mathrm{g}. \tag{7.1}$$

The chemical composition of the gas can be written down analogously to the notation introduced for stars:

$$X_i = \frac{M_i}{M_\mathrm{g}}, \sum_i X_i = 1, \tag{7.2}$$

where M_i is the mass in the form of the specific element i. Usually the models start without stars and a primordial composition of the gas (ratios from Big-Bang-nucleosynthesis), but also a pre-enriched IGM can be used, e. g., Schönrich & Binney (2009a). The change in the amount of mass found in stars is governed by

$$\frac{dM_\mathrm{s}}{\mathrm{d}t} = \psi - e, \tag{7.3}$$

where ψ is the star formation rate (by mass) and e the rate at which dying stars restore material into the ISM. For the time evolution of the gas mass, additional flows of material into and out of the region have to be considered:

$$\frac{dM_\mathrm{g}}{\mathrm{d}t} = -\psi + e + F - E, \tag{7.4}$$

where F is is the inflow rate and E the ejection rate. The exchange can be with the IGM or adjacent cells of the model.

The driving force behind the chemical evolution of galaxies is the exchange of matter between stars and interstellar gas. The crucial factor hereby is the star formation rate ψ. Schmidt (1959) suggested that the star formation rate is proportional to some power of the surface density σ_g of the gas mass:

$$\psi = \nu \sigma_\mathrm{g}^k, \tag{7.5}$$

where ν is the efficiency of star formation per unit of time. This is the most widely adopted formulation. The surface gas density was originally chosen as a parameter because it is more easily measured than the volume gas density. Kennicutt (1998) found that $k = 1.4$ describes the observational data well (the star formation rate is commonly inferred from the counts of luminous stars, or alternatively from UV or far-IR fluxes associated with star formation). GCE-models often implement modifications to the simple picture, based on physical considerations: For example Chiappini et al. (2001) introduce a minimum threshold for the surface gas density, below which no star formation occurs, whereas Schönrich & Binney (2009a) differentiate between cold gas and warm gas, the latter not being involved in the formation of stars. Note, however, that there are other more complicated approaches to star formation laws, e. g., by incorporating Galactic rotation constants.
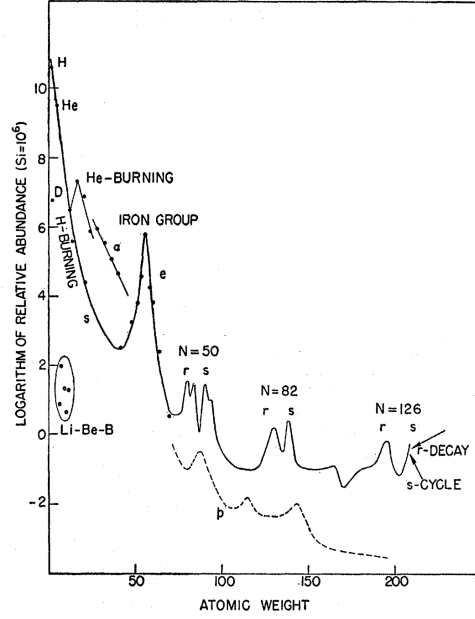
Figure 7.1: Schematic abundance curve as a function of atomic weight, taken from Burbidge, Burbidge, Fowler, & Hoyle (1957). The major processes forming the elements (α-, e-, s-, and p-process) are all indicated, see the text for more details. The p-process was later identified as being based on photodisintegration of heavy nuclei.

The star formation rate determines how much gas is converted into stars. The rate of the reverse process – the stellar ejection rate $e(t)$ – can be written as:

$$e(t) = \int_{m(\tau=t)}^{\infty} (M - M_{\mathrm{rem}})\psi(t - \tau(M))\varphi(M)dM, \qquad (7.6)$$

where $m - M_{\mathrm{rem}}$ is the total mass ejected from a star of mass m, $\tau(m)$ is the lifetime of a star of mass m and $\varphi(m)$ the *initial mass function* (IMF) and t is the time since the moment of star formation. This equation expresses the fact that the return of processed material depends on past star formation rates – the star formation history. Another important ingredient is the IMF, which is a probability distribution function often approximated by a normalized power law:

$$\frac{\mathrm{d}N}{\mathrm{d}m} \propto \varphi(M) = aM^{-(1+x)}, \qquad (7.7)$$

where a is a normalization constant. It simply controls the mass distribution of newly formed stars. The IMF is commonly derived from the present-day mass function, as obtained by star counts, which must involve a mass-luminosity relation and the consideration of stellar lifetimes. The slope $x = 1.35$ given by Salpeter (1955) is still widely in use.

7.1.2 Stellar Yields and Nucleosynthesis

Stellar nucleosynthesis was firmly established, when Burbidge, Burbidge, Fowler, & Hoyle (1957) published their well-known paper "Synthesis of the Elements in Stars". Their detailed picture contains the general features of nearly all of the nuclear processes involved, and only very few entirely new aspects have been added in the last 50 years. Within the scope of this thesis, only a short overview within the context of GCE can be given.

The starting point of most models of chemical evolution is the pristine intergalactic matter, that contains only the light elements H, D, ^{3}He, ^{4}He, ^{7}Li produced during the Big-Bang. The bulk of nearly all other elements is produced in stars, with the notable exception of some light elements formed in spallation processes initiated by cosmic rays. Several key processes were identified, which allows to roughly group the elements according to the necessary environments for their formation in stars. The elements with mass number A from 12 to 60 are formed during the nuclear burning stages occurring before the end of the stellar lifetime (this includes the α-elements synthesized by α-capture). Only in massive stars all the nuclear fuels capable of releasing significant amounts of energy are ignited, until a maximum in binding energy is reached in medium-sized nuclei and an iron core is formed (the origin of the iron-peak is also known as e(quilibrium)-process). Elements heavier than the iron-group elements are produced by means of neutron capture, starting from iron seed nuclei. Two separate processes are distinguished: the s(low)-process and the r(apid)-process, so named because the neutron capture rate is either slow or rapid compared to the rates of β- decay. Both processes leave characteristic abundance patterns. The s-process is assumed to occur during quiescent He-shell-burning in both massive and intermediate mass stars, where the necessary intensity levels of the neutron fluxes are reached, whereas the r-process, which needs very intense neutron fluxes, is thought to occur during supernova explosions. The exact details, however, are still up to discussion.

After production, a sizable fraction of the nuclearly enriched material is returned to the ISM via supernovae, stellar winds and planetary nebulae. Essential parameters for GCE-models are the time delay between star formation and ejection and the exact chemical composition of the ejected material. The yield $p_i(m)$ of a certain species i from a star is given by

$$p_i(M) = \left(\frac{M_{\mathrm{ej,i}}}{M} \right). \tag{7.8}$$

From stellar evolution theory, it is reasonable to assume that the total ejected mass $M_{\mathrm{ej}} = M - M_{\mathrm{rem}}$ and the chemical composition of the ejecta are primarily a function of initial mass M, which is adopted in GCE-models.

While considerable effort went into the determination of the nucleosynthetic yields by evaluating models of stellar evolution and supernova explosions, they are still subject to significant uncertainties. Indeed, chemical evolution models are used to constrain them (François et al. 2004). Generally stars can roughly be divided into three groups:

1. low mass stars ($M < 0.8\ M_\odot$), which do not eject matter to the ISM but only lock up gas;

2. intermediate mass stars ($0.8\ M_\odot < M < 8\ M_\odot$), which contribute mostly to He, C, N, and to some s-process elements;
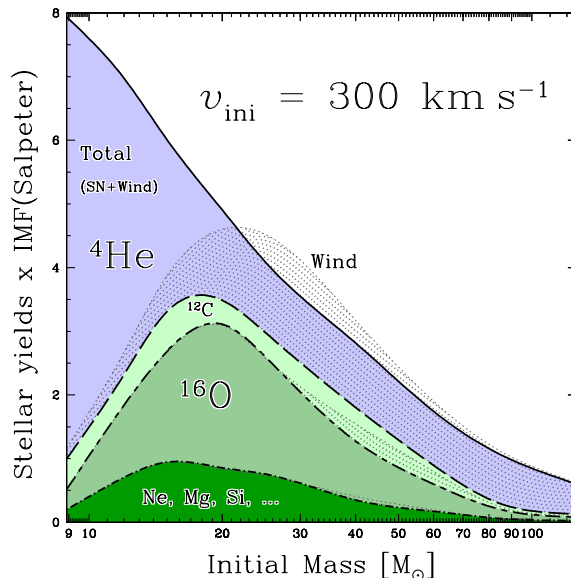
Figure 7.2: Mass fractions of the α-elements ejected as a function of initial masses convolved by a Salpeter evolution initial mass function, as computed from evolutionary models with solar metallicity including rotation. Dotted areas show the wind contributions, which for helium may be larger than the total yield, because some of it is destroyed in the supernova. From Hirschi et al. (2005).

3. massive stars ($M > 8\,M_\odot$), which are responsible for the formation of the bulk of elements, in particular α-elements (like O, Mg, Ne, Si, S, Ca, Ti) and some Fe-peak elements (Fig. 7.1.3).

The longer lifetimes of intermediate mass stars delay the injection of stellar matter processed by them into the ISM compared to the nearly instantaneous recycling of the massive star yields. Another important contribution comes from supernovae of type Ia, which produce a large amount of ^{56}Ni (which shortly turns into ^{56}Fe via two electron captures) and leave no remnant behind. Their progenitors are assumed to be C-O white dwarfs in close binary systems (but see Gilfanov & Bogdán 2010). They therefore fall into the intermediate mass range and thus their occurrence is delayed compared to the supernovae of type II, which mark the end of a short-lived massive star.

7.1.3 Required Constraints

While the amount of parameters in models of Galactochemical evolutions typically increases with the degree of sophistication, they are also facing an ever-growing number of observations that provide more and better constraints. Most of these observational constraints are not part of this study and can not be discussed in great detail, but a short overview will be given, since the properties of GCE-models are defined by them.

A first demand on any chemical evolution model of the Milky Way is to reproduce the abundance pattern of the single star with the most complete set of abundance measurements, the Sun. The latest revision of the photospheric abundances, complemented by

meteoritic abundances, was presented by Asplund et al. (2009). These values also represent the abundance pattern of the ISM 4.5 Gyr ago at the radius where the Sun was born. Also of major importance are detailed studies of the stellar population in the solar neighborhood, like for example the GenevaCopenhagen survey (GCS) published by Nordström et al. (2004) and Holmberg et al. (2007), which presents ages, metallicities, and kinematic properties of 14 000 F and G dwarfs. Many constraints are derived from the composition of the solar neighborhood. GCE-models try to reproduce, e.g., the metallicity distribution, the age-metallicity relationship and the evolution of abundance ratios, the latter being encoded in diagnostic diagrams like [Fe/O] vs. [Fe/H].

The observed properties of the solar neighborhood had direct consequences on the development of GCE models. For example, it was found that a simple closed-box model leads to an excess of metal-poor stars compared to the observed metallicity distribution of nearby long-lived stars like G-dwarfs: the so-called "G-dwarf problem"(e.g. Pagel 1997) This problem is now generally solved by introducing a continual accretion of gas from intergalactic space, that most commonly takes the form of an exponential:

$$F(t) = A\mathrm{e}^{-t/B}, \tag{7.9}$$

where B is the timescale (typical several Gyr) and A is a normalization constant, chosen so that the integrated inflow yields the present-day density profile.

Another important constraint that had to be met is the dichotomy found between thick disc and thin disc populations. The division of the disk into two components was first identified by Gilmore & Reid (1983), who found that the vertical density profile obtained by star counts can be described by a multi-component stellar population model consisting of two separate disk components and a halo. The so-called *thick disk* is characterized by a high velocity dispersion, old age and high [α/Fe], all compared to the *thin disk*. This distinction lead to models that separated the halo/thick disk evolution from the thin disk evolution, as, e.g., in the two-infall approach (Chiappini et al. 1997, 2001; Cescutti et al. 2007). In this, Eq. 7.9 is replaced by two components, a rapid first gas infall ($B \approx 1$ Gyr) that forms the thick disk and the halo, and a slower, delayed second infall ($B \approx 8$ Gyr) that forms the thin disk. Star formation halts in between these two major episodes (see Fig. 7.9).

A very successful recent model developed by Schönrich & Binney (2009a) introduces kinematic effects in the form of radial mixing of stars into models of Galactochemical evolution. With this, it can reproduce the properties of the thin and thick disk-components including the bimodality in [α/Fe] without any artificial dip in the star formation rate (Schönrich & Binney 2009b). Furthermore, the simultaneous modelling of chemistry and kinematics allows interesting new sorts of comparisons to observation.

7.2 Observational Constraints

A lot of constraints for models of Galactochemical evolution were mentioned, but the constraints examined in this study were so far unstated: the elemental abundance gradients along the Galactic disk. The most successful recent models of GCE differ a lot in their
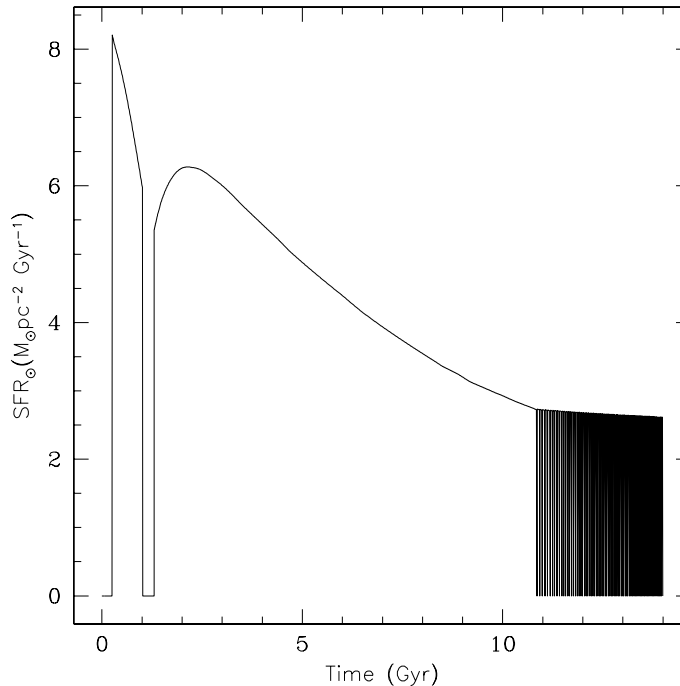
Figure 7.3: Predicted star formation rate in two-infall models with a threshold in gas density. There is a hiatus between the formation of the halo/thick disk and that of the thin disk. The threshold also leadds to the oscillations in the last phase. From Chiappini et al. (2001).

methods to include and simulate abundance gradients of the ISM. On one hand Chiappini et al. (1997) and the succeeding studies of Chiappini et al. (2001) and Cescutti et al. (2007) use the inside-out scenario of Galaxy formation, i.e., the infall rates decrease with increasing Galactocentric radius, to ensure the formation of abundance gradients. The individual annuli of the disk are, however, not connected in any way. On the other hand Schönrich & Binney (2009a) model a radial gas inflow, which connects adjacent annuli and transports enriched matter from the outskirts of the disk to the center. Curiously, the abundance gradients of the current ISM in the models differ by a factor of two. The model of Cescutti et al. (2007) successfully reproduces the slopes of a number of elemental abundance gradients as given by one of the largest observational data sets, the combined Cepheid sample of Andrievsky et al. (2002b,a, 2004, 2002c) and Luck et al. (2003) (hereafter AL4). In contrast, Schönrich & Binney (2009a) use abundance gradients from other sources (e.g., Rolleston et al. 2000; Shaver et al. 1983), that indicate steeper gradients of the ISM, to constrain the parameters that govern the radial gas flow. Obviously further observational constraints are needed concerning the abundance gradients of the ISM.

This study introduces the use of new tracers for the current abundance gradient of the ISM – BA-type supergiants. In the next few sections the derived abundances and distance estimates are discussed, before the suitability of the sample stars as tracers of the current ISM is examined. Finally the resulting abundance gradients are presented and compared to other observations and model predictions.
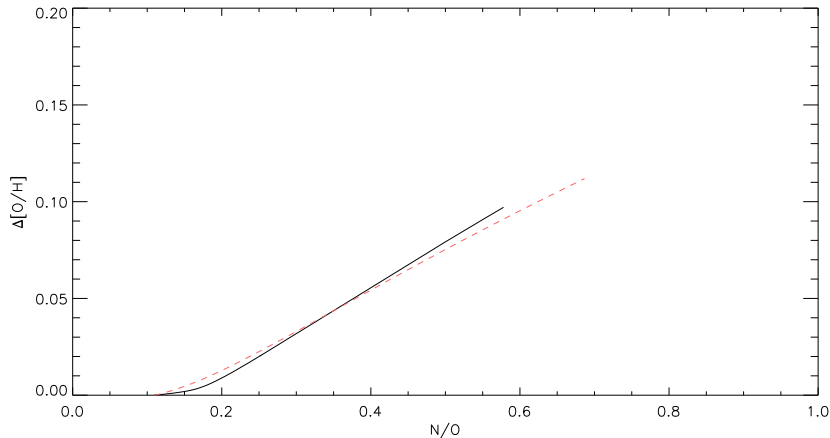
Figure 7.4: Predictions for the amount of oxygen depletion Δ (O/H) vs the spectral indicator N/O from evolution calculations, for a rotating $15M_\odot$ star ($v_{\mathrm{rot}}^{\mathrm{ini}} = 300\,\mathrm{km/s}$, Meynet & Maeder (2003) until the end of He burning: continuous line) and for a star of the same mass and $v_{\mathrm{rot}}^{\mathrm{ini}} = 300\,\mathrm{km/s}$ that in addition takes the interaction of rotation and a magnetic dynamo into account (Maeder & Meynet (2005); until the end of the MS: dashed line), respectively. The construction of a linear approximation seems reasonable in the relevant range ($N/O = 0.25\ldots0.9$, models with higher mass continue the trend).

7.2.1 Abundances

Many lines were analyzed to derive the abundance gradients and the individual results are listed in the Appendix. Most details of the abundance analysis are too tiresome and redundant to be discussed here, but some characteristics and peculiarities of the abundance analysis will be outlined in the following.

The surface abundances of several elements were examined in this study, but only some are useful for investigating spatial abundance patterns in the ISM. The abundances of carbon and nitrogen, presented in the previous chapter, are not suited for this task, since they show large scatter due to mixing of the stellar atmospheres with nuclear-processed matter from the core. In principle, the oxygen abundances are also affected, although to a minor extent. As the oxygen abundances show only minor scatter across the sample and are amongst the most accurate, it was decided to construct a correction scheme from evolutionary models. This seems reasonable, since the models of Meynet & Maeder (2003) fit the N/C vs N/O distribution of the stars very well (compare Fig. 6.15b). As Fig. 7.2.1 shows, it is possible to approximately calculate the evolutionary correction $\Delta(O/H)$ by a linear relation:

$$\Delta(O/H) = (N/O - 0.11) * c_{\mathrm{O}}, \tag{7.10}$$

where $c_{\mathrm{O}}=0.19$, the average of the slopes of the magnetic and non-magnetic $15\,M_\odot$-models, has been adopted. Models of other masses can slightly deviate, the largest discrepancy is seen in the $15\,M_\odot$-model with $c_{\mathrm{O}} = 0.22$. Note that the gradient was computed both with and without correction and both approaches give well-defined gradients.

As was explained in the discussion about the Mg I/II ionization equilibrium, a few weak Mg I-lines were excluded from the analysis in the objects indicated in Fig 5.3. The magne-
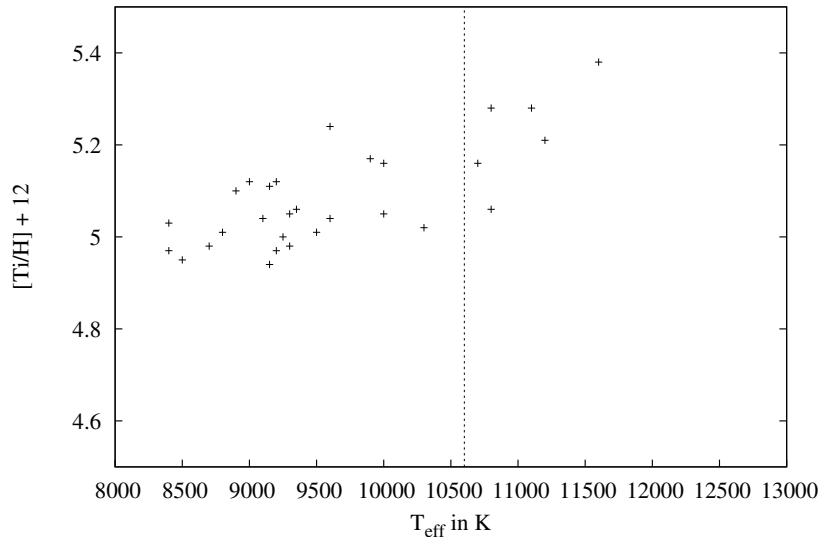
Figure 7.5: The surface titanium abundances as a function of T_{eff}. A clear trend is visible, indicating major systematic uncertainties. The line at $10\,600$ K represents the cut-off temperature, above which the stars were excluded from the calculation of the abundance gradient.

sium abundances show low line-to-line scatter apart from those few lines and no significant trend with effective temperature, and are therefore considered reliable.

This is different for the titanium abundances, as displayed in Fig 7.2.1. Titanium is therefore the only element, for which a significant trend with temperature is found, indicating the presence of residual systematics in the abundance determination. This trend is present over the whole parameter range, but is especially pronounced at high temperatures. To at least reduce the systematic effects introduced by the temperature dependency of the abundance analysis, the stars with $T_{\text{eff}} > 10600$ K were excluded from the determination of the abundance gradient, which is only a minor loss, as many of the hotter stars only show weak Ti II-lines or no Ti II-lines at all. In addition to this problem, the line-to-line scatter is the largest of all elements, which indicates significant uncertainties from within the model atom, and the sensitivity to atmospheric parameters is extreme. Considering all this, it is not surprising, that the constraints for the Ti-gradient are the weakest, indicating the presence of residual systematics in the abundance determination.

The derived sulfur and iron abundances show no such peculiarities. It should be noted that, in the case of iron, the metallicity of the ODFs was reduced by a factor of two for stars below $11\,800$ K. These objects show a very rich Fe II-spectrum, which is responsible for a significant part of the total opacity. Thus this measure was proposed by Przybilla et al. (2006) to avoid an overestimate of the total opacity in the models, since the ODFs include the effects of Fe II.

7.2.2 Distance Determination

Accurate distances to BA-type supergiants would help to better constrain their masses, luminosities and other fundamental parameters. Unfortunately even the closest of these stars is still too far away to get accurate astrometric measurements of the *trigonometric parallax* – the most fundamental method of distance determination in stellar astronomy, which forms the basis of the cosmic distance ladder. The distance d of an object with a trigonometric parallax of π is

$$d = 1/\pi, \tag{7.11}$$

where d is measured in pc and π in arcseconds.

Note that the luminosities of the sample stars were already derived in Chapter 5 via the empirical FGLR – which in itself is based on the estimated distances of nearby galaxies, typically derived from the well known period-luminosity relationship for Cepheids. To transform this luminosity into a distance, some more calculations are necessary.

The apparent magnitude m and the absolute magnitude M of a star are connected to the distance via the so-called *true distance modulus*

$$(m - M)_0 = 5 \log d - 5.$$

The absolute magnitude is defined to equal the apparent magnitude of an object at a standard distance of 10 pc. However, to complicate things, the distance modulus is affected by reddening and absorption by interstellar matter, which shifts and redistributes the stellar flux. To account for that, the *apparent distance modulus*

$$(m - M) = 5 \log d - 5 + A \tag{7.12}$$

includes the interstellar extinction A between object and observer. This quantity can be estimated from the difference between observed and theoretical color indices (the latter derived from synthetic spectra), the so-called *color excess*. In this study Johnson B and V are used:

$$E(B - V) = (B - V) - (B - V)_{\text{theo}}. \tag{7.13}$$

Using a standard reddening scheme, extinction and color excess are related via

$$A_V = R_V \times E(B - V), \tag{7.14}$$

where the proportionality constant R_V is called the total-to-selective extinction ratio. Determining this quantity was possible during the analysis of the spectral energy distribution, the results – which have direct consequences for the distance – are discussed in one of the next sections.

In a next step, the absolute visual magnitude M_V is derived from the absolute bolometric magnitude M_{bol} via

$$M_{\text{bol}} = M_V + B.C. \tag{7.15}$$

For this, the bolometric corrections $B.C.$ – connecting the visual flux with the absolute flux – must be known, which are derived in the next section. Finally, the distance to the star can be derived:

$$(m_V - M_V) = 5 \log d - 5 + A_V, \tag{7.16}$$

given the apparent visual magnitude m_V is known from observation.

Additionally to this empirical distance scale, a theoretical spectroscopic distance scale can be constructed, using the masses M_{evol}, derived from evolutionary models earlier, and the Eddington flux H_ν at the *effective* frequency for the Johnson V filter, determined for each object via the synthetic fluxes. The flux at earth f_ν and the flux at the star F_ν are related by

$$\frac{f_\nu}{F_\nu} = \frac{R^2}{d^2} \tag{7.17}$$

due to flux conservation. The calibration of Bessell et al. (1998),

$$f_\nu = 3.636 \times 10^{-20} \times 10^{-0.4m_0}, \tag{7.18}$$

is used to transform $m_0 = m_V - A_V$ – the apparent visual magnitude corrected for reddening – into the flux at earth (in cgs units). With $F_\nu = 4\pi H_\nu$ the distance transforms to

$$d = \sqrt{R^2 \frac{4\pi H_\nu}{f_\nu}}. \tag{7.19}$$

Using Eq. 6.17 to express R in terms of M and g yields

$$d = 7.06 \times 10^4 \sqrt{(M/M_\odot)H_\nu 10^{-0.4m_0 - \log g}} \tag{7.20}$$

for the distance in pc. Inserting the evolutionary mass in Eq. 7.20 results in a new distance estimate d_{evol}.

The differences between the two presented distance scales correspond to the differences between M_{evol} and M_{FGLR} discussed in the previous chapter, as both distances are functions of the stellar parameters T_{eff} $\log g$ and M, and only the estimate for M changes in both approaches. So once again, the major differences occur at high masses and luminosities, where the evolutionary tracks predict more massive, luminous and therefore more distant stars, while there is good agreement in the low-to-mid mass range. All the derived distances are listed in Table 7.1. Tests using both distance scales to determine abundance gradients show only marginal differences in the results, which more often than not would not even show in any significant digit. Therefore the empirical distance scale based on the FGLR is used throughout the rest of the work.

To study the abundance patterns of the Milky Way in a suitable set of coordinates, the position of the stars is expressed in Galactocentric coordinates X, Y and Z, a non-rotating frame of reference with the Galactic center at the origin, X and Y spanning the plane of the Galactic disk, and the Galactic north pole in Z-direction. Following these measurements, the Galactocentric radius is defined as

$$R_{\text{g}} = \sqrt{X^2 + Y^2 + Z^2}. \tag{7.21}$$
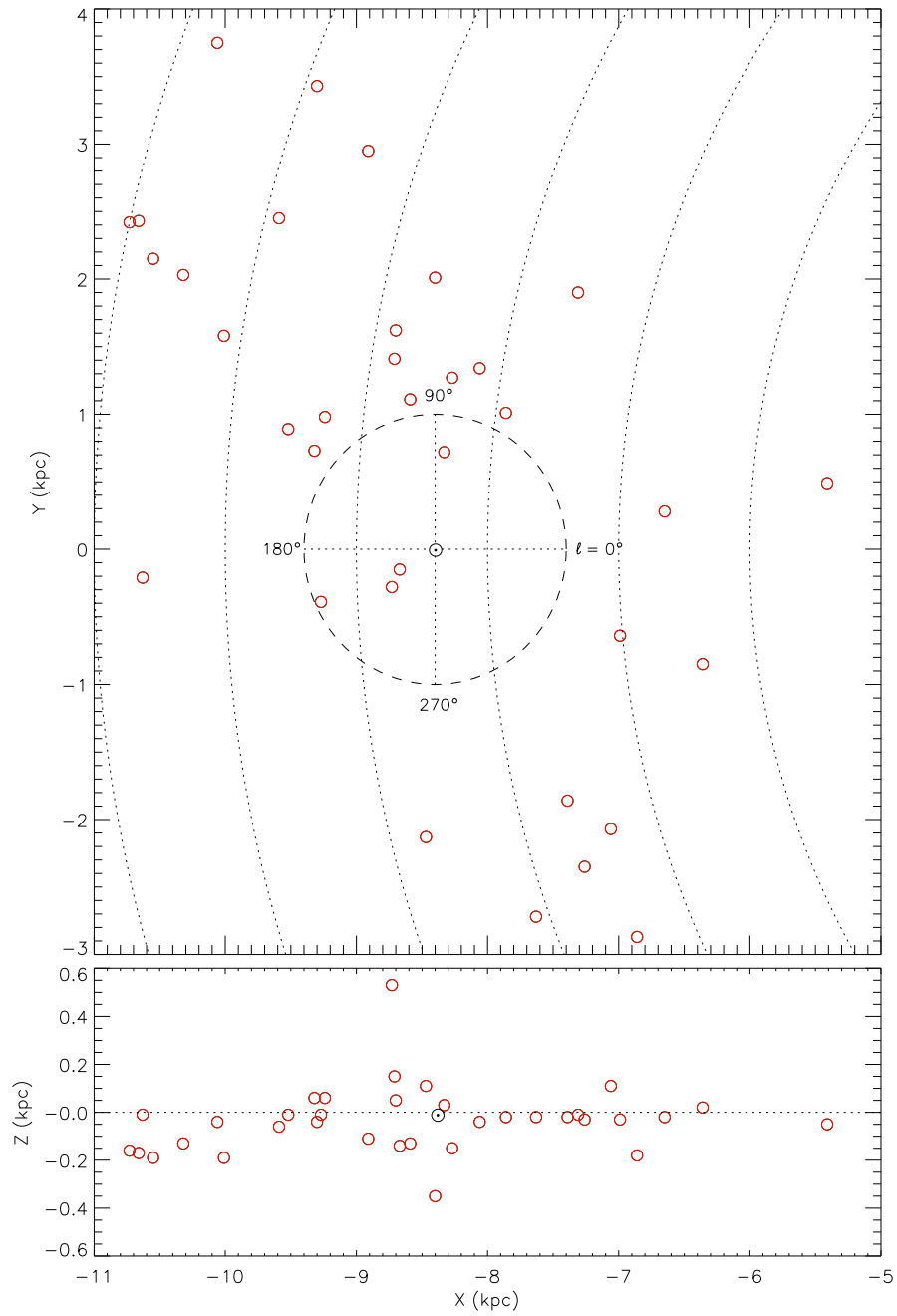
Figure 7.6: Positions of the sample stars (circles) and the Sun (⊙) in Galactocentric coordinates X, Y and Z. The dashed lines in the upper panel mark circles of equal distance to the Galactic center.
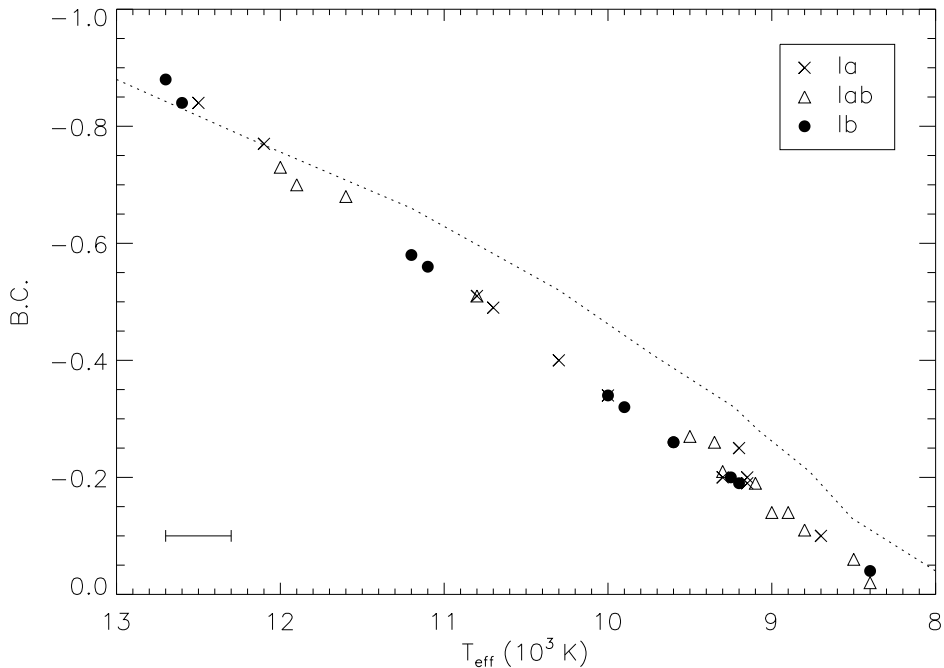
Figure 7.7: Comparison of bolometric corrections determined here for the individual sample supergiants with the relation given by Schmidt-Kaler (1982, dotted line). A typical error bar is indicated.

The position of the Sun is determined by its distance from the Galactic center, which in recent years converged to R_0=8.4 kpc in the literature: Ghez et al. (2008) give a value of 8.4 ± 0.4 kpc and Gillessen et al. (2009) 8.33 ± 0.35 kpc, both using long-term observations of stellar orbits, while Reid et al. (2009) estimated 8.4 ± 0.6 kpc based on the measurement of trigonometric parallaxes of masers throughout the galaxy. The Sun's current position is therefore set to be $X = -8.4$ kpc, $Y = 0$ and $Z = 0$ in this work. Note, however, that sometimes $X = -8.0$ kpc – which is widely adopted – will be used for the purpose of comparison with the literature. Given the coordinates of the stars in the sky, the position of the Galactic center, and the distances, the Galactocentric coordinates can be computed. The results are given in Table 7.1 and displayed in Fig. 7.6. Since the crucial distance estimates contain corrections for interstellar reddening based on the values of R_V and $B.C.$, the methods to derive these quantities and their distribution in the sample are discussed the next two sections.

Bolometric Correction

Closely related to the spectral-type–T_{eff} relation is the question of the behavior of bolometric corrections with spectral type, or more precisely, with effective temperature. The bolometric corrections were determined from the model fluxes for each individual star. Following the approach of Bessell et al. (1998) an absolute solar bolometric magnitude
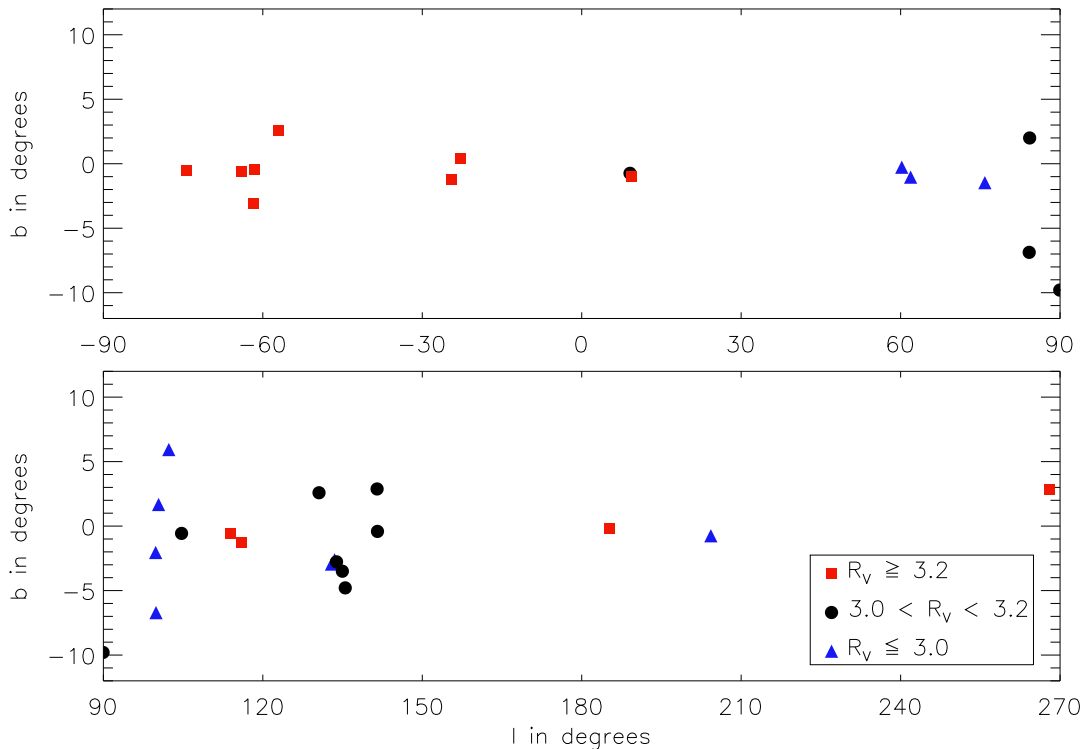
Figure 7.8: The distribution of our sample stars in the Galactic plane, coded according to the legend for the respective values of the total-to-selective extinction ratio R_V along the line-of-sight. Galactic coordinates l and b are used, note that two stars fall outside the displayed range, HD 34085 and HD 87737, which are located at higher Galactic latitude.

$M_{\mathrm{bol},\odot} = +4.74 \, \mathrm{mag}$ and a zeropoint flux $f_{\nu,0} = 3.636 \times 10^{-20} \, \mathrm{erg \, cm^{-2} \, s^{-1} \, Hz^{-1}}$ for Johnson V were adopted. The bolometric correction is then given by

$$B.C. = M_{\mathrm{bol}} - M_V = C - 10 \log(T_{\mathrm{eff}}/T_{\mathrm{eff},\odot}) + 2.5 \log H_\nu \,, \qquad (7.22)$$

where $C = 12.854$ for a solar radius $R_\odot = 6.95 \times 10^{10} \, \mathrm{cm}$. The resulting theoretical bolometric corrections deviate less than $0^{\mathrm{m}}03$ from a recent analytical fit formula given by Kudritzki et al. (2008 their Eq. 6) for solar metallicity.

The derived values are compared to the reference calibration of Schmidt-Kaler (1982 for stars of luminosity class Iab) in Fig. 7.7. In order to adjust for the different zeropoints used, we correct our values by $-0^{\mathrm{m}}12$[1]. The remaining differences can reach values up to $0^{\mathrm{m}}13$. A general trend towards larger $B.C.$-values is seen in our data, except for the hottest objects in the sample, which have slightly lower bolometric corrections.

---

[1] Schmidt-Kaler (1982) gives a solar bolometric correction of $-0.19 \, \mathrm{mag}$, whereas the value provided by Bessell et al. (1998) is $-0.07 \, \mathrm{mag}$

7.2.3 The Ratio of Total to Selective Extinction

The total to selective extinction ratios R_V are usually investigated by using early-type stars as background light sources, facilitating to study absorption and scattering by the intervening interstellar material. Therefore the R_V along the line of sight can be derived during the comparison of theoretical and observed SEDs of BA-type supergiants.

The R_V-values (see Table 7.1) are displayed in Fig. 7.8, as a function of position in the Galactic plane. High uncertainties are to be expected for low values of $E(B-V)$ (≤ 0.1). The standard value of $R_V = 3.1$ (e.g. Savage & Mathis 1979) was adopted, when no reliable estimates were possible. Another error source are the rather high uncertainties ($\approx$ 0.2 mag) attached to *some* magnitudes from 2MASS. Objects with higher values than the standard value are concentrated in the southern Milky Way around 260° to 360° Galactic longitude, and many objects with lower values in the opposite direction, at $l \approx 60$ to 110°. This is in good agreement with previous findings of Whittet (1977).

Of course the sample is too small to provide any significant extension to modern studies (see e.g. Winkler 1997; Wegner 2003), which consider hundreds of OB stars. Despite their rarity, however, BA-type supergiants are highly useful for probing lines-of-sight towards very distant (or highly reddened) objects in the Milky Way because of their much higher intrinsic visual magnitudes. Moreover, their usefulness for simple investigations like presented here extends to distances even far beyond the Milky Way (e.g. Kudritzki et al. 2008), and also for more sophisticated studies of the ISM in other galaxies based on high/intermediate-resolution spectroscopy (e.g. Cordiner et al. 2008a,b).

Table 7.1: Abundances and Locations of the Sample Stars.

#	Object	$\log X/\text{H}+12$				$E(B-V)$	R_V	$B.C$	d_{evol}	d_{FGLR}	X	Y	Z	R_{g}
		Mg	S	Ti	Fe	mag		mag	kpc	kpc	kpc	kpc	kpc	kpc
1	HD12301	7.42±0.07	6.97±0.07	. . . ±. . .	7.48±0.08	0.48±0.02	3.1	−0.72	1.31±0.19	1.30±0.23	−9.24	0.98	0.06	9.30±0.17
2	HD12953	7.39±0.11	6.95±0.04	4.97±0.09	7.30±0.07	0.58±0.02	2.9	−0.13	3.54±0.52	3.32±0.61	−10.66	2.43	−0.17	10.93±0.51
3	HD13476	7.45±0.04	6.96±0.05	4.95±0.06	7.47±0.08	0.59±0.02	2.8	0.06	2.90±0.43	2.80±0.50	−10.32	2.03	−0.13	10.52±0.41
4	HD13744	7.42±0.08	6.98±0.07	5.01±0.09	7.39±0.06	0.76±0.02	3.1	−0.15	3.53±0.98	3.36±0.94	−10.73	2.42	−0.16	11.00±0.79
5	HD14433	7.42±0.06	6.93±0.04	4.94±0.11	7.38±0.08	0.56±0.02	3.1	−0.07	3.24±0.47	3.05±0.55	−10.55	2.15	−0.19	10.77±0.45
6	HD14489	7.43±0.05	7.01±0.07	5.06±0.08	7.45±0.07	0.38±0.02	3.1	−0.14	2.38±0.35	2.23±0.41	−9.99	1.56	−0.19	10.11±0.33
7	HD20041	7.35±0.09	6.84±0.05	5.05±0.07	7.38±0.06	0.75±0.03	3.1	−0.22	1.48±0.22	1.43±0.26	−9.52	0.89	−0.01	9.56±0.22
8	HD21291	7.40±0.08	6.89±0.07	5.28±0.09	7.50±0.06	0.46±0.02	3.1	−0.39	1.23±0.18	1.18±0.21	−9.32	0.73	0.06	9.35±0.18
9	HD39970	7.36±0.09	6.86±0.06	5.02±0.09	7.40±0.07	0.43±0.02	3.5	−0.28	2.29±0.34	2.24±0.41	−10.63	−0.21	−0.01	10.63±0.41
10	HD46300	7.53±0.09	6.94±0.06	5.16±0.10	7.57±0.07	0.07±0.02	2.5	−0.22	0.96±0.14	0.96±0.18	−9.27	−0.39	−0.01	9.28±0.17
11	HD186745	7.50±0.13	7.02±0.08	. . . ±. . .	7.64±0.12	1.01±0.02	2.9	−0.72	2.34±0.34	2.19±0.39	−7.31	1.90	−0.01	7.55±0.10
12	HD187983	7.52±0.05	6.99±0.08	5.05±0.11	7.56±0.08	0.70±0.02	3.0	−0.08	1.33±0.37	1.31±0.37	−7.78	1.15	−0.02	7.87±0.12
13	HD197345	7.48±0.05	6.97±0.06	4.98±0.11	7.50±0.06	0.06±0.02	3.1	0.02	0.77±0.11	0.72±0.13	−8.33	0.72	0.03	8.36±0.00
14	HD202850	7.47±0.03	7.08±0.10	5.06±0.11	7.62±0.07	0.19±0.02	3.1	−0.39	1.31±0.19	1.29±0.23	−8.27	1.27	−0.15	8.37±0.01
15	HD207260	7.49±0.03	7.03±0.07	5.01±0.08	7.51±0.05	0.51±0.02	2.5	0.01	1.53±0.22	1.45±0.26	−8.71	1.41	0.15	8.82±0.10
16	HD207673	7.47±0.06	7.04±0.06	5.00±0.11	7.56±0.09	0.44±0.02	3.1	−0.08	2.06±0.30	2.04±0.36	−8.40	2.01	−0.35	8.64±0.09
17	HD208501	7.53±0.07	6.95±0.08	. . . ±. . .	7.55±0.10	0.82±0.02	2.7	−0.76	1.75±0.26	1.65±0.29	−8.70	1.62	0.05	8.85±0.10
18	HD210221	7.50±0.05	6.99±0.08	5.03±0.07	7.47±0.06	0.40±0.02	2.9	0.08	3.08±0.45	3.00±0.54	−8.91	2.95	−0.11	9.39±0.26
19	HD212593	7.45±0.05	7.01±0.04	5.21±0.10	7.59±0.07	0.17±0.02	2.8	−0.46	1.16±0.17	1.14±0.21	−8.59	1.11	−0.13	8.67±0.06
20	HD213470	7.48±0.05	6.97±0.08	4.97±0.12	7.46±0.07	0.54±0.03	3.1	0.10	3.73±0.55	3.55±0.64	−9.30	3.43	−0.04	9.92±0.37
21	BD+602582	7.43±0.09	6.88±0.09	. . . ±. . .	7.47±0.12	0.85±0.02	3.4	−0.58	4.28±0.63	4.10±0.73	−10.06	3.75	−0.04	10.74±0.51
22	HD223960	7.38±0.07	6.92±0.08	5.16±0.13	7.45±0.06	0.76±0.02	3.2	−0.37	2.89±0.42	2.73±0.49	−9.59	2.45	−0.06	9.90±0.32
23	HD195324	7.57±0.04	7.01±0.05	5.12±0.07	7.59±0.06	0.56±0.02	2.6	−0.07	1.36±0.20	1.38±0.25	−8.06	1.34	−0.04	8.17±0.02
24	HD34085	7.44±0.07	7.02±0.07	. . . ±. . .	7.56±0.09	0.05±0.02	3.1	−0.65	0.36±0.05	0.34±0.06	−8.67	−0.15	−0.14	8.67±0.05
25	HD87737	7.53±0.04	7.04±0.08	5.04±0.10	7.55±0.07	0.02±0.02	3.1	−0.14	0.69±0.10	0.68±0.13	−8.73	−0.28	0.53	8.75±0.07
26	HD91533	7.47±0.09	7.04±0.09	5.04±0.13	7.51±0.08	0.33±0.02	3.5	−0.07	2.90±0.43	2.83±0.51	−7.63	−2.72	−0.02	8.10±0.03
27	HD111613	7.48±0.05	7.05±0.06	5.11±0.12	7.53±0.06	0.39±0.03	3.5	−0.08	2.55±0.38	2.47±0.44	−7.06	−2.07	0.11	7.36±0.13
28	HD149076	7.50±0.06	7.16±0.06	5.28±0.09	7.64±0.05	0.56±0.02	3.5	−0.44	2.26±0.33	2.21±0.40	−6.36	−0.85	0.02	6.42±0.35
29	HD149077	7.54±0.05	7.05±0.06	5.17±0.09	7.61±0.06	0.53±0.03	3.5	−0.20	1.55±0.23	1.55±0.29	−6.99	−0.64	−0.03	7.02±0.25
30	HD165784	7.56±0.08	7.17±0.07	5.12±0.06	7.63±0.08	0.86±0.02	3.1	−0.02	1.83±0.27	1.77±0.33	−6.65	0.28	−0.02	6.66±0.32
31	HD166167	7.69±0.05	7.27±0.07	5.24±0.12	7.70±0.08	0.61±0.02	3.5	−0.14	3.01±0.44	3.03±0.56	−5.41	0.49	−0.05	5.44±0.54
32	HD80057	7.41±0.06	7.02±0.07	4.98±0.09	7.45±0.09	0.32±0.02	3.3	−0.09	2.19±0.32	2.14±0.39	−8.47	−2.13	0.11	8.74±0.11
33	HD102878	7.47±0.06	7.04±0.02	5.10±0.08	7.56±0.08	0.27±0.02	3.4	−0.02	2.68±0.39	2.61±0.47	−7.26	−2.35	−0.03	7.63±0.07
34	HD105071	7.52±0.06	7.13±0.08	5.53±0.08	7.66±0.09	0.28±0.02	3.7	−0.61	3.42±0.50	3.26±0.57	−6.86	−2.87	−0.18	7.44±0.05
35	HD106068	7.42±0.05	7.03±0.09	5.38±0.11	7.56±0.07	0.38±0.02	3.4	−0.56	2.19±0.32	2.11±0.38	−7.39	−1.86	−0.02	7.62±0.09
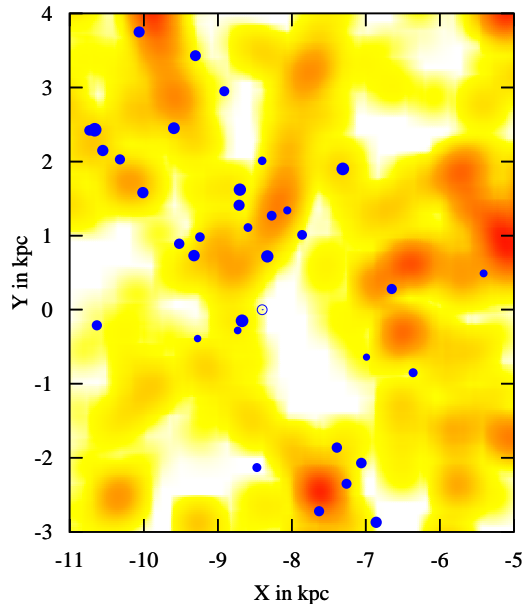
Figure 7.9: Map of the Galactic plane around the Sun using Galactocentric coordinates X and Y. The yellow and red colored areas indicate the distribution of the H II regions and GMCs as given by Hou et al. (2009), red representing the highest concentrations. The filled blue circles mark the positions of the BA-type supergiants. The symbol size encodes M_{ZAMS}, larger means more mass, and therefore younger. The position of the Sun is is also indicated ($\odot$).

7.2.4 BA-type Supergiants as Tracers for the ISM

One advantage of using massive stars as tracers for Galactic abundance gradients are their short lifetimes. Abundance studies of less massive stars normally encompass stars spread over a wide range of ages. As age determinations often bear large uncertainties, this makes it difficult to disentangle the history of Galactochemical evolution. The ages of massive stars are well constrained – we estimate the lifetimes of the least massive stars of our sample ($M_{\mathrm{ZAMS}} = 9\,M_\odot$) to approximately 40 million years from evolutionary model calculations. Thus, they only recently formed from interstellar gas, and clearly represent the current status in terms of GCE.

Comparison to H II Regions and GMCs

By using the sample stars to trace patterns in the current abundances of the ISM, we assume that the supergiants are close to their birth places. To confirm this assumption, the positions of the sample stars are compared to spiral tracer data of the Milky Way in Fig 7.9, which were collected by Hou et al. (2009), who kindly provided us with the numbers
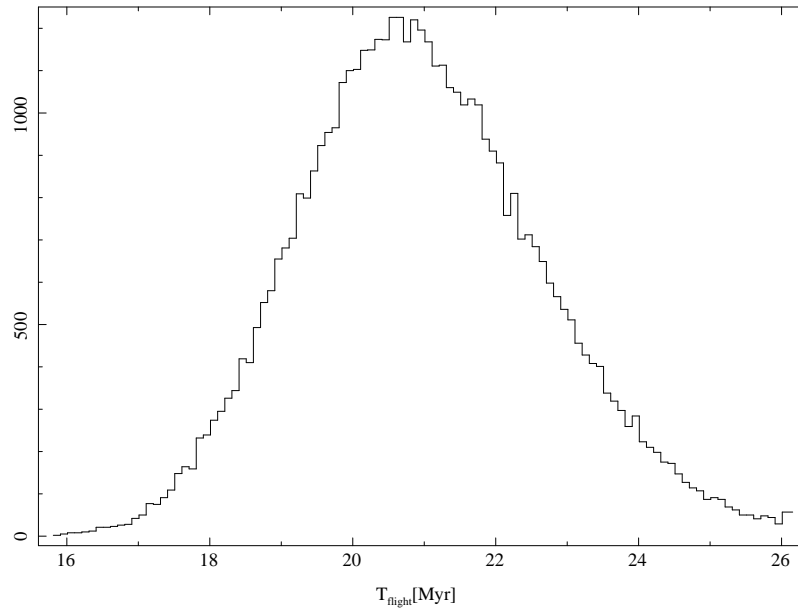
Figure 7.10: The distribution of resulting flight times from the Monte Carlo sample.

and a Fortran program for interpretation. The tracer data consist of H II regions and giant molecular clouds (GMCs), objects associated with recent and current star formation, respectively. The masses of the GMCs and the excitation parameters of the H II regions are adopted as weighting factors.

The overall agreement suggests that our sample stars trace the distribution well, as even the least massive and therefore oldest stars are not far from gas concentrations. The correlation of positions also indicates, that the adopted distance scale gives at least comparable results to the method of Hou et al. (2009). Their kinematic distances are based on the Galactic rotation curve, which in turn was gauged by maser parallaxes. The resulting distribution of the spiral tracers represents the current picture of our Galaxy, as the newly derived Solar parameters $R_0 = 8.4$ kpc and a circular orbit speed of $\theta_0 = 254$ km/s based on trigonometric parallaxes of masers (Reid et al. 2009) were adopted.

The described exercise might seem redundant, as many objects are known to be part of OB-associations (see Table A.3). However, OB-associations can be quite extended, and, moreover, we found that the distances of at least two objects are incompatible with the assigned associations.

The Case of HD 87737

It was previously established, that the sample stars have not wandered off too far from their birthplaces. HD 87737, better known as η Leonis, seems to be evidence for the contrary, as it is located high above the Galactic plane at $z = 0.53$ kpc – more distant from the disk than any other star in the sample. As it is also one of the closest of the examined objects, the space velocity can be constrained reasonably well by proper motion measurements. Thus the object lends itself for a kinematic analysis of its orbit.

Table 7.2: Results of the kinematic study of HD 87737. Parameters at the moment of disk intersection bear the subscript 'int'. Velocity components in X, Y, Z-direction are labeled with v_X, v_Y, v_Z.

Variable	Median	Average	Uncertainty
$R\,[\mathrm{kpc}]$	8.36	8.36	0.05
$v_X\,[\mathrm{km\,s^{-1}}]$	4.0	4.0	2.6
$v_Y\,[\mathrm{km\,s^{-1}}]$	221.4	221.3	1.5
$v_Z\,[\mathrm{km\,s^{-1}}]$	5.7	5.6	2.0
$T_{\mathrm{flight}}\,[\mathrm{Myr}]$	20.9	21.0	1.7
$R_{\mathrm{int}}\,[\mathrm{kpc}]$	8.59	8.60	0.02
$v_{X\,\mathrm{int}}\,[\mathrm{km\,s^{-1}}]$	-108.7	-109.2	9.1
$v_{Y\,\mathrm{int}}\,[\mathrm{km\,s^{-1}}]$	185.2	184.6	6.2
$v_{Z\,\mathrm{int}}\,[\mathrm{km\,s^{-1}}]$	38.1	38.2	3.2
$v_{\mathrm{ej}}\,[\mathrm{km\,s^{-1}}]$	40.1	40.2	3.3

Since we assumed the star formed much closer to the disk, a method to numerically trace back the orbit of a star to the Galactic disk was adopted, which was successfully tested by Irrgang et al. (2010) for runaway stars. It is based on the code of Odenkirchen & Brosche (1992) and the Galactic potential of Allen & Santillan (1991). According to Przybilla et al. (2006), the proper motions are given by $\mu_\alpha = -1.94 \pm 0.92$ milli-arcseconds per year and $\mu_\delta = -0.53 \pm 0.43$ milli-arcseconds per year, and the radial velocity by $v_{\mathrm{rad}} = 3.3 \pm 0.9\,\mathrm{km/s}$. Together with the distance derived earlier, this is enough information to compute 3D coordinates and velocities.

Following this, the orbit can be computed back in time to the moment of disk intersection. Uncertainties in these calculations were constrained via a Monte Carlo method that randomly varies the uncertainties within the error bounds, assuming a Gaussian distribution (errors in α and δ are negligible). The resulting average and median values of a sample of 10 000 trajectories are listed in Table 7.2, for selected parameters.

There are several interesting results of this kinematical study. The flight time of $21.0 \pm 1.7\,\mathrm{Myr}$ is consistent with the estimated age of the star, which is $28 \pm 5\,\mathrm{Myr}$ for both a rotating star evolving directly from the main sequence and a non-rotating star evolving through a blue loop – the possible scenarios as predicted by the models of Meynet & Maeder (2003). This suggests a cluster ejection close to the disk shortly after star formation. The ejection velocity $v_{\mathrm{ej}} = 40 \pm 3\,\mathrm{km/s}$, which is the velocity relative to the rotating Galactic rest frame at the disk intersection, is very close to v_Z at that moment, and therefore mostly pointed in Z-direction. This explains the unusual height over the Galactic plane, unusual for a massive star. The high ejection velocity shows that HD 87737 should be the exception rather than the norm. OB-field stars, which already escaped their cluster of origin, have typical space velocities of $\sim 10\,\mathrm{km/s}$, whereas stars exceeding velocities of $30\,\mathrm{km/s}$ are classified as runaway stars (e.g. Gvaramadze & Bomans 2008). Considering that HD 87737 is one of the oldest stars in the sample with an exceptionally high ejection velocity, it is reasonable to assume, that other sample stars should be much closer to their point of origin. As the difference between the Galactocentric radius at disk intersection and the current one is only $0.23 \pm 0.06\,\mathrm{kpc}$, even the inclusion of HD 87737 into the abundance gradient determination seems justified.

7.3 The Galactic Abundance Gradients

Many types of astronomical objects have been used to estimate Galactic abundance gradients, namely planetary nebulae, giant stars, old open clusters, H II regions, and young, B-type main sequence stars. The existence of gradients is widely accepted, their precise value, however, still needs to be established. In fact, there is a huge number of abundance gradient determinations available, in particular for the most studied element oxygen, and it is possible to find support in the literature for nearly any abundance gradient prediction within reasonable bounds. A comparison with data from the literature will therefore be restricted to studies of the past ten years in this section. Earlier studies certainly had their merits, but the considerable advances in stellar spectroscopy and the diagnostics of nebulae – like, e. g., the introduction of non-LTE and high-resolution spectroscopy into the studies of B-type stars – should provide improved accuracy to more recent analyses. For a discussion of earlier results, refer to, e. g., Rolleston et al. (2000). In the following, the characteristics of the different tracers of Galactic abundance gradients are shortly outlined, before the results of this study are presented and discussed.

7.3.1 Other Tracers

One great advantage of BA-type supergiants over other stellar tracers is the high luminosity, especially in the visual part of the spectrum, which exceeds even that of the most luminous Cepheids ($M_V \approx -6$). This allows high-quality spectra with ground-based telescopes to be obtained even at considerable distances. Consequently the quality of our observations surpasses that of most previous studies of stellar abundance gradients.

- **Planetary Nebulae**

  Planetary nebulae (PNe) are evolutionary products of intermediate mass stars, ejected and ionized by the remnant of the progenitor. Abundances are derived from emission lines, which are relatively easy to measure. The results, however, are plagued by systematic uncertainties, like, e. g., the depletion of heavy elements by dust formation, and a known discrepancy between recombination lines and collisionally excited lines (see Stasińska 2004 for an overview). Naturally, the analyses concentrate on elements less affected by dust formation, e. g., N, O, and Ne. Substantial comparisons with studies of PNe are difficult, as they sample a variety of ages from 1 to 10 Gyr, and therefore different epochs of GCE. Recent results for the oxygen gradient are -0.05 dex/kpc (Costa et al. 2004, 4–14 kpc) and -0.023 dex/kpc (Stanghellini & Haywood 2010, 3–23 kpc). The latter study divided the objects into different age groups and found a steepening gradient with time. The also reduced the considerable distance uncertainties by adopting a distance scale newly calibrated in the Magellanic Clouds.

- **H II Regions**

  H II regions are ionized clouds of gas powered by massive stars, and therefore closely related to the objects examined here. They are also direct tracers of the ISM. The diagnostic methods are similar in nature to those applied to PNe, sharing the advantages but also some of the problems. H II regions are frequently used to determine

abundance gradients in surveys of other galaxies, in fact the existence of large-scale abundance gradients was first substantiated in such a study (Searle 1971).

- **Cepheids**

  Cepheids are luminous pulsating stars of spectral type F and G, probably crossing the instability strip in the HRD on a blue loop. They have several advantages over other abundance tracers: they are excellent distance indicators based on the period-luminosity relationship, show rich absorption line spectra of many elements, and are luminous enough to sample abundances over a significant fraction of the Galactic disk. A large number of studies in recent years (AL4, Lemasle et al. 2008; Yong et al. 2006) concentrated on deriving spatial abundance patterns in the Milky Way using Cepheids, encompassing well over a hundred individual stars. Detrimental to the accuracy of their results are the constantly changing atmospheres of these stars, making accurate atmospheric parameter determination difficult (Mihalas 2003), and the reliance on the assumption of LTE. Cepheids are significantly older on average then BA-type supergiants, but can still be considered young on the timescales of Galactic evolution.

- **B-type Main Sequence Stars**

  B-type main sequence stars are the evolutionary progenitors of BA-type supergiants and therefore perfectly suited for comparisons to this study. The accuracy of the analysis method was improved by the introduction of non-LTE models. While Rolleston et al. (2000) used non-LTE corrections only for some elements, Daflon & Cunha (2004) applied non-LTE line-formation calculations throughout their entire analysis. Objects in clusters were analyzed in these studies, since cluster distances are better constrained than any of the spectroscopic distance indicators for these stars..

7.3.2 Results and Discussion

To estimate the Galactic abundance gradient, a linear relation centered on the position of the Sun

$$\varepsilon(X) = m_X(R_g - 8.4) + \varepsilon_0(X) \qquad (7.23)$$

was fitted to the data, accounting for errors in both stellar abundance $\varepsilon(X)$[1] and distance following the iterative scheme of Fasano & Vio (1988). m_X is an approximation to the abundance gradient $d\varepsilon(X)/dR_g$ over the sampled region, while $\varepsilon_0(X)$ is a measure of the abundance average at solar Galactic radius.

The resulting abundance gradients are listed in Table 7.3, together with some of the most recent results from the literature from objects tracing the current ISM. The 1σ-uncertainties of the derived trends are remarkably small, given that most of the other studies encompass a larger range of Galactocentric radii, which should add to the significance of their results. As a comparison gradients predicted by Cescutti et al. (2007) are shown, who calculated the behavior of a large number of elements. In general – independent of the exact details of the model – elements produced on a longer timescale should have steeper gradients, i.e.

---

[1]from here on the notation $\varepsilon(X) = \log(N_X/N_H) + 12$ with absolute number densities N_X and N_H is adopted

Table 7.3: A comparison of observed radial metallicity gradients in the galaxy and the the GCE-model predictions by Cescutti et al. (2007)

Objects	R_g	$d\varepsilon(O)/dR_g$	$d\varepsilon(Mg)/dR_g$	$d\varepsilon(S)/dR_g$	$d\varepsilon(Ti)/dR_g$	$d\varepsilon(Fe)/dR_g$
H II regions[1]	6-11 kpc	-0.044±0.010				
H II regions[2]	1-17 kpc	-0.043±0.007				
MS-B-stars [3]	4-13 kpc	-0.031±0.012	-0.052±0.014	-0.040±0.011		
MS-B-stars[4]	6-18 kpc	-0.061±0.006	-0.074±0.010			
Cepheids[5]	8-12 kpc	-0.051±0.022				-0.056±0.022
PNe type I[6]	3-16 kpc	-0.035±0.024				
BA-Supergiants[7]	6-12 kpc	-0.041[8]±0.005	-0.034±0.007	-0.049±0.008	-0.038±0.012	-0.058±0.009
GCE-model	6-14 kpc	-0.035	-0.039	-0.047	-0.043	-0.052

[1] Esteban et al. (2005); [2] Rood et al. (2007); [3]Daflon & Cunha (2004); [4]Rolleston et al. (2000); [5]Lemasle et al. (2007); [6]Stanghellini & Haywood (2010); [7]this work; [8]corrected: 0.033 ± 0.005

the gradient of oxygen, mainly produced in short-lived massive stars, should be flatter than the gradient of iron, produced mainly in supernovae of type Ia after long evolution.

The derived abundances for oxygen follow the fitted trend very tightly, no major outliers are found (see Fig. 7.11a, corrected for mixing with processed material). While there are no significant differences in the quality of the fit with or without correction, the resulting slope changes considerably with the correction: from 0.041 dex/kpc to 0.033 dex/kpc. This actually coincides with stellar evolution theory, as stars with lower metallicity show more pronounced signs of mixing (Maeder & Meynet 2001), and thus the average correction in the outer parts of the Milky Way should be larger, flattening the gradient. The results with corrections show very good agreement with the predictions of the GCE-models by Cescutti et al. (2007). The abundance gradients found in more recent studies agree with our values within the uncertainties, except for the study by Rolleston et al. (2000), which shows a steeper gradient. There seems to form an agreement between the results from H II regions, main sequence B-stars, Cepheids and young PNe in the most recent studies. Fig. 7.11b shows, however, that, while the *relative* abundance analysis might agree, there are still differences in the *absolute* abundances. There is, however, excellent agreement of the present abundances and those derived from H II regions by Esteban et al. (2005). Note that the values are corrected for dust depletion by 0.08 dex, as Esteban et al. (2004) suggested for Orion.

The results for magnesium differ more from the values in the literature. The results from the analysis of B-stars seem to advocate a steeper gradient (compare Table 7.3), whereas the data from the Cepheids seem to show not much of a gradient at all (AL4, see Fig. 7.12b). The results from the non-LTE abundance analysis of B-stars (Daflon & Cunha 2004) are at least consistent within the error estimates. Once again, agreement with the predictions of Cescutti et al. (2007) is found (see Fig. 7.12a), in contrast to the other studies.

The sulfur gradient is tightly constrained and the resulting slope is in good agreement with predictions (see Fig. 7.13a) and the value of Daflon & Cunha (2004), but once again the absolute abundances differ (see Fig. 7.13b). There is disagreement in absolute abundances for all elements in common with this study, while the actual results for the abundance gradient agree. This demonstrates how dangerous it is to combine the results from different studies, in particular those using different tracers, as it is frequently done in the literature.

Table 7.4: A comparison of the element abundances $\varepsilon_0(X)$ found in the linear fits at the solar Galactocentric radius to abundance standards in the solar neighborhood.

Objects	$\varepsilon(O)$	$\varepsilon(Mg)$	$\varepsilon(S)$	$\varepsilon(Ti)$	$\varepsilon(Fe)$
Sun[1]	8.69±0.05	7.53±0.01	7.15±0.03	4.91±0.03	7.45±0.01
MS-B-stars[2]	8.76±0.03	7.56±0.05			7.44±0.04
Cepheids[3]	8.60±0.13	7.34±0.13	7.23±0.10	4.95±0.07	7.46±0.06
BA-Supergiants[4]	8.73[5]±0.01	7.49±0.02	7.02±0.02	5.07±0.03	7.53±0.02

[1]Asplund et al. (2009); [2]Przybilla et al. (2008); [3]AL4; [4]this work; [5]corrected: 8.79 ± 0.01

Major systematic effects may bias the interpretation in such a case. Results from various studies should only be combined when the different methods have been shown to yield consistent results.

With the introduction of the cut-off in effective temperature to increase the homogeneity of the analysis of the titanium abundances, the significance of the result could be improved. Given the high uncertainties in abundances of individual stars, however, and the remaining systematic effects, the analysis constrains the gradient less well than for the other elements (see Fig. 7.14a). Agreement with the predictions of Cescutti et al. (2007) is obtained, but at lower significance.

Apart from a slight offset in abundance, good agreement with the Cepheids (AL4) is found for the iron abundances (see Fig. 7.15b). The iron gradient also confirms the predictions of the GCE-model within the uncertainties (see Fig. 7.15a).

No sign of any abundance patterns beside a linear decline could be found. The picture of a purely radial gradient appears to be a good approximation in the – admittedly limited – sample space. Other authors report a steepening towards the center (e. g. Andrievsky et al. 2002a), a flattening (e. g. Andrievsky et al. 2004) or, on the contrary, a steepening (Rolleston et al. 2000) towards the outskirts of the disk. Lemasle et al. (2008) found a considerable trend in the iron abundance with Galactic longitude in the outer disk (10–12 kpc). This could not be verified in the present study, since the sampling in longitude is too limited in that range.

Another result of the fit to the surface abundances as a function of Galactocentric radius is the abundance $\varepsilon_0(X)$ at the Solar distance from the Galactic center. This value is compared to the element abundances in the Solar System, the B-star standard of the Solar neighborhood and the average of the Cepheid abundances in the bin at $R_g = R_0$ in Table.7.4.

Several problems come up in comparisons to Solar abundances. For one, it is not clear if the Sun is representative for the current Solar neighborhood. Not only is it 4.5 Gyr old, but also its distance from the Galactic center could have shifted during this time due to the mechanisms behind radial mixing, which is an important ingredient of the currently most successful GCE-model to describe the F- and G-dwarfs in the Solar neighborhood (Schönrich & Binney 2009b). The photospheric abundances of the Sun are also still subject to change, as a comparison of the oxygen abundances of Grevesse & Sauval (1998) (8.83 dex) and Asplund et al. (2009) (8.69 dex) shows. A more appropriate test might be the comparison to the cosmic abundance standard defined by Przybilla et al. (2008) from
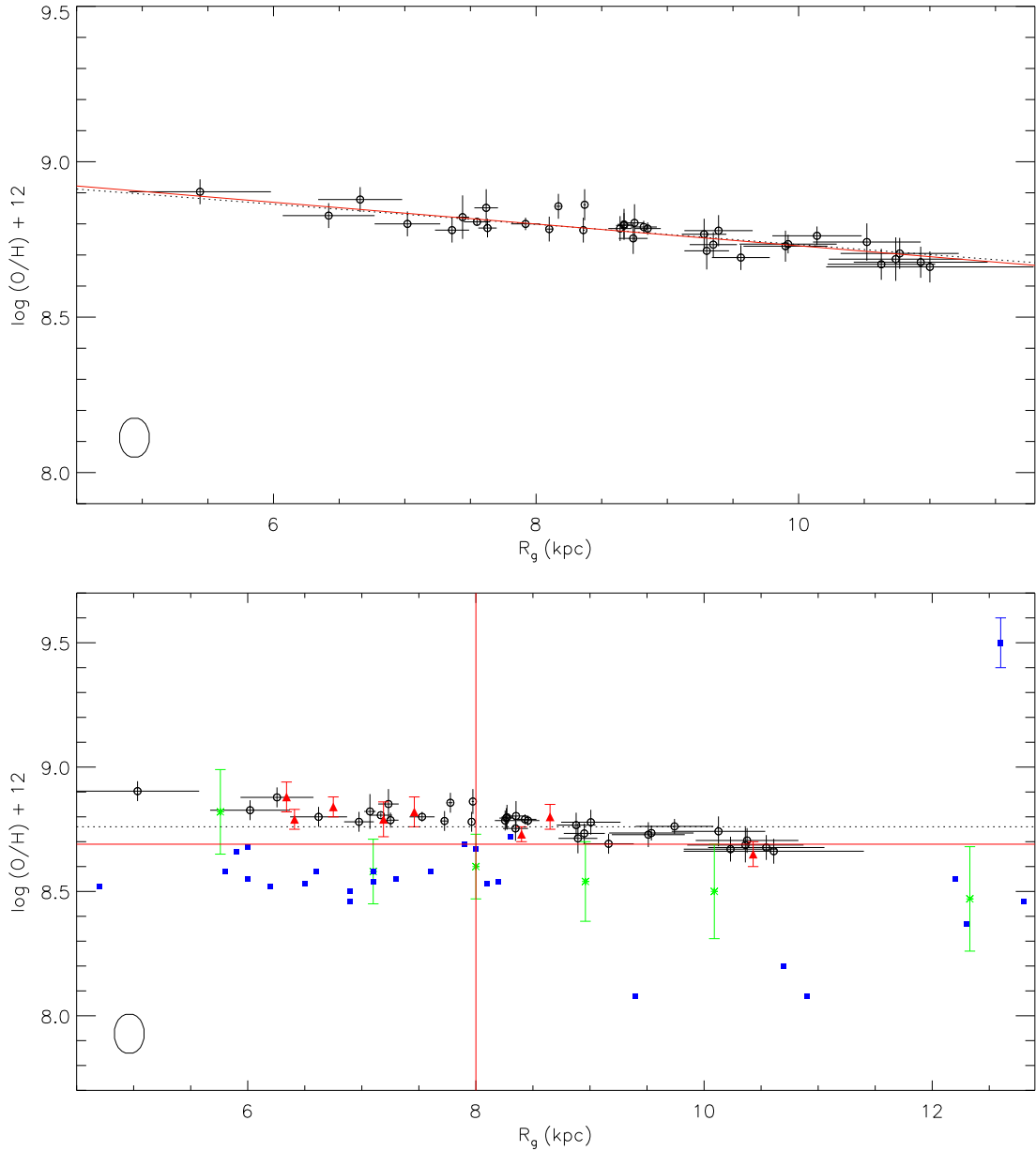
Figure 7.11: **Both Panels:** Oxygen abundances of the sample stars (circles), corrected for the effect of CNO-mixing, as a function of Galactocentric radius R_g. Note that a modern value of $R_0 = 8.4\,\text{kpc}$ is used in the upper panel, while $R_0 = 8.0\,\text{kpc}$ was adopted in the lower panel in order to facilitate comparison with literature data. **Upper Panel:** The dashed line indicates the derived linear trend, the continuous red line marks the abundance gradient predicted by the models of Cescutti et al. (2007) for a range of 4–14 kpc, normalized to match the trend at 8.4 kpc. **Lower Panel:** Comparison to abundance determinations from H II regions (Esteban et al. 2005, triangles), OB-type stars (Daflon & Cunha 2004, filled boxes, typical uncertainties indicated in the top right corner), the solar abundance (Asplund et al. 2009, red cross), the abundance standard derived from B-stars in the solar neighborhood (Przybilla et al. 2008, dashed line) and the results from Cepheids (AL4: asterisks) divided into 6 bins as a function of R_g, where the points mark the mean values and the bars indicate the scatter in each bin (taken from Cescutti et al. 2007).
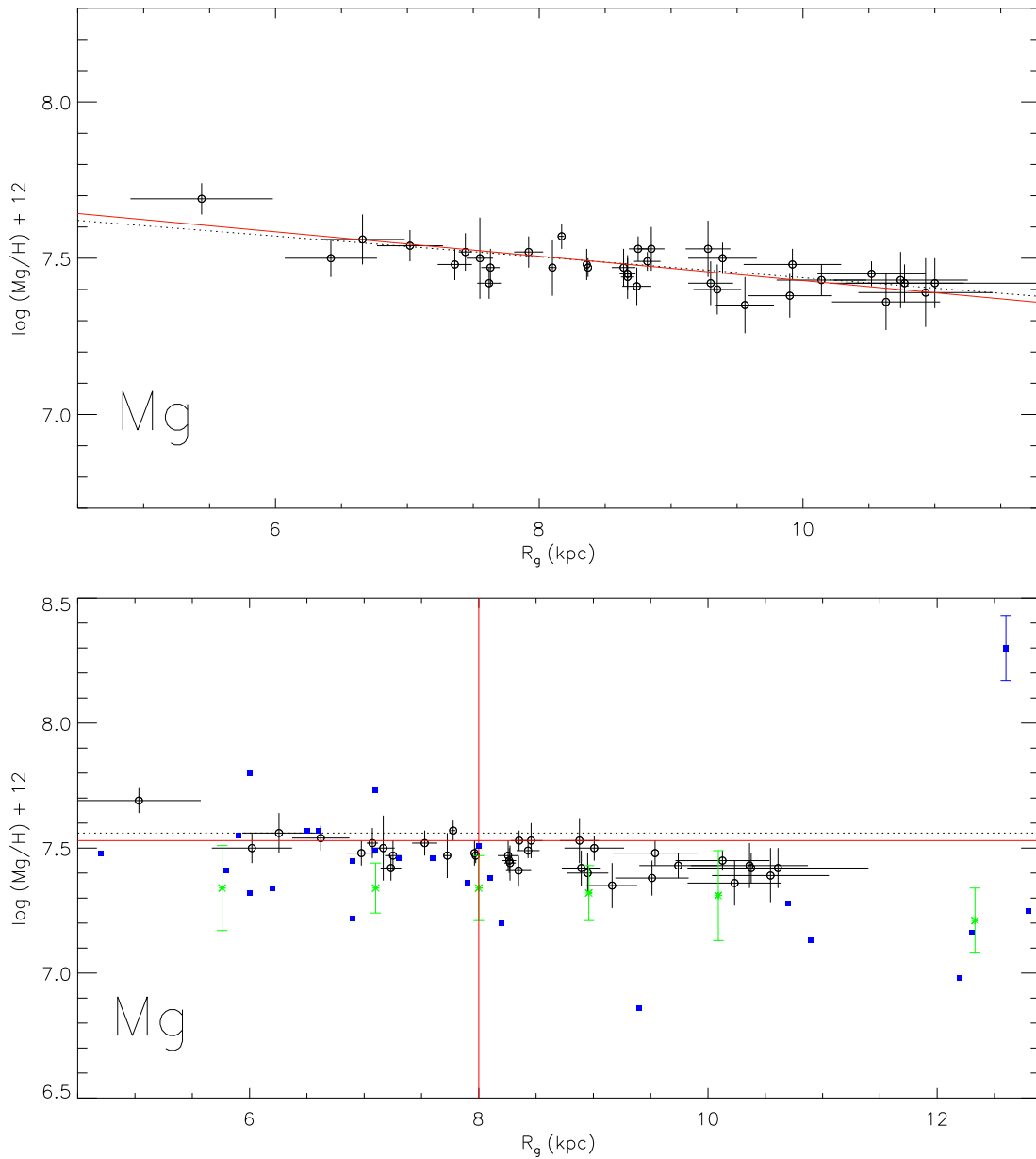
Figure 7.12: **Both Panels:** Magnesium abundances of the sample stars (circles) as a function of Galactocentric radius R_g. Note that a modern value of $R_0 = 8.4\,\mathrm{kpc}$ is used in the upper panel, while $R_0 = 8.0\,\mathrm{kpc}$ was adopted in the lower panel in order to facilitate comparison with literature data. **Upper Panel:** The dashed line indicates the derived linear trend, the continuous red line marks the abundance gradient predicted by the models of Cescutti et al. (2007) for a range of 4–14 kpc, normalized to match the trend at 8.4 kpc. **Lower Panel:** Comparison to abundance determinations from OB-type stars (Daflon & Cunha 2004, filled boxes, typical uncertainties indicated in the top right corner), the solar abundance (Asplund et al. 2009, red cross), the abundance standard derived from B-stars in the solar neighborhood (Przybilla et al. 2008, dashed line) and the results from Cepheids (AL4: asterisks) divided into 6 bins as a function of R_g, where the points mark the mean values and the bars indicate the scatter in each bin (taken from Cescutti et al. 2007).

Figure 7.13: **Both Panels:** Sulfur abundances of the sample stars (circles) as a function of Galactocentric radius R_g. Note that a modern value of $R_0 = 8.4$ kpc is used in the upper panel, while $R_0 = 8.0$ kpc was adopted in the lower panel in order to facilitate comparison with literature data. **Upper Panel:** The dashed line indicates the derived linear trend, the continuous red line marks the abundance gradient predicted by the models of Cescutti et al. (2007) for a range of 4–14 kpc, normalized to match the trend at 8.4 kpc. **Lower Panel:** Comparison to abundance determinations from OB-type stars (Daflon & Cunha 2004, filled boxes, typical uncertainties indicated in the top right corner), the solar abundance (Asplund et al. 2009, red cross), the abundance standard derived from B-stars in the solar neighborhood (Przybilla et al. 2008, dashed line) and the results from Cepheids (AL4: asterisks) divided into 6 bins as a function of R_g, where the points mark the mean values and the bars indicate the scatter in each bin (taken from Cescutti et al. 2007).

Figure 7.14: **Both Panels:** Titanium abundances of the sample stars (circles) as a function of Galactocentric radius R_g, stars without error bars were excluded from the gradient determination. Note that a modern value of $R_0 = 8.4\,\mathrm{kpc}$ is used in the upper panel, while $R_0 = 8.0\,\mathrm{kpc}$ was adopted in the lower panel in order to facilitate comparison with literature data. **Upper Panel:** The dashed line indicates the derived linear trend, the continuous red line marks the abundance gradient predicted by the models of Cescutti et al. (2007) for a range of 4–14 kpc, normalized to match the trend at 8.4 kpc. **Lower Panel:** Comparison to the solar abundance (Asplund et al. 2009, red cross), the abundance standard derived from B-stars in the solar neighborhood (Przybilla et al. 2008, dashed line) and the results from Cepheids (AL4: asterisks) divided into 6 bins as a function of R_g, where the points mark the mean values and the bars indicate the scatter in each bin (taken from Cescutti et al. 2007).

Figure 7.15: **Both Panels:** Iron abundances of the sample stars (circles) as a function of Galactocentric radius R_g. Note that a modern value of $R_0 = 8.4\,\mathrm{kpc}$ is used in the upper panel, while $R_0 = 8.0\,\mathrm{kpc}$ was adopted in the lower panel in order to facilitate comparison with literature data. **Upper Panel:** The dashed line indicates the derived linear trend, the continuous red line marks the abundance gradient predicted by the models of Cescutti et al. (2007) for a range of 4–14 kpc, normalized to match the trend at 8.4 kpc. **Lower Panel:** Comparison to the solar abundance (Asplund et al. 2009, red cross), the abundance standard derived from B-stars in the solar neighborhood (Przybilla et al. 2008, dashed line) and the results from Cepheids (AL4: asterisks) divided into 6 bins as a function of R_g, where the points mark the mean values and the bars indicate the scatter in each bin (taken from Cescutti et al. 2007).

Figure 7.16: Abundance gradients determined in this study (filled circles), compared to those predicted by Cescutti et al. (2007) (boxes). The triangle represents the oxygen abundance gradient corrected for CNO-mixing. All the predictions are confirmed within the errors, provided the correction for oxygen is talen into account.

analyses of main sequence B-stars in the solar neighborhood. Their study found very low star-to-star scatter in the perimeter of the Sun, which is supported by the small scatter in abundance at a given Galactocentric radius established for most elements in this thesis. Agreement with this standard is found for oxygen and magnesium, whereas the iron abundances show some disagreement, although this is within the bounds of what can be expected from systematic uncertainties.

7.3.3 Conclusions for Models of GCE

In conclusion, the result confirms the trend towards moderate radial abundance gradients found in the more recent studies on the subject. In light of this, the usage of older results advocating steeper gradients for oxygen, like, e. g., Shaver et al. (1983, -0.07 dex/kpc) or Rolleston et al. (2000, -0.07 dex/kpc), to constrain GCE-models needs to be reconsidered. In addition, the careful, this homogeneous study suggests that the interstellar matter is well-mixed and adheres the *local* abundance profile, as was suggested by Przybilla et al. (2008). The comparison with other data sets shows, however, that combining the results of different studies in order to determine the Galactic abundance gradient can be misleading, as the systematic differences might be of the same order of magnitude as the parameter of interest.

The relative amplitudes of the derived gradients are consistent with what is expected in the general picture of GCE, with iron abundances most rapidly declining with increasing Galactocentric radius. More specifically, the values predicted by the model of Cescutti et al. (2007) for the current gradients in the ISM are confirmed by the results for all elements

considered with remarkable accuracy (see Fig. 7.16). It was therefore demonstrated, that numerical models of GCE can be very well constrained in this particular aspect by state-of-the-art quantitative spectroscopy of BA-type supergiants..

8 Conclusions and Outlook

The aim of this thesis was to perform quantitative spectroscopic analyses on a large sample of Galactic BA-type supergiants in a homogeneous way. The analysis method described by Przybilla et al. (2006) was adapted for this task by calculating large model grids and devising a new data analysis strategy based on line-profile fits, to accelerate and automatize the parameter and abundance determination.

Indeed, the atmospheric parameters T_{eff}, $\log g$, ξ and y, derived from high-S/N and high-resolution spectra of 35 objects, show a continuous distribution over the temperature range from 8400 to 12 700 K, displaying no signs of systematic shifts or gaps stemming from the use of different temperature indicators. The results were – in general successfully – checked for consistency, utilizing ionization equilibria of several elements and spectrophotometric data, whenever possible. This meticulous procedure allowed to set a new standard for the properties of BA-type supergiants in the form of an improved empirical spectral-type–T_{eff} relation. The homogeneity of the atmospheric parameter determination reduces systematic uncertainties in the abundance analysis, which, in combination with well-constructed model atoms, allows to derive the surface abundances of He, C, N, O, Mg, S, Ti and Fe for a large sample of Galactic BA-type supergiants with unprecedented accuracy.

The results can be put to use in various fields of modern astronomy, in particular in the Galactic context. In nearly all applications a significant reduction of systematic scatter is noticed in comparison to most previous studies. Specifically the uncertainties in *relative* abundances appear to be reduced by a large amount.

Signatures of CNO-mixing were found in all stars, in agreement with previous findings: for example the derived nitrogen to carbon mass ratio N/C takes values from 0.63 to 4.66, compared to values around 0.31 found in unmixed B-type-progenitor stars on the main sequence (Przybilla et al. 2010). For the first time it was shown that the two main indicators for CNO-processing, N/C and N/O, obey a tight relation in Galactic BA-type supergiants, in excellent agreement with the predictions of stellar evolution models (compare Fig 6.15b). Furthermore, helium abundances – mostly ignored in previous studies – show a correlation with the other indicators of CNO-mixing – as predicted by theory.

Despite this, no definite conclusions for the evolutionary status of BA-type supergiants in the framework of current evolutionary models are possible. However, direct evolution from the main sequence – a scenario favored by previous studies (e. g. Venn 1995b) – appears less likely due to the absence of objects in the sample that do not show signs of CNO-mixing. This would favor scenarios involving convective dredge-up for all or at least a major part of the objects, but neither possibility can be ruled out yet. A surprising outcome is that the distribution of projected rotational velocities is inverse to what is predicted by evolutionary models, namely the less massive a star is the slower it rotates. Another important result is the tight correlation of luminosity and microturbulence found

in the data, which agrees very well with the predictions of Cantiello et al. (2009) based on the modelling of the iron convection zone for the BA-type supergiant regime. The detailed results of this study provide a benchmark to calibrate future models of stellar evolution or to draw more definite conclusions about the evolutionary status not readily apparent.

Possible expansions of the current study towards hotter and lower temperatures and/or lower luminosities could yield a more complete picture of massive star evolution. In particular, the homogeneous analysis of objects at different stages of massive star evolution in a single star cluster would be an interesting test for the method and for stellar evolution models.

The results for the abundance gradients for Galactocentric radii of 6–12 kpc were determined for several elements, yielding -0.041 ± 0.005 dex/kpc for oxygen, -0.034 ± 0.007 dex /kpc for magnesium, -0.049 ± 0.008 dex/kpc for sulfur, -0.038 ± 0.012 dex/kpc for titanium and -0.058 ± 0.009 dex/kpc for iron. The results establish the existence of comparably flat gradients within firm constraints. In recent times, a trend towards flatter gradients is found in the literature. Comparison to some of the most recent studies using various tracers shows reasonable agreement in the gradients, but systematic differences in absolute abundances. In consequence, a combination of results from various studies for an extension of sample size is *not* recommended because of these systematic differences. An exception to this are the oxygen abundances derived by Esteban et al. (2005) from H II-regions, which show excellent agreement with the present results in both absolute and relative values.

The relative amplitudes of the derived gradients, based mostly on the timescales on which the elements are produced, are consistent with what is expected in the general picture of Galactochemical evolution, with iron abundances most rapidly declining with increasing Galactocentric radius. More specifically, the values predicted by the model of Cescutti et al. (2007) for the current gradients in the ISM are confirmed by the results for all elements considered (compare Fig. 7.16). Given the limited spatial extent of the study in Galactocentric radius, the tight constraints on the abundance gradients – with the possible exception of titanium, where the uncertainties are large – show that the ISM in the Solar neighborhood is well described by a linear gradient.

Additionally to the tight relations found between abundances and Galactocentric radius, the remaining star-to-star scatter appears to be of the same magnitude as the uncertainties in the abundances of individual stars, implying a well-mixed, *locally* homogeneous interstellar medium. This confirms the results of Przybilla et al. (2008), who found uniform abundances in the B-stars of the Solar neighborhood.

An extension of the study towards larger distances could provide insight into the large-scale abundance patterns. For example, the frequently claimed steepening towards the inner disk and flattening towards the outer disk could be investigated, and a possible variation with Galactic longitude or the extension of spiral arms could be verified.

Interesting targets towards the Galactic Center are, e.g., the members of the rich supergiant population in the starburst cluster Westerlund1 (Clark et al. 2005), readily observable with ground-based telescopes despite the strong reddening. As for the outer disk, systematic spectroscopic surveys to identify tepid supergiants among the many BA-type

main sequence foreground stars would be necessary to obtain the required spatial coverage. Given high-quality observations, lines of many other elements like Ne, Na, Al, Si, Ca, Sc, V, Cr, Mn, Ni, Sr and Ba (compare, e.g., Schiller & Przybilla 2008) are in principle available for abundance determinations in (B)A-type supergiant spectra, but new sophisticated model atoms have to be constructed first in order to incorporate them into the analysis method presented in this thesis.

The major uncertainties in the distance determination, that are troubling most astronomical studies including this one, could be considerably reduced in the near future. Astrometric satellite missions like Gaia (e.g. Lindegren et al. 2008) will be able to calibrate the Cepheid-based distance scale and to measure accurate distances of Galactic BA-type supergiants for the first time, thereby providing a crucial test for the suitability of the distance scale adopted in this study. Reduced distance uncertainties would allow tighter constraints not only for the Galactic abundance gradients to be obtained, but also for the fundamental stellar parameters relevant for the comparison to stellar evolution models.

A Appendix

Correlation Coefficient

Pearson's correlation is used throughout this study, as defined by

$$\text{corr}(x, y) = \frac{\sum_{i=1}^{n}(x_i - \bar{x})(y_i - \bar{y})}{(n-1)\sigma_x \sigma_y},$$ (A.1)

where $\bar{x}$ and $\bar{y}$ are the sample means and σ_x and σ_y are the sample standard deviations. A value of 0 means the variables are statistically independent, -1 or $+1$ indicate perfect negative or positive linear relations, respectively.

Constants and Units

Table A.1: Constants and Units (see e.g. **?**)

Constant	Symbol	Numerical value [SI]	Numerical value [cgs]
Gravitational constant	G	$6.673 \cdot 10^{-11}\,\mathrm{m^3\,s^{-2}\,kg^{-1}}$	$6.673 \cdot 10^{-8}\,\mathrm{cm^3\,s^{-2}\,g^{-1}}$
Planck's constant	h	$6.626 \cdot 10^{-34}\,\mathrm{J\,s}$	$6.626 \cdot 10^{-27}\,\mathrm{erg\,s}$
Boltzmann constant	k	$1.381 \cdot 10^{-23}\,\mathrm{J\,K^{-1}}$	$1.381 \cdot 10^{-16}\,\mathrm{erg\,K^{-1}}$
Stefan-Boltzmann constant	σ	$5.670 \cdot 10^{-8}\,\mathrm{J\,m^{-2}\,s^{-1}\,K^{-4}}$	$5.670 \cdot 10^{-5}\,\mathrm{erg\,cm^{-2}\,s^{-1}\,K^{-4}}$
Speed of light	c	$299\,792\,458\,\mathrm{m\,s^{-1}}$	$29\,979\,245\,800\,\mathrm{cm\,s^{-1}}$
Parsec	pc	$3.086 \cdot 10^{16}\,\mathrm{m}$	$3.086 \cdot 10^{18}\,\mathrm{cm}$
Solar Values	**Symbol**	**Numerical value [SI]**	**Numerical value [cgs]**
Mass	$M_\odot$	$1.989 \cdot 10^{30}\,\mathrm{kg}$	$1.989 \cdot 10^{33}\,\mathrm{g}$
Radius	$R_\odot$	$6.96 \cdot 10^{8}\,\mathrm{m}$	$6.96 \cdot 10^{10}\,\mathrm{cm}$
Luminosity	$L_\odot$	$3.85 \cdot 10^{26}\,\mathrm{J\,s^{-1}}$	$3.85\,10^{33}\,\mathrm{erg\,s^{-1}}$

Table A.2: IUE spectra used in this thesis (`http://archive.stsci.edu/`).

#	Object	SW	Date	LW	Date
1	HD12301	P07282	01/12/1979	R06276	01/12/1979
2	HD12953	P42698	12/10/1991	P21249	15/09/1991
6	HD14489	P21812	19/12/1983	...	...
7	HD20041	P56064	09/10/1995	P31581	09/10/1995
8	HD21291	P07280	01/12/1979	R06274	01/12/1979
9	HD39970	P56171	09/11/1995	P31675	09/11/1995
10	HD46300	P56165	08/11/1995	P31667	08/11/1995
12	HD187983	P48688	19/09/1993	P26414	19/09/1993
13	HD197345	P09133	26/05/1980	R07864	26/05/1980
14	HD202850	P15099	25/09/1981	R11614	23/09/1981
15	HD207260	P03368	17/11/1978	R02957	17/11/1978
17	HD208501	P55805	03/09/1995	P31403	03/09/1995
18	HD210221	P18682	28/11/1982	R14745	28/11/1982
19	HD212593	P33852	03/07/1988	P13556	03/07/1988
23	HD87737	P08566	26/03/1980	R07305	26/03/1980

Table A.3: Optical photometry (UBV)[1] and infrared photometry (JHK)[2].

#	Object	V (mag)	$B - V$ (mag)	$U - B$ (mag)	J (mag)	H (mag)	K (mag)
1	HD12301	5.589±0.011	0.370±0.014	−0.276±0.009	4.740±0.037	4.651±0.033	4.533±0.051
2	HD12953	5.691±0.021	0.614±0.007	−0.014±0.009	4.062±0.228	4.095±0.036	3.646±0.268
3	HD13476	6.431±0.020	0.600±0.013	0.220±0.028	5.378±0.316	4.928±0.112	4.727±0.021
4	HD13744	7.592±0.014	0.741±0.012	0.180±0.000	5.828±0.024	5.650±0.057	5.480±0.017
5	HD14433	6.401±0.019	0.567±0.008	0.030±0.010	5.082±0.019	4.863±0.024	4.769±0.017
6	HD14489	5.178±0.009	0.369±0.004	−0.110±0.000	4.528±0.232	4.243±0.053	4.242±0.244
7	HD20041	5.795±0.019	0.712±0.020	0.090±...	4.057±0.180	3.880±0.206	3.761±0.268
8	HD21291	4.213±0.019	0.412±0.008	−0.234±0.009	2.712±0.230	2.603±0.192	2.413±0.236
9	HD39970	6.018±0.004	0.386±0.005	−0.192±0.010	4.933±0.037	4.847±0.036	4.749±0.020
10	HD46300	4.498±0.008	0.007±0.009	−0.217±0.041	4.531±0.242	4.410±0.076	4.301±0.020
11	HD186745	7.030±0.008	0.930±0.002	0.028±0.007	5.499±0.310	4.813±0.036	4.622±0.018
12	HD187983	5.590±0.026	0.684±0.017	0.173±0.149	3.972±0.250	3.762±0.214	3.752±0.264
13	HD197345	1.246±0.015	0.092±0.007	−0.233±0.008	1.139±0.254	0.902±0.188	1.010±0.202
14	HD202850	4.233±0.009	0.123±0.011	−0.386±0.026	3.973±0.254	3.864±0.222	3.683±0.036
15	HD207260	4.289±0.007	0.518±0.011	0.119±0.018	3.296±0.244	3.215±0.208	2.942±0.260
16	HD207673	6.467±0.005	0.410±0.000	0.060±...	5.398±0.024	5.309±0.026	5.210±0.029
17	HD208501	5.796±0.004	0.724±0.008	−0.022±0.007	4.312±0.254	4.098±0.224	3.934±0.272
18	HD210221	6.140±0.000	0.414±0.017	0.240±0.000	5.104±0.029	4.955±0.024	4.841±0.017
19	HD212593	4.569±0.018	0.086±0.004	−0.342±0.006	4.401±0.294	4.250±0.036	4.283±0.036
20	HD213470	6.650±...	0.560±...	0.240±...	5.284±0.021	5.037±0.024	4.951±0.016
21	BD+602582	8.694±0.261	0.770±0.016	0.017±0.011	6.780±0.023	6.505±0.021	6.365±0.017
22	HD223960	6.895±0.009	0.715±0.009	−0.050±0.047	5.185±0.037	4.983±0.031	4.791±0.018
23	HD195324	5.880±0.000	0.524±0.014	0.100±...	5.100±0.288	4.776±0.228	4.501±0.018
24	HD34085	0.138±0.032	−0.029±0.004	−0.666±0.018	0.206±0.228	0.176±0.352	0.213±0.396
25	HD87737	3.486±0.053	−0.026±0.015	−0.206±0.028	3.499±0.272	3.499±0.212	3.299±0.256
26	HD91533	6.005±0.019	0.318±0.011	−0.075±0.034	5.092±0.039	5.022±0.029	4.839±0.023
27	HD111613	5.741±0.019	0.384±0.022	−0.088±0.026	4.737±0.017	4.635±0.076	4.450±0.026
28	HD149076	7.373±0.018	0.485±0.009	−0.118±0.021	6.096±0.026	5.916±0.029	5.774±0.018
29	HD149077	7.433±0.082	0.470±0.021	0.097±0.049	6.131±0.032	5.960±0.027	5.856±0.024
30	HD165784	6.538±0.016	0.856±0.005	0.279±0.056	4.643±0.200	4.174±0.210	4.151±0.220
31	HD166167	8.605±0.009	0.560±0.000	0.036±0.047	7.103±0.027	6.872±0.047	6.759±0.020
32	HD80057	6.044±0.016	0.285±0.006	−0.117±0.021	5.253±0.041	5.169±0.017	5.037±0.018
33	HD102878	5.695±0.017	0.265±0.009	−0.119±0.057	5.004±0.032	4.918±0.036	4.765±0.016
34	HD105071	6.316±0.024	0.200±0.010	−0.436±0.034	5.694±0.019	5.670±0.026	5.569±0.023
35	HD106068	5.920±0.010	0.297±0.007	−0.284±0.151	5.164±0.032	5.043±0.026	4.933±0.018

[1]Mermilliod & Mermilliod (1994); [2]Cutri et al. (2003);

Table A.4: Spectral line analysis of the programme stars

Ion	λ (Å)	χ (eV)	log gf	Acc.	Src.	1	2	3	4	5	6	7	8	9	10	11	12	13	14	15	16	17	18
												log X/H + 12 (star number)										
He I	4009.26	21.22	−1.47	C	WSG	11.14	...	...	11.21	11.21	11.15	11.15	11.13	11.06	...	11.11	11.16	11.16	11.24	11.2	11.18	11.08	...
He I	4026.18	20.96	−2.63	A	WSG	10.99	11.08	11.02	11.10	10.98	11.18	11.09	11.08	11.01	11.05	11.03	11.12	...	11.25	11.13	10.93	11.09	11.11
He I	4026.19	20.96	−0.63	A	WSG																		
He I	4026.20	20.96	−0.85	A	WSG																		
He I	4026.36	20.96	−1.32	A	WSG																		
He I	4120.81	20.96	−1.74	B	WSG	11.04	11.15	11.23	...	11.19	11.12	11.07	11.13	11.10	11.06	11.04	10.98	11.17	11.18	11.21	11.02	11.02	...
He I	4120.82	20.96	−1.96	B	WSG																		
He I	4120.99	20.96	−2.44	B	WSG																		
He I	4168.97	21.22	−2.34	A	WSG	11.11	...	...	...	...	...	11.04	11.16	11.14	...	11.12	...	...	...	...	11.12	11.10	...
He I	4387.93	21.22	−0.88	A	WSG	11.00	...	11.23	...	...	11.11	11.09	11.05	11.14	11.11	10.98	11.04	11.25	11.09	11.14	11.03	11.04	...
He I	4437.55	21.22	−2.03	B	WSG	11.06	...	...	...	...	...	11.12	11.09	11.08	11.25	11.09	11.11	11.16	...	...	...	10.98	...
He I	4471.47	20.96	−0.20	A	WSG	...	11.15	11.11	11.13	11.05	11.11	11.07	11.11	11.06	11.08	11.09	11.10	11.16	...	11.15	11.19	11.16	11.13
He I	4471.49	20.96	−0.42	A	WSG																		
He I	4471.68	20.96	−0.90	A	WSG																		
He I	4713.14	20.96	−1.23	B	WSG	11.04	11.11	11.21	11.15	11.07	11.13	11.01	11.08	11.02	...	10.99	11.04	11.18	11.23	11.11	11.19	11.10	11.18
He I	4713.16	20.96	−1.45	B	WSG																		
He I	4713.38	20.96	−1.93	B	WSG																		
He I	4921.93	21.22	−0.44	A	WSG	...	...	...	...	11.09	11.14	11.06	...	...	11.08	11.07	10.96	11.24	11.12	11.2	11.17	...	...
He I	5015.68	20.62	−0.82	AA	WSG	11.13	...	...	...	...	11.24	11.10	11.15	11.12	11.10	11.07	11.16	11.27	11.26	...	...	...	...
He I	5875.60	20.96	−1.52	A	WSG	...	11.10	11.19	11.22	11.07	11.19	11.11	...	...	11.10	...	11.12	11.06	...	11.22	...	...	11.08
He I	5875.61	20.96	0.48	A	WSG																		
He I	5875.63	20.96	−0.34	A	WSG																		
He I	5875.64	20.96	0.14	A	WSG																		
He I	5875.97	20.96	−0.22	A	WSG																		
C I	4771.74	7.49	−1.87	C	WFD	...	...	8.26	...	...	...	...	...	...	...	...	8.13	...	...	8.18	...	8.31	
C I	4775.90	7.49	−2.30	C	WFD	...	...	8.33	...	...	...	...	...	...	...	...	...	...	8.31	...	...	8.27	
C I	4932.05	7.68	−1.70	B	LP	...	...	8.07	...	...	...	...	...	...	...	...	8.16	...	8.21	...	...	8.17	
C I	5052.17	7.68	−1.45	C	LP	...	...	8.06	...	...	...	...	...	...	...	8.25	8.05	...	...	...	...	8.19	
C I	7113.18	8.65	−0.77	B−	WFD	...	...	8.16	...	...	...	...	...	...	...	...	...	...	...	...	...	...	
C I	9111.81	7.49	−0.30	B	WFD	...	...	...	...	8.25	...	...	...	...	...	...	...	...	...	...	...	...	
C II	4267.00	18.05	0.56	C+	WFD	8.35	...	...	...	...	...	...	...	...	...	...	...	...	...	...	...	8.13	...
C II	4267.26	18.05	0.74	C+	WFD																		
C II	5132.95	20.70	−0.21	B	WFD	...	8.03	8.11	8.21	8.19	8.08	8.1	8.09	8.14	8.05	8.15	8.23	7.97	8.11	8.11	8.03	8.13	8.16
C II	5133.28	20.70	−0.18	B	WFD																		
C II	5145.16	20.71	0.19	B	WFD	8.35	...	...	...	...	...	...	...	...	...	8.39	...	...	...	...	...	8.35	...
C II	5151.08	20.71	−0.18	B	WFD	8.48	...	...	...	...	...	...	...	...	...	8.28	...	...	...	...	...	8.21	...
C II	6151.27	20.84	−0.15	D	F	8.33	...	...	...	...	...	...	...	...	...	...	...	...	...	...	...	...	...
C II	6578.05	14.45	−0.03	B	WFD	8.50	8.20	8.30	8.16	8.29	8.17	8.24	8.25	8.30	8.15	8.33	...	8.09	8.15	8.24	8.23	...	8.17
C II	6582.88	14.45	−0.33	B	WFD	8.45	8.15	...	8.21	8.21	8.23	8.28	8.29	8.25	...	8.26	8.40	8.14	8.19	...	8.20	8.45	...
N I	6008.47	11.60	−1.11	C+	WFD	...	...	...	...	...	8.49	...	...	...	8.55	...	...	8.59	8.71	8.53	8.44	...	8.61

Table A.4: continued.

Ion	λ (Å)	χ (eV)	log gf	Acc.	Src.	log X/H + 12 (star number)																	
						1	2	3	4	5	6	7	8	9	10	11	12	13	14	15	16	17	18
N I	7423.64	10.33	−0.71	B+	WFD	...	8.4	8.54	8.3	8.27	8.55	8.3	8.43	8.22	8.4	...	8.17	8.65	8.71	8.61	8.5	...	8.48
N I	7442.30	10.33	−0.38	B+	WFD	8.13	8.43	8.58	8.33	8.24	8.54	8.26	8.46	8.13	8.45	8.44	8.19	8.6	8.66	8.62	8.46	8.18	8.56
N I	7468.31	10.34	−0.19	B+	WFD	8.14	8.44	8.61	8.32	8.25	8.56	8.28	8.45	8.16	8.39	8.4	8.16	8.61	8.69	8.58	8.52	8.17	8.5
N I	7898.98	12.36	0.02	C	WFD	...	...	...	...	...	...	...	...	...	8.33	...	...	8.44	...	8.46	...	...	...
N I	7899.28	12.36	−0.91	C	WFD																		
N I	8680.28	10.34	0.35	B+	WFD	8.11	...	...	8.22	8.2	...	8.2	8.35	8.07	8.52	8.34	8.25	...	8.61	...	...	8.32	...
N I	8703.25	10.33	−0.32	B+	WFD	8.16	8.39	8.64	8.31	8.25	8.51	8.25	8.46	8.11	8.41	8.37	8.21	8.53	8.72	8.52	8.49	8.22	8.55
N I	8711.70	10.33	−0.23	B+	WFD	8.25	8.36	8.6	8.29	8.22	8.49	8.22	8.45	8.13	8.45	8.38	8.16	8.56	8.68	8.51	8.48	8.35	8.48
N I	8718.84	10.34	−0.34	B+	WFD	8.21	8.38	8.52	8.29	8.21	8.42	8.21	8.45	8.1	8.35	8.28	...	8.49	8.63	8.45	8.44	...	8.42
N II	3995.00	18.50	0.21	B	WFD	8.09	...	...	...	...	8.6	8.32	8.45	8.12	8.42	8.28	...	...	8.63	...	8.45	8.24	...
N II	4447.03	20.41	0.23	B	WFD	8.11	...	...	...	...	...	...	8.51	...	...	...	...	...	...	...	...	8.24	...
N II	4601.48	18.46	−0.43	B+	WFD	8.19	...	...	...	...	...	...	...	...	...	8.37	...	...	...	...	...	8.29	...
N II	4607.15	18.46	−0.51	B+	WFD	8.12	...	...	...	...	...	...	8.45	...	...	8.32	...	...	8.78	...	...	8.1	...
N II	4643.09	18.48	−0.36	B+	WFD	8.09	...	...	...	...	...	...	...	...	...	8.33	...	...	8.72	...	...	8.19	...
N II	5666.63	18.47	−0.05	A	WFD	8.1	...	...	...	...	...	...	...	...	...	8.33	...	...	8.74	...	...	8.16	...
N II	5679.56	18.48	0.25	A	WFD	8.19	8.49	...	...	...	8.48	8.38	8.51	8.32	...	8.36	...	...	8.8	...	...	8.31	...
O I	3947.29	9.15	−2.10	B	WFD	...	...	8.62	...	...	...	...	...	...	...	...	...	8.64	8.72	8.7	...	...	8.68
O I	3947.59	9.15	−2.47	B	WFD																		
O I	4772.45	10.74	−1.92	C+	WFD	8.7	...	8.56	...	...	8.67	...	...	...	8.66	...	...	...	8.72	...	8.71	...	8.63
O I	4772.91	10.74	−1.70	C+	WFD																		
O I	4773.75	10.74	−1.55	C+	WFD																		
O I	4967.38	10.74	−1.63	C+	WFD	...	...	8.59	...	8.67	8.72	8.69	8.62	8.7	8.66	...	8.75	8.68	8.73	8.7	8.7	...	8.76
O I	4967.88	10.74	−1.41	C+	WFD																		
O I	4968.79	10.74	−1.26	C+	WFD																		
O I	5329.10	10.74	−1.24	C+	WFD	8.79	8.66	...	8.56	8.72	8.7	8.67	8.71	8.67	8.78	...	8.78	8.73	8.83	8.71	8.77	...	8.67
O I	5329.68	10.74	−1.02	C+	WFD																		
O I	5330.73	10.74	−0.87	C+	WFD																		
O I	6155.96	10.74	−1.36	B+	WFD	8.69	8.57	8.68	8.63	8.63	8.67	8.62	8.64	8.6	8.73	8.76	8.81	8.67	8.75	8.69	8.68	8.74	8.7
O I	6155.97	10.74	−1.01	B+	WFD																		
O I	6155.99	10.74	−1.12	B+	WFD																		
O I	6156.74	10.74	−1.49	B+	WFD																		
O I	6156.76	10.74	−0.90	B+	WFD																		
O I	6156.78	10.74	−0.69	B+	WFD																		
O I	6158.15	10.74	−1.84	B+	WFD																		
O I	6158.17	10.74	−1.00	B+	WFD																		
O I	6158.19	10.74	−0.41	B+	WFD																		
O I	7001.90	10.99	−1.49	B	WFD	...	8.6	8.71	...	...	8.64	8.68	8.69	8.63	...	8.78	8.78	8.71	...	8.73	...	...	8.73
O I	7001.92	10.99	−1.01	B	WFD																		
O I	7002.17	10.99	−2.66	B	WFD																		
O I	7002.20	10.99	−1.49	B	WFD																		

Table A.4: continued.

Ion	$\lambda\,(\text{Å})$	$\chi\,(\text{eV})$	$\log gf$	Acc.	Src.	1	2	3	4	5	6	7	8	9	10	11	12	13	14	15	16	17	18
												$\log\mathrm{X/H}+12$ (star number)											
O I	7002.23	10.99	−0.74	B	WFD																		
O I	7002.25	10.99	−1.36	B	WFD																		
O I	9262.58	10.74	−0.37	A	WFD	...	8.56	...	8.65	...	...	8.59	8.61	8.58	8.73	...	8.76	...	...	...	...	...	...
O I	9262.67	10.74	0.22	A	WFD																		
O I	9262.78	10.74	0.42	A	WFD																		
O II	3954.36	23.42	−0.40	B	WFD	...	...	...	...	...	...	...	...	...	...	...	...	...	...	...	...	...	...
O II	4349.43	23.00	0.06	B	WFD	...	...	...	...	...	...	...	...	...	...	...	...	...	...	...	...	8.77	...
O II	4641.81	22.98	0.05	B	WFD	8.67	...	...	...	...	...	...	...	...	...	...	...	...	...	...	...	...	...
O II	4649.13	23.00	0.31	B	WFD	8.68	...	...	...	...	...	...	...	...	...	8.77	...	...	...	...	...	8.78	...
O II	4661.63	22.98	−0.28	B	WFD	8.62	...	...	...	...	...	...	...	...	...	...	...	...	...	...	...	...	...
Mg I	4702.99	4.35	−0.42	C+	BMZ	...	...	7.46	...	...	...	...	...	...	7.65	...	...	...	...	...	7.57	...	7.59
Mg I	5167.32	2.71	−0.86	B	WSM	...	...	7.45	...	...	...	...	...	...	...	...	...	...	...	...	7.54	...	7.51
Mg I	5172.68	2.71	−0.38	B	WSM	...	...	7.46	7.52	7.53	...	...	...	...	7.65	...	7.61	7.50	...	7.50	7.43	...	7.45
Mg I	5183.60	2.72	−0.16	B	WSM	...	7.58	7.44	7.47	7.44	...	7.51	...	...	7.60	...	7.56	7.45	...	7.46	7.43	...	...
Mg I	5528.41	4.35	−0.40	C+	BMZ	...	...	...	...	...	...	...	...	...	...	...	...	...	...	...	7.55	...	7.52
Mg I	8806.76	4.35	−0.16	C+	BMZ	...	...	7.38	...	...	...	...	...	...	7.55	...	...	7.54	...	7.56	...	...	7.46
Mg II	4384.64	10.00	−0.79	C+	WSM	7.44	...	...	...	...	...	...	...	...	...	...	...	...	...	...	...	...	...
Mg II	4390.51	10.00	−1.71	D	WSM	7.41	7.40	7.53	7.37	7.46	7.50	7.36	7.48	7.51	7.50	7.49	7.54	7.53	7.49	7.52	7.49	7.52	7.52
Mg II	4390.57	10.00	−0.53	D	WSM																		
Mg II	4427.99	10.00	−1.20	C+	WSM	...	7.39	7.44	7.43	7.41	7.47	7.33	...	7.36	7.40	7.64	7.52	7.49	7.46	7.49	7.44	...	...
Mg II	4433.99	10.00	−0.90	C+	WSM	7.35	7.26	7.46	7.29	7.35	7.41	7.24	7.35	7.28	7.43	...	7.47	7.41	7.44	7.46	7.40	...	7.45
Mg II	4739.59	11.57	−0.66	C+	T	7.37	7.38	7.45	7.48	7.40	7.39	7.37	7.46	7.36	7.45	...	7.49	7.46	7.49	7.47	7.41	...	7.47
Mg II	4739.71	11.57	−0.77	C+	T																		
Mg II	5264.22	11.57	−0.36	C+	T	7.52	...	...	...	...	...	...	...	...	...	...	...	...	...	...	...	7.61	...
Mg II	5264.36	11.57	−0.53	C+	T																		
Mg II	6545.97	11.63	0.41	C	CA	...	7.29	7.44	7.38	7.36	7.39	7.27	7.31	7.31	7.48	7.38	7.46	...	7.44	7.48	7.46	7.47	7.47
S II	4153.07	15.90	0.62	D−	WSM	7.02	6.98	...	6.99	6.92	7.05	6.88	6.93	6.9	6.94	7.03	6.89	6.96	7.16	...	7.12	...	7.08
S II	4162.67	15.94	0.78	D−	WSM	6.94	...	...	...	6.91	6.89	6.82	6.79	6.79	6.98	6.97	7.04	...	6.9	...	7.1	...	...
S II	4716.27	13.62	−0.41	D	WSM	7.07	6.96	...	...	6.93	7.07	6.81	6.88	6.92	7	7.17	7.08	6.94	7.1	...	7.01	...	6.96
S II	4815.55	13.67	0.09	D	WSM	6.98	6.93	6.93	6.9	6.99	6.94	6.84	6.81	6.81	6.87	6.99	6.94	6.92	7.05	6.96	6.95	6.96	6.88
S II	5009.57	13.62	−0.28	D	WSM	7.04	...	...	7.08	...	7.1	...	...	...	6.98	7.02	...	...	7.18	...	...	7	...
S II	5032.43	13.67	0.27	D	WSM	6.95	...	...	...	...	...	6.88	6.88	6.88	...	6.88	...	...	7.13	...	...	6.89	...
S II	5320.72	15.07	0.50	D	WSM	6.81	6.87	...	6.91	...	6.96	6.78	...	6.78	...	6.95	7.02	...	6.93	6.99	7.06	6.82	...
S II	5428.66	13.58	−0.13	D	WSM	6.95	6.95	...	...	...	...	...	6.91	...	7.02	7.09	...	...	...	...	...	6.97	...
S II	5453.86	13.67	0.48	D	WSM	7.04	6.99	7	7.02	6.89	7.02	6.93	7.02	6.92	6.86	7.09	...	7.05	7.17	7.1	6.98	7.05	7.01
S II	5509.71	13.62	−0.14	D	WSM	6.96	...	...	...	...	7.01	...	6.89	6.82	6.87	7.01	...	...	7.06	...	7.04	6.89	...
S II	5660.00	13.68	−0.05	D	WSM	7.02	6.97	...	6.99	...	7.06	6.82	6.88	6.93	...	7.01	...	...	7.07	7.07	...	7.04	...
S III	4253.50	18.24	0.36	D	WSM	6.92	...	...	...	...	...	...	...	...	...	...	...	...	...	...	...	...	...
Ti II	3900.56	1.13	−0.45	D	MFW	...	...	...	5.05	...	5.04	...	...	...	5.24	...	...	4.97	...	5.02	...	...	...
Ti II	3913.48	1.12	−0.53	D	MFW	...	...	...	5.06	...	...	...	...	...	5.16	...	...	...	...	...	...	...	...

Table A.4: continued.

Ion	λ (Å)	χ (eV)	log gf	Acc.	Src.	log X/H + 12 (star number)																	
						1	2	3	4	5	6	7	8	9	10	11	12	13	14	15	16	17	18
Ti II	4028.36	1.89	−1.00	D	MFW	...	...	5	...	...	...	...	...	...	5.21	...	5.16	5.07	...	5.08	...	...	5.07
Ti II	4163.63	2.59	−0.40	D	MFW	...	5.10	...	...	5.08	...	...	5.21	5.09	5.28	...	5.22	5.08	...	5.13	5.15	...	5.09
Ti II	4290.22	1.16	−1.12	D−	MFW	...	...	...	...	4.99	5.09	5.09	5.3	4.99	5.23	...	5.07	5	5.03	5	5.02	...	...
Ti II	4290.35	2.06	−1.53	X	KB																		
Ti II	4300.06	1.18	−0.77	D−	MFW	...	...	...	...	5.06	5.18	...	...	...	...	...	...	5.11	...	...	...	...	...
Ti II	4301.92	1.16	−1.16	D−	MFW																		
Ti II	4394.02	1.22	−1.59	D−	MFW	...	4.95	...	5.02	4.88	5.06	5.02	5.29	5.05	5.12	...	5	4.86	5.11	...	4.92	...	...
Ti II	4395.00	1.08	−0.66	D−	MFW																		
Ti II	4443.78	1.08	−0.70	D−	MFW	...	4.87	...	4.91	4.79	4.95	4.97	5.11	4.88	5.03	...	4.91	...	5.04	4.86	4.87	...	...
Ti II	4450.50	1.08	−1.45	D−	MFW	...	4.9	...	4.95	4.87	5.10	5.05	...	5.10	5.04	...	5	4.87	...	4.9	4.91	...	...
Ti II	4468.52	1.13	−0.60	D−	MFW	...	4.87	...	4.9	4.75	4.95	4.96	...	4.9	4.98	...	4.87	...	4.84	...	4.85	...	...
Ti II	4501.27	1.12	−0.75	D−	MFW	...	4.9	...	4.92	4.82	4.99	...	5.29	...	5	...	4.97	4.75	5.05	...	4.89	...	...
Ti II	4563.77	1.22	−0.96	D−	MFW	...	5.04	...	5.13	4.99	5.11	5.13	5.36	5.08	5.21	...	5.13	5	5.13	5.03	5.05	...	...
Ti II	4571.96	1.57	−0.53	D−	MFW	...	5.07	...	5.14	4.99	5.17	5.14	5.35	5.13	5.29	...	5.12	4.99	5.2	5.01	5.06	...	...
Ti II	4779.98	2.05	−1.37	D−	MFW	...	...	...	...	5.07	...	...	...	...	5.22	...	...	...	...	...	...	...	...
Ti II	4805.09	2.06	−1.10	D−	MFW	...	5.06	5.04	...	4.95	...	5.07	...	4.98	5.16	...	...	5.12	...	5.08	5.16	...	5.11
Ti II	5129.16	1.89	−1.39	D−	MFW	...	...	4.91	...	...	...	...	...	...	5.18	...	5.15	5.02	...	5.03	...	...	4.95
Ti II	5188.68	1.58	−1.21	D−	MFW	...	4.92	4.9	5.07	4.91	5.09	...	...	4.97	5.17	...	5.05	4.91	...	4.98	...	...	4.97
Ti II	5336.78	1.58	−1.70	D−	MFW	...	...	4.92	...	...	...	...	...	...	...	...	...	...	...	5.06	5.07	...	4.95
Fe II	3945.21	1.70	−4.25	D	FMW	...	...	7.41	7.36	7.34	7.43	7.30	...	...	7.50	...	7.46	7.47	...	7.49	7.50	...	7.45
Fe II	4041.64	5.57	−3.13	X	KB	...	...	...	...	...	...	...	...	...	...	...	...	7.59	...	...	...	...	...
Fe II	4233.17	2.58	−2.00	C	FMW	7.41	...	...	...	...	...	...	7.53	7.53	...	7.52	...	...	...	...	...	7.53	...
Fe II	4273.32	2.70	−3.34	D	FMW	7.50	7.29	7.51	7.31	7.29	7.33	7.33	7.42	7.35	7.48	...	7.46	7.44	7.50	7.46	7.47	...	7.40
Fe II	4296.57	2.70	−3.01	D	FMW	7.44	7.32	7.40	7.46	7.38	7.45	7.35	7.52	7.37	7.65	7.62	7.54	7.46	7.59	7.53	7.67	...	7.45
Fe II	4489.19	2.83	−2.97	D	FMW	7.50	7.24	...	7.37	7.35	7.44	7.36	7.51	7.33	7.52	...	7.51	7.47	7.57	7.50	7.63	7.71	...
Fe II	4491.40	2.86	−2.70	C	FMW	7.41	7.17	7.56	7.30	7.30	7.36	7.26	7.40	7.24	7.47	7.7	7.48	7.40	7.52	7.48	7.62	7.55	...
Fe II	4508.28	2.86	−2.31	D	KB	7.39	...	...	...	...	...	...	7.41	7.35	...	7.55	...	...	...	...	...	7.53	...
Fe II	4522.63	2.84	−2.11	C	KB	7.33	...	...	...	...	...	...	7.41	7.31	...	7.47	...	...	...	...	...	7.45	...
Fe II	4541.52	2.86	−3.05	D	FMW	7.57	7.30	7.59	7.42	7.39	7.48	7.41	7.53	7.40	7.54	...	7.57	7.52	7.66	7.55	7.64	...	7.45
Fe II	4576.33	2.84	−3.04	D	FMW	7.53	7.36	...	7.40	7.47	7.51	7.39	7.51	7.39	7.59	...	7.61	7.48	7.63	7.58	7.60	...	7.53
Fe II	4620.51	2.83	−3.28	D	FMW	...	7.22	7.40	...	7.29	7.33	...	...	7.35	7.55	...	7.45	...	7.58	7.43	7.50	...	7.38
Fe II	4656.97	2.89	−3.63	E	FMW	...	...	...	...	7.41	...	7.41	...	7.49	7.51	...	7.59	...	...	...	...	...	...
Fe II	4666.75	2.83	−3.33	D	FMW	7.46	7.27	7.49	7.36	7.39	7.43	7.36	7.52	7.38	7.50	...	7.51	7.51	7.64	7.49	7.49	...	7.47
Fe II	4993.35	2.81	−3.65	E	FMW	...	7.33	7.39	...	...	7.40	7.36	...	7.43	7.55	...	7.47	7.45	...	...	7.45	...	7.46
Fe II	5074.05	6.81	−1.97	X	KB	...	...	...	...	...	...	7.49	...	...	7.58	...	7.68	7.58	...	...	7.59	...	...
Fe II	5278.94	5.91	−2.41	X	KB	...	...	7.40	7.45	...	...	...	...	...	7.52	...	...	...	...	...	...	...	...
Fe II	5325.56	3.22	−3.22	X	KB	7.55	7.31	7.49	7.36	7.41	7.44	7.42	7.52	7.39	7.60	7.73	7.57	7.55	7.64	7.51	7.57	...	7.45
Fe II	5427.83	6.72	−1.66	X	KB	...	...	7.38	...	...	...	...	...	...	7.53	...	...	...	...	...	7.46	...	7.46
Fe II	5534.83	3.24	−2.93	D	FMW	...	7.40	7.66	7.51	7.55	7.54	...	...	7.52	7.76	...	7.75	7.59	7.75	7.58	...	...	7.57
Fe II	6147.74	3.89	−2.72	X	KB	7.49	7.39	7.48	7.42	7.41	7.47	7.48	7.58	7.43	7.60	7.8	7.61	7.51	7.69	7.54	7.62	...	7.54

Table A.4: continued.

Ion	λ (Å)	χ (eV)	log gf	Acc.	Src.	1	2	3	4	5	6	7	8	9	10	11	12	13	14	15	16	17	18
														log X/H + 12 (star number)								
Fe II	6149.26	3.89	−2.72	X	KB																		
Fe II	6238.39	3.89	−2.63	X	KB	7.57	...	7.46	7.33	7.28	7.46	...	7.52	7.40	7.60	7.72	...	...	7.61	7.42	7.58	...	7.37
Fe II	6416.92	3.89	−2.85	D	FMW	7.60	7.31	7.51	7.45	7.39	7.44	7.42	7.56	7.44	7.62	...	7.61	7.52	7.65	7.54	7.69	...	7.50
Fe II	6432.68	2.89	−3.74	D	FWM	...	...	7.47	7.41	7.40	7.49	7.40	...	...	7.59	...	7.62	7.49	...	7.56	...	...	7.50
Fe II	6433.81	6.22	−2.47	X	KB																		

Table A.1: Spectral line analysis of the programme stars

Ion	λ (Å)	χ (eV)	log gf	Acc.	Src.	19	20	21	22	23	24	25	26	27	28	29	30	31	32	33	34	35
												log X/H + 12 (star number)										
He I	4009.26	21.22	−1.47	C	WSG	11.21	...	11.11	11.25	...	11.10	11.13	11.15	11.10	11.15	11.19	...	...	11.16	11.11	11.23	11.13
He I	4026.18	20.96	−2.63	A	WSG	11.23	11.14	...	...	...	...	11.23	11.17	11.11	11.17	11.05	11.10	11.11	11.2	11.13	...	...
He I	4026.19	20.96	−0.63	A	WSG																	
He I	4026.20	20.96	−0.85	A	WSG																	
He I	4026.36	20.96	−1.32	A	WSG																	
He I	4120.81	20.96	−1.74	B	WSG	11.13	...	11.06	11.10	11.26	11.04	11.18	11.11	11.15	11.07	11.06	...	...	11.12	...	11.10	11.14
He I	4120.82	20.96	−1.96	B	WSG																	
He I	4120.99	20.96	−2.44	B	WSG																	
He I	4168.97	21.22	−2.34	A	WSG	11.15	...	11.21	...	...	11.11	11.16	...	11.17	11.19	11.19	...	...	...	...	11.08	11.12
He I	4387.93	21.22	−0.88	A	WSG	11.04	...	11.09	...	11.14	...	11.14	11.18	11.07	...	11.16	...	11.11	11.23	11.17	11.12	11.11
He I	4437.55	21.22	−2.03	B	WSG	11.2	...	11.23	11.18	11.08	11.04	11.09	11.09	...	11.11	11.2	...	...	11.16	11.12	11.11	11.13
He I	4471.47	20.96	−0.20	A	WSG	11.17	...	...	11.03	11.18	...	...	11.11	11.08	11.17	11.17	11.14	11.14	11.13	11.11	...	...
He I	4471.49	20.96	−0.42	A	WSG																	
He I	4471.68	20.96	−0.90	A	WSG																	
He I	4713.14	20.96	−1.23	B	WSG	11.06	...	11.17	11.00	11.21	11.03	11.19	11.18	11.18	11.15	...	11.17	10.99	11.15	11.22	11.19	11.10
He I	4713.16	20.96	−1.45	B	WSG																	
He I	4713.38	20.96	−1.93	B	WSG																	
He I	4921.93	21.22	−0.44	A	WSG	11.16	10.99	...	11.15	11.23	11.14	11.21	...	11.24	11.06	11.08	...	11.03	11.17	11.11	...	...
He I	5015.68	20.62	−0.82	AA	WSG		11.2	11.18	...	11.12	...	...	...	...	...	11.16	...	...	...	...	...	...
He I	5875.60	20.96	−1.52	A	WSG	...	11.03	...	11.09	11.2	...	...	11.2	...	...	11.16	11.14	11.15	...	11.23	...	...
He I	5875.61	20.96	0.48	A	WSG																	
He I	5875.63	20.96	−0.34	A	WSG																	
He I	5875.64	20.96	0.14	A	WSG																	
He I	5875.97	20.96	−0.22	A	WSG																	
C I	4771.74	7.49	−1.87	C	WFD		...	8.26	...	...	8.21	...	8.30	8.24	8.21	...	...	...	...	8.16	8.29	...
C I	4775.90	7.49	−2.30	C	WFD		...	8.15	...	...	8.24	...	...	...	...	...	...	...	...	...	8.43	...
C I	4932.05	7.68	−1.70	B	LP		...	...	...	...	...	...	...	...	...	...	...	...	...	...	8.23	...
C I	5052.17	7.68	−1.45	C	LP		...	8.17	...	...	7.96	...	8.16	...	...	...	...	8.41	...	...	8.1	...
C I	7113.18	8.65	−0.77	B−	WFD	...	8.20	...	...	8.02	...	...	...	...	...	...	...	...	...	8.28	8.26	...

Table A.1: continued.

Ion	λ (Å)	χ (eV)	log gf	Acc.	Src.	log X/H + 12 (star number)																	
						19	20	21	22	23	24	25	26	27	28	29	30	31	32	33	34	35	
C I	9111.81	7.49	−0.30	B	WFD	...	...	...	...	...	...	...	...	...	...	...	...	...	...	...	...	...	
C II	4267.00	18.05	0.56	C+	WFD	...	...	8.16	...	...	8.22	8.27	...	...	...	...	...	...	...	...	8.20	8.30	
C II	4267.26	18.05	0.74	C+	WFD																		
C II	5132.95	20.70	−0.21	B	WFD	8.22	8.04	8.06	7.94	8.04	8.1	8.20	8.13	8.26	8.45	8.21	8.41	8.55	8.19	8.18	8.07	8.13	
C II	5133.28	20.70	−0.18	B	WFD																		
C II	5145.16	20.71	0.19	B	WFD		...	...	...	...	...	8.21	...	...	...	...	...	...	...	...	8.25	8.45	
C II	5151.08	20.71	−0.18	B	WFD		...	...	...	...	...	...	...	...	...	...	...	...	...	...	...	...	...
C II	6151.27	20.84	−0.15	D	F	...	...	...	...	...	8.25	...	...	...	...	...	...	...	...	...	...	...	
C II	6578.05	14.45	−0.03	B	WFD	8.36	...	8.31	8.17	8.12	8.36	8.26	8.17	8.41	8.56	8.16	8.34	8.47	8.38	...	8.38	8.40	
C II	6582.88	14.45	−0.33	B	WFD	8.34	...	...	8.23	...	...	8.30	...	...	...	8.11	...	...	...	8.36	8.36	8.44	
N I	6008.47	11.60	−1.11	C+	WFD	...	8.52	...	...	8.68	...	8.63	...	8.43	...	8.51	...	8.6	...	8.52	...	...	
N I	7423.64	10.33	−0.71	B+	WFD	8.48	8.52	8.48	8.66	8.64	8.51	8.47	8.43	8.42	8.35	8.47	8.55	8.43	8.32	8.47	...	8.57	
N I	7442.30	10.33	−0.38	B+	WFD	8.45	8.53	8.5	8.55	8.63	8.48	8.5	8.46	8.44	8.35	8.45	8.6	8.37	8.31	8.48	8.52	8.56	
N I	7468.31	10.34	−0.19	B+	WFD	8.44	8.54	8.51	8.56	8.62	8.44	8.49	8.45	8.45	8.32	8.4	8.59	8.44	8.35	8.57	8.59	8.6	
N I	7898.98	12.36	0.02	C	WFD	8.42	...	...	...	...	...	8.43	...	...	...	8.43	...	8.45	8.31	8.49	...	...	
N I	7899.28	12.36	−0.91	C	WFD																		
N I	8680.28	10.34	0.35	B+	WFD	8.44	...	8.48	8.44	...	8.53	8.6	...	...	8.45	...	8.64	...	...	...	8.46	8.66	
N I	8703.25	10.33	−0.32	B+	WFD	8.48	8.61	8.59	8.62	8.81	8.49	8.63	8.63	8.55	8.44	8.51	8.69	8.51	8.41	8.61	8.54	8.61	
N I	8711.70	10.33	−0.23	B+	WFD	8.46	8.52	...	8.58	8.79	8.54	8.56	8.52	8.48	8.54	8.55	8.65	8.59	8.37	8.56	8.62	8.64	
N I	8718.84	10.34	−0.34	B+	WFD	...	8.49	8.54	8.53	8.73	8.53	8.56	8.57	8.47	8.53	8.52	8.66	8.56	8.32	8.51	8.61	8.56	
N II	3995.00	18.50	0.21	B	WFD	8.37	...	...	8.52	...	8.36	8.45	...	8.43	8.4	8.41	...	...	8.29	...	8.46	8.52	
N II	4447.03	20.41	0.23	B	WFD	...	...	8.64	...	...	8.45	...	...	...	8.38	...	...	...	...	...	8.64	8.61	
N II	4601.48	18.46	−0.43	B+	WFD	8.54	...	8.53	...	...	8.4	...	...	...	...	...	...	...	...	...	8.55	8.62	
N II	4607.15	18.46	−0.51	B+	WFD	8.56	...	8.49	...	...	8.41	...	...	...	8.53	...	...	...	...	...	8.53	8.61	
N II	4643.09	18.48	−0.36	B+	WFD	8.39	...	8.61	...	...	8.41	8.53	...	...	8.34	...	...	...	...	...	8.53	8.55	
N II	5666.63	18.47	−0.05	A	WFD	8.36	...	8.5	...	...	8.4	...	...	...	...	...	...	...	...	...	8.48	8.61	
N II	5679.56	18.48	0.25	A	WFD	8.38	...	8.63	...	...	8.52	...	...	...	8.56	...	...	...	...	...	8.62	8.65	
O I	3947.29	9.15	−2.10	B	WFD	...	8.65	...	...	...	8.74	8.64	8.66	8.66	8.74	8.69	8.78	8.81	...	...	8.76	8.67	
O I	3947.59	9.15	−2.47	B	WFD																		
O I	4772.45	10.74	−1.92	C+	WFD	8.69	...	...	...	8.67	8.7	8.73	...	8.75	8.78	8.74	...	...	8.63	8.68	...	...	
O I	4772.91	10.74	−1.70	C+	WFD																		
O I	4773.75	10.74	−1.55	C+	WFD																		
O I	4967.38	10.74	−1.63	C+	WFD	8.76	8.59	...	8.6	8.72	8.72	8.74	8.72	8.74	8.74	8.71	8.8	8.86	8.68	8.7	8.83	8.75	
O I	4967.88	10.74	−1.41	C+	WFD																		
O I	4968.79	10.74	−1.26	C+	WFD																		
O I	5329.10	10.74	−1.24	C+	WFD	8.76	8.64	...	8.62	8.77	8.79	8.79	8.76	8.78	8.79	8.78	8.77	8.86	8.76	8.76	8.78	8.79	
O I	5329.68	10.74	−1.02	C+	WFD																		
O I	5330.73	10.74	−0.87	C+	WFD																		
O I	6155.96	10.74	−1.36	B+	WFD	8.76	8.68	8.51	8.55	8.73	8.69	8.77	8.71	8.73	8.77	8.73	8.86	8.89	8.73	8.74	8.75	8.74	
O I	6155.97	10.74	−1.01	B+	WFD																		

Table A.1: continued.

Ion	λ (Å)	χ (eV)	log gf	Acc.	Src.	log X/H + 12 (star number)																
---	---	---	---	---	---	19	20	21	22	23	24	25	26	27	28	29	30	31	32	33	34	35
O I	6155.99	10.74	−1.12	B+	WFD																	
O I	6156.74	10.74	−1.49	B+	WFD																	
O I	6156.76	10.74	−0.90	B+	WFD																	
O I	6156.78	10.74	−0.69	B+	WFD																	
O I	6158.15	10.74	−1.84	B+	WFD																	
O I	6158.17	10.74	−1.00	B+	WFD																	
O I	6158.19	10.74	−0.41	B+	WFD																	
O I	7001.90	10.99	−1.49	B	WFD	...	8.66	...	8.63	8.78	...	...	8.7	8.71	8.84	8.79	8.83	8.9	8.74	8.7	...	8.76
O I	7001.92	10.99	−1.01	B	WFD																	
O I	7002.17	10.99	−2.66	B	WFD																	
O I	7002.20	10.99	−1.49	B	WFD																	
O I	7002.23	10.99	−0.74	B	WFD																	
O I	7002.25	10.99	−1.36	B	WFD																	
O I	9262.58	10.74	−0.37	A	WFD		...	...	8.56	8.69	...	...	...	...	...	...	...	...	...	...	...	...
O I	9262.67	10.74	0.22	A	WFD																	
O I	9262.78	10.74	0.42	A	WFD																	
O II	3954.36	23.42	−0.40	B	WFD	...	...	...	...	...	8.78	...	...	...	...	...	...	...	...	...	...	...
O II	4349.43	23.00	0.06	B	WFD	...	...	...	...	...	...	...	...	...	...	...	...	...	...	...	8.67	...
O II	4641.81	22.98	0.05	B	WFD	...	...	...	...	...	8.75	...	...	...	...	...	...	...	...	...	8.66	8.79
O II	4649.13	23.00	0.31	B	WFD	...	...	...	...	...	8.82	...	...	...	8.83	...	...	...	...	...	8.85	8.85
O II	4661.63	22.98	−0.28	B	WFD	...	...	...	...	...	8.68	...	...	...	...	...	...	...	...	...	8.76	...
Mg I	4702.99	4.35	−0.42	C+	BMZ	...	7.49	...	...	7.63	...	7.61	7.63	...	...	7.57	7.71	7.73	7.47	7.57	...	...
Mg I	5167.32	2.71	−0.86	B	WSM	...	7.40	...	...	7.62	...	7.55	...	...	...	7.63	7.62	...	...	...	...	...
Mg I	5172.68	2.71	−0.38	B	WSM	...	7.46	...	...	7.58	...	7.52	7.46	7.56	...	7.61	7.55	7.66	7.38	7.47	...	...
Mg I	5183.60	2.72	−0.16	B	WSM	...	7.47	...	...	7.55	...	7.48	7.40	7.52	...	7.57	7.55	7.60	7.36	7.45	...	...
Mg I	5528.41	4.35	−0.40	C+	BMZ	...	7.45	...	...	7.56	...	7.54	...	...	...	7.53	...	...	...	...	...	...
Mg I	8806.76	4.35	−0.16	C+	BMZ	...	7.47	...	...	7.60	...	...	...	...	...	...	7.50	...	7.46	7.54	...	...
Mg II	4384.64	10.00	−0.79	C+	WSM	...	...	7.51	...	...	...	...	...	...	...	...	...	...	...	...	...	...
Mg II	4390.51	10.00	−1.71	D	WSM	7.53	7.60	7.33	7.41	7.59	7.38	7.54	7.60	7.53	7.57	7.57	7.66	7.76	7.49	7.54	7.61	7.47
Mg II	4390.57	10.00	−0.53	D	WSM																	
Mg II	4427.99	10.00	−1.20	C+	WSM	7.43	7.49	...	...	7.55	...	7.53	7.47	7.47	7.56	7.54	7.45	7.68	7.34	7.46	7.51	7.40
Mg II	4433.99	10.00	−0.90	C+	WSM	7.42	7.44	...	7.28	7.51	...	7.49	7.43	7.41	7.46	7.50	7.57	7.65	7.34	7.40	7.46	7.36
Mg II	4739.59	11.57	−0.66	C+	T	7.47	7.46	7.46	7.44	7.51	7.42	7.48	7.40	7.46	7.48	7.49	7.51	7.68	7.40	7.39	7.50	7.45
Mg II	4739.71	11.57	−0.77	C+	T																	
Mg II	5264.22	11.57	−0.36	C+	T	...	...	...	...	...	7.52	...	...	...	...	...	...	...	...	...	...	...
Mg II	5264.36	11.57	−0.53	C+	T																	
Mg II	6545.97	11.63	0.41	C	CA	7.40	7.52	...	7.36	7.53	...	7.58	7.43	7.46	7.45	7.47	7.52	7.72	7.42	7.48	...	...
S II	4153.07	15.90	0.62	D−	WSM	7.08	...	6.91	6.84	7.04	7.03	7.13	7.16	7	7.24	...	...	7.28	7.08	7.02	7.14	6.99
S II	4162.67	15.94	0.78	D−	WSM	6.99	...	6.86	6.87	7	6.94	6.99	...	7.01	7.12	7.08	7.2	...	6.93	...	7.03	6.89
S II	4716.27	13.62	−0.41	D	WSM	7.02	7.08	6.82	6.84	7.08	7.08	7.01	6.94	7.1	7.14	7.12	...	7.35	7.03	7.05	7.17	7

Table A.1: continued.

Ion	λ (Å)	χ (eV)	log gf	Acc.	Src.	log X/H + 12 (star number)																
						19	20	21	22	23	24	25	26	27	28	29	30	31	32	33	34	35
S II	4815.55	13.67	0.09	D	WSM	6.98	6.89	6.87	6.85	6.96	7.02	6.96	6.96	7.01	7.13	6.99	7.23	7.22	6.93	7.01	7.13	7.02
S II	5009.57	13.62	−0.28	D	WSM	7.05	...	6.89	6.93	...	7.06	...	...	...	7.19	7.14	...	...	...	...	7.14	7.03
S II	5032.43	13.67	0.27	D	WSM	7.04	...	6.8	6.93	...	6.95	...	...	...	7.2	7.03	...	...	...	...	7.07	6.97
S II	5320.72	15.07	0.50	D	WSM	6.93	6.96	6.77	6.84	6.97	6.87	6.94	7.08	7.11	7.06	7.01	...	7.15	7.01	7.04	7.03	6.9
S II	5428.66	13.58	−0.13	D	WSM	...	...	6.87	6.92	7.06	7.01	7.14	...	...	7.14	7.13	...	7.26	...	...	7.15	7.1
S II	5453.86	13.67	0.48	D	WSM	7.01	6.94	7.05	7.05	6.92	7.13	7.02	7.1	7.11	7.26	6.96	7.1	7.25	7.13	7.04	7.33	7.21
S II	5509.71	13.62	−0.14	D	WSM	7.02	...	7.03	7.04	7.01	7.04	7.11	...	...	...	7.06	...	7.36	7.05	7.07	7.18	7.06
S II	5660.00	13.68	−0.05	D	WSM	7.04	...	6.89	6.99	...	7.06	...	...	...	7.1	...	...	...	...	...	7.15	7.07
S III	4253.50	18.24	0.36	D	WSM	...	...	...	...	...	...	...	...	...	...	...	...	...	...	...	...	...
Ti II	3900.56	1.13	−0.45	D	MFW	...	...	...	...	...	...	5.10	5.17	5.17	5.36	5.26	5.12	5.35	4.96	...	5.55	5.43
Ti II	3913.48	1.12	−0.53	D	MFW	...	...	...	...	...	...	5.08	5.12	5.21	5.28	5.21	5.15	5.4	4.96	...	...	...
Ti II	4028.36	1.89	−1.00	D	MFW	...	5.05	...	...	...	...	5.11	5.07	5.16	...	5.2	5.13	5.25	5.02	5.14	...	...
Ti II	4163.63	2.59	−0.40	D	MFW	5.31	5.12	...	...	5.2	...	5.17	5.15	5.24	5.28	5.28	5.18	...	5.06	5.22	...	...
Ti II	4290.22	1.16	−1.12	D−	MFW	5.22	5.03	...	...	5.10	...	5.08	5.07	5.13	5.36	5.2	5.14	...	4.96	5.13	5.54	5.24
Ti II	4290.35	2.06	−1.53	X	KB																	
Ti II	4300.06	1.18	−0.77	D−	MFW	...	...	...	...	...	...	5.06	...	5.32	...	...	...	...	5.12	...	...	5.52
Ti II	4301.92	1.16	−1.16	D−	MFW																	
Ti II	4394.02	1.22	−1.59	D−	MFW	5.26	...	...	5.23	...	...	4.98	4.95	5.06	5.28	5.12	5.11	5.17	4.86	...	...	...
Ti II	4395.00	1.08	−0.66	D−	MFW																	
Ti II	4443.78	1.08	−0.70	D−	MFW	5.13	...	...	5.11	...	...	4.88	4.88	4.94	5.06	5.04	5.04	5.05	...	...	5.39	...
Ti II	4450.50	1.08	−1.45	D−	MFW	...	4.83	...	...	4.98	...	4.89	4.9	5	5.23	5.06	5.10	...	4.83	4.94	...	...
Ti II	4468.52	1.13	−0.60	D−	MFW	5.11	4.82	...	5	...	...	4.85	4.79	4.91	...	5.01	5.02	5.05	...	...	...	...
Ti II	4501.27	1.12	−0.75	D−	MFW	5.13	4.81	...	...	...	...	4.87	4.89	4.92	...	5.05	5.04	5.10	...	...	5.56	...
Ti II	4563.77	1.22	−0.96	D−	MFW	...	5.04	...	...	5.11	...	5.10	5.08	5.17	5.3	5.25	5.15	5.29	4.96	5.07	5.54	5.28
Ti II	4571.96	1.57	−0.53	D−	MFW	5.36	...	...	5.3	5.18	...	5.13	5.14	5.21	5.37	5.27	5.15	5.37	5.06	...	5.63	5.41
Ti II	4779.98	2.05	−1.37	D−	MFW	...	5.10	...	...	...	...	5.15	5.23	5.25	...	...	...	...	5.15	5.21	...	...
Ti II	4805.09	2.06	−1.10	D−	MFW	...	5.07	...	...	5.17	...	5.09	5.10	5.16	...	5.22	5.26	5.32	5	5.14	...	...
Ti II	5129.16	1.89	−1.39	D−	MFW	...	4.95	...	...	5.14	...	...	5.11	5.09	...	5.19	5.10	5.26	4.94	5.10	...	...
Ti II	5188.68	1.58	−1.21	D−	MFW	...	4.9	...	...	5.08	...	5.08	4.98	5.06	...	5.18	5.07	5.22	4.9	5.07	...	...
Ti II	5336.78	1.58	−1.70	D−	MFW	...	...	...	...	5.11	...	5.09	...	...	...	5.19	5.16	...	...	5.02	...	...
Fe II	3945.21	1.70	−4.25	D	FMW	7.55	...	...	...	...	...	7.46	7.50	7.46	7.64	7.59	7.65	7.71	7.37	7.52	7.74	...
Fe II	4041.64	5.57	−3.13	X	KB	...	...	...	...	7.56	...	7.55	7.52	...	...	...	...	...	7.37	7.53	...	...
Fe II	4233.17	2.58	−2.00	C	FMW	...	...	7.45	7.45	...	7.51	...	...	...	...	...	...	...	...	...	7.67	7.71
Fe II	4273.32	2.70	−3.34	D	FMW	7.52	7.46	...	7.46	7.55	7.61	7.46	7.44	7.46	7.62	7.54	7.59	7.66	7.36	7.54	7.72	7.49
Fe II	4296.57	2.70	−3.01	D	FMW	7.57	7.51	7.59	7.51	...	7.57	7.59	7.53	7.60	7.66	7.7	7.64	7.83	7.56	7.61	7.71	7.54
Fe II	4489.19	2.83	−2.97	D	FMW	7.53	7.57	7.34	7.42	7.61	...	7.55	7.51	7.55	7.59	7.57	7.64	7.74	7.45	...	7.64	7.47
Fe II	4491.40	2.86	−2.70	C	FMW	7.48	7.46	7.33	7.36	7.61	7.46	7.45	7.47	7.55	7.55	7.56	7.58	...	7.43	7.58	7.53	7.42
Fe II	4508.28	2.86	−2.31	D	KB	...	...	7.38	7.39	...	7.48	...	...	...	7.65	...	...	...	...	...	7.58	7.55
Fe II	4522.63	2.84	−2.11	C	KB	...	...	7.38	7.36	...	7.42	...	...	...	...	...	...	...	...	...	7.48	7.48
Fe II	4541.52	2.86	−3.05	D	FMW	7.60	7.54	7.51	7.54	7.65	7.62	7.58	7.59	7.61	7.67	7.60	7.68	...	7.49	7.62	7.73	7.59

Table A.1: continued.

Ion	λ (Å)	χ (eV)	log gf	Acc.	Src.	19	20	21	22	23	24	25	26	27	28	29	30	31	32	33	34	35
													log X/H + 12 (star number)									
Fe II	4576.33	2.84	−3.04	D	FMW	7.55	7.53	...	7.52	7.7	7.53	7.58	7.61	7.60	7.63	7.72	7.7	...	7.53	7.68	7.63	7.55
Fe II	4620.51	2.83	−3.28	D	FMW	7.52	7.36	...	7.37	7.53	...	7.47	7.41	...	7.59	7.58	7.51	7.68	7.30	7.47	...	...
Fe II	4656.97	2.89	−3.63	E	FMW	...	...	...	...	7.65	...	7.56	7.57	...	...	7.56	7.7	...	7.41	...	...	...
Fe II	4666.75	2.83	−3.33	D	FMW	7.51	7.49	...	7.41	7.59	7.52	7.49	7.48	7.49	7.56	7.60	7.62	7.67	7.37	7.62	7.69	7.54
Fe II	4993.35	2.81	−3.65	E	FMW	7.67	7.43	...	7.48	7.55	7.64	7.53	7.40	7.50	...	7.58	...	7.67	7.36	7.48	7.58	7.50
Fe II	5074.05	6.81	−1.97	X	KB	...	...	...	...	7.56	...	7.59	7.57	...	...	7.59	7.59	...	7.52	7.51	...	...
Fe II	5278.94	5.91	−2.41	X	KB	...	...	...	...	...	...	7.59	7.45	7.52	...	7.67	...	...	7.44	...	...	...
Fe II	5325.56	3.22	−3.22	X	KB	7.62	7.38	7.65	7.51	7.65	7.59	7.55	7.52	7.48	7.67	7.69	7.60	7.78	7.44	7.67	7.76	7.59
Fe II	5427.83	6.72	−1.66	X	KB	7.64	...	...	...	7.48	...	7.53	...	...	...	7.60	...	7.56	...	...	...	...
Fe II	5534.83	3.24	−2.93	D	FMW	7.74	...	7.43	7.49	...	7.48	7.69	7.7	7.69	7.76	...	7.74	...	7.71	...	...	7.65
Fe II	6147.74	3.89	−2.72	X	KB	7.60	7.51	7.44	7.52	7.63	7.68	7.57	7.51	7.52	7.68	7.65	7.66	7.73	7.46	7.56	7.73	7.55
Fe II	6149.26	3.89	−2.72	X	KB																	
Fe II	6238.39	3.89	−2.63	X	KB	7.66	7.39	7.67	7.45	7.57	7.73	7.66	7.44	7.54	7.59	7.57	7.57	7.63	7.50	7.45	7.74	7.60
Fe II	6416.92	3.89	−2.85	D	FMW	7.67	7.49	7.53	7.37	7.62	...	7.61	7.53	7.51	7.68	7.68	7.60	7.78	7.47	7.65	...	7.58
Fe II	6432.68	2.89	−3.74	D	FWM	...	7.51	...	...	7.60	...	7.56	7.45	7.48	...	7.66	7.63	7.68	7.48	7.47	...	...
Fe II	6433.81	6.22	−2.47	X	KB																	

accuracy indicators – uncertainties within: AA: 1%; A: 3%; B: 10%; C: 25%; D: 50%; E: larger than 50%; X: unknown

sources of gf-values – BMZ: Butler et al. (1993); CA: Coulomb approximation, Bates & Damgaard (1949); FMW: Fuhr et al. (1988); KB: Kurucz & Bell (1995); LP: Luo & Pradhan (1989); MFW: Martin et al. (1988); T: Taylor (available from Topbase); WFD: Wiese et al. (1996); WSM: Wiese et al. (1969); sources for Stark broadening parameters – H I: Stehlé & Hutcheon (1999); He I: Barnard et al. (1969), Barnard et al. (1974), Dimitrijevic & Sahal-Brechot (1990); C I: Griem (1974), Cowley (1971); C II: Griem (1964), Griem (1974), Cowley (1971); N I/II: Griem (1964), Griem (1974), Cowley (1971); O I/II: Cowley (1971)); Mg I: Dimitrijevic & Sahal-Brechot (1996)), Cowley (1971); Mg II: Griem (1964), Griem (1974),Cowley (1971); S II/III: (Cowley (1971);

Bibliography

Abramowitz, M., Stegun, I. A., & Romer, R. H. 1988, American Journal of Physics, 56, 958

Adelman, S. J. & Albayrak, B. 1997, Information Bulletin on Variable Stars, 4541, 1

Aerts, C., Puls, J., Godart, M., & Dupret, M. 2009, A&A, 508, 409

Allen, C. & Santillan, A. 1991, RMxAA, 22, 255

Aller, L. H. 1991, Atoms, Stars, and Nebulae, ed. Aller, L. H.

Andrievsky, S. M., Bersier, D., Kovtyukh, V. V., et al. 2002a, A&A, 384, 140

Andrievsky, S. M., Kovtyukh, V. V., Luck, R. E., et al. 2002b, A&A, 381, 32

Andrievsky, S. M., Kovtyukh, V. V., Luck, R. E., et al. 2002c, A&A, 392, 491

Andrievsky, S. M., Luck, R. E., Martin, P., & Lépine, J. R. D. 2004, A&A, 413, 159

Asplund, M., Grevesse, N., Sauval, A. J., & Scott, P. 2009, ARA&A, 47, 481

Asplund, M., Nordlund, Å., Trampedach, R., Allende Prieto, C., & Stein, R. F. 2000, A&A, 359, 729

Auer, L. H. & Mihalas, D. 1969, ApJ, 158, 641

Avrett, E. H. & Krook, M. 1963, ApJ, 137, 874

Bagnulo, S., Jehin, E., Ledoux, C., et al. 2003, The Messenger, 114, 10

Barnard, A. J., Cooper, J., & Shamey, L. J. 1969, A&A, 1, 28

Barnard, A. J., Cooper, J., & Smith, E. W. 1974, J. Quant. Spec. Radiat. Transf., 14, 1025

Bates, D. R. & Damgaard, A. 1949, Royal Society of London Philosophical Transactions Series A, 242, 101

Becker, S. R. 1998, in ASP Conf. Ser., Vol. 131, ASP Conf. Ser., 137–+

Bessell, M. S., Castelli, F., & Plez, B. 1998, A&A, 333, 231

Bethe, H. A. 1939, Phys. Rev., 55, 434

Blaha, C. & Humphreys, R. M. 1989, AJ, 98, 1598

Bohlin, R. C. & Gilliland, R. L. 2004, AJ, 127, 3508

Bresolin, F., Pietrzyński, G., Gieren, W., et al. 2004, ApJ, 600, 182

Bresolin, F., Urbaneja, M. A., Gieren, W., Pietrzyński, G., & Kudritzki, R.-P. 2007, ApJ, 671, 2028

Burbidge, E. M., Burbidge, G. R., Fowler, W. A., & Hoyle, F. 1957, Rev. Mod. Phys., 29, 547

Butler, K. & Giddings, J. R. 1985, in: Newsletter on Analysis of Astronomical Spectra No. 9 ((Univ. London))

Butler, K., Mendoza, C., & Zeippen, C. J. 1993, Journal of Physics B, 26, 4409

Cantiello, M., Langer, N., Brott, I., et al. 2009, A&A, 499, 279

Cardelli, J. A., Clayton, G. C., & Mathis, J. S. 1989, ApJ, 345, 245

Caughlan, G. R. & Fowler, W. A. 1962, ApJ, 136, 453

Cescutti, G., Matteucci, F., François, P., & Chiappini, C. 2007, A&A, 462, 943

Chiappini, C., Matteucci, F., & Gratton, R. 1997, ApJ, 477, 765

Chiappini, C., Matteucci, F., & Romano, D. 2001, ApJ, 554, 1044

Chiosi, C., Bertellis, G., & Bressan, A. 1992, in Instabilities in Evolved Super- and Hypergiants ((Amsterdam: North-Holland), 145–+

Clark, J. S., Negueruela, I., Crowther, P. A., & Goodwin, S. P. 2005, A&A, 434, 949

Clayton, D. D. 1983, Principles of stellar evolution and nucleosynthesis (Chicago: University of Chicago Press)

Cohen, M., Wheaton, W. A., & Megeath, S. T. 2003, AJ, 126, 1090

Collins, G. W. 1989, The fundamentals of stellar astrophysics (New York: Freeman)

Cordiner, M. A., Cox, N. L. J., Trundle, C., et al. 2008a, A&A, 480, L13

Cordiner, M. A., Smith, K. T., Cox, N. L. J., et al. 2008b, A&A, 492, L5

Costa, R. D. D., Uchida, M. M. M., & Maciel, W. J. 2004, A&A, 423, 199

Cowley, C. R. 1971, The Observatory, 91, 139

Cox, A. N. 2000, Allen's astrophysical quantities (New York: Springer-Verlag)

Crowther, P. A., Lennon, D. J., & Walborn, N. R. 2006, A&A, 446, 279

Cutri, R. M., Skrutskie, M. F., van Dyk, S., et al. 2003, 2MASS All Sky Catalog of point sources

Daflon, S. & Cunha, K. 2004, ApJ, 617, 1115

Daflon, S., Cunha, K., & Becker, S. R. 1999, ApJ, 522, 950

de Jager, C., Nieuwenhuijzen, H., & van der Hucht, K. A. 1988, A&AS, 72, 259

Dekker, H., D'Odorico, S., Kaufer, A., Delabre, B., & Kotzlowski, H. 2000, in Proc. SPIE, Vol. 4008, , 534–545

Dimitrijevic, M. S. & Sahal-Brechot, S. 1990, A&AS, 82, 519

Dimitrijevic, M. S. & Sahal-Brechot, S. 1996, A&AS, 117, 127

Dufton, P. L., Ryans, R. S. I., Trundle, C., et al. 2005, A&A, 434, 1125

Dufton, P. L., Smartt, S. J., Lee, J. K., et al. 2006, A&A, 457, 265

Eddington, A. S. 1926, The Internal Constitution of the Stars (Cambridge: Cambridge University Press)

Eggenberger, P., Meynet, G., & Maeder, A. 2002, A&A, 386, 576

Esteban, C., García-Rojas, J., Peimbert, M., et al. 2005, ApJ, 618, L95

Bibliography

Esteban, C., Peimbert, M., García-Rojas, J., et al. 2004, MNRAS, 355, 229

Evans, C. J., Bresolin, F., Urbaneja, M. A., et al. 2007, ApJ, 659, 1198

Fasano, G. & Vio, R. 1988, Bulletin d'Information du Centre de Donnees Stellaires, 35, 191

Firnstein, M. & Przybilla, N. 2006, PoSNIC-IX:095

François, P., Matteucci, F., Cayrel, R., et al. 2004, A&A, 421, 613

Fraser, M., Dufton, P. L., Hunter, I., & Ryans, R. S. I. 2010, MNRAS, 404, 1306

Fryer, C. L. 1999, ApJ, 522, 413

Fuhr, J. R., Martin, G. A., & Wiese, W. L. 1988, 17, 4

Gallart, C., Zoccali, M., & Aparicio, A. 2005, ARA&A, 43, 387

Gamow, G. 1928, Z.f.Physik, 5, 510

Gautschy, A. 2009, A&A, 498, 273

Ghez, A. M., Salim, S., Weinberg, N. N., et al. 2008, ApJ, 689, 1044

Giddings, J. R. 1981, Ph.D. Thesis, (Univ. London)

Gilfanov, M. & Bogdán, Á. 2010, Nature, 463, 924

Gillessen, S., Eisenhauer, F., Trippe, S., et al. 2009, ApJ, 692, 1075

Gilmore, G. & Reid, N. 1983, MNRAS, 202, 1025

Gray, D. F. 1997, High resolution spectroscopy., ed. Rodríguez Espinosa, J. M., Herrero, A., & Sánchez, F. , 163–202

Gray, D. F. 2005, The Observation and Analysis of Stellar Photospheres, 3rd ed. (New York: Cambridge University Press, Cambridge)

Grevesse, N. & Sauval, A. J. 1998, Space Science Reviews, 85, 161

Griem, H. R. 1964, Plasma spectroscopy (New York: McGraw-Hill)

Griem, H. R. 1974, Spectral line broadening by plasmas (New York: Academic Press)

Griem, H. R. 2005, Principles of Plasma Spectroscopy (Cambridge: Cambridge University Press)

Grosbøl, P. & Ponz, D. 1990, in Acquisition, Processing and Archiving of Astronomical Images, 111–123

Gummersbach, C. A., Kaufer, A., Schaefer, D. R., Szeifert, T., & Wolf, B. 1998, A&A, 338, 881

Gustafsson, B., Bell, R. A., Eriksson, K., & Nordlund, A. 1975, A&A, 42, 407

Gvaramadze, V. V. & Bomans, D. J. 2008, A&A, 490, 1071

Hayashi, C., Nishida, M., & Sugimoto, D. 1962, Progress of Theoretical Physics, 27, 1233

Heger, A. & Langer, N. 1998, A&A, 334, 210

Heger, A. & Langer, N. 2000, ApJ, 544, 1016

Heger, A., Langer, N., & Woosley, S. E. 2000, ApJ, 528, 368

Heger, A., Woosley, S. E., & , H. C. 2005, ApJ, 626, 350

Hendry, E. M. 1981, AJ, 86, 1540

Hilborn, R. C. 1982, American Journal of Physics, 50, 982

Hirsch, H. A. 2009, Ph.D. Thesis, (Univ. Erlangen-Nuremberg)

Hirschi, R., Meynet, G., & Maeder, A. 2004, A&A, 425, 649

Hirschi, R., Meynet, G., & Maeder, A. 2005, A&A, 433, 1013

Holmberg, J., Nordström, B., & Andersen, J. 2007, A&A, 475, 519

Hou, L. G., Han, J. L., & Shi, W. B. 2009, A&A, 499, 473

Huang, W. & Gies, D. R. 2006a, ApJ, 648, 580

Huang, W. & Gies, D. R. 2006b, ApJ, 648, 591

Hubeny, I. 1997, in: Stellar Atmospheres: Theory and Observations ((Berlin: Springer)

Hubeny, I. 2003, in ASP Conf. Ser., Vol. 288, ASP Conf. Ser., 17–+

Hubeny, I. & Lanz, T. 1995, ApJ, 439, 875

Hummer, D. G., Berrington, K. A., Eissner, W., et al. 1993, A&A, 279, 298

Hunter, I., Brott, I., Langer, N., et al. 2009, A&A, 496, 841

Hunter, I., Lennon, D. J., Dufton, P. L., et al. 2008, A&A, 479, 541

Irrgang, A., Przybilla, N., Heber, U., Nieva, M. F., & Schuh, S. 2010, ApJ, 711, 138

Johnson, H. L. 1958, Lowell Observatory Bulletin, 4, 37

Johnson, H. L. & Morgan, W. W. 1953, ApJ, 117, 313

Kaufer, A., Stahl, O., Tubbesing, S., et al. 1999, The Messenger, 95, 8

Kaufer, A., Stahl, O., Wolf, B., et al. 1997, A&A, 320, 273

Kaufer, A., Stahl, O., Wolf, B., et al. 1996, A&A, 314, 599

Kaufer, A., Venn, K. A., Tolstoy, E., Pinte, C., & Kudritzki, R.-P. 2004, AJ, 127, 2723

Kennicutt, Jr., R. C. 1998, ApJ, 498, 541

Kippenhahn, R. & Weigert, A. 1990, Stellar Structure and Evolution (Berlin: Springer-Verlag)

Kudritzki, R. P. 1973, A&A, 28, 103

Kudritzki, R. P., Bresolin, F., & Przybilla, N. 2003, ApJ, 582, L83

Kudritzki, R.-P., Urbaneja, M. A., Bresolin, F., et al. 2008, ApJ, 681, 269

Kun, M., Prusti, T., Nikolić, S., Johansson, L. E. B., & Walton, N. A. 2004, A&A, 418, 89

Kurucz, R. L. 1970, SAO Special Report, 309

Kurucz, R. L. 1992, Revista Mexicana de Astronomia y Astrofisica, 23, 45

Kurucz, R. L. 1993a, CD-ROM No. 13 (SAO, Cambridge, MA)

Kurucz, R. L. 1993b, CD-ROM No. 1–12 (SAO, Cambridge, MA)

Kurucz, R. L. & Bell, B. 1995, CD-ROM No. 13 (SAO, Cambridge, MA)

Landstreet, J. D., Kupka, F., Ford, H. A., et al. 2009, A&A, 503, 973

Lemasle, B., François, P., Bono, G., et al. 2007, A&A, 467, 283

Lemasle, B., François, P., Piersimoni, A., et al. 2008, A&A, 490, 613

Lemut, A., Bemmerer, D., Confortola, F., et al. 2006, Physics Letters B, 634, 483

Levesque, E. M., Massey, P., Olsen, K. A. G., et al. 2005, ApJ, 628, 973

Lindegren, L., Babusiaux, C., Bailer-Jones, C., et al. 2008, in IAU Symposium, Vol. 248, IAU Symposium, 217–223

Luck, R. E., Gieren, W. P., Andrievsky, S. M., et al. 2003, A&A, 401, 939

Lucy, L. B. 1976, ApJ, 206, 499

Luo, D. & Pradhan, A. K. 1989, Journal of Physics B, 22, 3377

Lyubimkov, L. S., Lambert, D. L., Rostopchin, S. I., Rachkovskaya, T. M., & Poklad, D. B. 2010, MNRAS, 402, 1369

Lyubimkov, L. S., Rachkovskaya, T. M., Rostopchin, S. I., & Lambert, D. L. 2002, MNRAS, 333, 9

Maeder, A. 1980, A&A, 90, 311

Maeder, A. 2009, Physics, Formation and Evolution of Rotating Stars (Berlin: Springer)

Maeder, A. & Meynet, G. 2000, ARA&A, 38, 143

Maeder, A. & Meynet, G. 2001, A&A, 373, 555

Maeder, A. & Meynet, G. 2005, A&A, 440, 1041

Maeder, A., Meynet, G., Ekström, S., & Georgy, C. 2009, CoAst, 158, 72

Maeder, A. & Zahn, J. 1998, A&A, 334, 1000

Markova, N. & Puls, J. 2008, A&A, 478, 823

Martin, G. A., Fuhr, J. R., & Wiese, W. L. 1988, J. Phys. & Chem. Ref. Data, 17, 3

Matteucci, F. 2004, in Cosmochemistry. The melting pot of the elements, 217–256

McErlean, N. D., Lennon, D. J., & Dufton, P. L. 1999, A&A, 349, 553

Mermilliod, J. & Mermilliod, M. 1994, Catalogue of Mean UBV Data on Stars ((Berlin: Springer)

Meynet, G. & Maeder, A. 2003, A&A, 404, 975

Meynet, G. & Maeder, A. 2005, A&A, 429, 581

Mihalas, D. 1978, Stellar atmospheres /2nd edition/ (San Francisco: Freeman)

Mihalas, D. 2003, in ASP Conf. Ser., Vol. 288, ASP Conf. Ser., 471–+

Milne, E. A. 1929, Royal Society of London Philosophical Transactions Series A, 228, 421

Morrison, N. D., Richardson, N. D., & Allgaier, E. 2005, in Bulletin of the American Astronomical Society, Vol. 37, Bulletin of the American Astronomical Society, 487–+

Napiwotzki, R. 1999, A&A, 350, 101

Nelder, J. A. & Mead, R. 1965, Computer Journal, 7, 308

Nieva, M. F. & Przybilla, N. 2006, ApJ, 639, L39

Nieva, M. F. & Przybilla, N. 2008, A&A, 481, 199

Nordström, B., Mayor, M., Andersen, J., et al. 2004, A&A, 418, 989

Odenkirchen, M. & Brosche, P. 1992, Astronomische Nachrichten, 313, 69

Pagel, B. E. J. 1997, Nucleosynthesis and Chemical Evolution of Galaxies (Cambridge: Cambridge University Press)

Peytremann, E. 1974, A&A, 33, 203

Pfeiffer, M. J., Frank, C., Baumueller, D., Fuhrmann, K., & Gehren, T. 1998, A&AS, 130, 381

Prieur, J., Scardia, M., Pansecchi, L., et al. 2008, MNRAS, 387, 772

Przybilla, N. 2005, A&A, 443, 293

Przybilla, N. & Butler, K. 2001, A&A, 379, 955

Przybilla, N. & Butler, K. 2004, ApJ, 609, 1181

Przybilla, N., Butler, K., Becker, S. R., & Kudritzki, R. P. 2001a, A&A, 369, 1009

Przybilla, N., Butler, K., Becker, S. R., & Kudritzki, R. P. 2006, A&A, 445, 1099

Przybilla, N., Butler, K., Becker, S. R., Kudritzki, R. P., & Venn, K. A. 2000, A&A, 359, 1085

Przybilla, N., Butler, K., & Kudritzki, R. P. 2001b, A&A, 379, 936

Przybilla, N., Firnstein, M., Nieva, M. F., Meynet, G., & Maeder, A. 2010, A&A, 517, A38+

Przybilla, N., Nieva, M., & Butler, K. 2008, ApJ, 688, L103

Puls, J., Urbaneja, M. A., Venero, R., et al. 2005, A&A, 435, 669

Puls, J., Vink, J. S., & Najarro, F. 2008, A&A Rev., 16, 209

Reader, J., Wiese, W. L., Martin, W. C., Musgrove, A., & Fuhr, J. R. 2002, in NASA Laboratory Astrophysics Workshop, 80–+

Reed, B. C. 2000, AJ, 119, 1855

Reid, M. J., Menten, K. M., Zheng, X. W., et al. 2009, ApJ, 700, 137

Renzini, A., Greggio, L., Ritossa, C., & Ferrario, L. 1992, ApJ, 400, 280

Repolust, T., Puls, J., & Herrero, A. 2004, A&A, 415, 349

Rolleston, W. R. J., Smartt, S. J., Dufton, P. L., & Ryans, R. S. I. 2000, A&A, 363, 537

Rood, R. T., Quireza, C., Bania, T. M., Balser, D. S., & Maciel, W. J. 2007, in ASP Conf. Ser., Vol. 374, ASP Conf. Ser., 169–+

Rudolph, A. L., Fich, M., Bell, G. R., et al. 2006, ApJS, 162, 346

Ryans, R. S. I., Dufton, P. L., Rolleston, W. R. J., et al. 2002, MNRAS, 336, 577

Rybicki, G. B. & Hummer, D. G. 1991, A&A, 245, 171

Salasnich, B., Bressan, A., & Chiosi, C. 1999, in ASP Conf. Ser., Vol. 173, ASP Conf. Ser., 241–+

Salpeter, E. E. 1955, ApJ, 121, 161

Santolaya-Rey, A. E., Puls, J., & Herrero, A. 1997, A&A, 323, 488

Bibliography

Savage, B. D. & Mathis, J. S. 1979, ARA&A, 17, 73

Schaller, G., Schaerer, D., Meynet, G., & Maeder, A. 1992, A&AS, 96, 269

Schiller, F. 2010, Ph.D. Thesis, (Univ. Erlangen-Nuremberg)

Schiller, F. & Przybilla, N. 2008, A&A, 479, 849

Schmidt, M. 1959, ApJ, 129, 243

Schmidt-Kaler, T. 1982, in: Landolt-Börnstein: Numerical Data and Functional Relationships in Science and Technology - Group 6 Volume 2 (Berlin: Springer)

Schönrich, R. & Binney, J. 2009a, MNRAS, 396, 203

Schönrich, R. & Binney, J. 2009b, MNRAS, 399, 1145

Schroeder, D. J., ed. 2000, Astronomical optics (San Diego: Academic Press)

Schwarzschild, K. 1906, Nachr. Kgl. Ges. d. Wiss. zu Gött., 1, 47

Schwarzschild, K. 1914, Sitzungsberichte der Königlichen Preussischen Akademie der Wissenschaften, 47, 1183

Searle, L. 1971, ApJ, 168, 327

Searle, S. C., Prinja, R. K., Massa, D., & Ryans, R. 2008, A&A, 481, 777

Seaton, M. J., Yan, Y., Mihalas, D., & Pradhan, A. K. 1994, MNRAS, 266, 805

Shaver, P. A., McGee, R. X., Newton, L. M., Danks, A. C., & Pottasch, S. R. 1983, MNRAS, 204, 53

Skrutskie, M. F., Cutri, R. M., Stiening, R., et al. 2006, AJ, 131, 1163

Smartt, S. J. 2009, ARA&A, 47, 63

Spruit, H. C. 2002, A&A, 381, 923

Stanghellini, L. & Haywood, M. 2010, ApJ, 714, 1096

Stasińska, G. 2004, in Cosmochemistry. The melting pot of the elements, 115–170

Stehlé, C. & Hutcheon, R. 1999, A&AS, 140, 93

Sterken, C. 1977, A&A, 57, 361

Strom, S. 1966, J. Quant. Spec. Radiat. Transf., 6, 591

Strom, S. E. & Avrett, E. H. 1965, ApJS, 12, 1

Strömgren, B. 1940, Publ. Copenhagen Obs., 127

Takeda, Y. & Takada-Hidai, M. 2000, PASJ, 52, 113

Trundle, C., Dufton, P. L., Hunter, I., et al. 2007, A&A, 471, 625

U, V., Urbaneja, M. A., Kudritzki, R., et al. 2009, ApJ, 704, 1120

Unsöld, A. 1928, Zeitschrift für Physik, 46, 765

Unsöld, A. 1942, Zeitschrift für Astrophysik, 21, 22

Urbaneja, M. A., Kudritzki, R., Bresolin, F., et al. 2008, ApJ, 684, 118

van Loon, J. T. 2010, in ASP Conf. Ser., Vol. 425, ASP Conf. Ser., 279–+

Vanbeveren, D., De Loore, C., & Van Rensbergen, W. 1998, A&A Rev., 9, 63

Venn, K. A. 1995a, ApJS, 99, 659

Venn, K. A. 1995b, ApJ, 449, 839

Venn, K. A. & Przybilla, N. 2003, in ASP Conf. Ser., Vol. 304, 20

Verdugo, E., Talavera, A., & Gómez de Castro, A. I. 1999, A&A, 346, 819

Vink, J. S., Brott, I., Gräfener, G., et al. 2010, A&A, 512, L7

Vink, J. S., de Koter, A., & Lamers, H. J. G. L. M. 2001, A&A, 369, 574

von Weizsäcker, C. 1938, Phys.Z., 39, 633

Vrancken, M., Butler, K., & Becker, S. R. 1996, A&A, 311, 661

Wade, R. A. & Rucinski, S. M. 1985, A&AS, 60, 471

Walborn, N. R., Prevot, M. L., Prevot, L., et al. 1989, A&A, 219, 229

Wegner, W. 2003, Astronomische Nachrichten, 324, 219

Werner, K. & Husfeld, D. 1985, A&A, 148, 417

Whittet, D. C. B. 1977, MNRAS, 180, 29

Wiese, W. L., Fuhr, J. R., & Deters, T. M. 1996, J. Phys. Chem. Ref. Data Monograph No. 7

Wiese, W. L., Smith, M. W., & Miles, B. M. 1969, Atomic transition probabilities. Vol. 2: Sodium through Calcium. A critical data compilation (Washington, D.C: U.S. Government Printing Office)

Winkler, H. 1997, MNRAS, 287, 481

Xu, H. Y. & Li, Y. 2004a, A&A, 418, 213

Xu, H. Y. & Li, Y. 2004b, A&A, 418, 225

Yong, D., Carney, B. W., Teixera de Almeida, M. L., & Pohl, B. L. 2006, AJ, 131, 2256

Zahn, J. 1992, A&A, 265, 115

144

Danksagung

Mein erster Dank gilt meiner Familie, und hier insbesondere meinen Eltern, deren stete Unterstützung mir während Studienzeit und Dissertation eine großer Rückhalt war.

Ganz besonders zu Dank verpflichtet bin ich zudem meinem Betreuer Norbert Przybilla, der mir mit seinem extrem fundierten Wissen zu Sternatmosphären zur Seite stand und ohne dessen Pionierarbeit diese Dissertation nicht möglich gewesen wäre. In ähnlicher Weise wurde ich von Ulrich Heber mit Rat und Tat unterstützt, und sein enormer Erfahrungsschatz kam mir sehr zu Gute. Ebenfalls erwähnen möchte ich hier die anderen „Leitfiguren", die die Sternwarte prägten und prägen: Horst Drechsel, Joern Wilms und Irmela Bues.

Heiko Hirsch hat mich nicht nur als wunderbarer Freund durch Studium und Dissertation begleitet, sondern auch durch die Entwicklung von SPAS auch unschätzbare Dienste für die Beschleunigung dieser Arbeit geleistet. Viel schwerer wäre diese Zeit sicherlich geworden ohne die großartige Freundschaft mit Andreas Konrad. Danke dafür! Auch Jasmin möchte ich für die tolle gemeinsame Zeit danken, auch wenn es am Ende nicht ganz gereicht hat.

Sehr fruchtbare Diskussionen hatte ich mit meinen Zimmergenossen Stefan Neßlinger und Andreas Irrgang, was meine Arbeit enorm voranbrachte und auch für gute Stimmung sorgte. Mit Stephan Geier, Alfred Tillich, Maria Fernanda Nieva, Manfred Hanke und Florian Schiller gab es nicht nur erhellende Gespräche über Stellarastronomie, Gott und die Welt – von ihnen gab es auch noch viel Hilfe bei den Alltagsproblemen eines Astronomen.

Bei Heinz Edelmann und Ralf Napiwotzki bedanke ich mich für die Einführung in die Datenreduktion und -analyse.

Danken möchte ich auch noch Moritz, Christian, Veronika, Sebastian, Thomas, Felix, Roland, Maria und allen anderen, die die Sternwarte über die Jahre zu einem angenehmen Ort machten.